

Rui Manuel Maia Pinto de Matos

STEEL TOWERS FOR WIND TURBINES

Tese de doutoramento em Construção Metálica e Mista, orientada pelos
Professor Doutor Carlos Rebelo e o Professor Doutor Paulo Pinto, apresentada ao
Departamento de Engenharia Civil - Faculdade de Ciências e Tecnologia da Universidade de Coimbra.

Setembro de 2016



UNIVERSIDADE DE COIMBRA

Rui Manuel Maia Pinto de Matos

STEEL TOWERS FOR WIND TURBINES

Doctor of Philosophy Thesis in Steel and Composite Construction, supervised by Professor Carlos Alberto da Silva Rebelo and by Professor Paulo Miguel Cunha Matos Lopes Pinto and submitted to the Faculty of Sciences and Technology of the University of Coimbra

Coimbra, September 2016



UNIVERSIDADE DE COIMBRA



FCTUC DEPARTAMENTO DE ENGENHARIA CIVIL
FACULDADE DE CIÊNCIAS E TECNOLOGIA
UNIVERSIDADE DE COIMBRA

STEEL TOWERS FOR WIND TURBINES

(Torres metálicas de suporte a aerogeradores)

Dissertação científica na especialidade de Construção Metálica e Mista

Autor

Rui Manuel Maia Pinto de Matos

Orientadores

Prof. Doutor Carlos Alberto da Silva Rebelo

Prof. Doutor Paulo Miguel Cunha Matos Lopes Pinto

ISISE, Departamento de Engenharia Civil — Universidade de Coimbra

Coimbra, Setembro 2016

Supporting Institutions:

FCT

Fundação para a Ciência e a Tecnologia
MINISTÉRIO DA CIÊNCIA, TECNOLOGIA E ENSINO SUPERIOR



À minha família e amigos

“Live as if you were to die tomorrow. Learn as if you were to live forever.”

Mahatma Gandhi

“The best use of imagination is creativity. The worst use of imagination is anxiety.”

Deepak Chopra

“If you only read the books that everyone else is reading, you can only think what everyone else is thinking.”

Haruki Murakami

"Start with what is right rather than what is acceptable."

Franz Kafka

ABSTRACT

In the last few years it was registered an increase in the exploitation of renewable energies, namely wind energy, due to the increasing concern about the environmental problems related with the global warming. The forecast of the official entities is to increase the exploitation of the wind energy of around 61% in the European Union territory until 2020, with the implementation of newer structures for wind turbines. The same trend is followed worldwide with an increase of around 47% in the cumulative wind power installations in the same period.

The technological development of wind energy converters (WEC) makes it possible to increase the power and consequently the rotor diameter of horizontal axis wind turbines (HAWT). The main hypothesis to carry out this improvement is based on the premises of the increase in height of the wind towers to allow the exploitation of stronger and more stable wind shear profiles thus increasing the power production and the efficiency of the wind turbine. Therefore, higher towers and more efficient and cost effective foundations are required for the new generation of wind energy exploitation.

The increase in the height of the currently used tubular steel towers is possible given that the main problem that arises with the increase of diameter of the tube can be solved. Indeed, the transportation requirements with a maximum diameter of about 4.5 meters possible in public roads remains a major problem, allied with the increase of fatigue loads in the flange connections and increase in the foundations dimensions.

The work presented in this thesis has been developed in the scope of two European projects (HISTWIN and HISTWIN2) where the issues related to new type of connections in tubular towers, allowing for modularization and easier transportation, and to the improvement of foundations were studied.

The behaviour of the current tubular steel towers is presented based on a monitoring of a full functional steel tubular tower. Stresses, dynamic displacements, vibrations and vibration frequencies are presented and the estimation of a fatigue spectra based on the vertical stresses on the shell was obtained.

The feasibility of the production and assembly of a newer geometry for the towers is presented. The new geometry is composed by longitudinal bolted shear connection (modular segments) to allow the transportation and by friction connections to connect the segments together. Both these sets of connections withdraw the need of welding in and promotes the

use of bolts allowing for improvements in the fatigue resistance. One requirement of the friction connections is the need of use of bolts that allow the tightening only from the inner side of the tower. Some solutions are available in the market and the behaviour of one of them was analysed in a long term monitoring.

The improvement proposed for the foundation system focuses on the reinforcement of the shallow foundations using micropiles to improve the overturning resistance, bearing capacity and foundation stiffness. The behaviour of the micropiles to be used in this solution is studied in detail, based on experimental laboratory tests and the subsequent calibration of a 2D numerical model to implement a procedure to allow the estimation of the micropile behaviour under monotonic and cyclic loading. Recommendations on the use of grouting techniques such as IRS and IGU are made in order to increase the grout-to-soil bond strength and the micropile resistance. Finally, based on LCA and LCC analysis, the micropiles have been proven to be an environmentally friendly and economical solution for all sets of case studies under consideration.

Keywords: steel tubular towers, fatigue behaviour, BobTail bolts, friction connection, hybrid foundations, micropiles, Mohr-Coulomb model, Hardening Soil model

RESUMO

Nos últimos anos tem-se verificado um acréscimo na exploração de energias renováveis, nomeadamente na energia eólica, devido ao crescente aumento das preocupações com os problemas ambientais relacionados com o aquecimento global. As entidades oficiais preveem um crescimento da exploração de energias eólicas de cerca de 61% no território da União Europeia até 2020 com implementação de novas estruturas de suporte para torres eólicas. A mesma tendência é observada um pouco por todo o mundo com um acréscimo de cerca de 47% no acumulado de instalações de produção de energia eólica para o mesmo período.

O desenvolvimento tecnológico dos geradores de energia eólica tornou possível o aumento da potência e conseqüentemente do diâmetro do rotor nas turbinas eólicas de eixo horizontal. A principal alternativa para levar a cabo este melhoramento é baseada na premissa do aumento em altura das torres eólicas para permitir a exploração de perfis de vento mais fortes e mais estáveis aumentando conseqüentemente a produção de energia e a eficiência da turbina. Apesar das torres mais altas serem mais eficientes e economicamente vantajosas, torna-se necessária a definição de novas tipologias de fundações para esta nova vaga de exploração de energia eólica.

O aumento da altura das atuais torres eólicas tubulares metálicas é possível visto poder ser resolvido o problema inerente ao aumento do diâmetro das torres. O diâmetro máximo transportável de 4.5 metros em estradas públicas apresenta-se de facto como um problema importante, aliado ao aumento das cargas de fadiga nas ligações em flange e ao aumento das dimensões das fundações.

O trabalho apresentado foi desenvolvido no âmbito de dois projetos de investigação Europeus (HISTWIN e HISTWIN2) nos quais foram abordados os aspetos relacionados com a nova tipologia de ligações em torres metálicas tubulares que permite uma modularização da estrutura e um transporte mais fácil e com o melhoramento das fundações.

O comportamento das torres eólicas tubulares é apresentado com base na monitorização de uma torre eólica tubular em funcionamento. São apresentados esforços, deslocamentos dinâmicos, vibrações e frequências bem como a estimativa de um espectro de fadiga tendo como base os esforços verticais na casca.

É apresentada a viabilidade da produção e montagem da nova tipologia para as torres. A nova geometria é composta por ligações ao corte aparafusadas longitudinais (segmentos modulares) para permitir o transporte e ligações de atrito para unir os segmentos entre si. Ambos os

conjuntos de ligação removem qualquer necessidade de recurso a soldaduras e promovem o uso de parafusos conduzindo portanto a melhoramentos na resistência à fadiga. Um requisito das ligações de atrito é a necessidade de recurso a parafusos que permitam o aperto apenas pelo interior da torre. Existem no mercado algumas soluções disponíveis e o comportamento de uma delas foi analisado com uma monitorização de longa duração.

O melhoramento proposto para o sistema de fundação assenta no reforço das fundações diretas com recurso a microestacas para melhorar a resistência ao derrube, capacidade de carga e rigidez da fundação. O comportamento de microestacas a utilizar nesta solução é avaliado em detalhe, com recurso a ensaios laboratoriais e subsequente calibração de um modelo numérico 2D para implementar um procedimento que permita a estimativa do comportamento das microestacas sujeitas a cargas monotónicas e cíclicas. São feitas recomendações para o uso de técnicas de injeção dos tipos IRS e IGU para permitir o aumento da resistência da interface solo-calda e da própria microestacas. Por fim, e tendo como base uma análise LCA e LCC, mostrou-se que as microestacas são uma solução de reforço de fundações eficiente, quer ecológica quer ambientalmente, para todas as tipologias abordadas.

Palavras-chave: torres tubulares em aço, comportamento à fadiga, parafusos BobTail, ligações de atrito, fundações híbridas, microestacas, modelo Mohr-Coulomb, modelo Hardening Soil

ACKNOWLEDGEMENTS

Reaching this point, it is completely reassuring to have so many people to thank for their role in the development of the present study.

First of all, and obviously, my first words of gratitude are directed to the supervisors of my work. Without them, nothing that I scientifically achieved would be possible. To both Professor Carlos Rebelo and Professor Paulo Pinto I adress my honest gratitude and acknowledgments for all the patience, kindness and motivation that they gave me to accomplish this important task of my life. It was not an easy task for them however they never gave up on me. Some words of gratitude are owed to FCT for the grant conceded for the development of the work presented.

Acknowledgements are to be addressed also to Professor Carlos Rodrigues for the availability to conduct the DMT tests, to Alcoa for providing the BobTail bolts used for the long-term monitoring and to Sika for offering the adjuvants used in the preparation of the grout to be used in the experimental tests on micropiles.

Following, my gratitude is extended to my parents José and Manuela. My goal is to make them feel proud of me and of what I accomplished and I owe them that because, with all their sacrifice, they gave me all the possible chances and conditions to continue my education for as long as I wanted. A special thanks is addressed to them.

To my remaining family, I leave a special acknowledgement for being always there for me even in my absence and distance given to the needs of the work. I want to share this moment with my nephew Nuno and new member of family Maria, my sister Rosa, brother in law António, godmother Raquel and husband Bráulio, godfather Lino and wife Helena, my little cousin Bráulio, cousin Graça, cousin Fernando, uncle António. To my deceased uncles Conceição, Albertina, Armando, wherever they are, I am sure that they are looking for me and helping me on my way and that warms my soul in my darkest days.

The Professors of the rest of the group also deserve words of gratitude for all the technical help and friendship throughout this period. First of all, to Professor Luis Simões da Silva for keeping this group running so well and so efficiently, Rui Simões, Sandra Jordão, Helena Gervásio, Luis Costa Neves, Aldina Santiago, Maria Constança Rigueiro and to all of those responsible for my education.

It is usually said that “friends are the family that we can choose” and I am proud to say that, in that case, I have a huge family. All of you have a special place in my life. I just want you to know that.

It is fair that first I address an honest thank to all my roommates throughout this period. José Alexandre Henriques, my Brazilian “brother” André Tenchini, Laertes Mota, Miguel Serra, André Moura, Nuno Correia and nowadays Trayana Tankova, Hugo Augusto, Guiomar Vicente and Isabel Gomes. You are the main responsible for achieving this goal and I will never forget that neither forget you. All of you assured a special place in my life and in my mind. You have a huge share in this step.

A special thanks is also addressed to all my current colleagues in the Department Mohammad Mohammadi, Slobodanka Jovasevic, Hélder Craveiro, Jocelyn Reyes, Gabriela Lins, João Ribeiro, Ricardo Breda, João Pedro Martins, Ângela Lemos, Francisca Santos, Luis Laim, Hugo Caetano and also to the former colleagues Liliana Marques, Filippo Gentili, Ashkan Shahbazian, Marco Pinho, Rodolfo Martins, João Pereira which contributed in a huge way for the awesome working environment created which made me want to go up every morning and to go to Coimbra. A special thank is addressed to Cécile Haremza (and José Henriques) for the sweetheart Théo Henriques. All of you make me so proud of being my friend.

The role of those who helped me both in administrative processes as well as in the laboratory cannot be forgotten. Manuela Rodrigues, Cristina Carolino, Dulce Rodrigues, Dona Lucinda, Ricardo Oliveira, Nuno Almeida, Luis Gaspar, Fernando Rodrigues, Hélder Fabião, José António you played an important part in this outcome.

All my Brazilian “family” cannot be forgotten now. Rafael Lopes, Fernanda Lopes, new-born Carolina (to whom I am eager to meet in person), Tiago Anselmo, Thaisa Leal, Lauro Ribeiro even there is this lagoon in the middle of us, you are not forgotten and I hope to see all of you soon enough.

My friends from my hometown Carapinheira are the responsible for keeping me so motivated during my all life. They shaped my personality and all the qualities that I have I owe to them. A special thanks to Cátia Marques, Simão Rama, Marta Monteiro, Eduardo Santana (and their greatest achievement, the amazing and hilarious, dear Santiago), family Santos and Marques, Joana Rama, Ricardo Pires and the gorgeous Laura, Tiago Rodrigues, Celso Rama, Susana Cunha, Conceição Vaz, António Domingues, Luis Cavaleiro, Lara Azambujo, Eduardo Costa, Miguel Ângelo Silva, Mário Carapinheiro and Verónica Vidal. I love all and each one of you. Thank you for all the moments that we share together.

The former colleagues from the bachelor that remained close are a big piece in this puzzle. Luis Duarte, Inês Simões, Nuno Paulino, Nuno Resende, Ricardo Ceia, Ricardo Fonseca, David Branco, Marco Chaves, Zita Rosa, Ana Azevedo. Thank you for keeping in contact.

Freddy Mercury used to say “Friends will be friends / When you're in need of love / They give care and attention / Friends will be friends”. In my life, this sentence is full of meaning and I feel blessed for that.

Finally, the last acknowledgements are to be addressed to the two most important person in my life. To my two godsons, Amélia França and the new coming Tiago. They push me to be a better person because I have the duty to be a role model for them. I feel that I could do anything for them and for their wellbeing. They are the love of my life.

To all of you and even to those I forgot to mention but knows their meaning in my life, a huge thank. I always will be in debt with you.

"Friendship is the hardest thing in the world to explain. It's not something you learn in school. But if you haven't learned the meaning of friendship, you really haven't learned anything."

Muhammad Ali

CONTENTS

1. INTRODUCTION	1
1.1. WIND ENERGY IMPACT - GENERAL CONSIDERATIONS	1
1.2. OBJECTIVES.....	5
1.3. SCOPE OF THE THESIS.....	6
2. WIND TOWERS – ACTUAL SOLUTIONS	9
2.1. OVERVIEW ON THE EVOLUTION OF THE WIND ENERGY EXPLOITATION.....	9
2.2. BEHAVIOUR OF WIND TOWERS – LONG-TERM MONITORING	14
2.2.1. Description of the wind tower and measurement system	14
2.2.2. System calibration	23
2.2.3. Measurement results	26
2.2.4. Methodology for estimation of experimental Fatigue Spectra.....	40
2.3. FINAL COMMENTS	44
3. IMPROVED SOLUTIONS FOR HIGHER TOWERS	47
3.1. INTRODUCTION	47
3.2. TOWER DESIGN RECOMMENDATIONS.....	53
3.3. CONNECTIONS IN TUBULAR STEEL TOWERS.....	53
3.4. FINAL COMMENTS	76
4. FOUNDATION SOLUTIONS FOR ONSHORE WIND TOWERS	79
4.1. INTRODUCTION	79

4.2.	DESIGN OF HYBRID FOUNDATIONS	84
4.2.1.	Description of the case studies	84
4.2.2.	Foundation design criteria.....	87
4.2.3.	Foundation design.....	93
4.3.	LCA AND LCC ANALYSIS OF HYBRID FOUNDATIONS	99
4.4.	FINAL COMMENTS	106
5.	HYBRID FOUNDATIONS – EXPERIMENTAL TESTS ON MICROPILES	109
5.1.	INTRODUCTION.....	109
5.2.	BACKGROUND INFORMATION	110
5.3.	EXPERIMENTAL LAYOUT AND ASSEMBLY PROCEDURE.....	113
5.4.	TEST SET-UP	123
5.4.1.	Specimen properties.....	123
5.4.2.	Sand shear behaviour and stress-strain relation and experimental physical and mechanical properties.....	125
5.4.3.	Grout properties	133
5.5.	EXPERIMENTAL RESULTS	138
5.5.1.	Overview.....	138
5.5.2.	Resistance	138
5.5.3.	Stiffness	145
5.6.	FINAL COMMENTS	148
6.	HYBRID FOUNDATIONS – NUMERICAL ANALYSIS.....	151
6.1.	INTRODUCTION.....	151

6.2.	MATERIAL MODELS	152
6.2.1.	Overview	152
6.2.2.	Mohr-Coulomb model	154
6.2.3.	Hardening Soil model	155
6.3.	NUMERICAL PARAMETERS – SOIL PROPERTIES AND NUMERICAL MODEL VALUES	159
6.4.	NUMERICAL MODEL DESCRIPTION AND CALIBRATION	217
6.4.1.	Numerical model description.....	217
6.4.2.	Sensitivity analysis	217
6.4.3.	Numerical model calibration	217
6.5.	REAL-SCALE MICROPILE BEHAVIOUR	217
6.5.1.	Loose sand ($I_D=30\%$).....	217
6.5.2.	Dense sand ($I_D=70\%$)	217
6.6.	DESIGN REVIEW OF HYBRID FOUNDATIONS – DETAILED ANALYSIS OF MICROPILES INSTALLED IN HYBRID FOUNDATIONS FOR WIND TOWERS.....	217
6.7.	FINAL COMMENTS	217
7.	CONCLUSIONS.....	217
7.1.	GENERAL CONCLUSIONS AND FINAL REMARKS	217
7.2.	FUTURE WORK	217
7.3.	PERSONAL CONTRIBUTIONS AND PUBLICATIONS.....	217
	REFERENCES	217
	ANNEX A – CALIBRATION ERRORS FOR STRAIN GAUGES	219
	ANNEX B - INDIVIDUAL RESULTS OF BOLT STRAIN GAUGES CALIBRATION TESTS.....	223

ANNEX C - APPLIED FORCE VARIATION CURVES (BY ROW) – PROTOTYPE 2	229
ANNEX D - DMT CALCULATION PROCEDURE (MARCHETTI ET AL. 2001)....	231
ANNEX E – STATIC/POST-CYCLIC STIFFNESS (EXPERIMENTAL TESTS ON MICROPILES)	233
ANNEX F – HYBRID FOUNDATION DESIGN EXAMPLE (80M HIGH TUBULAR STEEL WIND TOWER).....	239

LIST OF FIGURES

Figure 1.1 – EU member state market shares for new wind energy capacity installed during 2014 (MW) (adapted from EWEA (2015))	2
Figure 1.2 – Share of new power capacity installations in EU (MW) (adapted from EWEA (2015))	2
Figure 1.3 – Cumulative wind power installations in the EU (GW) (adapted from EWEA (2015))	2
Figure 1.4 – Annual onshore and offshore installations (MW) (adapted from EWEA (2015)).	3
Figure 1.5 – Global cumulative wind power installations (GW) (adapted from GWEC (2015))	3
Figure 1.6 – Annual cumulative capacity (2011-2015) for offshore wind energy exploitation (adapted from GWEC (2015))	4
Figure 1.7 - Previous EWEA, NREAP, EC Primes and new EWEA 2020 scenarios (adapted from EWEA 2014)	4
Figure 1.8 – Market forecast for 2016-2020 (GW) (adapted from GWEC (2015))	5
Figure 2.1 – Ancient windmill/windwheel models (Hau, 2013)	9
Figure 2.2 – Poul La Cour’s first electricity producing wind turbine in 1891 in Askov, Denmark (Hau, 2013)	10
Figure 2.3 – Components of a horizontal-axis wind turbine (adapted from Hau, 2013)	10
Figure 2.4 - Free-standing tubular steel towers (adapted from Hau, 2013)	11
Figure 2.5 - Lattice tower of a Vestas V80 wind turbine (Hau, 2013)	12
Figure 2.6 – Concrete towers (Hau, 2013)	13

Figure 2.7 - Constructional concept of the concrete/steel hybrid tower designed for the Repower 3.3 MW wind turbine (Max Bögl Group) (adapted from Hau, 2013).....	13
Figure 2.8 - Instrumented tower in Marvila, Portugal	17
Figure 2.9 - Steel wind tower composed by three parts; Cut A-A (d) shows the ventilation opening (optional) and the door opening (adapted from Veljkovic et al., 2012).....	19
Figure 2.10 – Details of strain gauges application.....	20
Figure 2.11 - Sensors locations and identification (Rebello et al., 2012a)	21
Figure 2.12 – Layout of the communications inside the tower (Veljkovic et al., 2012)	22
Figure 2.13 – Time evolution of the several dynamic and quasi-static signal components (Rebello et al., 2012a).....	25
Figure 2.14 – Stress variation at Level 0 due to nacelle eccentricity depending on Nacelle azimuth.....	26
Figure 2.15 – Vertical stress fluctuation – level 0	27
Figure 2.16 – Vertical stress fluctuation – level 1	27
Figure 2.17 – Horizontal stress fluctuation – level 0	28
Figure 2.18 – Horizontal stress fluctuation – level 1	28
Figure 2.19 – Inclined stress fluctuation – level 0	28
Figure 2.20 – Inclined stress fluctuation – level 1	29
Figure 2.21 – Estimation procedure for principal stress direction and intensity (Beer et al., 2012)	29
Figure 2.22 – Principal stress fluctuation – level 0.....	30
Figure 2.23 – Principal stress fluctuation – level 1.....	30

Figure 2.24 - Typical time histories: a) vertical stress at points L0R22V and L0R25V and respective sum; b) nacelle azimuth – positive clockwise from North direction; c) wind speed at nacelle level – Phase I	31
Figure 2.25 - Time signals obtained during Phase II with trigger based on wind speed greater than 14m/s a) vertical stress at strain sensors L0R22V and L0R25V; b) nacelle azimuth – positive direction is clockwise; c) wind speed	32
Figure 2.26 - Comparison between bolt stresses and shell vertical stresses at level 1	33
Figure 2.27 - Comparison of stresses in bolts (dark curves) with vertical stresses in shell at level 1 during the second measurement period; a) L1B1 – L1R15V; b) L1B2 - L1R16V; c) L1B3 – L1R17V; d) L1B5 – L1R19V; e) L1B6 – L1R20V	34
Figure 2.28 - Stress increase in the bolts due to retightening.....	34
Figure 2.29 - Bending moment vectors represented by their amplitude and direction in polar coordinates; a) entire Phase II; b) selected 2000 seconds	35
Figure 2.30 - Typical time histories for bending moments obtained from strain measurements during wind speed average of 16.5m/s	35
Figure 2.31 - Bending moments M_x , M_y and resultant M obtained from selected shell stress measurements; mean values over 40 seconds; wind speed average is 16.5m/s	36
Figure 2.32 - Singular values of the spectral density matrices.....	37
Figure 2.33 - Power spectral densities of the acceleration at the tower level 3 obtained during operation	38
Figure 2.34 - Typical time window of tower inclination measured at levels 2 and 3	39
Figure 2.35 - Typical time window of horizontal displacements at level 3 in x- and y-direction obtained from time integration of filtered accelerations using a highpass Butterworth filter above 0.2Hz	40
Figure 2.36 – Characteristic occurrences of a load-time history $P(t)$ (Schijve, 2009)	40
Figure 2.37 - Measured fatigue spectra extrapolated for 20 years lifetime obtained for level 0	42

Figure 2.38 - Fatigue strength curves for direct stress ranges (EN 1993-1-9, 2005).....	42
Figure 2.39 - Comparison of measured fatigue spectrum extrapolated for 20 years lifetime with design spectrum and strength curve obtained from EN1993-1-9 (2005) for detail 71	43
Figure 3.1 – Wind shear profile (Hau, 2013).....	47
Figure 3.2 – Flow wake behind an obstacle (Hau, 2013)	48
Figure 3.3 – Problems associated with the increase in height	48
Figure 3.4: Steel tubular towers	49
Figure 3.5: Modular concrete INNEO tower (INNEO Torres, 2008).....	50
Figure 3.6 - 160m Fuhrländer Wind Turbine Laasow (Almeida, 2015).....	50
Figure 3.7: Space Frame Wind Tower (General Electric, 2014)	51
Figure 3.8: Timber wind tower (Engström et al., 2010)	51
Figure 3.9: Hybrid steel lattice-tubular tower.....	52
Figure 3.10 – Summary of tower alternatives (Engström et al., 2010).....	52
Figure 3.11 – Ring flange connections geometry (Seidel and Schaumann, 2001).....	54
Figure 3.12 – Segment joint with friction connection (Husson, 2008).....	56
Figure 3.13 – Modularized wind tower (Heistermann, 2014).....	57
Figure 3.14 - 15mm thick connection assembly	58
Figure 3.15 – Assembly of the lower segment (20mm thick connection)	58
Figure 3.16 – Final assembly of both segments (20mm thick connection)	58
Figure 3.17 – Types of bolts used	59

Figure 3.18 – Force and temperature variation in BobTail of prototype 1	60
Figure 3.19 – 1” BobTail bolts geometrical characteristics	61
Figure 3.20 – Pieces to connect the bolts to the hydraulic jack.....	62
Figure 3.21 - Bolts strain gauges calibration set-up	62
Figure 3.22 – Calibration tests protocols.....	63
Figure 3.23 – Gaps between bottom and top segments	63
Figure 3.24 – Data acquisition system	64
Figure 3.25 – Local area network scheme.....	64
Figure 3.26 – Isostatic specimen	64
Figure 3.27 – Instrumented bolts distribution	65
Figure 3.28 – Friction connection tightening sequence.....	66
Figure 3.29 – Marked bumps.....	66
Figure 3.30 – Friction connection (“finger” configuration example).....	68
Figure 3.31 - Hammerstein-Weiner Block Diagram (The MathWorks Inc., 2010)	68
Figure 3.32 - Schematic of the friction connection with the preloaded area.....	71
Figure 3.33 – Comparison between measured and identified force – isostatic bolt.....	73
Figure 3.34 – Error of identification – isostatic bolt	73
Figure 3.35 - Force time series in 1 year for constant temperature – isostatic bolt.....	74
Figure 3.36 - Force loss estimation in constant temperature for 20 years - isostatic bolt	74
Figure 3.37 - Logarithmic curve fitting vs Hammerstein-Weiner identification – isostatic bolt	75

Figure 3.38 - Force loss estimation in constant temperature for 20 years - overlapping bolt 876	
Figure 4.1 - Patrick and Handerson deep foundation solution (Earth Systems Global Inc., 2009)	80
Figure 4.2 – Foundation typologies considered (Khatri, 2010)	81
Figure 4.3 - Micropile application on wind turbine foundations (Aschenbroich, 2010)	83
Figure 4.4 – Star foundation system (Phuly, 2011)	83
Figure 4.5 - Geometry of the octagonal foundation.....	84
Figure 4.6 – Stress distribution in the foundation base.....	90
Figure 4.6 - Numerical model example - top view	94
Figure 4.7 - Spring models.....	94
Figure 4.8 - Micropile locations.....	96
Figure 4.9 - Comparison of global warming potential (GWP) for shallow and hybrid foundations.....	103
Figure 4.10 - Comparison of primary energy demand (PED) for shallow and hybrid foundations.....	103
Figure 4.11 - Construction and demolition costs of shallow and hybrid foundations	105
Figure 4.12 - Total present value (in €) of each foundation	106
Figure 5.1 - Micropile Classification System Based on Type of Grouting (FHWA, 2005) ..	110
Figure 5.2 – Test layout	113
Figure 5.3 - Soil container geometry	114
Figure 5.4 - Soil container.....	115
Figure 5.5 - 20 tons (200kN) actuator.....	115

Figure 5.6 - Micropile preparation (instrumentation and drilling)	116
Figure 5.7 - Grout exit holes protection (tube à manchette).....	116
Figure 5.8 - Micropile positions in layouts – front and top view	117
Figure 5.9 - Micropiles placing and levelling system	117
Figure 5.10 - Soil loading process	118
Figure 5.11 - Loading test apparatus	118
Figure 5.12 - Grout pressure system.....	119
Figure 5.13 – Grout injection process	119
Figure 5.14 – Soil discharging process.....	120
Figure 5.15 – Soil storing	120
Figure 5.16 – Single tests assembly procedure and duration	121
Figure 5.17 - Group tests assembly procedure and duration	121
Figure 5.18 - Loading protocols	123
Figure 5.19 - Single specimens geometry	123
Figure 5.20 - Group specimens geometry	124
Figure 5.21 – Strain gauges and micropile positions.....	124
Figure 5.22 – Mohr-Coulomb failure envelope (Matos Fernandes, 2011).....	126
Figure 5.23 – Linear approximation to the rupture envelope (adapted from Matos Fernandes (2011))	126
Figure 5.24 – Deviatoric stress evolution in triaxial tests (adapted from Matos Fernandes (2011)).....	127

Figure 5.25 – Evolution of the volumetric strain and void ratio with the axial strain – drained triaxial test (adapted from Matos Fernandes (2011)).....	127
Figure 5.26 – Definition of the dilatancy angle (Matos Fernandes, 2011)	128
Figure 5.27 – Analogy for dilatancy (without and with positive dilatancy) (Bolton, 1986) .	128
Figure 5.28 – Secant and tangential modulus (Matos Fernandes, 2011)	129
Figure 5.29 - Sieve analysis curves (Coelho, 2011)	130
Figure 5.30 - Friction angle vs. density index (triaxial tests) (adapted from Schmertmann (1978)).....	131
Figure 5.31 - DMT tests.....	131
Figure 5.32 - DMT results.....	132
Figure 5.33 - Grout control tests results.....	133
Figure 5.34 – Marsh cone standard measures	134
Figure 5.35 – Grout tests equipment	135
Figure 5.36 – Grout compressive test specimens.....	135
Figure 5.37 – Grout compression specimen appearance.....	136
Figure 5.38 - Single tests grout distribution.....	136
Figure 5.39 - Group tests grout distribution.....	137
Figure 5.40 - Force-displacement curves (single tests – compression)	139
Figure 5.41 - Cyclic detail (single tests – compression)	139
Figure 5.42 - Force-displacement curves (single tests – tension).....	139
Figure 5.43 - Cyclic detail (single tests – tension).....	140

Figure 5.44 - Force-displacement curves (group tests)	140
Figure 5.45 - Cyclic detail (group tests)	140
Figure 5.46 - Cyclic and monotonic stiffness estimation procedure	146
Figure 5.47 - Single tests cyclic stiffness	146
Figure 5.48 - Group tests cyclic stiffness	147
Figure 6.1 – Numerical modelling strategy	153
Figure 6.2 - Typical representation of stiffness variation in as a function of the shear strain amplitudes; comparison with the ranges for typical geotechnical problems and different tests (Obrzud, 2010)	154
Figure 6.3 - Recommendations for the soil model choice for soil type and types of analysis. Dashed line: may be used but not recommended in terms of quality of results; Solid line: can be applied; HS models: recommended (Obrzud, 2010).....	154
Figure 6.4 – Approximation of MC model result to a triaxial test curve	155
Figure 6.5 – HS characteristic stress-strain curve and parameter definition (Plaxis, 2006)...	156
Figure 6.6 – Principal stress space representation of HS model surfaces (Plaxis, 2006).....	157
Figure 6.7 – Illustration of vertical preconsolidation stress in relation to the in-situ vertical stress using OCR and POP (Plaxis, 2006).....	157
Figure 6.8 - Evolution of the stress state and yielding surfaces of HS model (Sture, 2004)..	158
Figure 6.9 – Shear model geometry.....	158
Figure 6.10 – Cap position influence (5 cycles).....	158
Figure 6.11 – Numerical model geometry and elements mesh (model 1).....	217
Figure 6.12 – Interface position and description (model 2)	217
Figure 6.13 – Compression force-displacement curves (different soil densities)	217

Figure 6.14 – Tension force-displacement curves (different soil densities).....	217
Figure 6.15 – Compression force-displacement curves comparison between real (experimental) and augmented model dimensions.....	217
Figure 6.16 – Effect of the E_{OED} (kPa) value on the response of a micropile (HS model with $R_{inter}=0.9$) – 12m long micropile	217
Figure 6.17 – Effect of the E_{UR} (kPa) value on the response of a micropile – 3m long micropile	217
Figure 6.18 – Effect of the dilatancy angle value on the response of a micropile	217
Figure 6.19 - Effect of the K_0 value on the response of a micropile.....	217
Figure 6.20 - Effect of the ν value on the response of a micropile ($R_{inter}=0,2$; MC – $E=5000kPa$; HS – $E_{50}^{ref}=10000kPa$)	217
Figure 6.21 – Calibration force-displacement curves for monotonic tests	217
Figure 6.22 – Power regression for E value (low density sand)	217
Figure 6.23 – Dependency of the elastic modulus and the effective confining stress (adapted from Matos Fernandes (2011))	217
Figure 6.24 – Equivalent grouted diameter estimation procedure	217
Figure 6.25 – Principal stress directions	217
Figure 6.26 – Principal stress intensity	217
Figure 6.27 – Shear stress comparison.....	217
Figure 6.28 – σ_x and σ_y variation along the radial distance (HS model with $R_{inter}=0.9$).....	217
Figure 6.29 – Calibration force-displacement curves for cyclic+monotonic tests	217
Figure 6.30 – Force-displacement curves for 12m long micropile and comparison with 3m long results (monotonic loading on grouted specimens)	217

Figure 6.31 – Force-displacement curves for 12m long micropile and comparison with 3m long results (cyclic+monotonic loading).....	217
Figure 6.32 – Cyclic secant stiffness on grouted specimens – D30	217
Figure 6.33 - Force-displacement curves for 12m long micropile in high density and comparison with 12m long micropiles in low density sand (monotonic loading).....	217
Figure 6.34 – Power regression for E value (high density sand).....	217
Figure 6.35 - Force-displacement curves for 12m long micropile in high density and comparison with 12m long micropiles in low density sand (cyclic+monotonic loading)	217
Figure 6.36 – Cyclic secant stiffness	217
Figure 6.37 – Abacus for the estimation of the value of q_s for sands including the estimations for the considered D30 and D70 sand (adapted from Bustamante and Doix (1985))	217
Figure 6.38 – Grout-to-ground bond strength variation in depth for IGU grouting	217
Figure 6.39 – Abacus for the estimation of the value of q_{s_gr} on soil nailing technique with gravitic grout injection (Presses de l’Ecole Nationale des Ponts et Chaussées, 2002) ..	217
Figure 6.40 – Bilinear curve comparison between the behaviour assumed for the design examples and the results obtained for each considered soil model on low and high density sand	217
Figure 6.41 – Real tests on micropile with IRS grouting technique (Tecnasol, 2010)	217
Figure 6.42 – Parametric analysis on the influence of relevant parameters for the behaviour of the foundation.....	217
Figure 6.43 – Characteristic base bending moment induced by wind loading on a 150m high wind tower – 12m/s wind speed	217
Figure 6.44 – Compressive force-displacement curves comparison between the response micropiles under wind induced vibration loading (NTM) and micropiles under initial cyclic loading.....	217

- Figure 6.45 – Tensile force-displacement curves including bilinear spring model approximation 217
- Figure 6.46 – Cyclic stiffness due to the wind induced vibration loading..... 217

LIST OF TABLES

Table 2.1 – Tube cross-section properties along the height	16
Table 2.2 – Sensitivity of accelerometers.....	23
Table 2.3 – Calibration factors for inclinometers.....	23
Table 2.4 – Calibration factors for strain gauges.....	24
Table 2.5 – Values measured with full nacelle rotation	25
Table 2.6 – Vertical stresses in the shell during the testing period of Phase I for which wind speed maximum was 25m/s and average was 8.3m/s.....	31
Table 2.7 - Vertical stresses computed from design load cases given for the instrumented tower	32
Table 2.8 - Natural frequencies, modes and damping	37
Table 2.9 - Transverse butt welds (fatigue detail category) (EN 1993-1-9 2005).....	43
Table 3.1 - EC 3 1-9 Fatigue detail categories (bolts in tension and butt welds) (EN 1993-1-9, 2005).....	55
Table 3.2 – Slip factors for various surface finishing of S690 and S355 (Heistermann, 2011)	56
Table 3.3 – Percentage of installed force after tightening on BobTail bolts – prototype 1.....	60
Table 3.4 – 1” BobTail bolts mechanical characteristics	61
Table 3.5 – Type and location of the BobTail used – prototype 2	62
Table 3.6 – Bolts tightening forces.....	67
Table 3.7 - Percentage of force loss after tightening of adjacent and non-adjacent bolts	70

Table 4.1 – Shallow and hybrid foundation comparison (Khatri, 2010)	82
Table 4.2 - Soil properties.....	85
Table 4.3 - Load resultants on the foundation base	87
Table 4.4 - Partial factors on actions (γ_F) and soil parameters (γ_M) (EN 1997-1, 2004).....	88
Table 4.5 - Partial factors on actions (γ_F) (IEC 61400-1, 2005)	89
Table 4.6 - Partial resistance factors (γ_S) for driven piles (EN 1997-1, 2004).....	93
Table 4.7 - Shallow foundations	97
Table 4.8 - Hybrid foundations	98
Table 4.9 - Environmental indicators considered for LCA.....	100
Table 4.10 - Results of the environmental analysis for the shallow foundations	101
Table 4.11 - Results of the environmental analysis for the hybrid foundations	102
Table 4.12 - Unit costs for the construction of hybrid and shallow foundations (prices valid for Portugal in year 2014)	104
Table 5.1 - Experimental tests description.....	122
Table 5.2 - Sand index density.....	122
Table 5.3 – Soil physical properties (Coelho, 2011).....	130
Table 5.4 – Friction angle and elasticity modulus (triaxial tests)	130
Table 5.5 – Grout geometry	138
Table 5.6 – Single tests resistance and static/post-cyclic stiffness	141
Table 5.7 – Group tests resistance and static/post-cyclic stiffness	142

Table 5.8 – Unit skin friction	144
Table 6.1 – Soil mechanical properties – triaxial tests (Ferreira (2014))	217
Table 6.2 – Calibration parameters for MC and HS models	217
Table 6.3 – E values for MC model (triaxial tests calibration) – loose sand.....	217
Table 6.4 – Calibration parameters (monotonic tests).....	217
Table 6.5 – Calibration parameters (cyclic+monotonic tests).....	217
Table 6.6 – Initial stiffness and resistance (monotonic compression ungrouted) – D30.....	217
Table 6.7 – Initial stiffness and resistance (monotonic tension grouted) – D30	217
Table 6.8 – Initial stiffness and resistance (cyclic+monotonic compression grouted) – D30	217
Table 6.9 – Initial stiffness and resistance (cyclic+ monotonic tension grouted) – D30	217
Table 6.10 – E values for MC model (triaxial tests calibration) – high density sand	217
Table 6.11 – Initial stiffness and resistance (monotonic compression grouted) – D70.....	217
Table 6.12 – Initial stiffness and resistance (monotonic tension grouted) – D70	217
Table 6.13 – Initial stiffness and resistance (cyclic+monotonic compression grouted) – D70	217
Table 6.14 – Initial stiffness and resistance (cyclic+monotonic tension grouted) – D70	217
Table 6.15 – Estimated values for q_s for IGU considering the method proposed by Bustamante and Doix (1985).....	217
Table 6.16 - Hybrid foundation geometry with grouted micropiles under very low pressure grout.....	217

NOTATIONS

Lowercases

c'	cohesion intercept in terms of effective stress
e	eccentricity/soil void index ratio
f_u	ultimate strength
f_y	yield strength
h	height of the grout (exudation tests)/depth of the soil
k_c	cyclic stiffness
k_m	monotonic stiffness
k_s	reduction factor for fatigue stress to account for size effects
k_z	soil's secant coefficient of subgrade reaction
m	slope of fatigue strength curve/ power for stress dependency (HS model)
n	number of the friction surfaces or the number of fastener holes on the shear face
n_{Ei}	number of cycles associated with the stress range $\gamma_{Fi}\Delta\sigma_i$
P_a	atmospheric pressure
p_{ref}	reference stress
q	behaviour factor
q_s	shear resistance
q_{s_gr}	ultimate grout-to-ground shear strength
r	total resistance of the leadwire per meter
t	thickness

Uppercases

$(N_1)_{60}$	SPT blow count adjusted to an effective overburden pressure of 100kPa
A_s	tensile stress area

B	foundation diameter
C_n	overburden correction factor
D	microple diameter
D_b	diameter of the bond length of the micropile
D_d	fatigue damage
E	Young's modulus
E_{50}	soil Young's modulus at 50% Stress Level
E_f	foundation Young's modulus
E_i	soil initial Young's modulus
E_{oed}	oedometer modulus
E_s	soil secant Young's modulus
E_t	soil tangent Young's modulus
E_{ur}	unloading/reloading Young's modulus
$F_{p,c}$	bolt preload force
$F_{S,R}$	slip resistance per bolt at the ultimate limit state
$F_{t,R}$	value of tension resistance
$F_{v,R}$	value of shear resistance
G	shear modulus
I_d	density index
I_f	foundation inertia modulus
K	gauge factor
K_0	at rest lateral earth pressure coefficient
L	length
L_b	bond length of the micropile
M	soil vertical drained constrained modulus
M_x, M_y	bending moment
N_{60}	energy corrected SPT blow count
N_R	design life time expressed as number of cycles related to a constant stress range
N_{Ri}	design life time expressed as number of cycles related to a constant stress range
N_{Rk}	characteristic value of tension resistance

N_{SPT}	SPT blow count
P_1	Ménard limit pressure
R	foundation radius/strain gauge resistance
R_c	micropile internal (structural) compressive resistance
R_{inter}	soil and interface strength relation parameter
R_t	micropile internal (structural) tensile resistance
$S_{j,\text{ini}}$	initial stiffness
$V_{a,\text{Rk}}$	characteristic value of shear resistance
V_{ref}	reference wind speed

Lowercases Greek Letters

α	thermal expansion coefficient
γ	weight density/distortion
γ_F	partial factors on actions
γ_{Ff}	partial factor for equivalent constant amplitude stress ranges $\Delta\sigma E$
γ_M	partial factors on materials
γ_{Mf}	partial factor for fatigue strength $\Delta\sigma C$
γ_{Mi}	partial safety factors
γ_n	partial safety factor for consequences of failure
γ_{Rd}	model factor for micropile resistance
γ_s	partial factor for the shear resistance in compression
$\gamma_{s,t}$	partial factor for the shear resistance in tension
δ	displacement
$\delta\varepsilon$	strain variation
ε	strain
εL	leadwire thermal output
ε_{vol}	volumetric strain
η	efficiency coefficient for micropiles

θ	stress inclination angle
μ_s	slip factor
ν_s	soil Poisson ration
ρ	density
σ'	effective stress
σ'_f	normal stress on failure
$\sigma_1, \sigma_2, \sigma_3$	principal stress
$\sigma_x, \sigma_y, \sigma_z$	stress
σ_θ	inclined stress with angle θ
τ'_f	shear stress at failure
τ_{xy}	shear stress
ϕ'	angle of shearing resistance in terms of effective stress
ϕ'_{cv}	critical state angle of shearing resistance
ψ	dilatancy angle

Uppercase Greek Letters

ΔF	force variation
ΔF_p	force variation in the bolts
Δt	time interval
$\Delta \sigma_C$	reference value of the fatigue strength at $N_C = 2$ million cycles
$\Delta \sigma_D$	fatigue limit for constant amplitude stress ranges at the number of cycles N_D
$\Delta \sigma_L$	cut-off limit for stress ranges at the number of cycle N_L
$\Delta \sigma_R$	direct stress range
Ω	cross-section of element

Abbreviations

ASTM	American Society for Testing and Materials
------	--------------------------------------------

CFD	Computational Fluid Dynamics
DEL	Damage Equivalent Load
DMT	Flat Dilatometer Test
DNV	Det Norske Veritas
EC	European Commission
EFDD	Enhanced Frequency Domain Decomposition
EO	Extreme Wind Load in Operating Condition
EQ	Earthquake Load
EU	European Union
EWM	Extreme Wind Load in Non-Operating Condition
EWEA	European Wind Energy Association
FCT	Fundação para a Ciência e Tecnologia
FHWA	Federal Highway Administration
GL	Germanischer Lloyd
GPRS	General Packet Radio Service
GSM	Global System for Mobile Communications
GWEC	Global Wind Energy Council
GWP	Global Warming Potential
HAWT	Horizontal Axis Wind Turbines
HS	Hardening Soil model
IEC	International Electrotechnical Commission
IGU	Injection Globale Unitaire
IRS	Injection Répétitive et Sélective
ISO	International Organization for Standardization
LCA	Life Cycle Analysis
LCC	Life Cycle Cost
MC	Mohr-Coulomb soil model
NDT	Nondestructive testing
NTM	Normal Turbulence Model
NREAP	National Renewable Energy Action Plan

ODP	Ozone Depletion
POP	Pre-Overburden Pressure
PV	Photovoltaic
RFCS	Research Fund for Coal and Steel
RMS	Root Mean Square
TCB	Tension Control Bolts
TCP-IP	Transmission Control Protocol-Internet Protocol
WEC	Wind Energy Converters
WT	Wind Towers

1. INTRODUCTION

1.1. Wind energy impact - general considerations

The concern about the environmental problems has led to an increase in the exploitation of renewable energy such as hydraulic, solar, geothermal, although the most significant increase can be observed in the wind energy exploitation.

This work is related with the theme of support structures for the wind energy converters, namely the evaluation and the feasibility of the use of taller steel tubular towers to support multi-megawatt wind turbine generators which will allow higher production rates.

The annual report of the European Wind Energy Association (EWEA, 2015) regarding the year of 2014 shows an increase in the installation of wind turbines across all Europe. This increase is led by Germany and UK which together represent an increase of 59.5% of the total European gain, according to Figure 1.1.

In comparison with other renewable and even non-renewable energies, wind energy presents the highest share of new power capacity installations in EU followed by Photovoltaic (PV) installations, according to the values presented in Figure 1.2. In 14 years, the market share for wind energy increased from 2.4% up to 14.1% (EWEA, 2015).

The increase in the exploitation of wind energy can also be concluded within the report provided by EWEA (EWEA, 2015) in which the tendency of the cumulative wind power installation is obvious, as it can be found in Figure 1.3. In the last years, there was also a tendency of increase in the exploitation of wind energy using offshore wind towers increasing that way the share in the wind energy market (Figure 1.4).

The observed tendency in wind energy exploitation presented to the European territory follows the same trend as the increase registered worldwide. Driven by Chinese and American markets which presents respectively 33.6% and 17.2% of the global wind energy market share (GWEC, 2015), these two markets represent also 48.5% and 13.5% of new installations within the period of January to December of 2015 standing as the international leaders in terms of new installations and empowering their position as the world biggest producers. Asia stands clearly as the continent with higher rates of new installation followed by Europe. North America follows the two leading continents and the rest of the world represents a marginal value in comparison with the three leading regions.

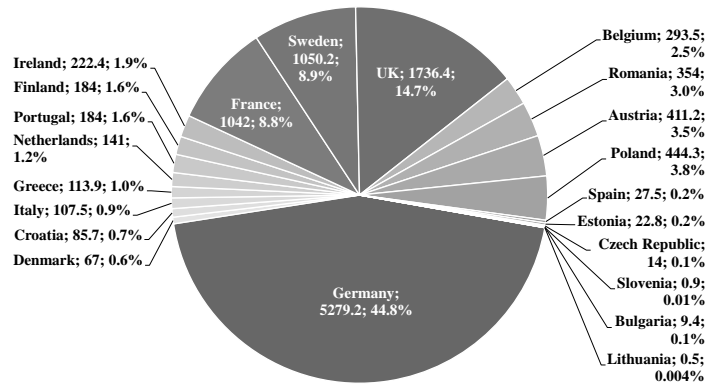


Figure 1.1 – EU member state market shares for new wind energy capacity installed during 2014 (MW) (adapted from EWEA (2015))

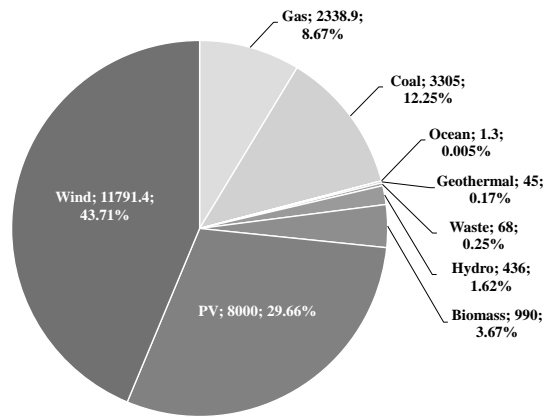


Figure 1.2 – Share of new power capacity installations in EU (MW) (adapted from EWEA (2015))

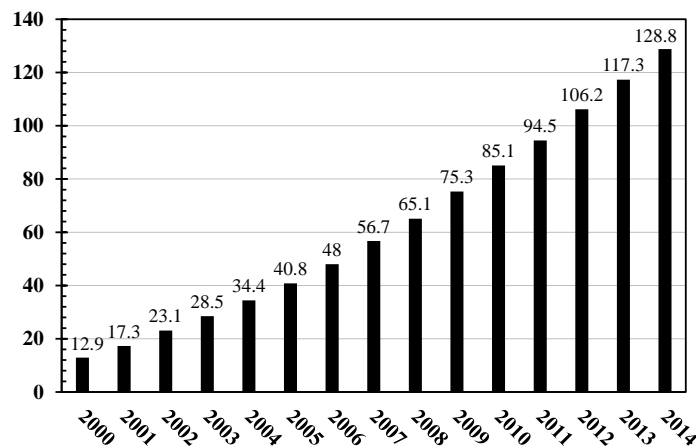


Figure 1.3 – Cumulative wind power installations in the EU (GW) (adapted from EWEA (2015))

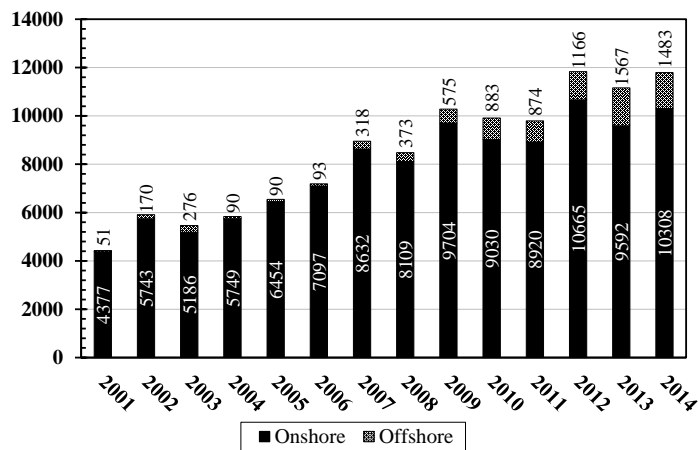


Figure 1.4 – Annual onshore and offshore installations (MW) (adapted from EWEA (2015))

The world global cumulative installed wind capacity within the period comprised between 2000 and 2015 is presented in Figure 1.5. In the last 15 years it was registered an increase in the installations following the same trend as in Figure 1.3. The tendency observed in the exploitation of offshore wind energy follows the same trend as the onshore increasing cumulative capacity. According to GWEC (2015) there was a worldwide increase in the exploitation of wind energy based on offshore wind turbines and the obtained data is presented in Figure 1.6.

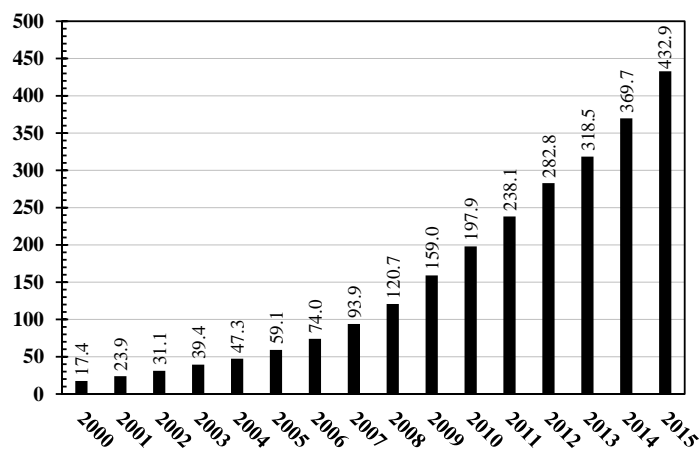


Figure 1.5 – Global cumulative wind power installations (GW) (adapted from GWEC (2015))

EWEA also presented a study to foresee the evaluation of the wind energy exploitation between 2013 and 2020 (EWEA, 2014). In this analysis 3 different scenarios were taken into account to correct some previous scenarios done by EWEA and by European Commission and National Renewable Energy Action Plan. The low scenario foresees an increase of 41% related with the installations of 2013 while the central scenario foresees an increase of 64% and the high scenario an increase of 84.9%. The outcome of the study is that not only the installations are foreseen to increase up to 2020 but also the market share of wind energy in the total energy consumption (Figure 1.7).

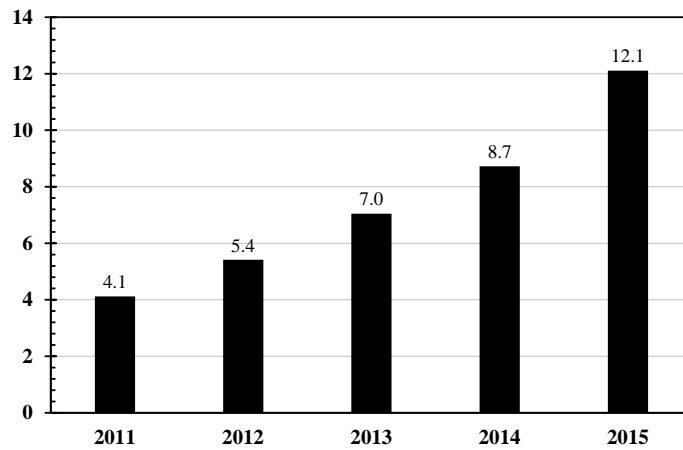
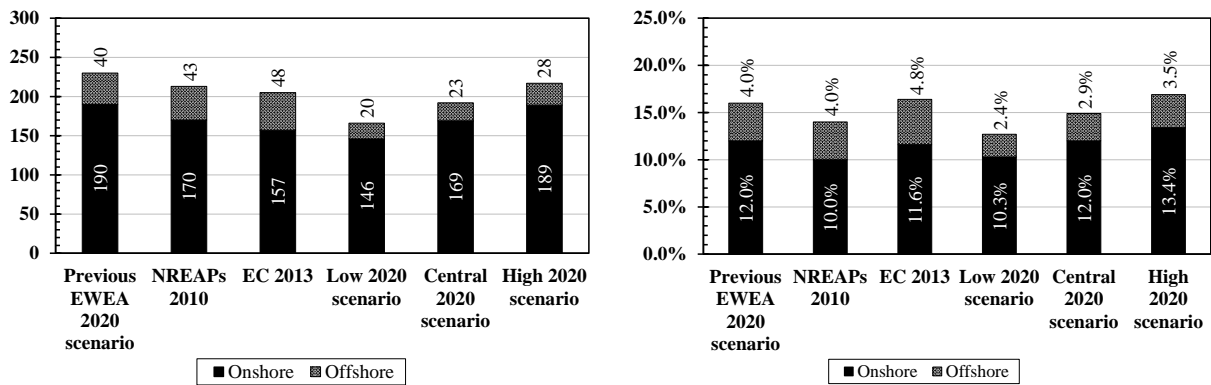


Figure 1.6 – Annual cumulative capacity (2011-2015) for offshore wind energy exploitation (adapted from GWEC (2015))



a. EU wind power installation scenarios in GW

b. Share of wind energy in EU electricity consumption

Figure 1.7 - Previous EWEA, NREAP, EC Primes and new EWEA 2020 scenarios (adapted from EWEA 2014)

The global forecast on the wind energy exploitation evaluated and presented by GWEC can be found in Figure 1.8 with results until 2020. The growth observed in GWEC (2015) is driven mainly by three main factors (climate, cratering prices and US market stability). The wind energy market will still be driven by China (with at least 50% share of the global market) with Europe following its steady pace up to the 2020 settled targets (however dependent on the growing political uncertainties registered in the last years) and North America continuing its strong growth driven by USA, Canada and Mexico.

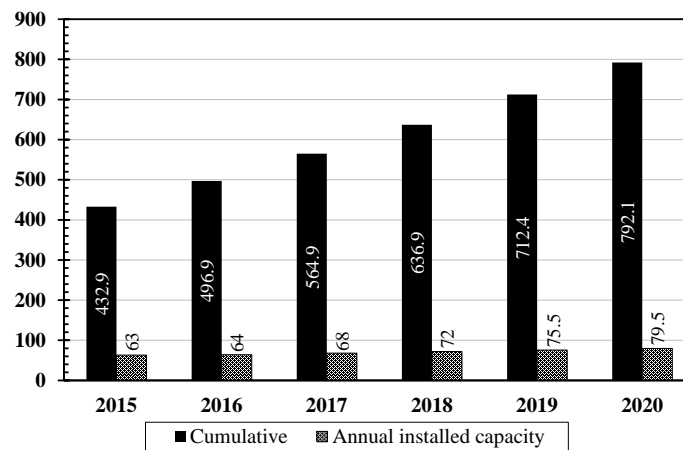


Figure 1.8 – Market forecast for 2016-2020 (GW) (adapted from GWEC (2015))

1.2. Objectives

The current work has the aim of proposing and analyzing improved solutions for the support structures of the new generation of steel tubular wind towers for more efficient and cost effective wind turbines.

In order to increase the energy production, it is required to increase the height of the towers in order to use a stronger and more stable wind shear profile. However, related to this increase in height, some main problems arise.

The increase in height results in higher loading that can withstand by considering higher steel grades. However this will only be possible by improving also fatigue details like those in the welded connection between the tube and the ring flanges or the bolts in tension. In order to overcome this fatigue problems, a new friction connection without welds and bolts under cyclic axial tension is analyzed.

Another problem found by the need of increasing the height are the transportation requirements for the segment pieces. Nowadays, the maximum allowable diameter to be transported in public roads is 4.5m. For the sake of comparison an 80m high wind tower has a 4.2m of diameter which is almost in the maximum transportable diameter. The idea to overcome this problem is to promote a modular construction of the steel tower segments connected with longitudinal bolted shear connections. Feasibility tests on this tower typology are presented and commented.

The third type of problems is related with the foundation system for these structures. The current foundation systems (shallow foundations) plays an important role in the final cost of the current steel tubular wind towers (80m/100m high). It can be easily understood that the increase in height of the free standing tube will lead to a considerable increase in the

foundation dimensions. A newer solution for these foundations is proposed by improving the current shallow foundations with micropiles, which will improve the overturning resistance of the system leading to a reduction in dimensions of the shallow part of the foundation. The study of this part will be accomplished by a detailed design example for this new solution and comparison with the shallow case in order to assess about the improvement of efficiency and costs in terms of Life Cycle Analysis. The behavior of the micropiles in sand, under monotonic and cyclic loading, will be evaluated with small scale experimental tests that will allow a calibration of a numerical model and extrapolation to real length of micropiles and to higher sand densities.

Some other problems are raised by the increase in height of the towers namely the availability and cost of higher cranes to allow the lift of the segments. Cost analysis of this procedure as well and/or the evaluation of a self-raising system should be considered however it was not taken into consideration in this study.

1.3. Scope of the thesis

The current work presented in this thesis is organized in the following chapters:

1. Introduction - introductory chapter to frame the actual exploitation of the wind energy and forecast of the growth for the next years to come along with the main objectives of the thesis;

2. Wind Towers – actual solutions – brief historical description of the evolution of the exploitation of the wind energy. Presentation of the monitoring of a full functional wind tower and the behaviour of an 80m high tubular steel wind tower. Estimation of a fatigue spectra and comparison with the values provided by the tower manufacturer;

3. Improved solutions – presentation of solutions for higher (150m or more) wind towers along with a description of the design considerations for some of the solutions presented. Detailed description and analysis on the feasibility tests on the manufacturing and assembly of tower segments with friction connections and longitudinal shear connections. Analysis and behaviour of the type of bolts to be used on the new geometry of connections between segments;

4. Foundation solutions for onshore wind towers – detailed design guide of foundation systems for wind towers both for shallow and hybrid (shallow reinforced with micropiles) foundations along with design examples assuming mechanical parameters for the soil and micropiles. Comparison between both solutions achieved with LCA and LCC analysis;

5. Hybrid Foundations – experimental tests on micropiles – detailed description and analysis of experimental tests on small scale micropiles (3m long) installed in loose sand and subjected to monotonic and reversal cyclic loading. The micropiles were tested both on ungrouted and grouted conditions as well as with single specimens and group specimens. The results in terms of resistance and stiffness (monotonic and cyclic) were evaluated and thoroughly compared;

6. Hybrid Foundations – numerical – numerical calibration of the experimental tests on single micropiles presented in chapter 5 using the 2D software Plaxis. The obtained results were extrapolated for long micropiles (12m) and for high density sand. Comments on the obtained results are presented along with the procedures to allow the use of the method on a real design case. Update of some of the design examples presented on chapter 4;

0. – final comments and summary of the main conclusions of the work. Proposals for future work on the theme and list of the publications presented within the scope of the work carried out for the thesis.

2. WIND TOWERS – ACTUAL SOLUTIONS

2.1. Overview on the evolution of the wind energy exploitation

The first reliable references about the use of windmills are reported to be around 644A.D in the Middle East with the report of usage of vertical axis windmills. Some centuries later (there are no certainties about the exact period) the Chinese developed a bamboo structure with fabric sails. By the time this system was used only to help people on basic needs such as milling grains or pumping water (Figure 2.1)



a. Vertical-axis windmill for milling grains, Afghanistan



b. Ancient chinese windwheel for pumping water and draining rice fields

Figure 2.1 – Ancient windmill/windwheel models (Hau, 2013)

One of the most important pioneer for turning windmills into wind energy generators was the Danish Poul La Cour. Based on his scientific knowledge he erected, in 1891, one of the first registered electricity producing wind turbine (Figure 2.2). In 1887 James Blythe built a cloth-sailed wind turbine to power his holiday home and that is was the world's first-known structure by which electricity was generated from wind power.

In meantime there were developments in the construction and exploitation of the actual generation of wind generators. There are two big groups of wind generators: vertical and horizontal axis generators. The horizontal axis wind turbines (HAWT) are currently the most common type of wind energy converters (WEC) and will be the scope of this study.

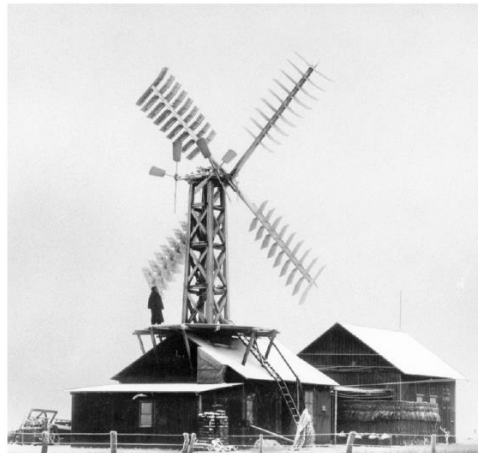


Figure 2.2 – Poul La Cour's first electricity producing wind turbine in 1891 in Askov, Denmark (Hau, 2013)

The components of a HAWT can be observed in Figure 2.3.

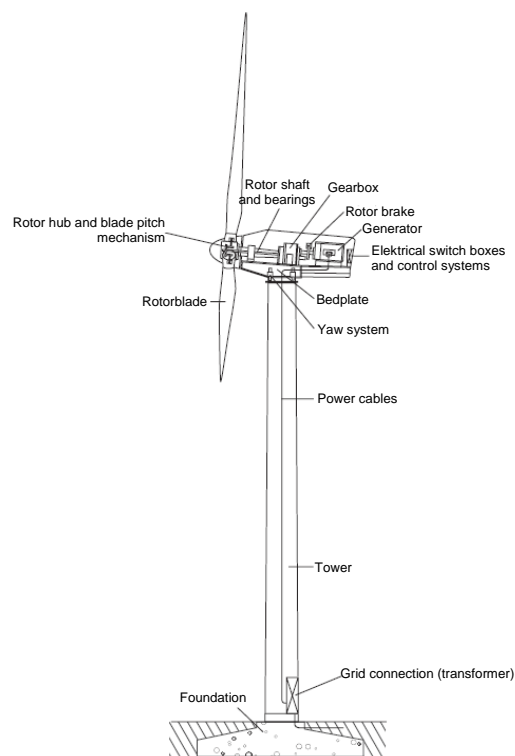
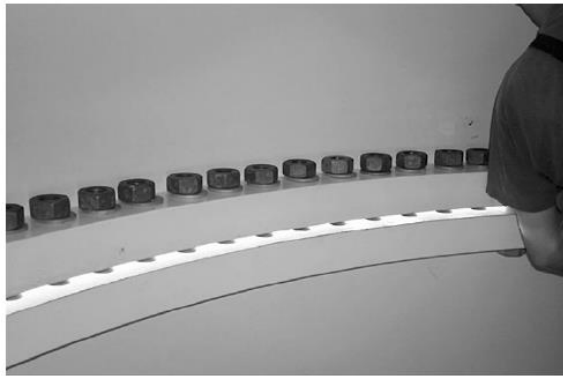


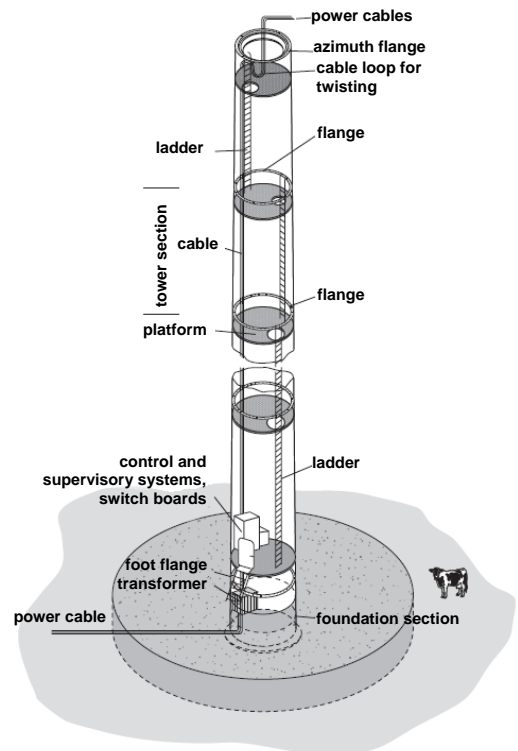
Figure 2.3 – Components of a horizontal-axis wind turbine (adapted from Hau, 2013)

The most current types of supporting towers for wind turbines are: free-standing tubular steel towers, lattice steel towers, site-mixed concrete or prefabricated concrete towers, concrete-steel hybrid towers and timber towers.

The free-standing tubular steel towers are the most common solution nowadays for the current heights (up to 100m). It is the economically most attractive solution mostly because of the light weight of the prefabricated tubular segments, suitable for transportation to construction site for assembling. For the current heights, the tubular segments with lengths of about 20-25 meters are completely prepared in the factory with all the internal equipment and cables and afterwards transported to the construction site where they are assembled using ring flange connection (Figure 2.4a.). A schematic representation of a common tubular tower is presented on Figure 2.4b.



a. Internal flange connection of the bolted tower sections



b. Tubular-steel tower with installations of a large wind turbine

Figure 2.4 - Free-standing tubular steel towers (adapted from Hau, 2013)

The lattice steel towers were very popular in the early years of wind energy in USA and are becoming again a suitable solution for higher structures. The strongest arguments against the use of lattice towers are the longer assembling times, due to the large number of connections, and the difficulty of maintenance of the tightening in the bolts in a structure subjected to important steady vibrations. Also, the safety of the maintenance workers is of concern in this type of towers. On the other hand, the mass of the structure is much lower (up to 40% less) which can be beneficial in terms of design and costs. Figure 2.5 shows a geometry of a lattice steel tower.



Figure 2.5 - Lattice tower of a Vestas V80 wind turbine (Hau, 2013)

The concrete towers can be divided in two big groups taking into consideration the type of construction adopted. They can be site-mixed concreted if the construction is performed *in-situ* or they can be assembled with prefabricated concrete segments.

Due to the time consumption, the solution with site-mixed concrete is nowadays almost disregarded when compared with the prefabricated concrete segments. The mass of the structure can be a handicap, however they can go up to higher heights.

Figure 2.6a shows an example of the construction of a site-mixed concrete tower while Figure 2.6b shows an example of a prefabricated concrete tower.

An interesting solution is the concrete-steel hybrid tower using a concrete part on the bottom of the tower connected to a steel part on the top. The main advantage of this tower is the reduction of the mass by using the steel part and the improvement of the dynamic behaviour due to the higher stiffness of the lower part, allowing therefore the construction of higher towers. Figure 2.7 shows a generic scheme of a hybrid tower.

A comparison between the current available solutions is presented in Hau (2013) for a wind tower with a 3 blade and 60m diameter rotor and a tower height of 46.6m. The considered tower shapes are: cylindrical (for steel towers), cylindrical with conical base, conical, cylindrical with guys and lattice. For concrete towers the considered shapes are: prefabricated prestressed, reinforced and prestressed.

This comparison showed that the steel towers are much lighter (around ¼ of the weight of the concrete towers). The cylindrical with guys shape is, by far, the lightest solution in this situation. On the other hand, this comparison shows that the concrete solution is, in general, less expensive than the steel towers and the lattice tower is the cheapest steel solution.



a. Construction of a tower for an Enercon E-66 with site-mixed concrete



b. Erection of a prefabricated prestressed-concrete tower for an E-66

Figure 2.6 – Concrete towers (Hau, 2013)

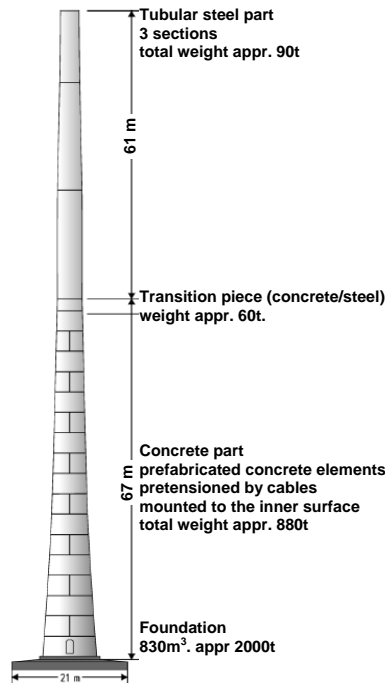


Figure 2.7 - Constructional concept of the concrete/steel hybrid tower designed for the Repower 3.3 MW wind turbine (Max Bögl Group) (adapted from Hau, 2013)

All the steel solutions present a better dynamic behaviour than the concrete solution except the prefabricated prestressed solution. For this specific analysis this concrete solution presents a dynamic behaviour similar to the steel towers.

In order to have a better insight into the behaviour of a fully functional free-standing tubular steel tower, a long term monitoring was carried out. A detailed description of the procedure as well as the obtained results and the obtained behaviour is presented.

2.2. Behaviour of wind towers – long-term monitoring

2.2.1. Description of the wind tower and measurement system

In order to understand and predict the behaviour of wind towers, a long term monitoring was carried out in a free standing and full operational wind tower. The presented monitoring was carried out under the scope of the European Research project HISTWIN (Veljkovic et al., 2012) and the results are presented in Rebelo et al. (2012a; 2012b).

In the current section, the monitoring results are presented, being obtained after calibration and tests on the monitoring system of the steel wind tower described. The total monitoring period was close to fifteen months, between September 2009 and November 2010. In the first phase (Phase I) of the monitoring period, until the end of April 2010, the signal recording was activated either manually or automatically for wind speeds over 4m/s and a total of 390 records were registered. During the second phase (Phase II) corresponding to the period from April to November 2010 the trigger level was updated to wind velocities greater than 14m/s and a total of 660 records were registered. When automatically started by the trigger the recording is activated during one hour and after that period the trigger becomes active again. Therefore, during persistent strong wind the recording is almost continuous.

Throughout the monitoring period there were interruptions due to system malfunction or maintenance works in the tower, used in Phase I to make some adjustments in the data transmission system. Some of the interruptions were relatively long, taking some days or even weeks. During Phase I system was active during 58% of time (139 days out of 240) and during Phase II system was active during 75% of time (159 days out of 210). For safety reasons, during all the time, the access to the interior of the tower was only possible with the presence of members of the maintenance staff contracted by the owner of the tower. The possibility of having some equipment (e.g. computer, GSM module, etc.) outside the tower, and therefore accessible without restrictions, was not an option because of safety reasons (vandalism, robbery).

Nevertheless, the main reason for the inactivity of the system after preliminary tests was simply lack of electric power inside the tower. The circuit breakers of the electric circuit used by the equipment were breaking frequently and it could take several days even weeks to get authorization for accessing the tower for reparation. The replacement of the circuit breaker with a more powerful one had to be accepted by the maintenance team, who tried to avoid changes in the original circuits because of liability reasons.

The monitoring results were numerically simulated using a finite element model presented in Rebelo et al. (2012a) and developed with the software LUSAS (2006a; 2006b). The model was composed by quadratic thick shell elements with 8 nodes. The shell elements considered are in accordance with the geometry presented in Table 2.1. The reinforced concrete foundation and the interaction with soil foundation were also included in the model. The plan view of the foundation is an octagon inscribed in a circle of 17m diameter. The thickness varies between 0.95m at the border up to 2.0m in the center. The FE model uses 3D solid continuum finite elements for the concrete foundation and linear springs for the contact with the soil.

The model parameters used for model updating were: i) the mass of the tower, ii) the stiffness of the springs simulating the soil-structure interaction and iii) the vertical eccentricity of the turbine's centre of gravity¹.

The mass of the tower was increased up to a value of 15% in order to take into account the effects of the interior elements such as cables, platforms, ladders, elevator and ancillary equipment, the soil subgrade coefficient varied taking into account a variation of the modulus of elasticity of the soil between 150MPa and 300MPa and considering the procedure and expressions provided by Bowles (2001), Adhikari and Bhattacharya (2011) and finally the nacelle eccentricity varied between 0m and 1.0m.

The following objectives were established for the information to be extracted from the measured data: i) the dynamic behaviour of the tower and an accurate modal identification of the system during operation; ii) the section loads acting on the top and bottom of the tower and on two intermediate levels, iii) the performance of the assembling joints and the behaviour of the thin walled section in the vicinity of those joints, iv) the estimation of the fatigue spectra for the tower under service loads.

¹ This parameter was not given in the information provided by the turbine fabricator and therefore had to be assumed variable in this study.

Table 2.1 – Tube cross-section properties along the height

Height [m]	Diameter [m]	Thickness [m]	Inertia [m ⁴]	Levels for instrumentation
0.000	4.300	0.030	0.9367	Connection Level 0
2.000	4.276	0.030	0.9211	
3.082	4.257	0.030	0.9089	
5.412	4.215	0.030	0.8823	
5.802	4.208	0.026	0.7608	Level 0
7.789	4.173	0.026	0.7420	
9.302	4.147	0.027	0.7562	
11.502	4.108	0.024	0.6534	
12.582	4.089	0.023	0.6175	
15.172	4.043	0.022	0.5710	
17.362	4.004	0.022	0.5546	
17.972	3.993	0.022	0.5500	Level 1
19.752	3.962	0.022	0.5373	Connection Level 1
22.182	3.917	0.021	0.4956	
22.362	3.917	0.020	0.4720	
25.252	3.864	0.020	0.4531	
28.002	3.816	0.020	0.4364	
30.752	3.768	0.020	0.4202	
31.982	3.746	0.019	0.3922	
34.382	3.704	0.019	0.3792	
36.252	3.671	0.019	0.3691	
39.002	3.622	0.018	0.3359	
41.752	3.574	0.018	0.3227	
43.982	3.535	0.017	0.2949	
44.592	3.524	0.017	0.2922	Level 2
46.382	3.492	0.017	0.2843	Connection Level 2
48.817	3.448	0.016	0.2576	
48.967	3.448	0.015	0.2415	
51.552	3.400	0.015	0.2315	
53.812	3.360	0.015	0.2234	
55.502	3.330	0.014	0.2030	
58.252	3.280	0.014	0.1940	
58.622	3.277	0.013	0.1797	
61.022	3.231	0.013	0.1722	
63.752	3.182	0.013	0.1645	
65.842	3.144	0.013	0.1587	
66.502	3.133	0.012	0.1449	
69.252	3.083	0.012	0.1381	
71.152	3.049	0.012	0.1336	Level 3
72.002	3.034	0.012	0.1316	
73.082	3.015	0.012	0.1292	
75.492	2.971	0.014	0.1442	
75.640	2.955	0.018	0.1824	

The instrumented tower was erected in a central area of Portugal and it is a tubular tower with varying diameter and thickness throughout the height (Figure 2.8). It is a 2.1MW turbine Wind Class III IEC2a and it is mounted on an 80 meters high steel tower. The instrumentation on the tower were placed at four levels. Level zero is at the tower bottom and level three is just below the nacelle. Intermediate levels coincide with tower segment connections and internal work platforms.

The tower is divided in three parts assembled on site (). The diameter varies between 2.955m at the tower top up to 4.30m at the tower bottom. The thickness varies between 12 and 30mm at the same sections. The connections between modules are achieved using very stiff end rings welded to the tower tubes and M36 e M42 class 10.9 bolts are used to connect the parts. The maintenance plan of the tower specifies tightening torques for the bolts of 2800Nm and 4500Nm, respectively.



Figure 2.8 - Instrumented tower in Marvila, Portugal

An important issue is the dimensional fabrication tolerances of the ring flanges used to connect the tower segments. Imperfections are responsible for the loss of contact between some parts of the flanges leading to water infiltrations and to low performance of the bolts which will be subjected to higher stress ranges. The fabrication tolerance limit for the 100mm thick flange is 1.5mm for the amplitude of the waviness and for the external-internal inclination of the ring surface. These tolerances are guaranteed by the tower manufacturer and

no imperfections were detected during the visual inspection made to the tower during assembling and thereafter.

Four types of signals are measured and recorded Rebelo et al. (2012a; 2012b):

1. accelerations at different levels of the tower, which will allow the identification of the modal parameters and will give information about the loads acting on the tower;
2. strains along the inner perimeter of the thin walled sections located near the top of the tower and near the assembling joints; strains inside the bolts of the assembling joints as well;
3. inner temperature variation of the steel section caused by the direct effect of the sunlight on the face of the tower; this will allow for the estimation of its static position;
4. inclination of the tower in x and y directions at two different levels, which may allow the estimation of the lateral displacements of the tower through the cross check with the displacements obtained from the time integration of the accelerations.

Efforts were made in order to get access to the information available in the monitoring system running under the responsibility of the tower manufacturer. Information about the turbine position (azimuth), wind velocity and direction, blade velocity of rotation and pitch are very important for the estimation of the wind loads acting on the turbine and for the correlation estimation between tower response and operating loads.

Following signals are obtained from the nacelle monitoring system and are included in the measurement system:

1. Wind speed and direction
2. Nacelle position (azimuth)
3. Operation status
4. Blade angle

The position of the accelerometers used for operational vibration measurements correspond to those defined for levels 0, 1, 2 and 3 in Figure 2.8. A total of 9 accelerometers and a

maximum sampling frequency of 50Hz are used. The accelerometers are of the type PCB393B04 and have a dynamic frequency range starting from about 0.1Hz.

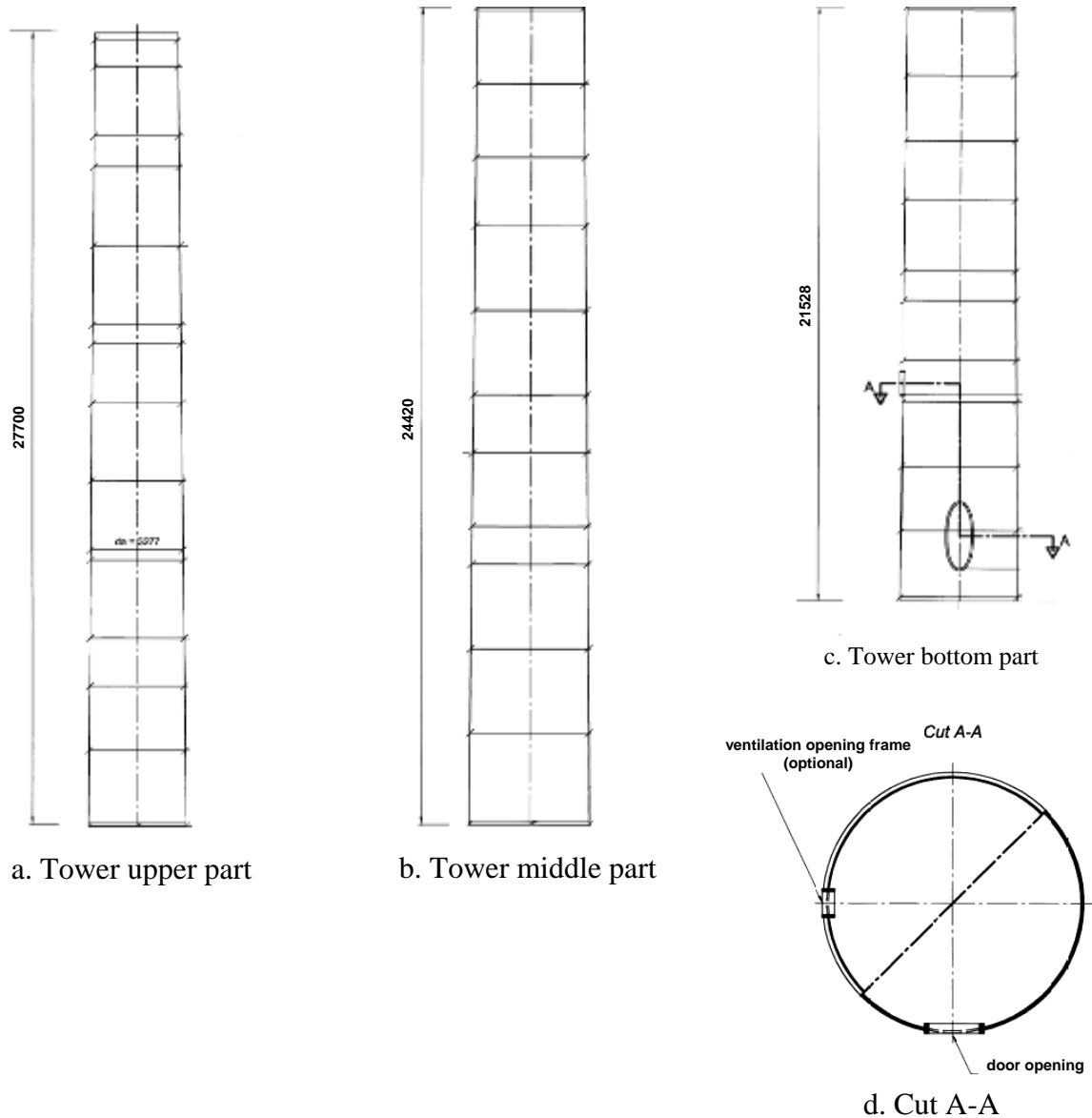


Figure 2.9 - Steel wind tower composed by three parts; Cut A-A (d) shows the ventilation opening (optional) and the door opening (adapted from Veljkovic et al., 2012)

The strain gauge rosettes type TML PFR-20-11 (three directions) and bolt gauges type TML BTM-6C were placed according to Figure 2.10. A total of 96 strain gauges are used.

Four thermocouples were placed at level 2 to measure the temperature in the inner surface of the steel.

Two inclinometers were placed at each of the levels 2 and 3 to measure the inclination of the tower and to calibrate the displacements obtained from the double integration of the accelerations.

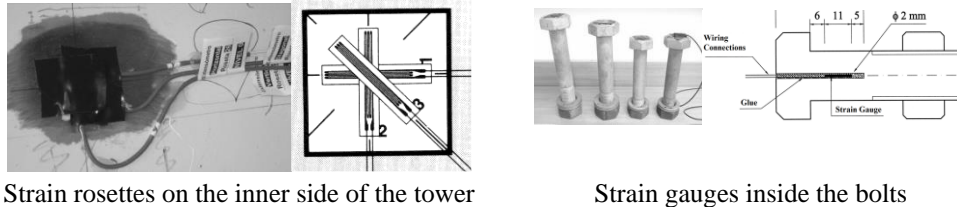


Figure 2.10 – Details of strain gauges application

The data acquisition (Figure 2.12) is performed using three dataloggers (NI cRio 9012) that can digitalize dynamic data and two dataloggers (NI cFP1808) with low sampling rates for slowly varying data and nacelle signals. A computer inside the tower assures the synchronization of all dataloggers using TCP-IP protocol, stores all measured data in a local database and sends it periodically to a remote system using GPRS. Separately, all signals can be visualized remotely in real time in order to detect malfunctions of the system. A dedicated application was developed in LabView (NI - National Instruments, 2006), which controls all the data acquisition and stores the data in the database.

The dynamic signals measured at levels 2 and 3 can be recorded at a rate of up to 50 Kilosamples/second. Since only much lower frequency contents are of interest, the recorded time histories are sampled down to 100Hz. This allows the unbiased estimation of up to about 50Hz of the frequency content of the measured signals. Triggering levels are established according to ongoing collection of information in order to record signals only above pertinent levels of the structural response.

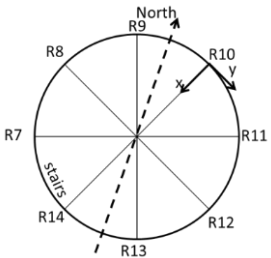
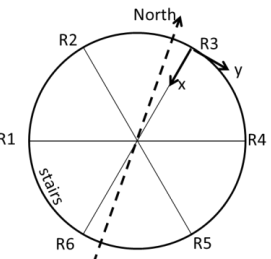
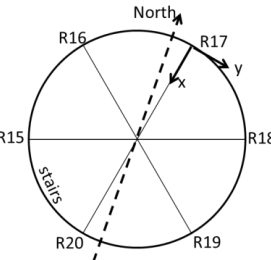
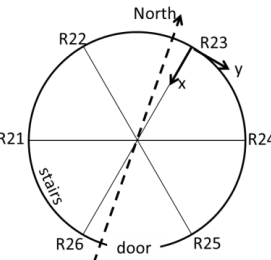
Cross section at different levels		Sensors and locations
Level 3		Accelerometers: positions R10-x, R10-y, R8-x (signals: L3AccX; L3AccY; L3AccT) Strain gauges - 1 rosette at each of the 8 locations along the inner perimeter of the section (signals: L3R7; L3R8; L3R9; L3R10; L3R11; L3R12; L3R13; L3R14) Inclinometers – R10-x and R10-y (signals: L3IncX; L3IncY)
		Section position and dimensions (mm): Height: 71152; Diameter:3049; Thickness: 12
Level 2		Accelerometer: R3-x and R3-y (signals: L2AccX; L2AccY) Strain gauges - 1 rosette at each of the 6 locations along the inner perimeter and 6 Strain gauge inside the bolts; (signals: L2R1; L2R2; L2R3; L2R4; L2R5; L2R6; L2B1; L2B2; L2B3; L2B4; L2B5; L2B6) Temperature - 4 Termocouples positions R1, R3 R4, R6 (signals: L3T1; L2T2; L2T3; L2T4) Inclinometers – R3-x and R3-y (signals: L2IncX; L2IncY)
		Section position and dimensions (mm): Height: 44592; Diameter:3524; Thickness: 17
Level 1		Accelerometer: R17-y and R17-y (signals: L1AccX; L2AccY) Strain gauges - 1 rosette at each of the 6 locations along the inner perimeter and 6 Strain gauge inside the bolts (signals: L1R15; L1R16; L1R17; L1R18; L1R19; L1R20; L1B1; L1B2; L1B3; L1B4; L1B5; L1B6)
		Section position and dimensions (mm): Height: 17972; Diameter:3993; Thickness: 22
Level 0		Accelerometer: R23-y and R23-y (signals: L0AccX; L0AccY) Strain gauges - 1 rosette at each of the 6 locations along the inner perimeter and 6 Strain gauge inside the bolts; (signals: L0R21; L0R22; L0R23; L0R24; L0R25; L0R26; L0B1; L0B2; L0B3; L0B4; L0B5; L0B6)
		Section position and dimensions (mm): Height: 5802; Diameter:4208; Thickness: 26
Initials for Signals' identification L(1)(2)(3)(4) level number Type of signal R – strain gauge Rosette Acc – accelerometer B – starin gauge in bolt Inc – inclinometer Tmp – temperature		Location(see figures above) Strain gauge direction in rosettes V – vertical along tower axis H – horizontal along section perimeter D – diagonal e.g. L2R21D: Level 2, Rosette 21, strain gauge in Diagonal direction

Figure 2.11 - Sensors locations and identification (Rebelo et al., 2012a)

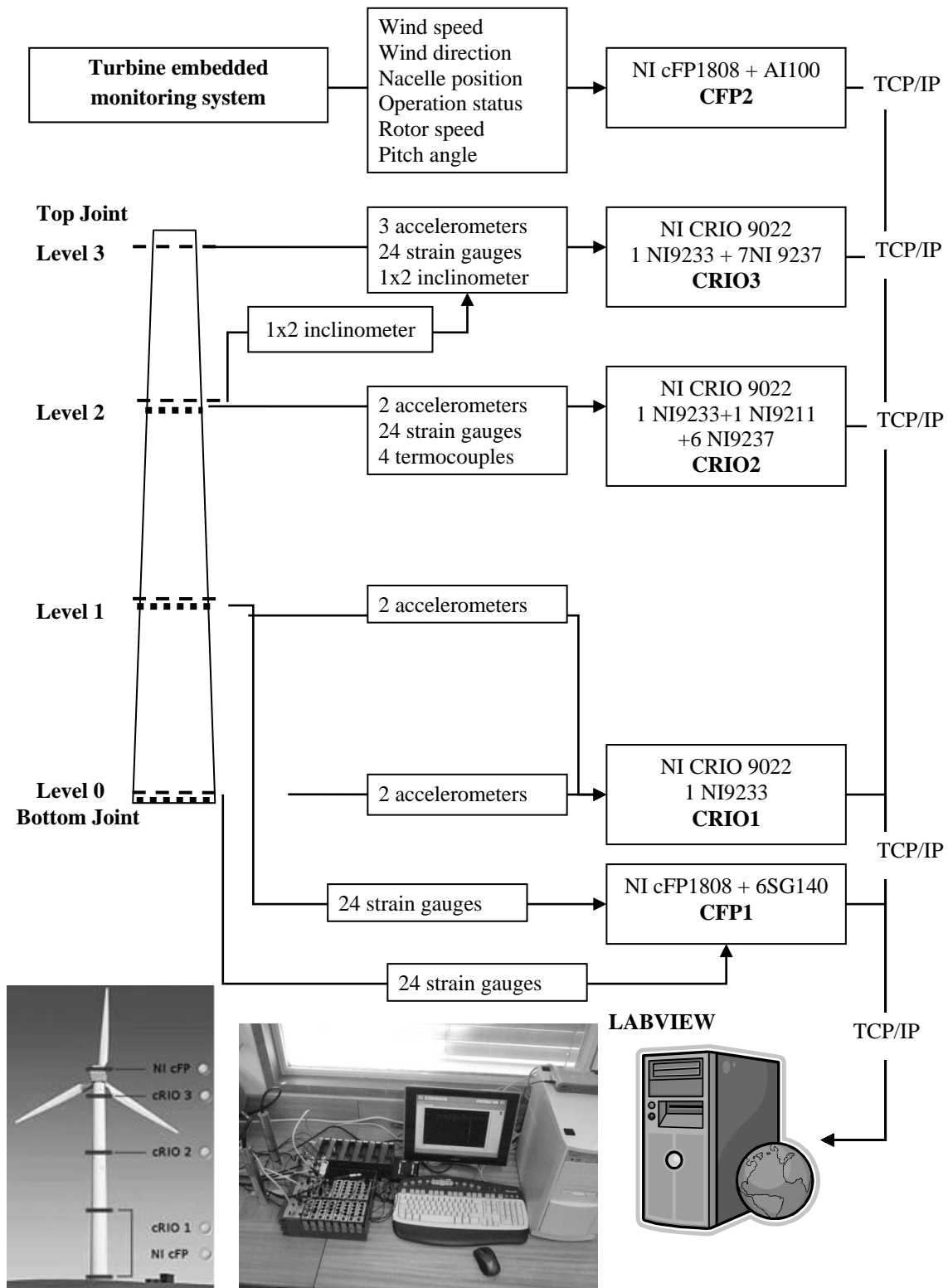


Figure 2.12 – Layout of the communications inside the tower (Veljkovic et al., 2012)

2.2.2. System calibration

The calibration of the measurement system must allow the assessment of two different types of coefficients: i) those inherent to the conversion of electrical into physical quantities and ii) those related to the baseline (zeroing) of the signal. Since only the dynamic part can be measured, the mean value over time should be zero when wind actions on tower are zero (very low wind as approximation).

The calibration factors inherent to the conversion of electrical into physical quantities are presented in the following topics, for each type of sensors used in the monitoring procedure.

- Accelerometers

The sensitivity of the PCB accelerometers type 393B04 are given in Table 2.2.

Table 2.2 – Sensitivity of accelerometers

Location	Serial number	Calibration sensitivity mV/ms ⁻²
Level 0 direction x (L0ACELX)	22523	103.3
Level 0 direction y (L0ACELY)	22524	102.5
Level 1 direction x (L1ACELX)	22484	102.8
Level 1 direction y (L1ACELY)	22485	103.2
Level 2 direction x (L2ACELX)	22288	101.7
Level 2 direction y (L2ACELY)	22482	103.4
Level 3 direction x (L3ACELX)	19741	102.6
Level 3 direction y (L3ACELY)	21978	100.9
Level 3 direction t (L3ACELT)	22195	103.8

- Inclinometers

The calibration factors of inclinometers TML – KB-5EB to transform measured voltage in degrees are given in Table 2.3.

Table 2.3 – Calibration factors for inclinometers

Location	Serial number	Calibration factor (degree)
Level 2 direction x (L2INCLX)	EDW07027	5.0
Level 2 direction y (L2INCLY)		5.0
Level 3 direction x (L3INCLX)	EDW07028	5.0
Level 3 direction y (L3INCLY)		5.0

- Strain Gauges

The calibration factors of strain gauges TML – KB-5EB and BTM-6C to transform measured voltage in stresses (MPa) are given in Table 2.4. Young's modulus used is $E=200\text{GPa}$.

Table 2.4 – Calibration factors for strain gauges

Location	Type	Calibration factor (MPa)
Rosettes of extensometers at all levels	PFR-20-11	375.6
Bolts	BTM-6C	381.0

To interpret the strains obtained from the measurements, it is necessary to take into account that the measurement system was powered on after erection of tower and mounting of all the equipment. Therefore, the measured strains are not absolute values but relative to the moment of system initialization, i.e., these values only reproduce the time varying response under external wind action and turbine operation. Since the mean value over time should be zero when wind actions acting on the tower are zero and the turbine is in an idle position, the calibration of the measurement system should be ideally performed under these conditions. In practice, only measurements during very low wind speed and rotor in idle position are possible and were performed as a good approximation for zeroing the measurement system.

Figure 2.13 schematically illustrates the absolute time dependent strain history obtained in a given measurement point during tower operation and its decomposition into several superposed components, either included or not in the measured values. The line showing the strain component due to time invariant self-weights cannot be measured because the data acquisition system was powered on after self-weight was acting. However, it can be accurately estimated numerically from the components' self-weight. For instance, at the measurement points on the tower shell, the following compressive vertical stresses due to tower self-weight were computed: 3.56 and 2.69MPa for levels 0 and 1 respectively. The axial force due to the nacelle self-weight is 1067.33kN and the corresponding compressive stresses at the same levels are, respectively, 3.11MPa and 3.87MPa.

The component representing the gauge calibration error in Figure 2.13 is included in the measured values. Since it is unknown, it must be dropped out from the measurement results zeroing the system during very low wind speed conditions, as it was explained above. This was done before starting monitoring under a mean wind speed of 4.62 m/s, a mean wind direction of 170° measured clockwise from North (see Figure 2.11) and a mean temperature of 13.7°C . The values obtained during the full nacelle rotation under low wind speed are represented on Table 2.5.

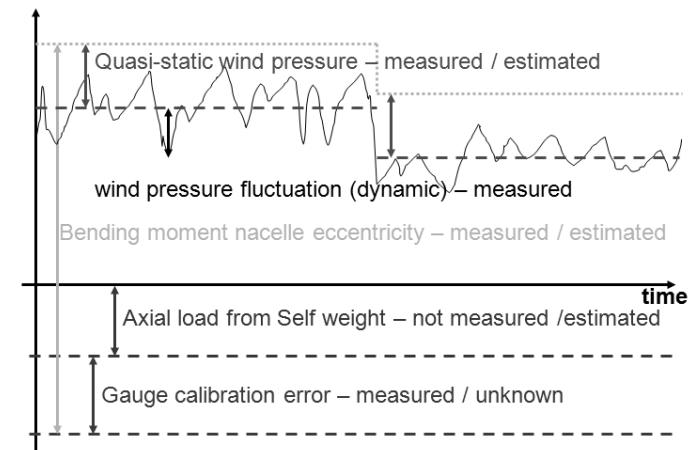


Figure 2.13 – Time evolution of the several dynamic and quasi-static signal components (Rebelo et al., 2012a)

Table 2.5 – Values measured with full nacelle rotation

Hour	Nacelle Pos. (°)	Wind Speed (m/s)	Wind Direction (°)	Temp. (°C)
11:50	0	4.6	175	13.6
11:56	20	5.6	156	13.8
11:58	40	6.2	182	13.6
00:00	60	5.6	188	13.6
00:03	80	4.0	136	13.6
00:05	100	6.5	170	13.6
00:09	120	6.7	173	13.5
00:12	140	5.0	172	13.6
00:15	160	4.0	156	13.8
00:18	180	3.2	188	13.6
00:22	200	3.0	120	14.0
00:26	220	4.1	170	13.6
00:28	240	4.4	178	13.8
00:32	260	6.0	175	14.4
00:34	280	3.1	183	14.3
00:37	300	3.4	185	14.0
00:40	320	3.9	180	13.8
00:42	340	5.0	183	13.5
00:45	360	3.6	175	13.5

Added to these two time invariant strain components (axial load from self-weight and gauge calibration error), there are the strains varying in time due to nacelle position and due to wind pressure. Considering the first one, it refers to the bending moment effect due to the nacelle self-weight eccentricity relatively to tower axis (0.725m).

The maximum vertical stress in the shell at level 0 due to this bending moment effect is numerically estimated as being 2.15MPa. However, for a given measurement point this effect varies during operation, since it depends on the nacelle orientation. In order to have the actual effect of the nacelle azimuth in the measured signals, the calibration was made using the mean values of twelve signal histories measured for nacelle positions varying from azimuth 0° to 360° with increments of 20° and observing the wind and temperature conditions mentioned above. A representation of the stress variation at level 0 due to the nacelle eccentricity and the nacelle azimuth is presented in Figure 2.14.

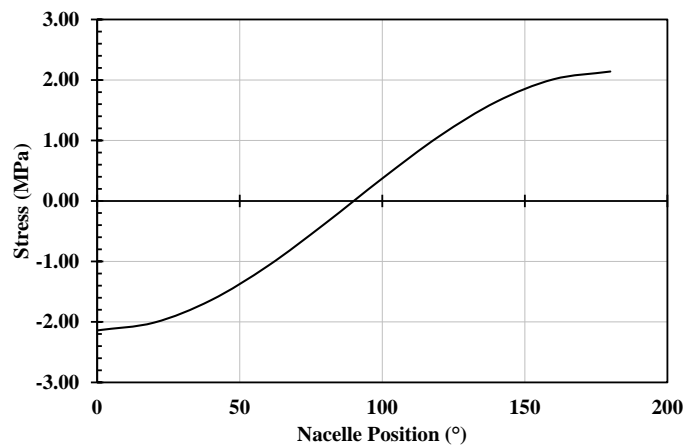


Figure 2.14 – Stress variation at Level 0 due to nacelle eccentricity depending on Nacelle azimuth

The final result of the calibration is to assure that the measurements related to strains accurately represent the static and dynamic effect of wind pressure on the turbine blades and on the tower including the effect of bending moment produced by the nacelle eccentricity. For instance, to compute the final stresses including static non measured axial force at levels 0 and 1 the values 6.67MPa and 6.56MPa, respectively, must be added as uniform compressive vertical stresses in the shell. The calibration factors obtained for each strain gauge are presented in Annex A.

2.2.3. Measurement results

2.2.3.1. Strain/Stresses and Forces

The wind loading variation induces stress variation in the components of the tower structure. In this monitoring the stress variation in the tower shell and in the ring flange connection bolts was measured and analysed.

The monitoring system acquires strain signals using two different sampling rates, low frequency at 2.5Hz and high frequency at 100Hz due to different acquisition equipment. In order to analyse the evolution of the time signals during the whole monitoring period the second type of signals were decimated and sampled at 2.5Hz.

- Wind induced stresses in the shell

In order to visualize the evolution of the shell stresses depending on wind speed, the maximum tensile and compressive stresses were computed from the measured time series segmented in periods of 10 seconds.

Figure 2.15 and Figure 2.16 represents the influence of the wind speed in the vertical stress fluctuation (maximum and minimum) obtained in vertical strain gauges placed at level 0 and level 1.

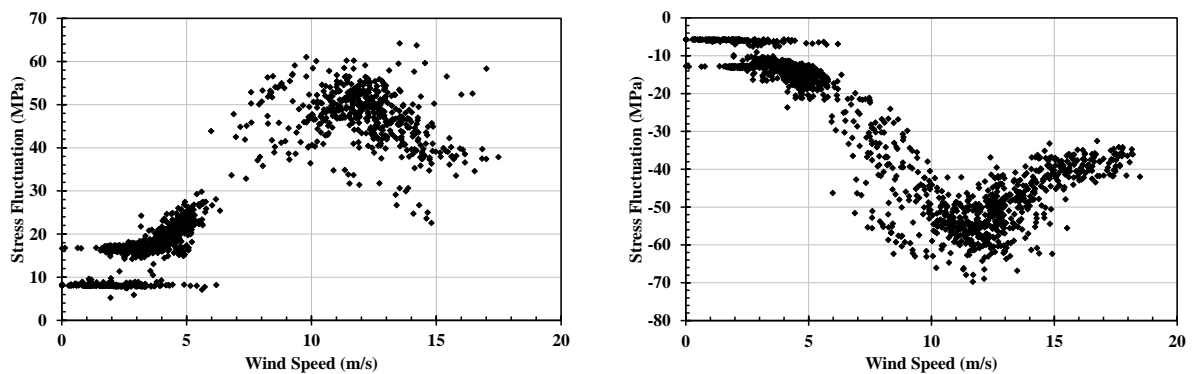


Figure 2.15 – Vertical stress fluctuation – level 0

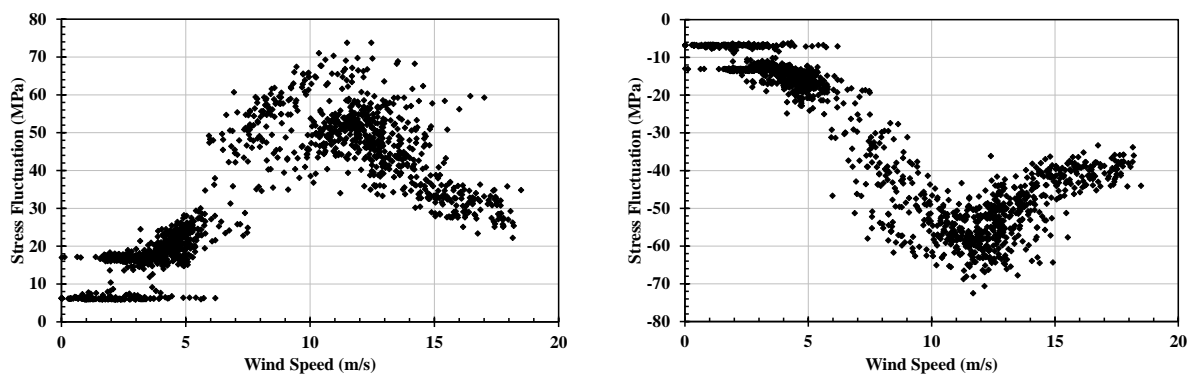


Figure 2.16 – Vertical stress fluctuation – level 1

Figure 2.17 and Figure 2.18 show the measured stress fluctuation in the horizontal direction both for level 0 and for level 1.

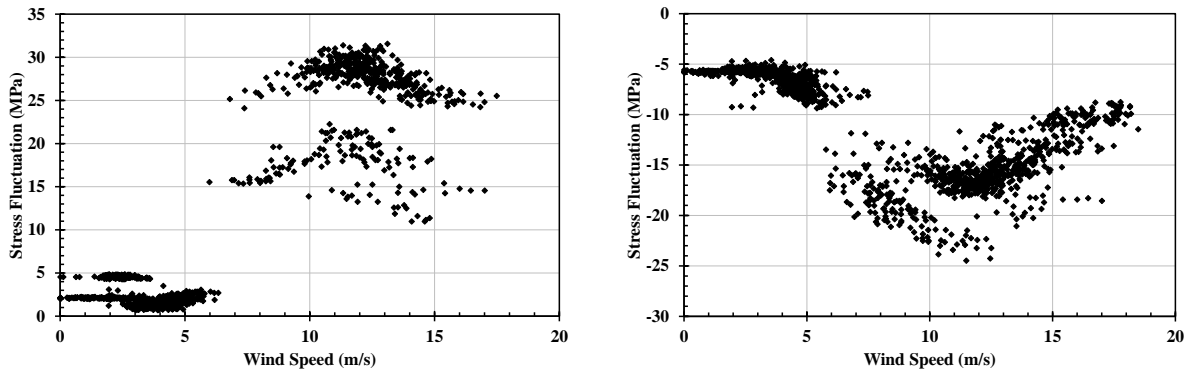


Figure 2.17 – Horizontal stress fluctuation – level 0

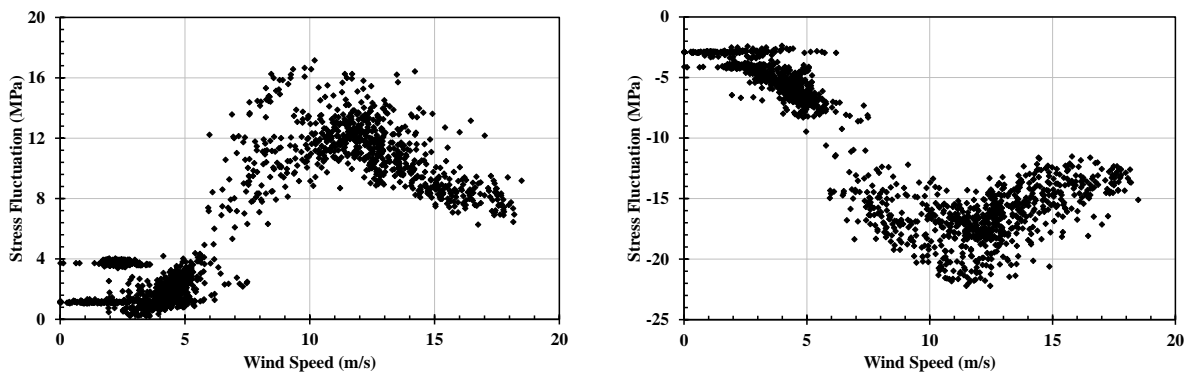


Figure 2.18 – Horizontal stress fluctuation – level 1

Figure 2.19 and Figure 2.20 shows the measured stress fluctuation in the inclined direction (45°) both for level 0 and for level 1.

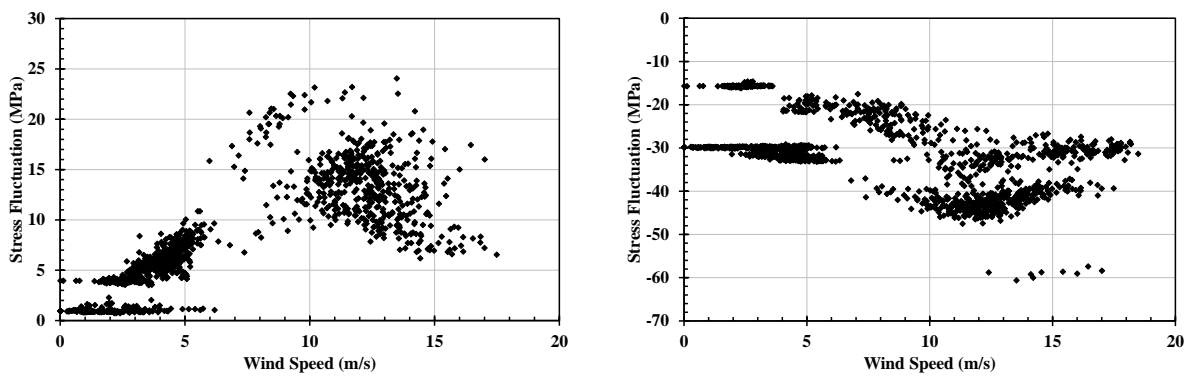


Figure 2.19 – Inclined stress fluctuation – level 0

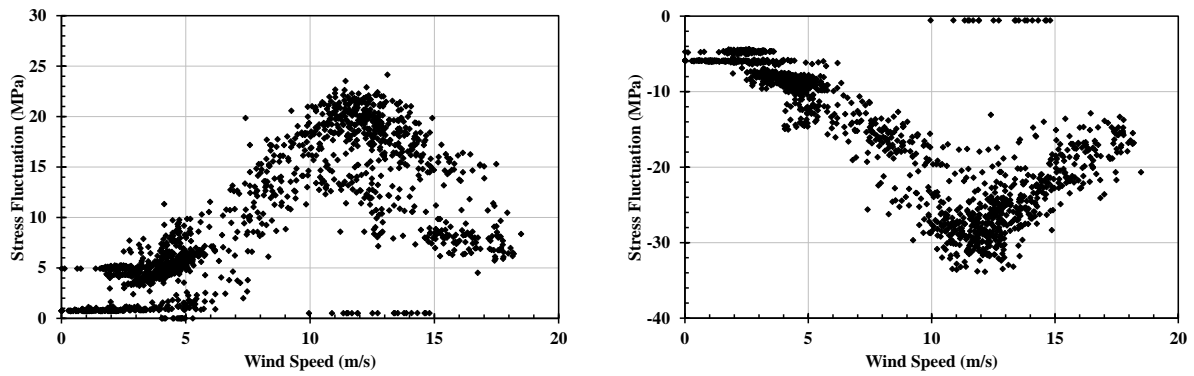
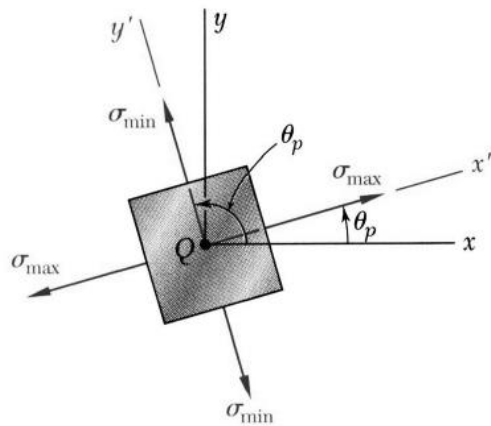


Figure 2.20 – Inclined stress fluctuation – level 1

Maximum stresses are achieved between 10 and 14m/s wind speed decreasing to a steady state level for higher wind velocities. This effect is due to the regulation of pitch angle for higher wind speeds, that is, the blade angle varies in order to decrease the tower loading while maintaining the production rates (Burton et al., 2001; Hau, 2013; Veljkovic et al., 2011).

Stresses in the shell are obtained from the strain measurements using a Young’s modulus given by $E=200\text{GPa}$. Three stress components can be obtained at each measurement point. The principal stresses can be estimated according to the equations (2.1) and (2.2). σ_x is the horizontal stress, σ_y is the vertical stress and τ_{xy} is obtained from equation (2.2) taking θ as 45° and σ_θ as the stress obtained with the inclined strain gauge.



$$\sigma_{\max,\min} = \frac{\sigma_x + \sigma_y}{2} \pm \sqrt{\left(\frac{\sigma_x - \sigma_y}{2}\right)^2 + \tau_{xy}^2} \quad (2.1)$$

$$\sigma_\theta = \frac{\sigma_x + \sigma_y}{2} + \frac{\sigma_x - \sigma_y}{2} \cos 2\theta + \tau_{xy} \cdot \sin 2\theta \quad (2.2)$$

$$\tan 2\theta_p = \frac{2\tau_{xy}}{\sigma_x - \sigma_y} \quad (2.3)$$

Figure 2.21 – Estimation procedure for principal stress direction and intensity (Beer et al., 2012)

With all this, the principal stresses obtained respectively for level 0 and for level 1 are presented in Figure 2.22 and Figure 2.23.

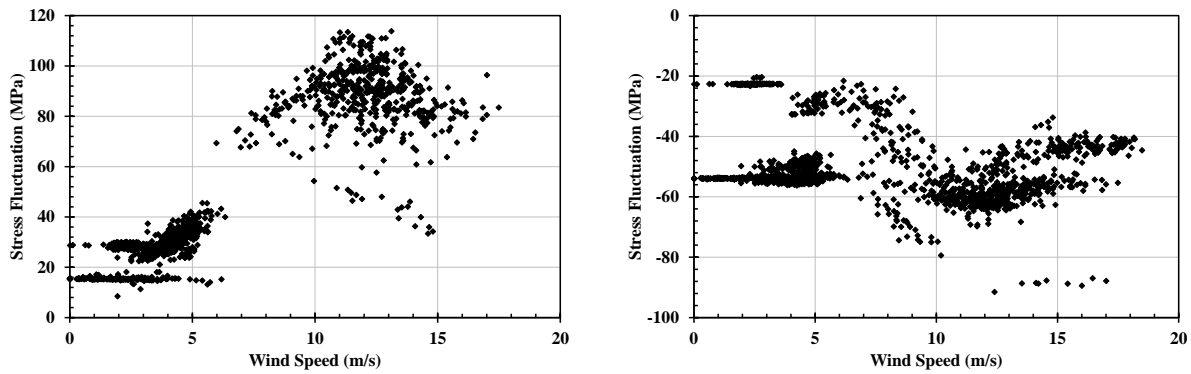


Figure 2.22 – Principal stress fluctuation – level 0

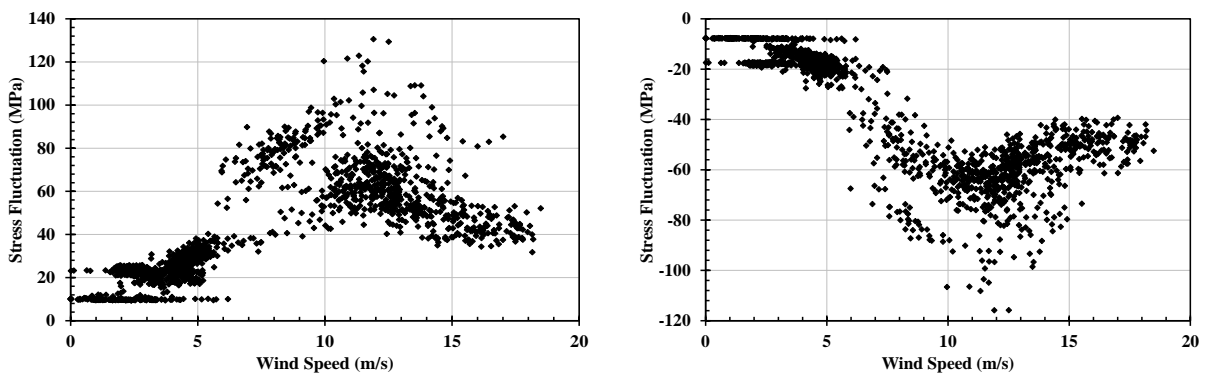


Figure 2.23 – Principal stress fluctuation – level 1

Figure 2.24 shows a set of time histories obtained during a certain period of operation put sequentially in time without the real time gaps. Figure 2.24a shows the vertical stress at two diametrical opposite measurement points located in the shell at level 0 – L0R22V and L0R25V (see Figure 2.11 for location). Values are plotted every 0.4 seconds corresponding to the acquisition rate of 2.5Hz. The additional subplot representing the vector sum of those signals shows an acceptable level of noise with a RMS equal to about 7% of the signal's RMS. The stress evolution is consistent with the nacelle direction represented in Figure 2.24b and with the wind speed (Figure 2.24c). It is noted that the stresses are relatively low and the nacelle azimuth changes frequently during an initial long period, probably due to the fact that most of the records were started manually due to software constrains (no trigger value programmed). The instantaneous extreme and average values of vertical stresses at level 0 and of the wind velocity measured during this period are given in Table 2.6. The extreme values must not coincide with the real maximum vertical stresses in the shell but should be very close to them. Adding the compression from self-weight a maximum compressive stress of about 80MPa can be estimated during Phase I.

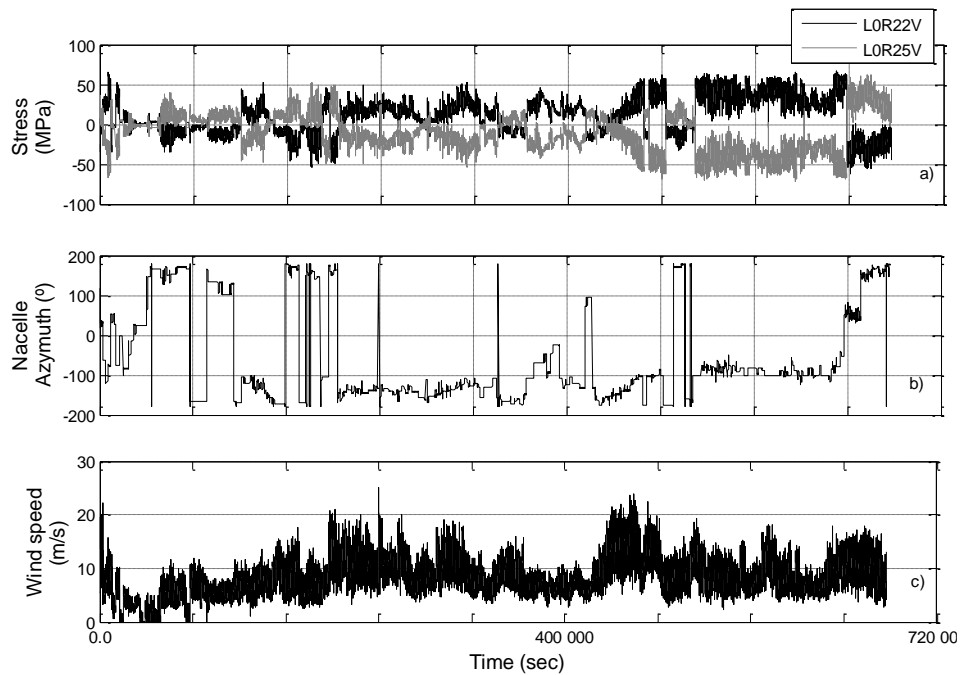


Figure 2.24 - Typical time histories: a) vertical stress at points L0R22V and L0R25V and respective sum; b) nacelle azimuth – positive clockwise from North direction; c) wind speed at nacelle level – Phase I

Table 2.6 – Vertical stresses in the shell during the testing period of Phase I for which wind speed maximum was 25m/s and average was 8.3m/s

	Vertical stresses (MPa)			
	L0R22V	L0R23V	L0R24V	L0R25V
Maximum	67.1	62.2	65.6	62.7
Minimum	-61.8	-72.7	-71.8	-71.3
Average	10.7	-13.2	-24.0	-11.0

For Phase II, considering the dominant direction of the nacelle the measurement points at L0R22V and L0R25V are at the most stressed part of the tower section by bending. Considering that the trigger is set to a wind speed of 14m/s the mean wind speed is relatively high, about 12.8m/s.

The same procedure used to display the results presented in Figure 2.24 for Phase I, was adopted for Phase II in Figure 2.25.

For the sake of comparison, stress computations were performed using the updated model and the load resultants given by the tower producer for several tower elevations. Two design load cases were considered of the type dlc 1.3 and dlc 1.5 (GL-Germanischer Lloyd, 2003), which

correspond to the simulation of the one-year-gust in combination with the loss of electrical connection followed by the rotor start positions which lead to the most unfavourable conditions for the wind tower. The stresses are given in Table 2.7 and are computed from the section loads without safety factor given in the design load tables of the tower manufacturer. The average wind speed is 26m/s and 9m/s and the wind direction relative to the nacelle orientation is 65.5° and 0.1° respectively for dlc 1.3 and dlc 1.5. The maximum measured stresses at levels 0 and 1 given in Figure 2.22 and Figure 2.23 are bounded by the design values of Table 2.7.

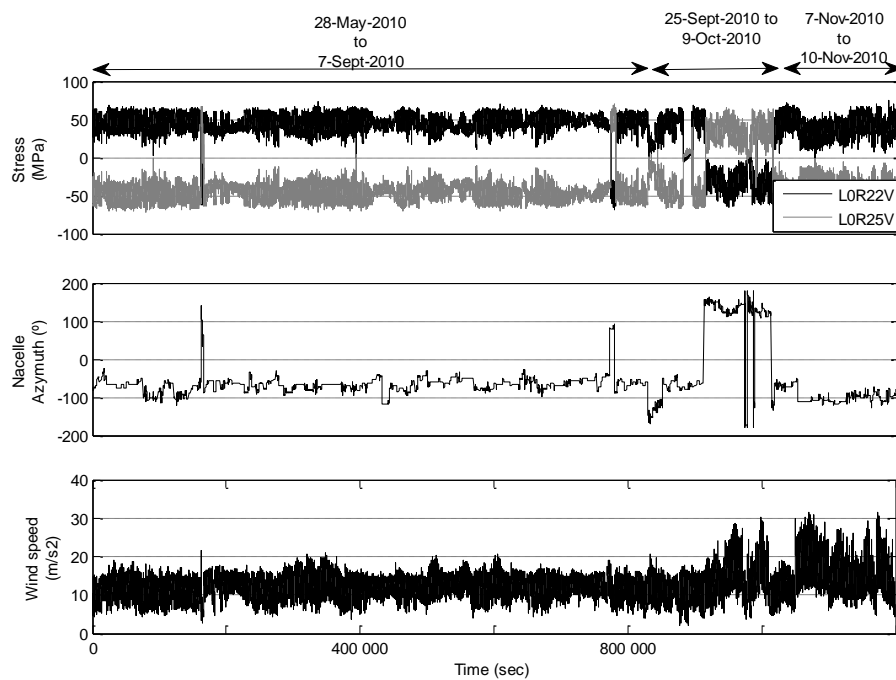


Figure 2.25 - Time signals obtained during Phase II with trigger based on wind speed greater than 14m/s a) vertical stress at strain sensors L0R22V and L0R25V; b) nacelle azimuth – positive direction is clockwise; c) wind speed

Table 2.7 - Vertical stresses computed from design load cases given for the instrumented tower

Section	Bending Moment (kN.m)		Bending Stress (MPa)	
	DLC13	DLC15	DLC13	DLC15
Bottom	14799.0	48196.4	34.0	110.6
Level 0	13947.1	44925.6	38.6	124.2
Level 1	12051.3	37378.4	43.8	135.7
Level 2	8531.1	21048.1	51.4	126.9
Level 3	5752.1	4961.7	65.6	56.6
Top	5227.9	1665.4	42.4	13.5

The highest principal stresses occur for wind speeds of about 12m/s with maximum values of about 130MPa, for the measurements conducted in Phase II.

- Wind induced stresses in the bolts

The bolts in the connections are pre-stressed and therefore the stresses induced by operation are expected to be much smaller than those in the shell. For the sake of comparison, at level 1 the external diameter of tube is 3917mm, the shell thickness is 20mm and the flange thickness is 175mm. Considering that the contact between flanges is perfect the ratio between vertical stresses in the shell and in the flange due to a bending moment is proportional to the inertia ratio at both section levels, which is about eight.

Figure 2.26 shows a comparison of stress histories measured in bolts and shell at level 1 during Phase I. The coefficient of variation (standard deviation divided by the mean value) of stress in the bolt is about five times smaller than in the shell. The mean value of about 20MPa represented as compression in the bolt corresponds to the pre-stress losses experimented by the bolt since the calibration of measurement system was completed.

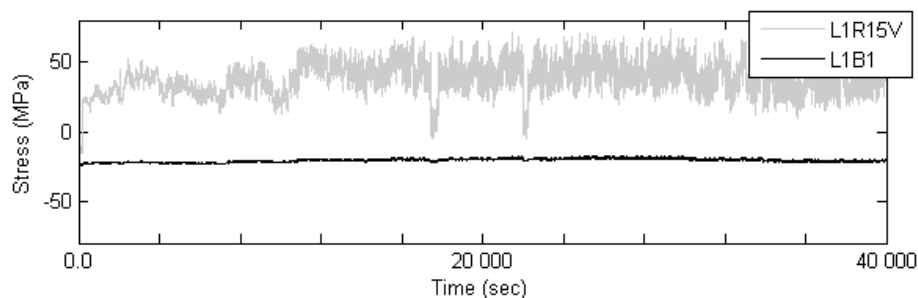


Figure 2.26 - Comparison between bolt stresses and shell vertical stresses at level 1

For the measurements conducted on Phase II, the bolt stress variation is computed against the shell vertical stress variation and the results are presented in Figure 2.27.

It is noted that the mean stress in the bolts is always compressive, revealing that between the time of calibration and the time of measurement there was loss of pre-stress in the bolts. Some of the bolts (e.g. L1B6) present an unsteady behaviour which is justified on one side by the natural interruption of the time line associated with the sequence of different recorded segments and on the other side by the adjustments of pre-stress in the measured bolt influenced by the alterations of the pre-stress in the neighbouring bolts (Veljkovic et al., 2010; Veljkovic et al., 2012). One must be aware that, in this connection there are 6 instrumented bolts among a total of 124 bolts. However, when all the instrumented bolts present an increase of tension, this can be correlated with the maintenance work performed in the tower that

includes retightening of the bolts. This is illustrated in Figure 2.28 where all bolts suffered a synchronized increase in stress, except the first which decreased the stress.

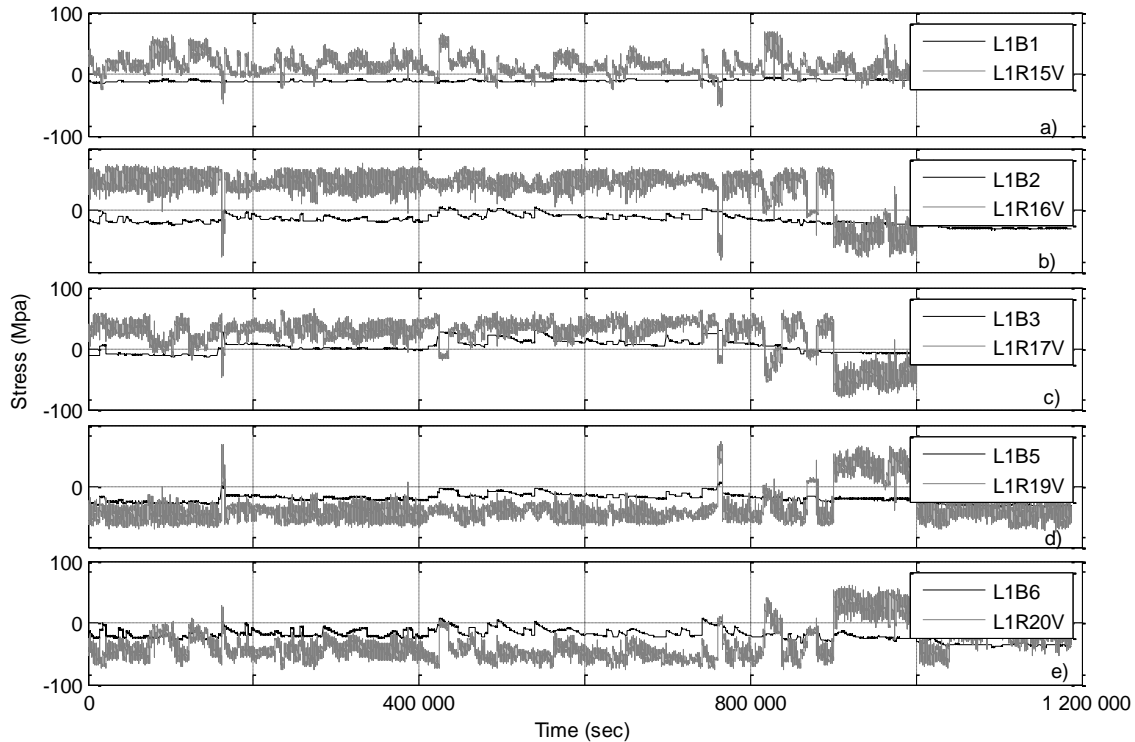


Figure 2.27 - Comparison of stresses in bolts (dark curves) with vertical stresses in shell at level 1 during the second measurement period; a) L1B1 – L1R15V; b) L1B2 - L1R16V; c) L1B3 – L1R17V; d) L1B5 – L1R19V; e) L1B6 – L1R20V

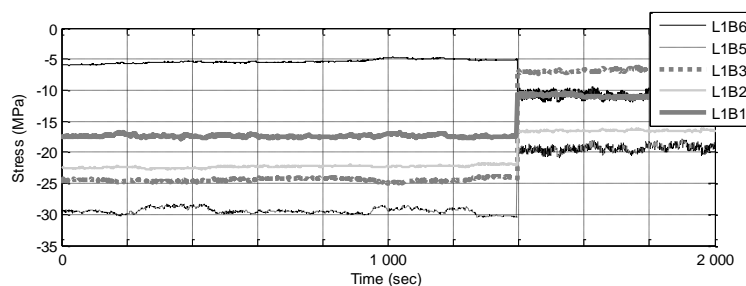


Figure 2.28 - Stress increase in the bolts due to retightening

- Section loads (bending moments)

The signals obtained directly from the measuring instruments can be converted in section resultants and in displacements using the known geometry of the tower. Figure 2.29a represents the bending moment vectors obtained from the shell stresses at different levels for each time increment of the measurements in Phase II. The representation of each vector is

only one point in the polar coordinates of the diagram. Bending moments at lower level are represented with lighter grey marks and at upper levels in darker grey marks. The bending moment vectors' dominant direction is orthogonal to the dominant wind direction as expected. Figure 2.29b shows the same representation for a shorter period of about thirty minutes, which is the same time window used to represent time histories in Figure 2.30. These are typical time histories of the bending moments at different levels obtained during wind speed average of 16.5m/s and nacelle azimuth average of 120°. A representation of the bending diagrams of M_x , M_y and resultant M along tower height for the same time period is shown in Figure 2.31. Comparing with design bending moments given in Table 2.7, measured values are in the range of values given for DLC13.

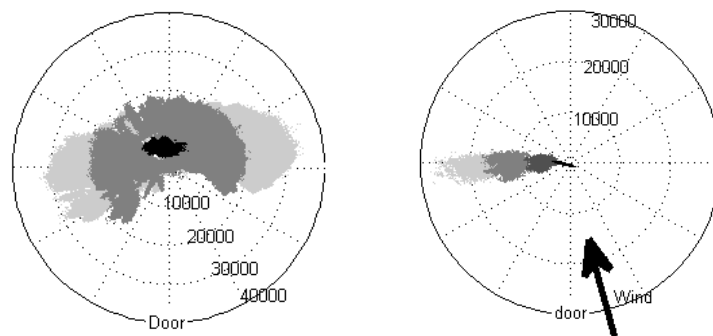


Figure 2.29 - Bending moment vectors represented by their amplitude and direction in polar coordinates; a) entire Phase II; b) selected 2000 seconds

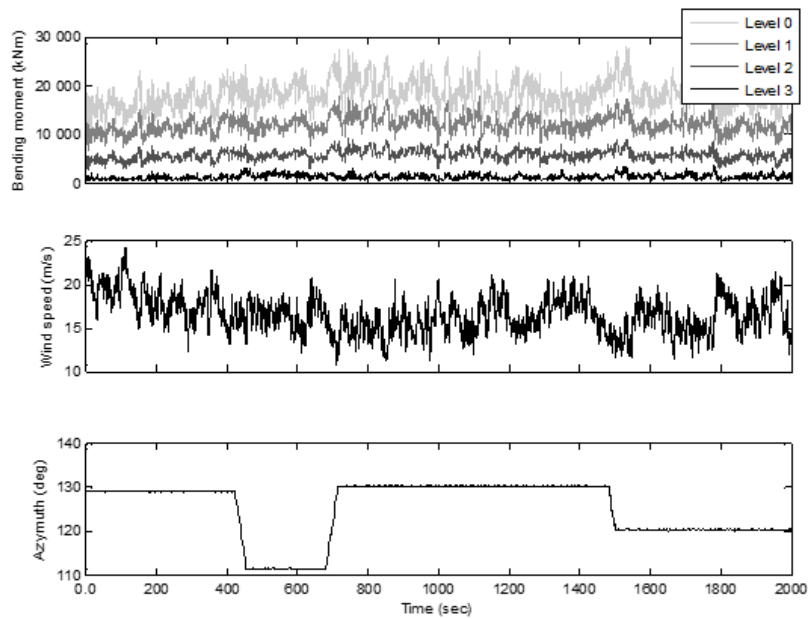


Figure 2.30 - Typical time histories for bending moments obtained from strain measurements during wind speed average of 16.5m/s

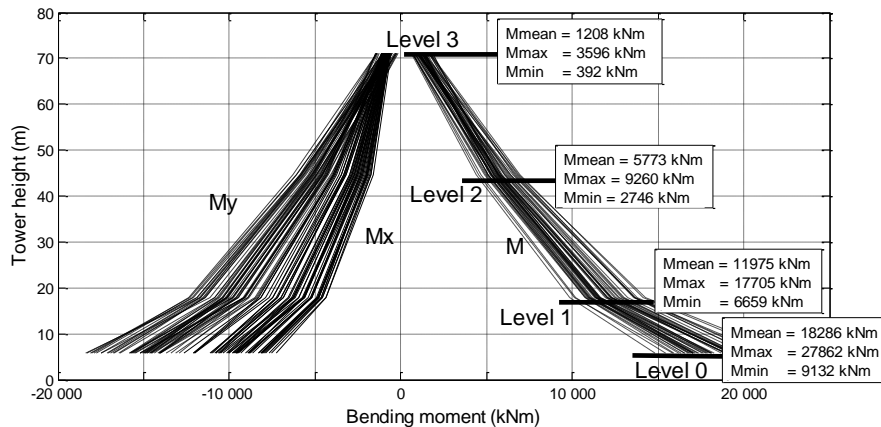


Figure 2.31 - Bending moments M_x , M_y and resultant M obtained from selected shell stress measurements; mean values over 40 seconds; wind speed average is 16.5m/s

2.2.3.2. Acceleration and modal identification

After erection of the tower and before operation starts a preliminary modal identification was performed. The methodology used relies on output-only methods and ambient vibration response analysis (Bendat and Piersol, 1993; Brincker et al., 2000; Kelly, 2000). The three accelerometers at the top of the tower (level 3) and two at each of the levels 1 and 2 were used. The acceleration measurements for modal extraction were made during the idle state of the turbine.

A methodology in the frequency domain (as function of frequency) was used to identify the modal parameters, which consists of simply picking the peaks of the spectral estimates of the measured signals to identify the natural frequencies. The Enhanced Frequency Domain Decomposition (EFDD) (Brincker et al., 2000) implemented in a software package for system identification (SVS, 2007) was used to extract the modal information from the ambient free vibration. The corresponding average of the normalized singular values of the spectral density matrices are shown in Figure 2.32. The marked peaks correspond to four flexural mode shapes of the tower, two bending modes in x and y directions. Table 2.8 summarizes the obtained results for the modal parameters. Some difference may be expected between the fore-aft and the side-to-side natural frequencies of the tower. However, it is to be noted that the accuracy of the measurements tends to be of the same order of that difference.

The viscous damping identified in the first and second mode is higher than expected for this type of structure (around 1%). Since the measurements were made during relatively strong wind, the aero elastic damping induced by the interaction with the wind is probably the cause for the increase of the damping ratio.

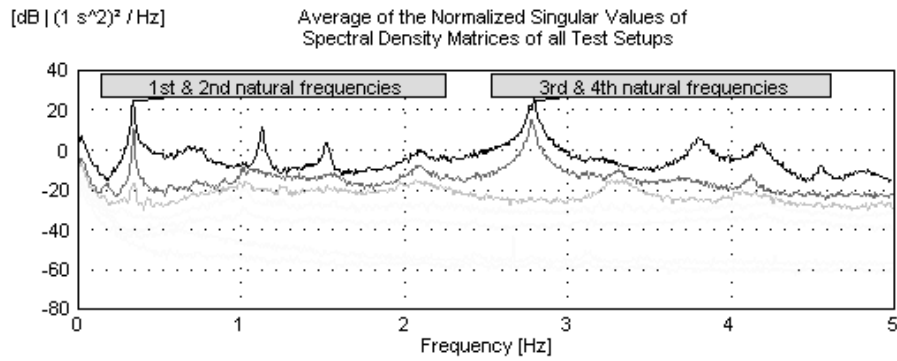


Figure 2.32 - Singular values of the spectral density matrices

The blades of the horizontal-axis wind turbine rotate in close proximity to the tower and important dynamic loading is induced when passing in front of it. The blade-passing frequency is equal to the turbine rotational frequency multiplied by the number of blades on the turbine rotor, which is three. The dynamic response of the wind tower is mainly due to the turbine rotation and is therefore almost periodic.

Table 2.8 - Natural frequencies, modes and damping

		Mode			
		1	2	3	4
Frequency (Hz)	Measured	0.340	0.343	2.767	2.794
	Updated FE model ($E_s=300\text{MPa}$; $e=1.0\text{m}$)	0.345	0.345	2.751	2.751
Damping (%)		1.32	0.96	0.13	0.23
Mode type		Bending Nacelle direction (x-x)	Bending Transversal to Nacelle direction (y-y)	Bending Nacelle direction (x-x)	Bending Transversal to Nacelle direction (y-y)

To avoid large vibration amplitudes, the lowest natural frequencies of the tower should be kept away from the rotational and/or blade-passing frequencies and their harmonics (Lavassas et al., 2003). Analysing the spectra obtained from the measurements of the accelerations at the top of the tower (Figure 2.33) three peaks are clearly identified in the range 0Hz to 1Hz and several other peaks are identified up to 3Hz. The first peak in the spectrum corresponds to the rotational frequency of 0.25Hz. The wind turbine manufacturer gives operating limits of 0.13Hz and 0.25Hz, for the lower and upper rotor speed, respectively. The upper limit is attained for average wind speeds around 12m/s, which is in the range of wind speed for which recording of the monitored signals is activated. The second spectral peak is at frequency 0.34Hz and corresponds to the first and second natural frequencies of the tower. The damping ratio measured during operation in these modes is 1.12%, close to the value obtained in the modal identification (Rebelo et al., 2012a). The third peak in the spectrum corresponds to the blade passing frequency of 0.75Hz.

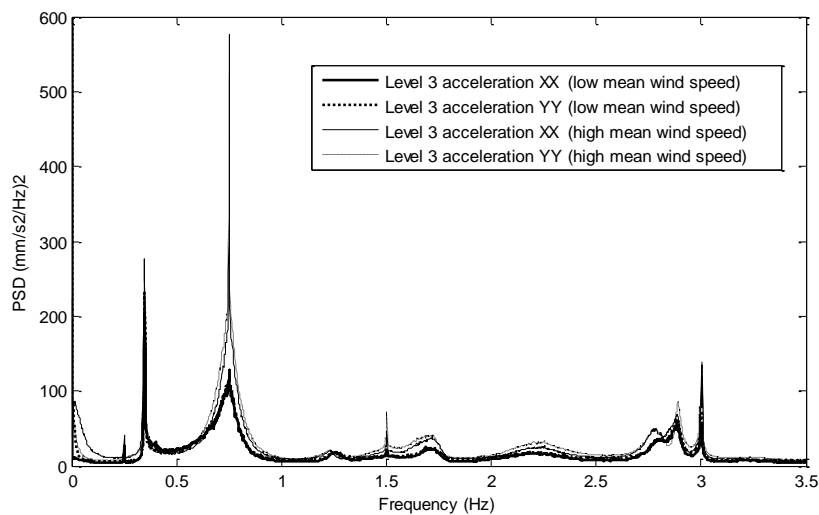


Figure 2.33 - Power spectral densities of the acceleration at the tower level 3 obtained during operation

It is expected that the wind load acting on the tower increases up to a certain limit defined by the type of turbine, in this case the load increases up to average wind speeds of about 12m/s. This effect can be observed in the spectral values shown in Figure 2.33 which increases for the time series corresponding to higher wind speed average (Phase II). The peaks at 1.5Hz and 3.0Hz are harmonics of the blade passing frequency. The third and fourth natural frequencies appear at about 2.8Hz near the third harmonic of the blade passing frequency. The measured damping was 1.4% and therefore higher than the one measured during modal identification.

2.2.3.3. Displacements

The design guidelines do not establish general limits for displacement of the tower. However, rules are given (IEC 61400-1, 2005; DNV/Risø, 2002; GL-Germanischer Lloyd, 2003) to compute the displacements and to verify that deflections do not affect structural integrity in the design conditions, e.g., no mechanical interference between blade and tower will occur. These deflections are composed by tower and blade displacements. Concerning the tower, the deflections are minimized by avoiding resonance and, therefore, by limiting the dynamic displacements. Note that the clearance between blade and tower is not only governed by the structural deflections, but also by a possible slip at the yaw bearing, by the perpendicularity of the tower flange, and by the tolerances on the tilt and on the rotor plane. (DNV/Risø, 2002; GL-Germanischer Lloyd, 2003).

The rotations at levels 2 and 3 are obtained directly from the inclinometers. Figure 2.34 shows a typical measured time history of tower inclination. The mean value of the measured rotation in the time window is 0.20° for Level 3 and 0.18° for Level 2.

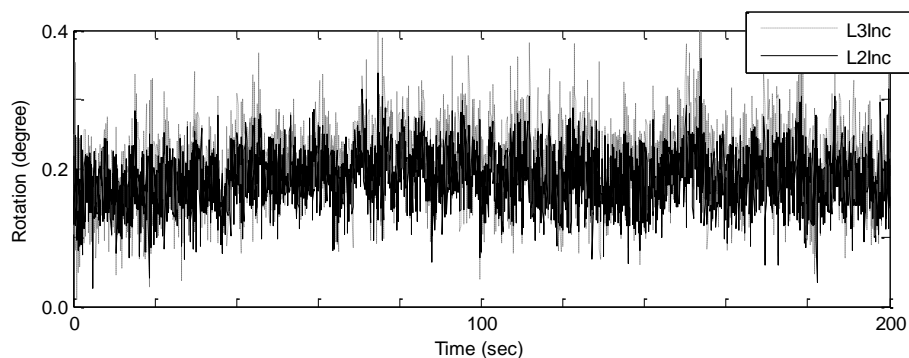


Figure 2.34 - Typical time window of tower inclination measured at levels 2 and 3

Displacements can be obtained from integration of the accelerations, although only the dynamic part of the signal can be obtained (Figure 2.35). Integration error was controlled through Baseline Correction and Filtering (Bendat and Piersol, 1993; Dally et al., 1993). The first process consists on (i) determining, through regression analysis (least-squares-fit method), the straight line that best fits the time-acceleration pairs of values and then (ii) subtracting from the actual acceleration values their corresponding counterparts as obtained with the regression-derived equation. In this manner, spurious baseline trends, usually well noticeable in the displacement time-history obtained from double time-integration of uncorrected acceleration history, are removed. Afterwards a Butterworth high pass filter above 0.2 Hz was applied in order to remove low frequency components not removed by the former procedure. Data processing was performed using Matlab (The MathWorks Inc., 2010).

These dynamic displacements are small compared to the quasi-static displacements expected for the tower top, which can reach values of the order of more than 1 meter. The small values shown in Figure 2.35 confirm the expected small vibration amplitudes during operation in a well-designed tower.

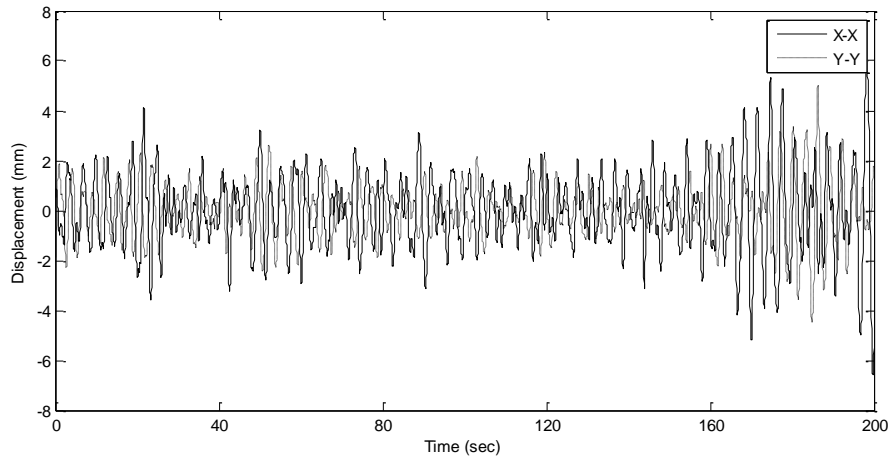


Figure 2.35 - Typical time window of horizontal displacements at level 3 in x- and y-direction obtained from time integration of filtered accelerations using a highpass Butterworth filter above 0.2Hz

2.2.4. Methodology for estimation of experimental Fatigue Spectra

Structures subjected to wind loading are prone to suffer failure under fatigue. In the case of the wind towers it can be even the governing load case for the design of some parts of the structure namely the segment connections. Figure 2.36 shows the generic loading characteristics of such structures.

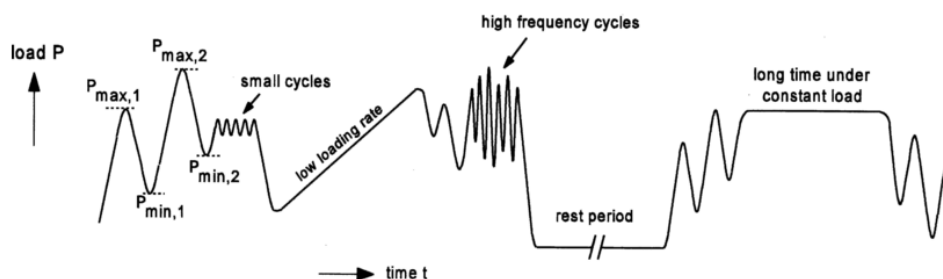


Figure 2.36 – Characteristic occurrences of a load-time history $P(t)$ (Schijve, 2009)

The design of these kind of structures is considered by comparing the design fatigue spectrum (number of cycles vs. stress amplitude) provided by the tower manufacturer and the S-N curve given by the proper design standard (for instance EN 1993-1-9 for design in Europe) for each fatigue detail category. The design fatigue spectrum from the tower manufacturer is currently obtained with numerical simulations using proper software based on CFD (Computational

Fluid Dynamics) method. With such software it is possible to simulate the tower subjected to different wind loadings and so to obtain the response in terms of number of cycles for each stress amplitude for one year. The design fatigue spectrum is afterwards extrapolated for the lifetime span of 20 years currently used to define operating lifetime of wind towers.

In order to count the number of cycles from a time history, some methods are available in the literature. One of them is the rainflow method (ASTM E1049-85, 2011). Downing and Socie (1982) created one of the more widely referenced and utilized rainflow cycle-counting algorithms.

The algorithm of the rainflow counting method is based on the following steps (Ko et al., 2012):

- A rainflow path is started at each peak and trough
- When a rainflow path that started at a trough comes to the tip of a roof, the flow stops if the opposite trough is more negative than that at the start of the path under consideration. Conversely, a path that started at a peak is stopped by a peak which is more positive than that at the start of the rain path under consideration.
- If the rain flowing down a roof intercepts flow from previous path the present path is stopped.
- A path is not started until the path under consideration is stopped

Considering the values obtained with tower live monitoring presented, the fatigue spectra were calculated for the shell vertical stresses using the presented rainflow method.

The original spectra were computed from measured time series with totals of 0.68×10^6 and 1.2×10^6 seconds length corresponding to monitoring periods of 139 and 159 days, respectively, for Phase I and Phase II. Subsequently, the number of cycles was linearly extrapolated for a 20 years lifetime (20×365 days) and the obtained spectra are given in Figure 2.37.

Differences in curves obtained for different phases are mainly due to the difference in the mean wind loading associated to the monitoring phases, that is, for Phase I with a lower mean wind speed the number of cycles increases in lower stress ranges and decreases in the upper stress ranges.

The design provided by the EN 1993-1-9 (2005) is based on the analysis of S-N curves (stress range vs. number of cycles) according to fatigue detail categories of the each element, named

with the design stress range for failure at 2×10^6 cycles. Figure 2.38 shows the design S-N curves for each considered detail category.

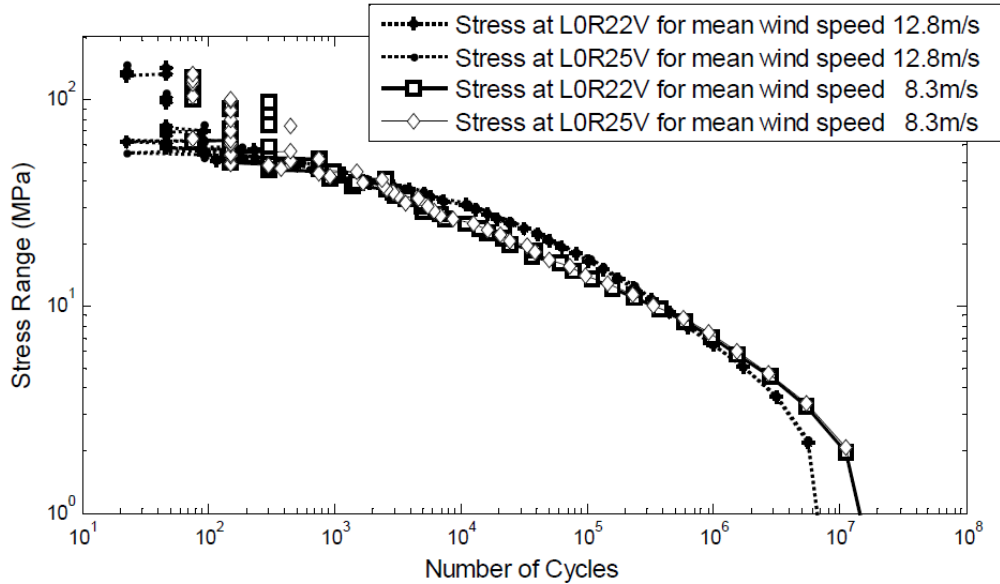


Figure 2.37 - Measured fatigue spectra extrapolated for 20 years lifetime obtained for level 0

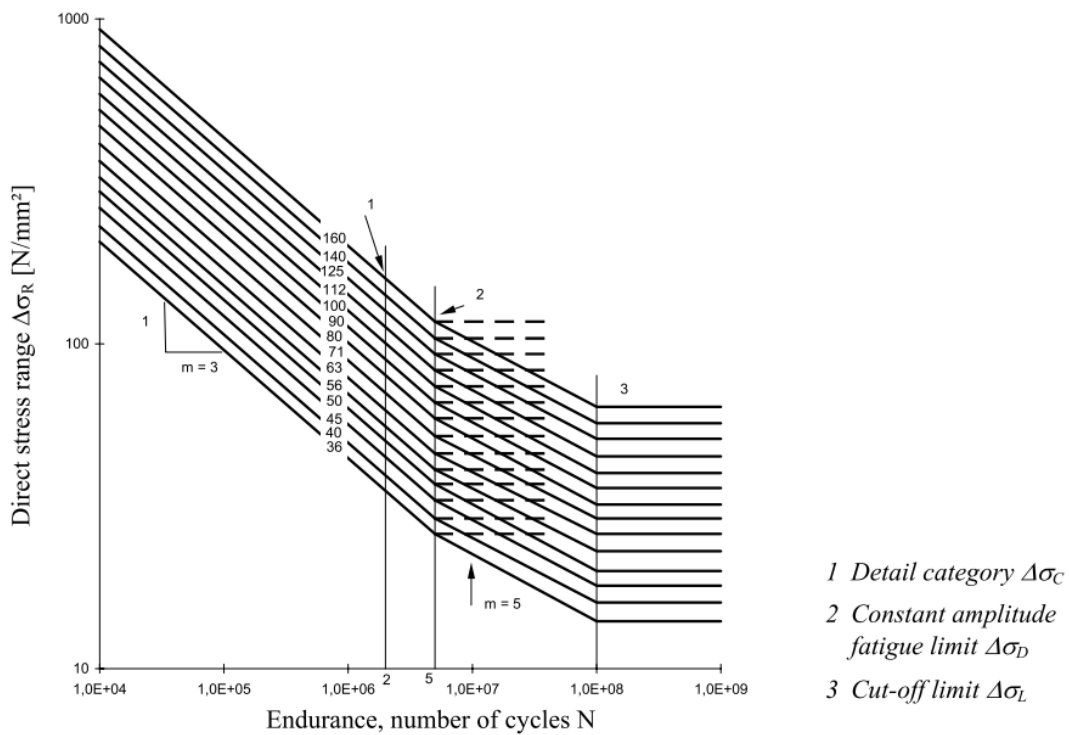


Figure 2.38 - Fatigue strength curves for direct stress ranges (EN 1993-1-9, 2005)

The equation of each one of the 3 slopes of the S-N curves are given by equations (2.4).

$$\Delta\sigma_R^m N_R = \Delta\sigma_C^m \cdot 2 \times 10^6 \text{ with } m=3 \text{ for } N \leq 5 \times 10^6$$

$$\Delta\sigma_R^m N_R = \Delta\sigma_D^m \cdot 5 \times 10^6 \text{ with } m=5 \text{ for } 5 \times 10^6 \leq N \leq 10^8$$

$$\Delta\sigma_L = \left(\frac{5}{100}\right)^{1/5} \Delta\sigma_D \text{ is the cut off limit}$$
(2.4)

The comparison between the measured spectra and the design load spectra given by the tower designer, as well as with the fatigue strength curve given by EN1993-1-9 (2005) for fatigue detail 71 (Table 2.9), considering the welded connections in the segment plates, are shown in Figure 2.39.

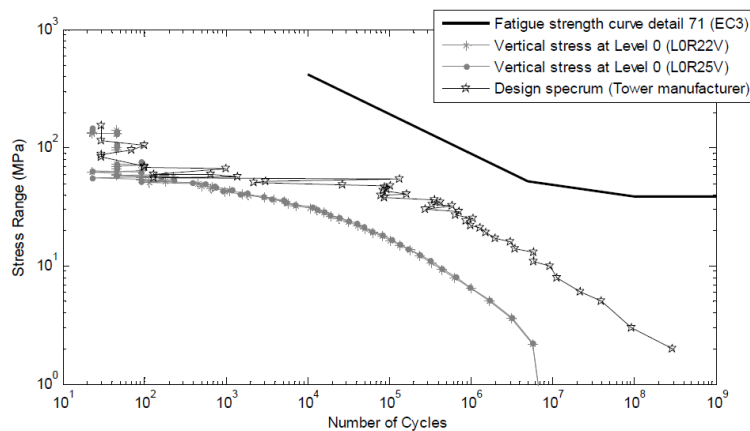
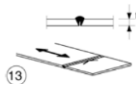

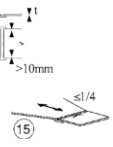


Figure 2.39 - Comparison of measured fatigue spectrum extrapolated for 20 years lifetime with design spectrum and strength curve obtained from EN1993-1-9 (2005) for detail 71

Table 2.9 - Transverse butt welds (fatigue detail category) (EN 1993-1-9 2005)

Detail category	Constructional detail	Description	Requirements
71		13) Butt welds made from one side only when full penetration checked by appropriate NDT	13) Without backing strip
	size effect for $t > 25\text{mm}$: $k_S = (25/t)^{0.2}$  	With backing strip: 14) Transverse splice 15) Transverse butt weld tapered in width or thickness with a slope $\leq 1/4$. Also valid for curved plates	Details 14) and 15) Fillet welds attaching the backing strip to terminate $\geq 10\text{mm}$ from the edges of the stressed plate. Tack welds inside the shape of butt welds

According to the Palmgren-Miner rule used in Annex A of the Eurocode (EN 1993-1-9, 2005) and given by expression (2.5) with $\gamma_{Mf}=1.35$ and $\gamma_{Ff}=1.0$ the damage index obtained for the stress history at point LOR22V during the Phase II is $D=7.4 \times 10^{-4}$.

$$D_d = \sum_i^n \frac{n_{Ei}}{N_{Ri}} \quad (2.5)$$

To compute the lifetime the most unfavorable situation would be based on the length of the measured time series, which gives the results presented in equation (2.6).

$$Lifetime = \frac{Time(years)}{D} = \frac{1.2 \times 10^6}{3600 \times 24 \times 365 \times 7.4 \times 10^{-4}} = 51 \text{ years} \quad (2.6)$$

2.3. Final comments

The exploitation of the renewable energies has increased in the last few years due to the increasing concerns about the world environment. An increase in the wind energy exploitation both in offshore and onshore locations is foreseen for all over the world. In onshore locations the current tendency will be the replacement of old outdated low-power turbines with more powerful and eventually higher located turbines.

Tubular steel towers proved to be the most suitable solution for current hub heights up to 100 meters, because of the low weight when comparing to concrete solutions, very suitable for transportation of the tower segments to construction site.

The monitoring system developed for the current steel tower allowed a deeper insight into the turbine operation and tower response through the updating and calibration of advanced FE models. In a preliminary phase prior to the development of this PhD thesis an experimental program was developed consisting of the instrumentation for monitoring of a 80 meters high steel wind tower supporting a 2.1MW turbine Wind Class III IEC2a erected in the central part of Portugal. This measurement system, presented in the first part of this chapter is able to measure strains in three directions of 26 points of the inner surface of the tower shell and in 18 pre-stressed bolts. Additionally, accelerations in three levels of the tower, inclinations at two levels and the inner temperature are measured.

Within the framework of this PhD thesis the calibration of the equipment was performed and preliminary measurements were used for consistency analysis of the data. A finite element model was developed and updated through modal identification performed before the turbine started production.

There was the need to assure the quality of the measured data. It was verified that, at each cross section, the sum of the vertical stresses was, as expected, near zero, since only stresses due to bending are measured. As expected, stress variations along the tower height are low, since the cross section varies in diameter and thickness along the height, corresponding to an optimized structural solution.

The strains measured on the cylinder shell (vertical, horizontal and inclined) vary with wind speed, increasing up to a wind speed of about 12 m/s and decreasing beyond that. This is typical of pitch regulated towers and is due to the pitch rotation of blades in order to maintain a constant production without overloading the tower. The maximum measured principal stress in the shell was about 130MPa, and the maximum vertical stress about 70MPa.

The stress variation inside the pre-stressed bolts is low and therefore almost independent of the wind speed. It is concluded that the bolt pre-stress is very effective and there is a good contact between the flanges due to the low force fluctuation measured in the bolts. This is an expected conclusion because it is not probable that service loads, mainly from measured wind speeds up to 20m/s, could induce the opening of the joints between the stiffening rings of the connection.

Dynamic response is evaluated through the acceleration spectra. It is clear that no resonance occurs in the tower in the range of identified natural frequencies. The dynamic deflections are computed by integration of the accelerations and therefore represent only the dynamic part of the response.

Stress fatigue spectra can be computed for the measured data. The spectra obtained for the shell stresses at level 0 section were extrapolated to lifetime of twenty years. They are clearly below the design spectra as expected, except for the higher stress ranges. Longer data acquisition will allow more clarification of this issue, since the number of large stress ranges is relatively low.

3. IMPROVED SOLUTIONS FOR HIGHER TOWERS

3.1. Introduction

As it was described previously, the increase in the exploitation of renewable energy, namely the wind energy, lead to the need for improving the current exploitation techniques.

The increase in height of the wind towers is pointed out as an efficient way of improving the energy production since it is possible to use a more powerful and stable wind profile.

The wind shear profile presents an increasing value in wind velocity with the height according to Figure 3.1. It should be kept in mind that the mechanical energy extractable from an air stream passing through a given cross-sectional area is proportional to the third power of the velocity. Thus, the wind shear profile in the top layers is more powerful but it is also more stable, since the turbulence at a certain level is smaller, and the slope of the wind shear profile is also lower which improve the dynamic behavior of the whole system including the tower.

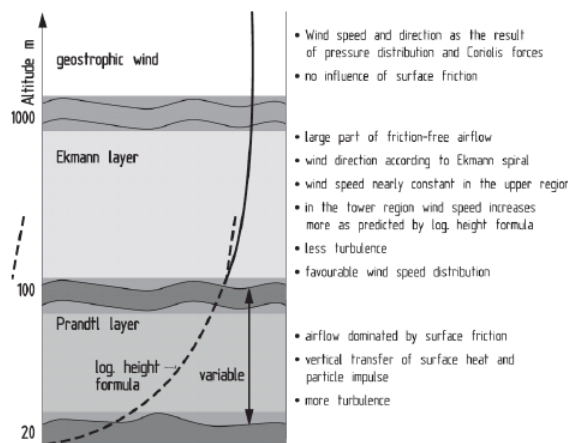


Figure 3.1 – Wind shear profile (Hau, 2013)

The increase in height will also avoid the turbulence due to the ground obstacles for instance in industrial areas or forests. The illustration of Figure 3.2 shows the flow wake behind an obstacle with a certain height.

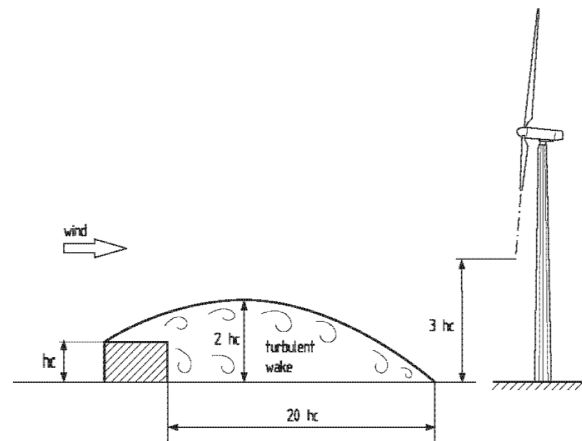


Figure 3.2 – Flow wake behind an obstacle (Hau, 2013)

The goal of increasing the tower height raises new problems that must be solved. The diagram of Figure 3.3 illustrate three major problems related with this increase.

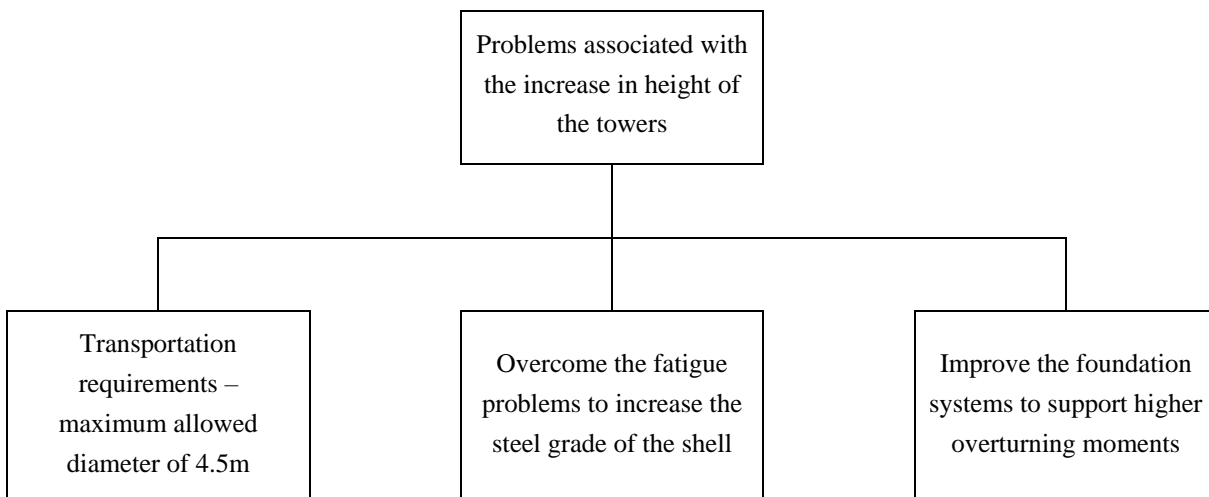


Figure 3.3 – Problems associated with the increase in height

Some ideas have been developed to overcome each one of the problems presented in Figure 3.3. The transportation requirements and respective solutions as well as the descriptions of the fatigue problems and proposed solutions will be addressed in this chapter while the improvement of the foundation systems will be thoroughly presented, analyzed and discussed in chapters 4, 5 and 6 with analytical, experimental and numerical analysis.

Currently the maximum dimensions that can be transported on roads are around 4.5m diameter, 36m of length and 70ton of weight. For an 80 meters high wind tower the required diameter is around 4.2 meters in the base and so an increase in height will very likely overcome the maximum allowed diameter.

A solution proposed for this problem is based on the modular steel construction by splitting the segments into different pieces and using longitudinal bolted connections. The proposed solution is presented in Figure 3.4a which was developed under the scope of HISTWIN2 project (Veljkovic et al., 2015). In this type of construction, the traditional welded ring flange connection of the current tubular towers is replaced by a bolted friction connection. This allows the improvement concerning fatigue problems by withdrawal of the welding in the segments in both longitudinal and transversal directions and bolts in tension. This solution also opens the possibility for using higher steel grades, given that the fatigue detail is improved and higher stress ranges are allowed.

Some manufacturers such as Andresen Towers, developed similar systems with longitudinal and transversal connections but with a polygonal shell as presented in Figure 3.4b.



a. Circular tubular tower



b. Polygonal tubular tower
(Andresen Towers, 2011)

Figure 3.4: Steel tubular towers

Along with the tubular steel towers, the most common wind towers typologies are pre-stressed tubular concrete towers, lattice towers, timber towers and hybrid towers (tubular + concrete and tubular + lattice). For each one of these typologies there are some implemented or in development solutions to allow the construction of towers higher than 100m and up to 160-170m.

In the case of the pre-stressed concrete towers the solution proposed for the use in higher heights is similar to the tubular towers. These concrete towers are composed by segments with longitudinal and transversal pre-stressed connections in order to allow an easier transportation as it can be seen in Figure 3.5.



Figure 3.5: Modular concrete INNEO tower (INNEO Torres, 2008)

The solution of lattice towers allows very high solutions like the one presented in Figure 3.6 that illustrates a 160 meters high wind tower. However, these solutions present some problems due to the high number of bolted connections which will lead to longer times of assembly and maintenance. The aesthetical aspects of the tower and specially the lack of protection for the workers are also important handicaps of this solution.



Figure 3.6 - 160m Fuhrländer Wind Turbine Laasow (Almeida, 2015)

A different proposal is presented by Wasatch Wind and it is called Space Frame Wind Tower. This is basically a lattice wind tower with all their advantages but it is covered outside by a special fabric which improves not only the aesthetics of the tower but also solves some problems such as the protection of the structural elements and also provides some protection to the workers. It can be seen in Figure 3.7.



Figure 3.7: Space Frame Wind Tower (General Electric, 2014)

Some solutions for timber tower structures can also be found. TimberTower company is a fair example of this possibility. This company expects to achieve heights up to 160m by keeping together cross-laminated timber panels in a polygonal profile. The shape of this system can be found in Figure 3.8.



Figure 3.8: Timber wind tower (Engström et al., 2010)

In terms of hybrid towers, the most common geometry is steel-concrete tubular towers. In this system, both technologies presented before can be implemented together in order to achieve higher heights.

Under development there is a new typology of hybrid systems using lattice and steel tubular elements as presented in Figure 3.9. It is similar to the technology used in jacket support structure for offshore wind towers.

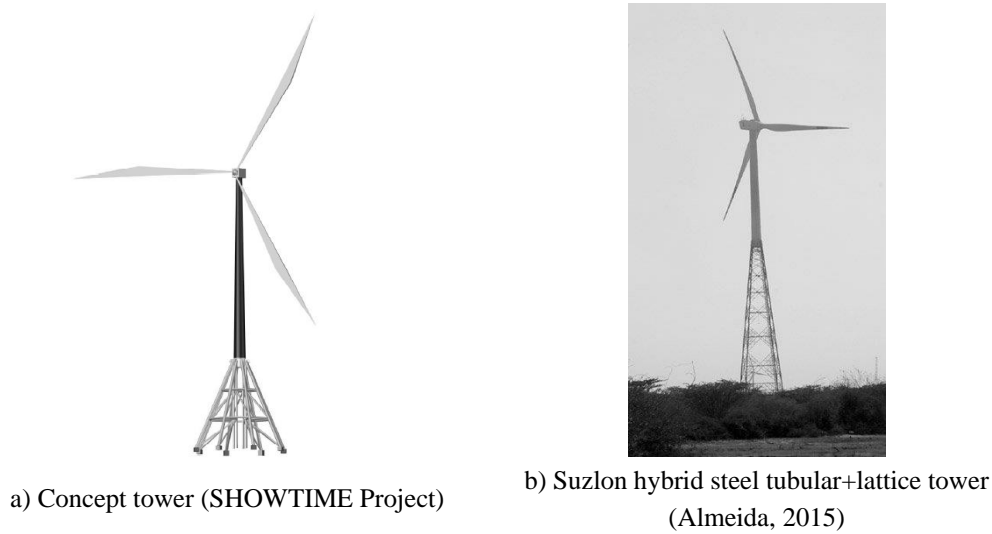


Figure 3.9: Hybrid steel lattice-tubular tower

The cost and performance of several typologies of high wind towers has been addressed by the study conducted by Engström et al. (2010). In this study it was considered the use of welded steel shell, steel shell friction joint, concrete slipformed, hybrid tubular+concrete, steel lattice and wood considering a 3 or 5MW wind turbine. Some of the obtained results of this study are presented in Figure 3.10 in terms of investment for the different typologies, for different heights and for the two different rated powers. This study reports the investment of a commissioned wind turbine divided by the yearly production. The proposed solution with friction connection (Veljkovic et al., 2015) is considered in this study to be a competitive solution, in terms of investment, for higher wind towers. Further details of this solution are discussed in following sections.

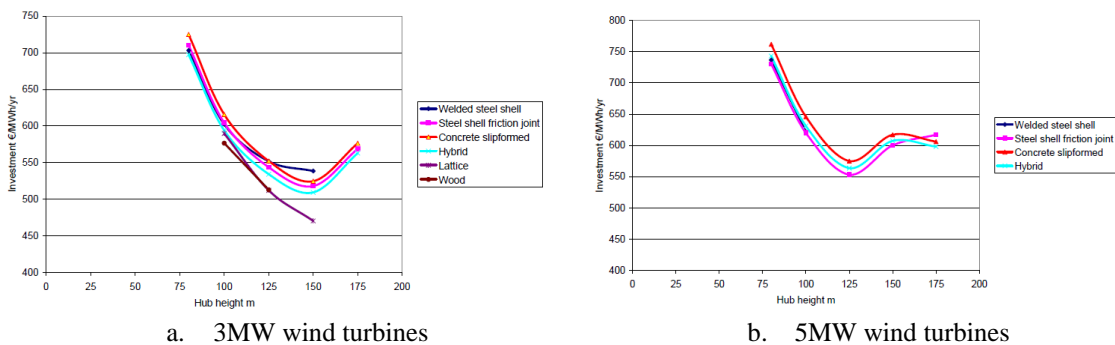


Figure 3.10 – Summary of tower alternatives (Engström et al., 2010)

3.2. Tower design recommendations

The guidelines for the design of wind towers (tubular steel, concrete and hybrid tubular + concrete) are presented in LaNier (2005), Moura (2012) and Rebelo et al. (2014). A comprehensive set of design examples applying the design procedures are provided along with LCA and LCC analysis of the obtained design results. Almeida (2015) presented a design example of a hybrid tubular and lattice tower along with the design of the correspondent transition piece.

The design procedure includes following steps:

- Definition of the wind turbine type. According to IEC 61400-1 (2005) the wind turbine type is defined according to the maximum wind velocity and turbulence expected at hub height. Definition of the control system parameters of the turbine and definition of the geometry of the blades;
- Preliminary definition of the wind loading acting on the rotor according to the load cases defined in IEC 61400-1 (2005). This loading can be used to predesign the tower and definition of geometry and mechanical parameters of the structure and foundation (dimensions, material and soil properties); Natural frequencies of the global system (Turbine+tower+foundation+soil interaction) must be checked in order to avoid resonance during operation. Tower design might be changed in order to fulfil this requirement or control system parameters adapted to avoid frequency of rotation close to eigenfrequencies of the tower;
- Final estimation of loads due to wind considering the whole system being acted by wind flow in CFD based software including tower and blades flexibility and considering all the load cases defined in IEC 61400-1 (2005). Such calculations are very time consuming and are usually performed with dedicated and extremely specialized software;
- Final design checks of the structure using final loads, extreme and fatigue loading, eventually combined with other type of loads, e.g. seismic loading.

3.3. Connections in tubular steel towers

The state-of-art connections are flange bolted connections as presented in Figure 3.11. This type of connection present two main difficulties, the first related to the high cost of the ring flange and the second to the low performance of the fatigue detail controlled by the weld

between shell and ring flange which is considered detail category 71 according to Eurocode (EN 1993-1-9, 2005). Both details are presented in Table 3.1.

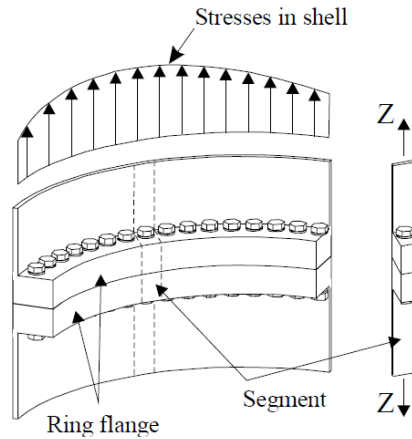


Figure 3.11 – Ring flange connections geometry (Seidel and Schaumann, 2001)

In order to increase the height of the tower it is recommended to increase the steel grade to a higher strength steel instead of the current S355. This increase will withstand the higher stresses in the shell and also the use of steel grades with better fatigue properties. Against the premises of EN 1993-1-9 (2005), Jesus et al. (2012) proved that an increase in the steel grade will lead to an improvement in the fatigue behaviour of the material. However, in order to be possible an increase in the steel grade, some problems related and referenced to this geometry of flange connections must be overcome.

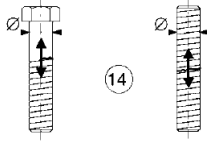
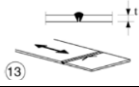

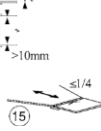
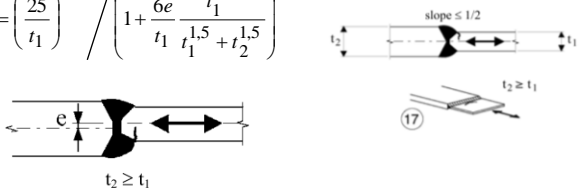
Even though the bolts in tension present a lower detail category in comparison with the butt welds, the induced stress is much lower in this elements since they are prestressed (Figure 2.26) and so the butt welding is commonly the governing load case.

To overcome the presented problems, a new connection system was proposed under the scope of the HISTWIN (Veljkovic et al., 2012) project. This connection, a friction connection geometry, presents a much better fatigue behaviour in comparison with the current flange connection. This geometry can withstand a detail category of 112 according to EN 1993-1-9 (2005).

The geometry of the friction connection is presented in Figure 3.12. This connection is a pure friction connection that connect two plates in which one is composed by normal round holes and another with long open slotted holes avoiding this way shear in the bolts and in the plates. In the inner side of the connection there is a cover plate to effectively transfer the preload force from the bolts to the shell.

This geometry of connection presents a specific requirement in terms of assembly. The prestressed bolts must allow the tightening of only one side (inner side) since there is no access to the outer side of the tower during the assembly.

Table 3.1 - EC 3 1-9 Fatigue detail categories (bolts in tension and butt welds) (EN 1993-1-9, 2005)

Detail category	Constructional detail	Description	Requirements
50	<p>size effect for $t > 30\text{mm}$: $k_s = (30/t)^{0.25}$</p> 	14) Bolts and rods with rolled or cut threads in tension. For large diameters (anchor bolts) the size effect has to be taken into account with k_s	14) $\Delta\sigma$ to be calculated using the tensile stress area of the bolt. Bending and tension resulting from prying effects and bending stresses from other sources must be taken into account. For preload bolts, the reduction of the stress range may be taken into account.
71	<p>size effect for $t > 25\text{mm}$: $k_s = (25/t)^{0.2}$</p>   	<p>13) Butt welds made from one side only when full penetration checked by appropriate NDT</p> <p>With backing strip: 14) Transverse splice 15) Transverse butt weld tapered in width or thickness with a slope $\leq 1/4$. Also valid for curved plates</p>	13) Without backing strip Details 14) and 15) Fillet welds attaching the backing strip to terminate $\geq 10\text{mm}$ from the edges of the stressed plate. Tack welds inside the shape of butt welds
71	<p>size effect for $t > 25\text{mm}$ and/or generalization of eccentricity: $k_s = \left(\frac{25}{t_1}\right)^{0.2} \left/ \left(1 + \frac{6e}{t_1} \frac{t_1^{1.5}}{t_1^{1.5} + t_2^{1.5}}\right)\right.$</p> 	17) Transverse butt weld, different thicknesses without transition, centrelines aligned.	

The slip resistance of the connection is given by the expression (3.1) according to Eurocode (EN 1993-1-8, 2005). It is possible to check the influence of some parameters such as the rugosity of the surface (μ_s) and the prestress force in the bolts ($F_{p,c}$).

$$F_{S,Rd} = \frac{n \cdot k_s \cdot \mu_s}{\gamma_{M3}} \cdot F_{p,c} \tag{3.1}$$

Values for the rugosity coefficient were estimated by Heistermann (2011) for different steel grades and for different surface treatment. The results obtained can be found in Table 3.2.

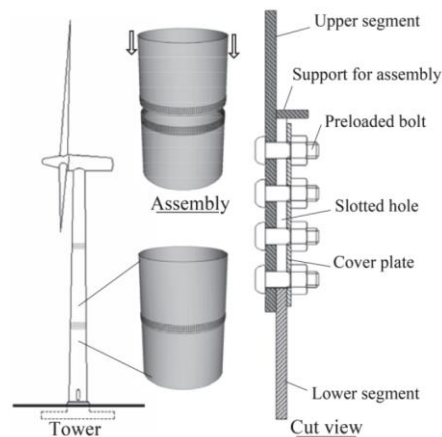


Figure 3.12 – Segment joint with friction connection (Husson, 2008)

Table 3.2 – Slip factors for various surface finishing of S690 and S355 (Heistermann, 2011)

	High strength steel S690			Cor-Ten steel S355		
	Type B	Type C	Type F	Type BI	Type BE	Type BEE
Surface blasted	with shot steel, degree Sa 2½	with shot steel, degree Sa 3	with shot steel, degree Sa 2½	with shot steel, degree Sa 2½	with shot steel, degree Sa 2½	with shot steel, degree Sa 2½
Surface treatment	without treatment	spray metalized with zinc 75µm nominal (75µm real)	painted with zinc epoxy (one layer) with 70µm nominal (135µm real) (current product in Portugal)	without treatment exposed to the environment in Interior of the Laboratory – 10 days	without treatment exposed to the environment in Interior of the Laboratory – 15 days + Exposed to the outside environment – 20 days	without treatment exposed to the environment in the Interior of the Laboratory – 15 days + Exposed to the outside environment – 80 days
Surface appearance	0,50	0,40	0,20	0,50	0,56	0,30

A detailed description about the design of friction connections can be found in Heistermann (2014) along with the influence of each parameter on the resistance and stability of the connection.

In order to understand the feasibility of the solution in terms of production and assembly, some tests were conducted.

Two different prototypes were assembled. The first prototype (prototype 1) was a reduced scale (around 1:2) of a tower with a longitudinal welding and a friction connection to assemble the segments. The second prototype (prototype 2) was produced with longitudinal shear connections with normalized holes and friction transversal connection.

The concept of the modularized tower of prototype 2 is presented on Figure 3.13. This system idealized and performed under the scope of HISTWIN2 project (Veljkovic et al., 2015) will allow at the same the improvement of the fatigue behaviour of the tower by removing the need of longitudinal welding of the plates but also will overcome the problem related with the transportation requirements (Figure 3.3).

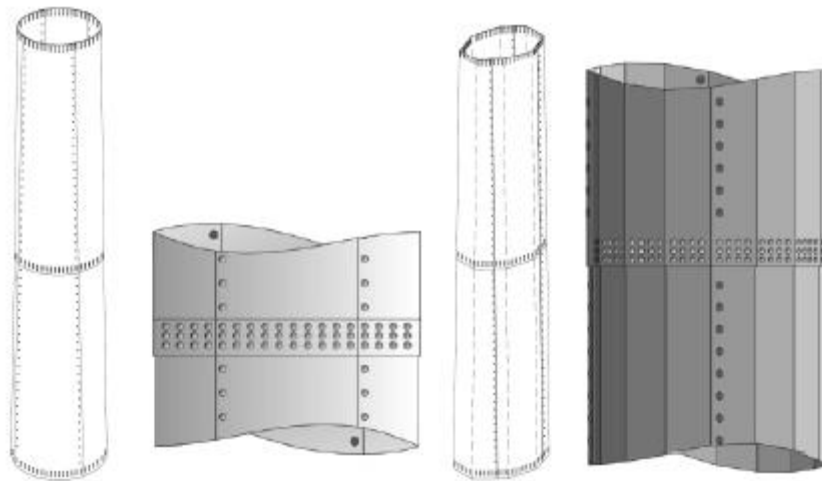


Figure 3.13 – Modularized wind tower (Heistermann, 2014)

The assembly of both segments was accomplished with a 16ton crane, chains with 2 arms and elevation claws. The position of the claws was fundamental to ensure the levelling of the pieces.

In both prototypes, the assembly started for the lower segment by placing together all four pieces. In order to keep them together and close to the final shape, some bolts were used in the longitudinal connection.

After the assembly of the lower segment, the installation of the upper segment follows two different paths.

For the 15mm thick connection, the upper level was assembled by placing individually all four pieces above the lower level, as presented in Figure 3.14.

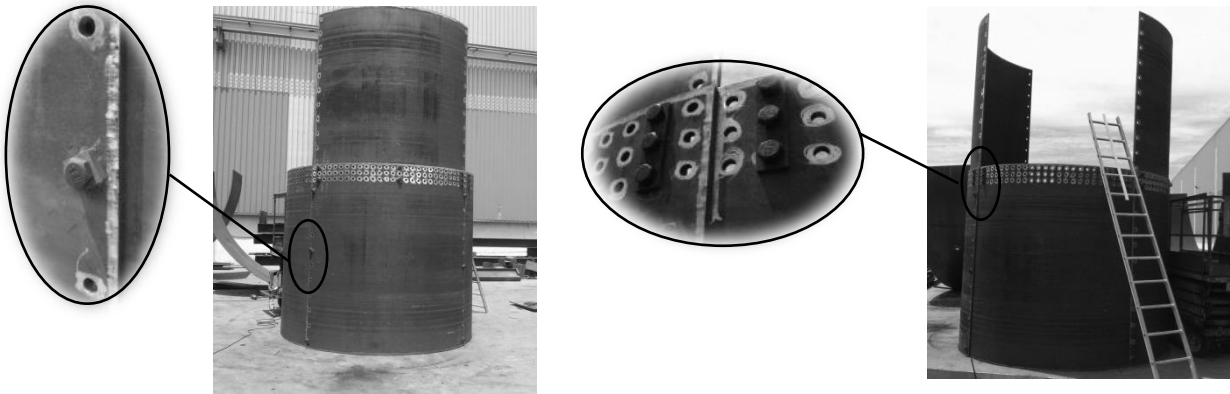


Figure 3.14 - 15mm thick connection assembly

In the case of the 20 mm thick prototype, the assembly of both segments was carried out individually according to Figure 3.15 and Figure 3.16.

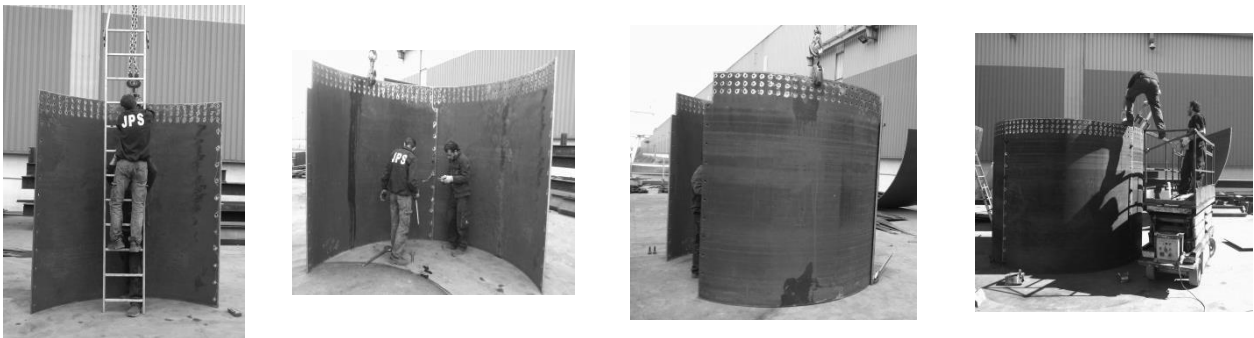


Figure 3.15 – Assembly of the lower segment (20mm thick connection)

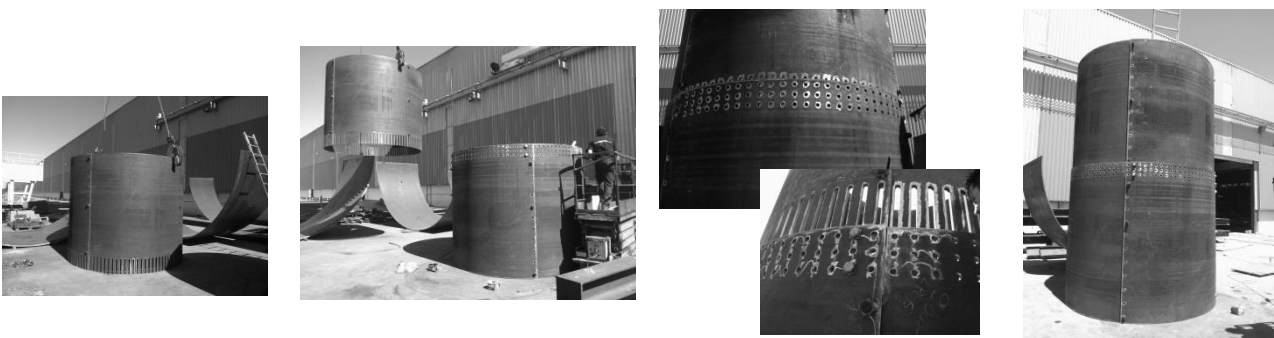


Figure 3.16 – Final assembly of both segments (20mm thick connection)

Another concern about these connections is the gap between segments.

In order to allow a proper and feasible assembly of the segments, it is required to have some gap between the top and the bottom parts however one must keep in mind that after the

tightening of the bolts, the contact of the segments must be effective in order to mobilize the friction resistance. To evaluate that, it was observed if the gaps introduced in the production were closed after the tightening.

The bolts required for this system must allow the tightening only from the inner side of the tower. In order to evaluate the behavior of bolts possible to use in this system, two different types of bolts were considered and evaluated. In prototype 1 it was used M30 TCB bolts (Figure 3.17a) in the first stage and BobTail bolts (Figure 3.17.) in a second stage. In prototype 2 only BobTail bolts were considered.

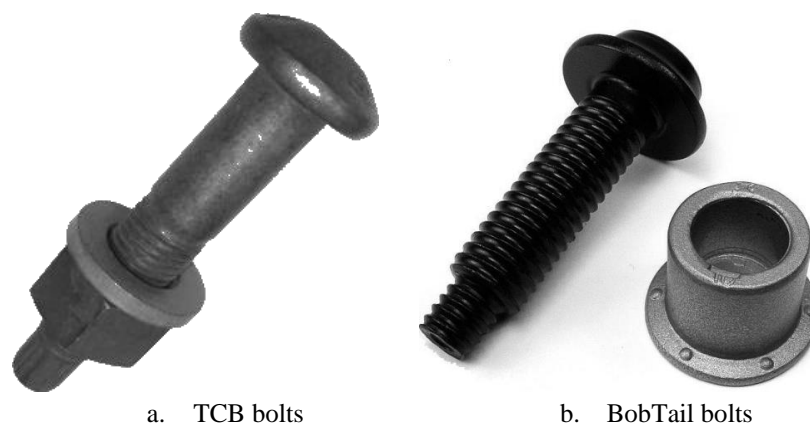


Figure 3.17 – Types of bolts used

In prototype 1 it was not possible to make a fair estimation of the long-term behavior of the bolts since they were not monitored long enough however it was possible to make some conclusions about these experiments.

In the case of the TCB bolts it was observed that the value recommended by the manufacturer and by the relevant standard for the installed prestress ($70\%f_u=700\text{MPa}$) is achieved in most of the bolts and it was observed a bigger loss (relaxation) immediately after the tightening which tends to decrease in time.

In the case of the BobTail bolts it was also observed that the achieved force is coherent with the values given by the manufacturer (Table 3.3) and it was observed a drop in the installed force when the bolts in the same row are tightened. A force drop of around 10% was observed when the adjacent bolts are tightened and around 1% when the non-adjacent bolts were tightened.

Table 3.3 – Percentage of installed force after tightening on BobTail bolts – prototype 1

Bolt	1st Quadrant			2nd Quadrant		
	Row 1	Row 3	Row 5	Row 19	Row 21	Row 23
Top	104	102	105	90	91	-
Center	106	99	-	84	88	96
Base	106	108	105	89	97	102
Bolt	3rd Quadrant			4th Quadrant		
	Row 38	Row 40	Row 42	Row 57	Row 59	Row 61
Top	-	38	44	111	98	-
Center	97	67	80	-	99	104
Base	-	84	-	101	103	97

It was also possible to identify a relation between the force and the temperature variation as it may be observed in Figure 3.18. As it was not foreseen such a relation between both parameters, this problem was analyzed more in detail in prototype 2 in order to make a proper assessment on the long term behavior of the bolts.

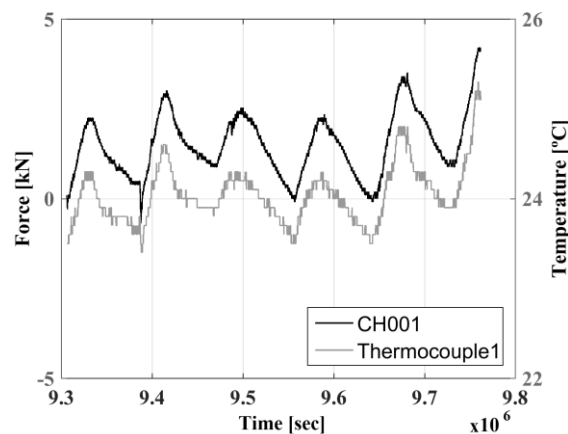


Figure 3.18 – Force and temperature variation in BobTail of prototype 1

On prototype 2 a 1-year monitoring was carried out in order to understand the long term behaviour of the BobTail.

For the monitoring procedure presented 1” BobTail bolts manufactured by Alcoa were used with different grip length. The geometrical properties of the bolts are presented in Figure 3.19 and, according to the manufacturer, the mechanical properties of the 1” bolts are presented on Table 3.4.

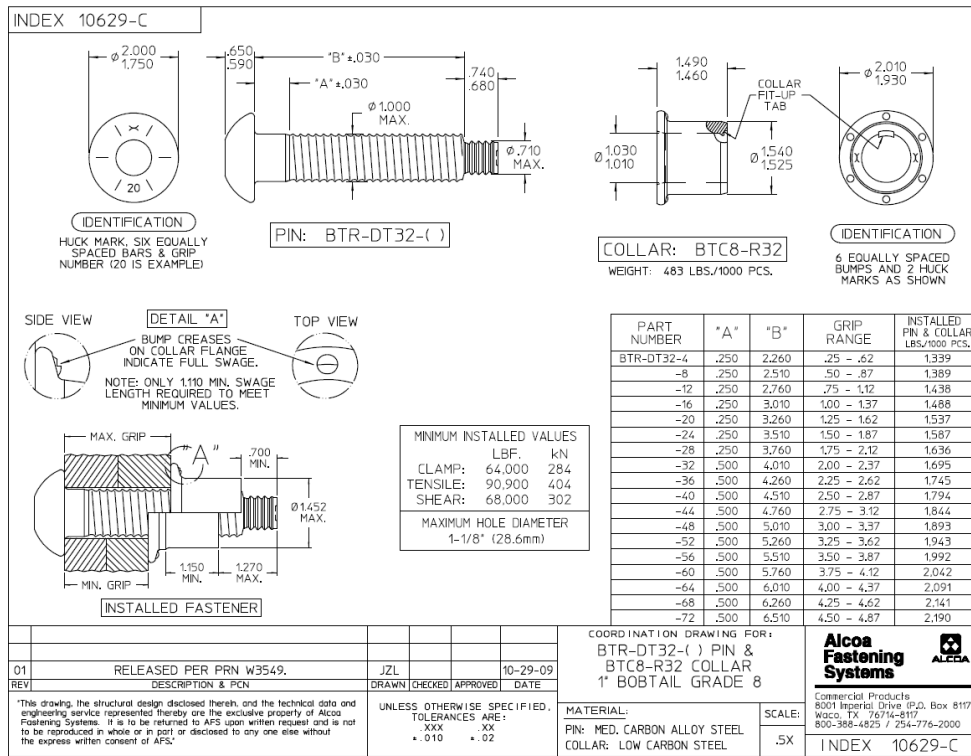


Figure 3.19 – 1” BobTail bolts geometrical characteristics

Table 3.4 – 1” BobTail bolts mechanical characteristics

Nom. Bolt Diameter	F _{v,Rk} (kN)	F _{t,Rk} (kN)	F _{p,C*} (kN)	V _{a,Rk} (kN)	N _{Rk} (kN)	A _s (mm ²)
1"	347	374,3	293,1	347	332,7	418,7

The geometry of the bolts used in each specimen is presented on Table 3.5, depending on the grip length required in each part of the model.

For this test, 33 bolts were instrumented, to be installed in the connection prototype.

A simple set-up was considered for this calibration. The bolts were placed in a hydraulic jack with special pieces presented in Figure 3.20 and were tested. The data acquisition of the strain (from the strain gauge) and the applied force (from the hydraulic jack) were measured. The full set-up considered is presented on Figure 3.21.

The bolts were loaded from 0 to 200kN with intervals of 25kN. The increase of the load was carried out under a slope of 9kN/s and the stabilization time in the end of each interval was variable (5 to 10 sec.). The unloading of the bolts was similar to the loading but the interval was of 50kN. The loading and unloading protocols are presented on Figure 3.22.

Table 3.5 – Type and location of the BobTail used – prototype 2

Prototype	Joint thickness + gap	Location	Number	AFS Bobtail part No.
20mm plates	20+20+10 (gap 0 to 10mm)	Friction connection	312	BTR-DT32-28
	20+20-20+10 (gap 0 to 10mm)	Overlapping connection	12	BTR-DT32-44
	20+20mm	Longitudinal connection	88	BTR-DT32-24



Figure 3.20 – Pieces to connect the bolts to the hydraulic jack



Figure 3.21 - Bolts strain gauges calibration set-up

The coefficient considered for each bolt was obtained by the average value between the loading and the unloading tests. The calibration coefficients obtained for each bolt are presented in Annex B.

Before the tightening of the segment, the gaps between the upper and the lower segments were measured over all the perimeter of the friction connection, both on the inner and on the outer side of the piece.

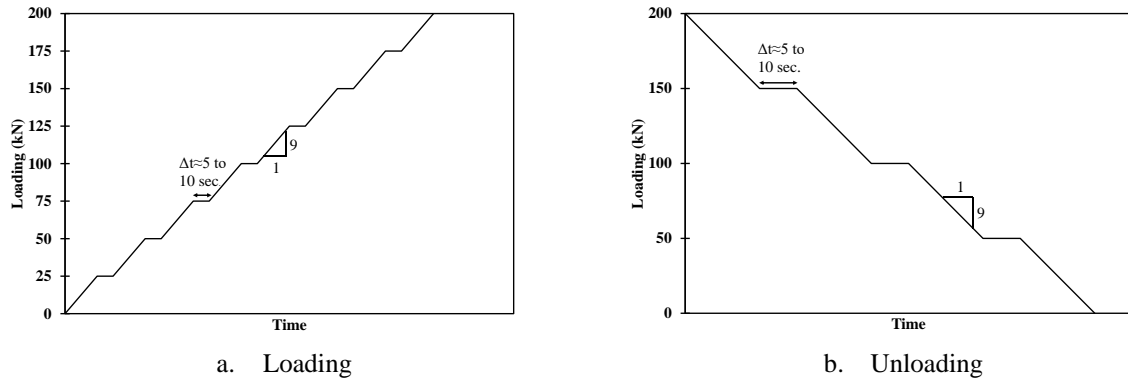


Figure 3.22 – Calibration tests protocols

The gap along the longitudinal connections was not measured since some regular bolts were used to keep the piece in place and consequently the gap on that area was approximately 0. After the start of the tightening of the BobTail bolts, the regular bolts were removed and changed to the correspondent BobTail.

The gaps between the top and the bottom segments were visible as presented in Figure 3.23.

The long term monitoring procedure was made using a data acquisition system HBM MX1615B (2 units) for measuring the strains in the bolts strain gauges and an HBM MX1609 (1 unit) for measuring the plate temperatures. All the devices are stored in a locker attached to the specimen (Figure 3.24).

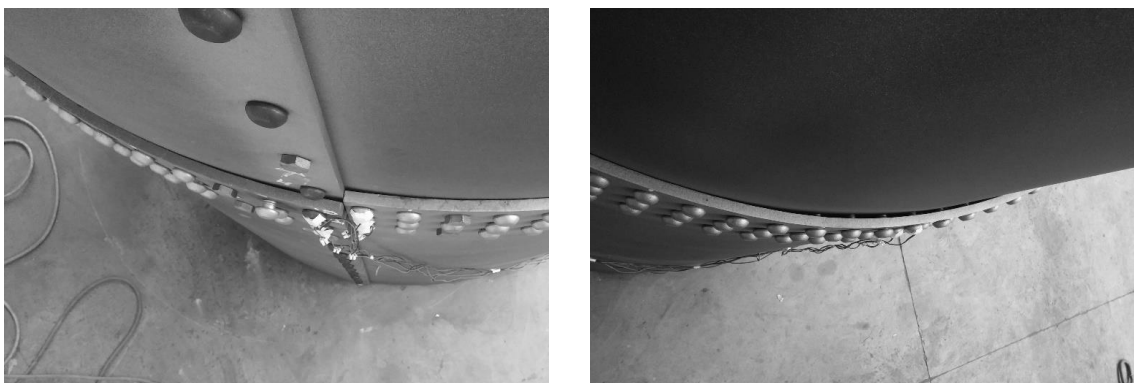


Figure 3.23 – Gaps between bottom and top segments

The data view and storage is conducted by a laptop using a local area connection and it is accessed remotely via internet, according to the connection scheme of Figure 3.25.

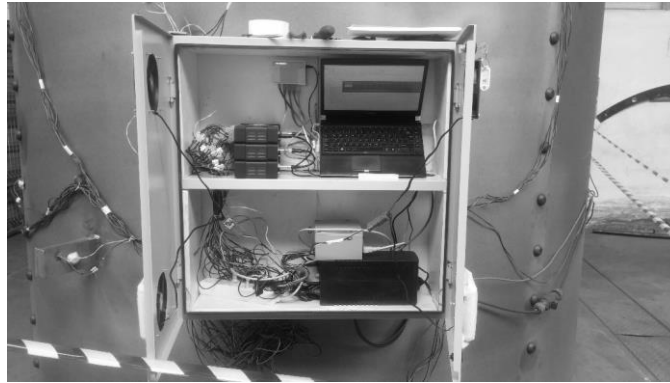


Figure 3.24 – Data acquisition system

Local Area Network

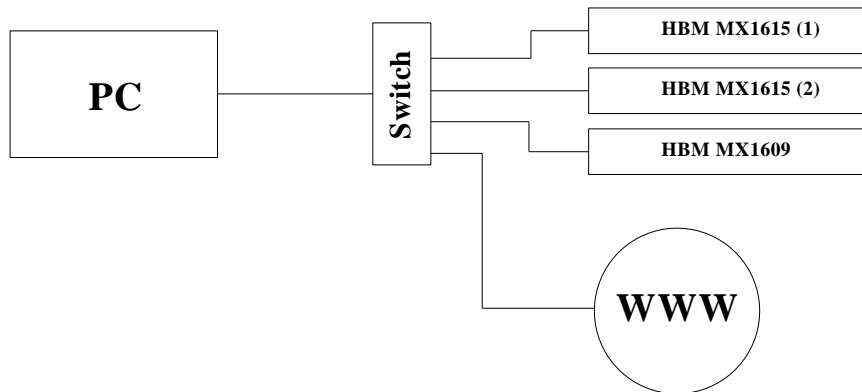


Figure 3.25 – Local area network scheme

In order to understand the isostatic behaviour of the connection, it was assembled one isostatic specimen with 2 plates 20mm thick and 1 plate 10mm thick connected by only one bolt, according to Figure 3.26. It was connected to the main specimen for the sake of storage.

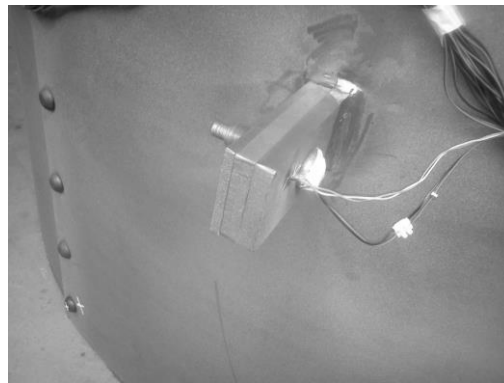


Figure 3.26 – Isostatic specimen

The location of the instrumented bolts along the perimeter (transversal connection) and along the height (longitudinal connection) is presented in Figure 3.27. The instrumented bolts used in the longitudinal connection were placed in the longitudinal connection correspondent to Q1.

The BobTail tightening sequence of this monitoring was the following:

- Tightening of the longitudinal connection of the top segment in Q1 direction (top to bottom)
- Tightening of the longitudinal connection of the top segment in Q3 direction (top to bottom)
- Tightening of the longitudinal connection of the top segment in Q2 direction (top to bottom)
- Tightening of the longitudinal connection of the top segment in Q4 direction (top to bottom)
- Tightening of the longitudinal connection of the bottom segment in Q1 direction (top to bottom)
- Tightening of the longitudinal connection of the bottom segment in Q3 direction (top to bottom)
- Tightening of the longitudinal connection of the bottom segment in Q2 direction (top to bottom)
- Tightening of the longitudinal connection of the bottom segment in Q4 direction (top to bottom)
- Tightening of the longitudinal friction connection according to the scheme of Figure 3.28. The tightening started always in the middle of each quadrant and it was tightened 2 - 3 rows from each side every time to try to gradually close the gap

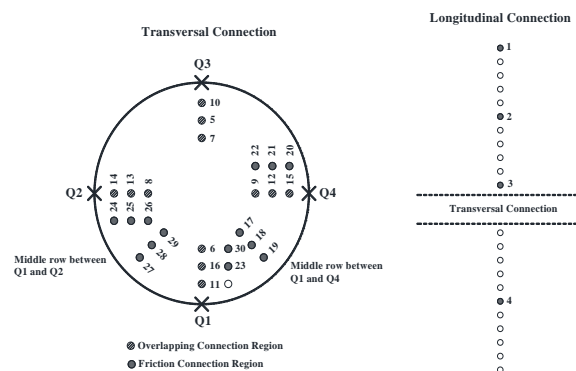


Figure 3.27 – Instrumented bolts distribution

The time consumption to tighten one bolt is around 20 sec. To tighten all the 412 bolts of this specimen took around 6 hours.

The quality control of the tightening considered in this work was the checking of the marks in, at least, one of the bumps in the collar, according to Figure 3.29.

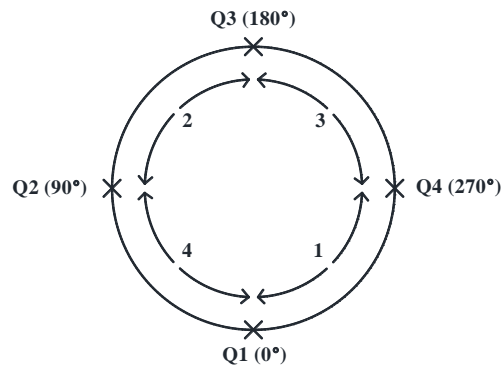


Figure 3.28 – Friction connection tightening sequence

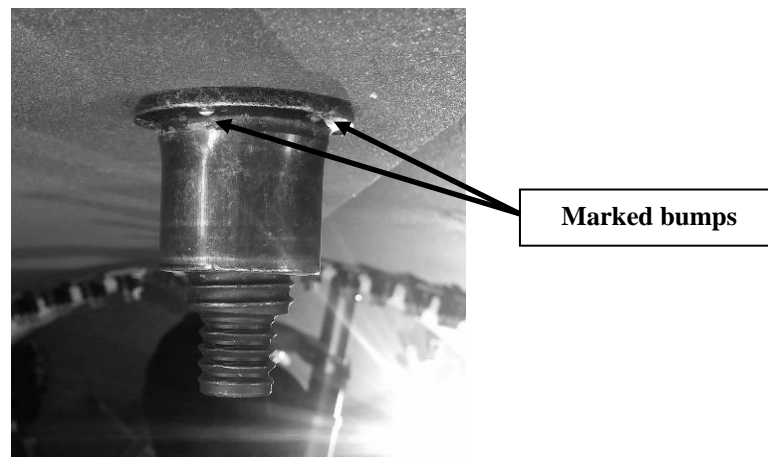


Figure 3.29 – Marked bumps

Since the bolts were instrumented with calibrated strain gauges, it was possible to estimate the applied force. The force values obtained for each bolt during the tightening are presented in Annex C.

In Table 3.6 it is possible to check both the maximum force applied by the wrenching machine, as well as the force applied after the uncoupling of the equipment (installed force). This last value is the one used as standard and it was compared with the nominal value of the installed force for this type of bolts according to the respective pin datasheet (284kN).

According to the values of Table 3.6, the majority of the results are close or higher than the nominal force value. However, the nominal value is given for an ideal condition of connection like plan plates with no gap, which is not the case in this test.

The only bolt under these optimal conditions is Bolt 31 installed in the isostatic specimen and which presents a very good result, in accordance to the provided nominal force value.

Table 3.6 – Bolts tightening forces

Bolt	Installed Force (kN)	% of the max. force	Notes	Bolt	Installed Force (kN)	% of the max. force	Notes
1	327	115		17	207	73	
2	278	98		18	208	73	
3	-	-	SG malfunction	19	287	101	
4	-	-	SG malfunction	20	276	97	
5	-	-		21	323	114	
6	309	109		22	211	74	
7	-	-		23	399	140	
8	303	107		24	305	107	
9	342	120		25	306	108	
10	273	96		26	376	132	
11	469	165		27	315	111	
12	-	-		28	283	100	
13	-	-		29	208	73	
14	202	71		30a	206	73	Tightened in 2 steps
15	222	78		30b			
16	-	-		31	310	109	

All of the bolts of the friction connection were tightened from the top to the bottom of the finger which means from the stiffer to less stiff part of the element. This procedure allows a gradually gap closing between the top and the bottom plates.

This procedure causes a force loss in the pre-tighten bolts after the tightening of the remaining bolts of the same row. For instance, take into consideration the example of Figure 3.30, the first bolt to be tightened was the bolt 22, followed by 21 and in the end bolt 20. Bolt 22 will suffer a force loss (bigger) after the tightening of bolt 21 (adjacent) and a slight force reduction after the tightening of 20 (non-adjacent). Bolt 21 will suffer a force reduction after the tightening of the adjacent bolt 20. Bolt 20 will suffer no major reductions since it is the last one to be tightened in this row.

Table 3.7 shows the percentage of force loss in comparison with the installed force in each bolt.

According to the results of Table 3.7, it is possible to obtain a mean value of 7% for the force loss after the tightening of the adjacent bolts (mean value of 8% of loss in the top bolts and 6% in the middle bolts) and a mean value of 1% for the force loss after the tightening of the non-adjacent bolts (applicable only for the top bolts) which is in good agreement with the corresponding values obtained for prototype 1.

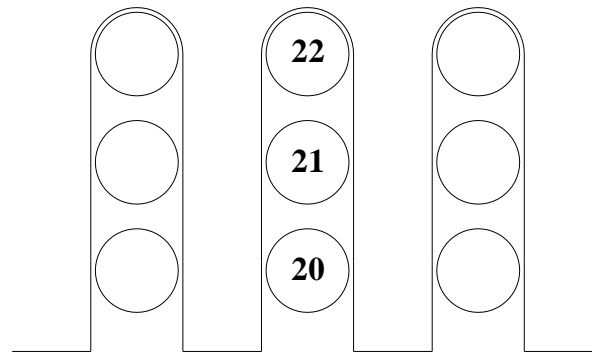


Figure 3.30 – Friction connection (“finger” configuration example)

The idea of the long term monitoring carried out in the prototype 2 is to estimate the clamp forces in the bolts. This analysis should be made by removing the temperature effect in the force variation as presented in Figure 3.18. To obtain the independent force results, the nonlinear Hammerstein-Wiener model is defined.

The Hammerstein-Wiener model can be used as a black-box model structure to obtain the physical information and characteristics of the procedure (Figure 3.31). For instance, the non-linear temperature deviation represents the physical knowledge as an input and from the force the characteristics of the process can be found.

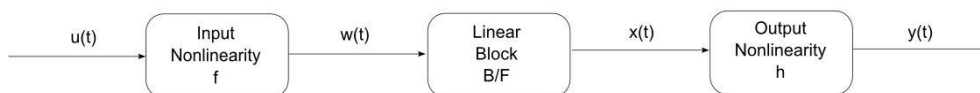


Figure 3.31 - Hammerstein-Wiener Block Diagram (The MathWorks Inc., 2010)

where:

$w(t) = f(u(t))$ is a nonlinear function transforming input data $u(t)$.

$x(t) = (B/F)w(t)$ is a linear transfer function. Where B and F are polynomials in the linear output-error model. The Output-Error model uses time or frequency domain data to estimate

the corresponding polynomial of the model. The polynomial can be represented by equation 3.2 (Guo, 2004):

$$y(t) = B(q)F(q)u(t - nk) + e(t) \quad (3.2)$$

where $y(t)$ is the output, the $u(t)$ is the input, and the $e(t)$ is the error.

For a set of input and output in order of n the polynomials are defined as $B_{j,i}(q)/F_{j,i}(q)$, where $j=1,2,\dots,n$, and $i=1,2,\dots,n$. $y(t)=h(x(t))$ is a nonlinear function that maps the output of the linear block to the system output and $w(t)$ and $x(t)$ are internal values which are defined in the input and output of the model respectively.

The Hammerstein-Wiener model computes the output y in three stages (Wills et al., 2013).

- Computes $w(t)=f(u(t))$ from the input data regarding the linear transfer function B/F . The input nonlinearity is a static function, which means the value of the output a given time ' t ' depends only on the input value at time ' t '. It is possible to configure the input nonlinearity as a sigmoid network, wavelet network, saturation, dead zone, piecewise linear function, one-dimensional polynomial, or a custom network or simply the input nonlinearity can be removed;
- Computes the output of the linear block using $w(t)$ and initial conditions: $x(t)=(B/F)w(t)$. You can configure the linear block by specifying the numerator B and denominator F orders;
- Compute the model output by transforming the output of the linear block $x(t)$ using the nonlinear function h : $y(t)=h(x(t))$. Similar to the input nonlinearity, the output nonlinearity is a static function. Configure the output nonlinearity in the same way as the input nonlinearity. You can also remove the output nonlinearity, such that $y(t)=x(t)$.

A simple mechanical model is assumed for the isostatic bolt in order to assess bolt preload variation induced by temperature. In Figure 3.32, the structure of the bolt is illustrated and the possible force variation is calculated based on the possible young modulus, thermal expansion coefficient and cross section area.

The structure of the connection is shown in Figure 3.32. The nut is not normal nut but a collar smashed against the bolt and the connected plate according to the tightening procedure reported previously.

Table 3.7 - Percentage of force loss after tightening of adjacent and non-adjacent bolts

% Force	Tightened Bolt																											
	6	Empty	11	30	23	No SG	29	28	27	24	25	26	14	13	8	10	5	7	22	21	20	9	12	15	17	18	19	
6	309	-	-	3																								
Empty	-	-	-	-																								
11	469	-	-	-																								
30	206				-	9	1																					
23	399				-	-	5																					
No SG	-				-	-	-																					
29	208							-	6	0																		
28	283							-	-	5																		
27	315							-	-	-																		
24	305										-	8	0															
25	306										-	-	6															
26	376										-	-	-															
14	202													-	6	1												
13	-													-	-	-												
8	303																											
10	273																											
5	-																											
7	-																											
22	211																											
21	323																											
20	276																											
9	342																											
12	-																											
15	222																											
17	207																											
18	208																											
19	287																											

Pre-tightened bolt

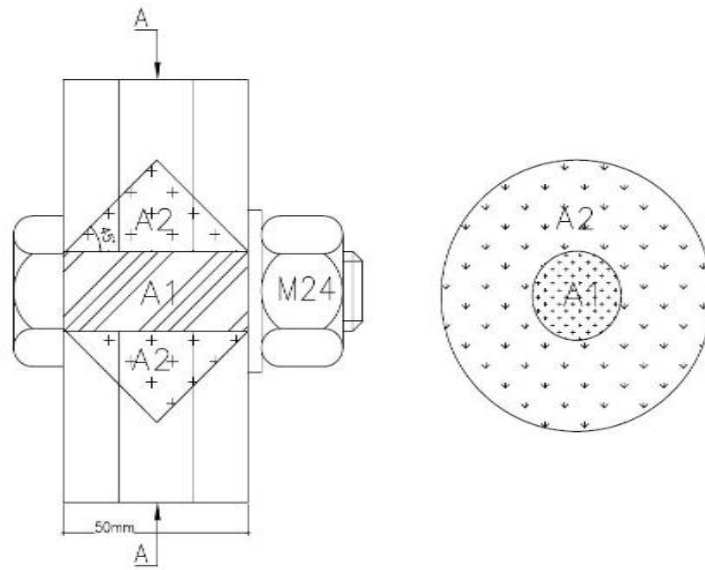


Figure 3.32 - Schematic of the friction connection with the preloaded area

The formula (3.3) can be applied to obtain the force variation in consequence of only temperature variation.

$$\Delta F_{\Delta t} = \Delta t \cdot (\alpha_2 - \alpha_1) \cdot E_1 A_1 \frac{E_2 A_2}{(E_1 A_1 + E_2 A_2)} \quad (3.3)$$

$$\Delta F = \Delta F_{\Delta t} + \Delta F_p$$

where ΔF is obtained directly from the measurements in the strain gauges inside the bolts and Δt is also measured. In the calculations of force in the bolt using the measured strains, a set of tension test has been performed on the bolts and the strain and the force is measured with the high accuracy equipment. Through the test results, an experimental ratio between strain and force is calculated as a conversion coefficient. The conversion coefficient for the isostatic bolt is $\Delta F = 0.11114 \cdot \varepsilon_{\text{measured}}$.

$\Delta F_{\Delta t}$ is not measured and estimation using equation (3.3) is not precise enough, since some of the parameters in equation are not known precisely. ΔF_p is the variation of force in the bolt independent of the environmental conditions and can be considered as the effective loss of preload. This is the quantity of interest but cannot be obtained directly from the measurements. However, since ΔF_p is expected to be very low for a short period of time, e.g. the last two months of measurements, a good estimation of $\Delta F_{\Delta t}$ can be obtained assuming that $\Delta F_p = 0$ and using the measurements of Δt and ΔF during that period of time to calibrate a mathematical model (e.g. the Hammerstein-Wiener model) and finally establish the equation for $\Delta F_{\Delta t}$. In this way, the comparison of the strain measurements with the values predict by

the mathematical model when using the measured temperature ΔF will give an estimation of ΔF_p at any time.

For the quick approximation, of highest and lowest possible difference in Young's modulus (200E6 – 210E6) and thermal expansion coefficient (9E-6 – 17E-6) is considered. Moreover, in isostatic specimen, the bolt is 1 inch which in metric system is similar to M24 and the hole's diameter for M24 is 27mm and the length of the bolt is equal 50mm. The A1 is the area of the bolt cross section and A2 is the cross sectional area of the pressure triangle with 45° angle as it is shown in Figure 3.32. The distance of boundary of pressure angle from the bolt is varying so the A2 can vary related to maximum and minimum value of pressure triangle around the bolt. Therefore, A1 is 575.55mm² and the maximum for A2 is 1390mm² and in average is 1164.156mm². After calculation regarding the mentioned equation, the maximum force variation of 30kN is obtained.

In a situation where the bolts are free of any kind of constraints, the effect of temperature variation in the elongation of bolts is included in the measurement obtained with the strain gauges and can be estimated as $\alpha\Delta t$ where α is the thermal expansion coefficient. Therefore, the variation in isostatic bolt force must take this effect into account providing $\Delta F = 0.11114 \cdot (\epsilon_{\text{measured}} - \alpha\Delta t)$.

For strain gauge measurement, the Wheatstone bridge circuit is used to convert resistance change of the strain gauge into voltage output. Nevertheless, a 2-wire leadwire is used for connecting the strain gauge to the instrument in the experimental setups. Furthermore, if the temperature of the leadwire changes, thermal output of the bridge is caused even if there is no change in actual strain. Therefore, the quarter bridge 2-wire method should be corrected due to the length and resistance of leadwire.

In quarter bridge 2-wire method changes in leadwire temperature cause changes in the lead wire resistance, which result in thermal output. The equation (3.4) is used to compensate for the thermal output.

$$\epsilon L = \frac{r \cdot L \cdot \alpha \cdot \Delta T}{K \cdot (R + r \cdot L)} \quad (3.4)$$

Where ϵL is leadwire thermal output, K is gauge factor, α is thermal coefficient of the leadwire (0.004 1/°C for copper), r is total resistance of the leadwire per meter, L is lead wire length (In the experiment setup it is between 2.5 and 3 meter) and ΔT is the temperature change of the lead wire. It should be noted that the temperature changes is considered uniform along the leadwire.

All sampling rate of the measured data are harmonized in 50s, then Hammerstein-Wiener model is estimated for isostatic bolt with 4 round of estimation. The fitness precision threshold of all models is set to convergence be more than 80%. Moreover, based on block-diagram method and using Simulink, the model is validated for same temperature profile (measured temperature). At the end, a range of temperature between minimum measured temperature of 10°C and maximum measured temperature of 30°C is investigated to understand the behaviour of loss force due to temperature.

The first bolt to be analysed is the isostatic. The maximum applied force is 396kN, the force after uncoupling is 315kN, and the installed force is 310kN. The tightening is performed at 20 °C. The predicted force is compared to the measured force on the bolt and the error is displayed in Figure 3.33 and Figure 3.34 respectively.

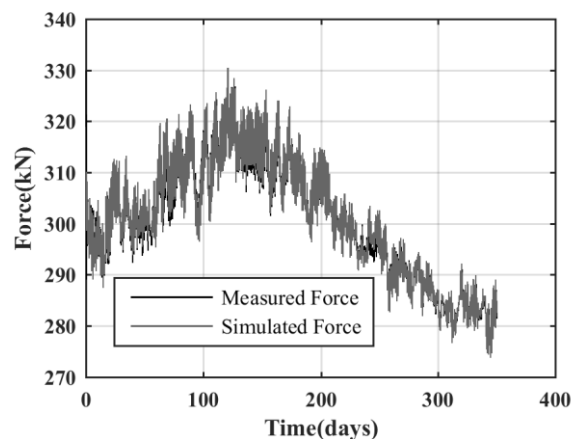


Figure 3.33 – Comparison between measured and identified force – isostatic bolt

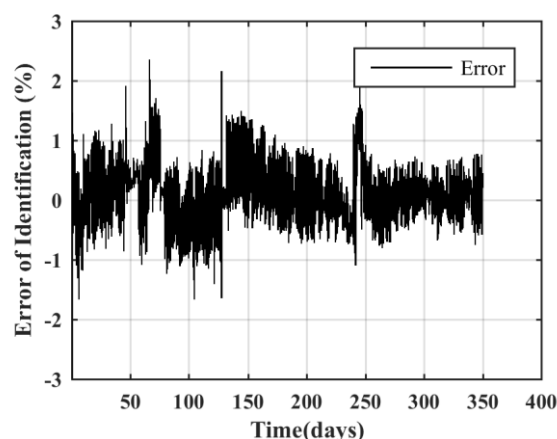


Figure 3.34 – Error of identification – isostatic bolt

An identification of force loss in constant temperature is made for measurement period using the Hammerstein-Wiener model. Moreover, an estimation of 20 years of life time loss is simulated to find out the total loss of the isostatic bolt in the system, considering a logarithmic

curve fitting on the data of the first year. The regression functions are presented in equation (3.5) as function of the time (X) and for constant temperatures.

$$\begin{aligned}
 y(10^{\circ}C) &= -3.123 \times \log(X) + 329.31 \\
 y(15^{\circ}C) &= -3.174 \times \log(X) + 336.62 \\
 y(20^{\circ}C) &= -3.158 \times \log(X) + 340.95 \\
 y(25^{\circ}C) &= -2.597 \times \log(X) + 338.48 \\
 y(30^{\circ}C) &= 0.015 \times \log(X) + 311.40
 \end{aligned}
 \tag{3.5}$$

Figure 3.35 and Figure 3.36 show the identification of constant temperature for a year and the estimation of lifetime loss respectively. Table 3.8 shows the obtained values for the force losses with constant values of temperature.

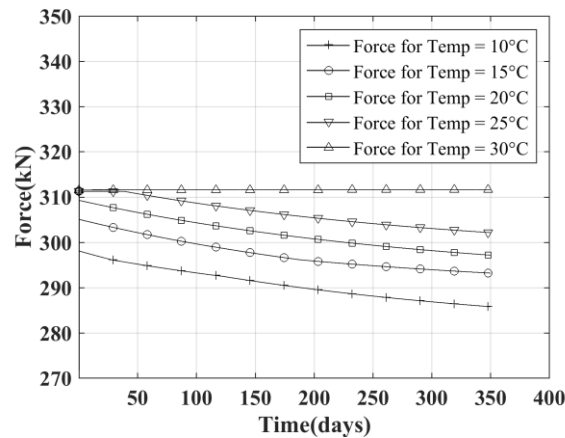


Figure 3.35 - Force time series in 1 year for constant temperature – isostatic bolt

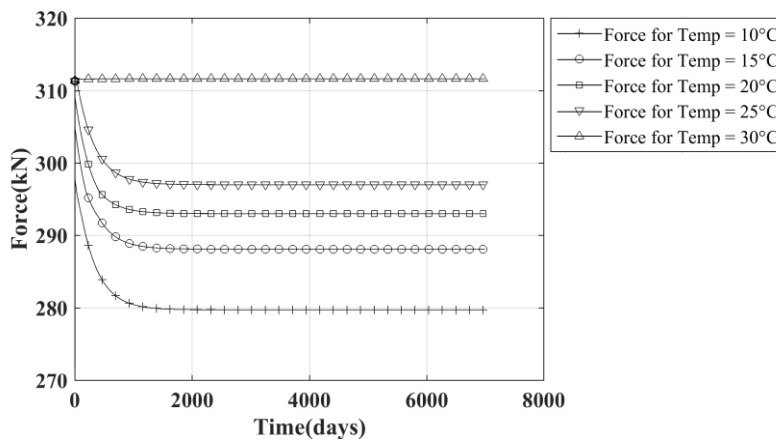


Figure 3.36 - Force loss estimation in constant temperature for 20 years - isostatic bolt

Table 3.8 – 20 years load loss in isostatic specimen

Constant Temp. (°C)	Loss (%)	Remaining preload (kN)
30	0.0	310.0
25	4.1	297.5
20 (tightening)	5.3	293.5
15	7.2	287.5
10	9.6	280.0

The estimations of force loss in 20 years from both methods are compared in Figure 3.37. The first 300 days of both curves are the measured data and are used in both Hammerstein-Weiner and logarithmic fitting. Therefore, they fit on each other.

A similar analysis was conducted for a bolt in the overlapping connection (bolt 8). The obtained error between the measured and estimated forces are located in between $\pm 2\%$ for this analysis for a 3m long leadwire.

The 20 years force loss estimated for the same constant temperatures is presented in Figure 3.38 and the obtained values are presented in Table 3.9.

Besides the slip resistance of the connection that was addressed before, it should also be estimated the buckling resistance and the yield resistance of the “finger” elements as in other plate elements. The spacing between bolt rows is also something that should be taken into account in the design of the connection.

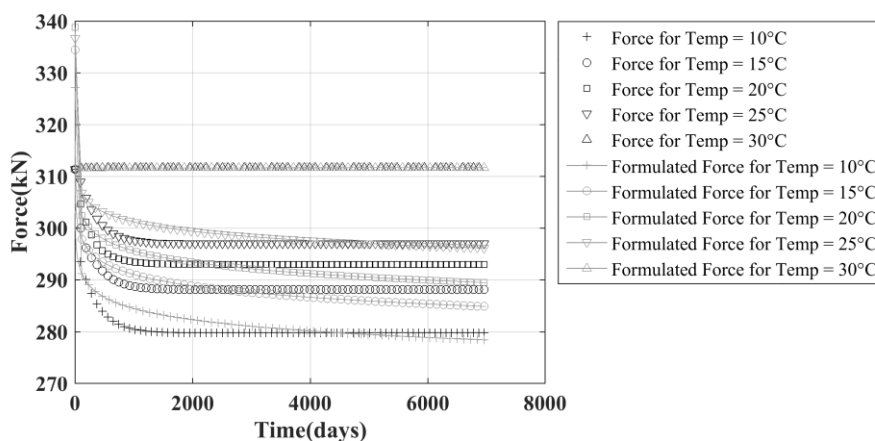


Figure 3.37 - Logarithmic curve fitting vs Hammerstein-Weiner identification – isostatic bolt

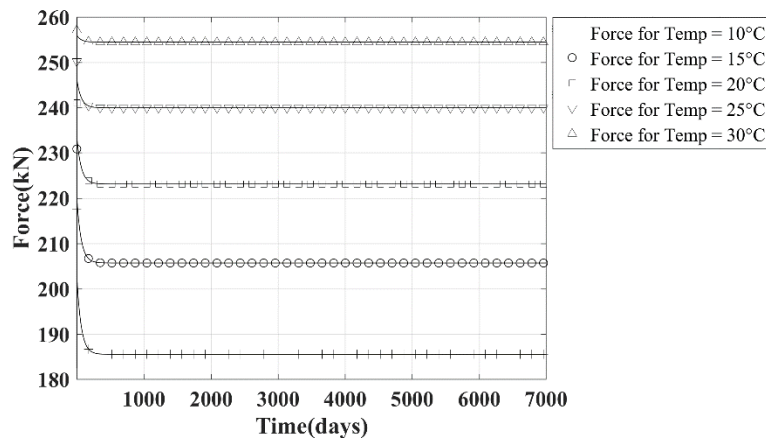


Figure 3.38 - Force loss estimation in constant temperature for 20 years - overlapping bolt 8

Table 3.9 – 20 years load loss in overlapping connection

Constant Temp. (°C)	Loss (%)	Remaining preload (kN)
30	1.7	255.5
25	6.0	244.3
20 (tightening)	11.5	230.2
15	17.1	215.5
10	24.2	197.4

3.4. Final comments

The increase in height of the towers raises problems that must be overcome. In order to solve those problems, some structural solutions have been presented. The most relevant problems related with the increase in height of the tower are the transportation of the elements on public roads (maximum diameter allowed of 4.5m), fatigue problems in the connections and behaviour of the foundation systems.

In order to overcome the transportation problems, the idea of the modularized construction of the tower for shell structures (steel or concrete) is presented as a viable solution to overcome this problem. This modularized system was the focus on a feasibility study on the manufacturing and assembly and it concluded that it is a valid solution. Some other solutions are already in the market and some new options are also under development.

The problem of the fatigue is more prominent in steel structures, especially in the connection of the segments. A new friction connection is proposed and presented to overcome this fatigue problem. There are some specifications and singularities related with this connection which is

dependent on the slip resistance. This connection requires the use of bolts that allow the tightening of only one side (inner side of the tower) and their long-time behaviour is a governing parameter in the resistance.

The experimental tests on BobTail bolts presented that losses during the tightening were around 7% for adjacent bolts and 1% in non-adjacent bolts, for bolts in the same row and for rows with 3 bolts. The clamp forces provided by the manufacturer were achieved in the experiments.

The long term monitoring showed a stabilization of the BobTail bolt losses for a time of around 1000 days (about 3 years) after the installation in the case of the isostatic bolt and around 500 days (about 1.5 years) for the overlapping bolt. For the isostatic bolt it was obtained a loss of 3.8% in the first year (310kN to 298kN) while for the 20 years it was obtained a loss of 5.3%. It was observed also higher losses for lower working temperatures and lower losses for higher working temperatures. About bolt 8 (overlapping connection) it 11.5% in the end of 20 years.

This values of force losses obtained for the long term monitoring were obtained using a properly calibrated Hammerstein-Weiner model with an error of less than $\pm 2\%$ between the measured and the estimated bolt forces.

The problems of the behaviour of the foundations will be thoroughly addressed in the following chapters with a detailed analysis on the behaviour of micropiles to be used as reinforcement of hybrid foundations.

4. FOUNDATION SOLUTIONS FOR ONSHORE WIND TOWERS

4.1. Introduction

According to the information presented in chapter 3, the behaviour and design of the foundation systems for the new generation (higher) wind towers is one of the most important problems that should be considered and improved.

The average diameter of a circular shallow foundation for a current 80m high steel wind tower based on a soil with good mechanical properties is about 17m with a concrete volume of close to 400m³ and represents approximately 20% of the full tower budget (IRENA, 2012). Doubling the tower height leads to about three times the concrete and excavation volumes needed to build the foundation. Therefore, alternative solutions should be considered for the foundations of the new generations of wind towers.

In this chapter a state of-the-art foundation solution will be presented and analysed for higher wind towers. This system is composed by a shallow foundation reinforced with steel micropiles and allows the improvement of the overturning resistance and soil stiffness along with the reduction of the applied stresses to the soil, potentiating also the construction of wind turbines in soils with poor resistant properties such as sandy soils due to the side friction load transfer provided by the micropiles. According to Moayed and Naeini (2012), the response of the considered loose sand under surface loading was significantly improved, the bearing capacity and the stiffness increased, and the settlements of the foundation reduced for foundations reinforced with micropiles and installed in loose sandy soils.

Micropiles are a deep foundation solution system with reduced diameter (usually smaller than 300 mm) used both in new structures as well as in retrofitting. They are commonly used as foundation support, seismic retrofitting of bridges, slope stabilization and earth retention. Micropiles are usually classified according to the type of grouting: gravity grouting (type A), pressure through casing (type B), single global postgrout (type C or IGU) and multiple repeatable postgrout (type D or IRS) (FHWA, 2005).

The advantages of this alternative solution will be highlighted in comparison with the standard shallow foundation solution in terms of structural performance, costs and potential environmental impacts using Life Cycle Analysis. Comprehensive design examples of the two foundation systems (shallow and hybrid) will be presented for 3 different tower heights/rated

power (80m/2MW, 100m/3.6MW and 150m/5MW) and for 3 different tower solutions (steel, concrete and hybrid steel-concrete). For the sake of comparison, generic parameters will be considered for the micropile and for the soil properties. This solution using micropiles is more viable for soils with good mechanical properties where the bearing capacity is not the governing situation. Therefore in this analysis a soil with good mechanical properties was considered where the overturning capacity is the governing case and the improvement gained by the introduction of the micropiles is more evident.

The micropile properties inputted in the numerical model are in accordance with high quality grouting techniques like IRS or IGU that allow the mobilization of higher grout-to-ground shear strength. In chapter 6 it will be presented some updated design examples of the hybrid foundation system taking into account the micropile properties estimated for the installation technique of the experimental tests presented in chapter 5.

The use of micropiles in the reinforcement of the shallow wind tower foundations has been referred by several authors and some practical solutions have been provided by companies. For instance, the manufacturers Patrick & Handerson (Earth Systems Global Inc., 2009) propose a commercial solution idealized for rocky ground which is based on the use of anchors similar to micropiles as shown in Figure 4.1.

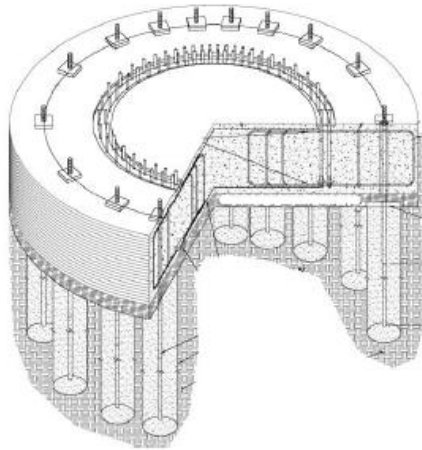


Figure 4.1 - Patrick and Handerson deep foundation solution (Earth Systems Global Inc., 2009)

According to Khatri (2010), the foundation solution is forecasted to be economically feasible when compared with other commercial solutions as presented in Figure 4.2 and the conclusions (advantages and disadvantages) about the comparison between shallow and hybrid foundations are presented in Table 4.1. According to the referred study, the use of reinforcement with micropiles for the foundation system could be favourable in some conditions namely for higher steel towers where a larger footprint is required for direct foundations.

The cost comparison presented by Khatri (2010) was performed for a determined geometry taking as base a reduction of the actual geometry of the direct foundations and applying some vertical micropiles in the extremities of the slab. This solution was not optimized by considering different diameters of micropiles (allowing the reduction of the material used in the slab) and/or using groups of inclined micropiles (*pali radice*).

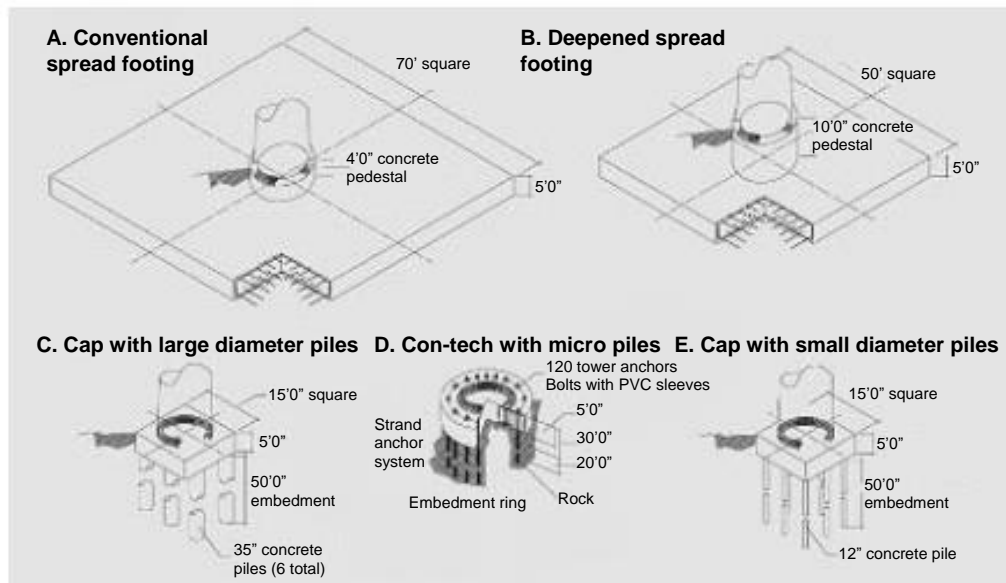


Figure 4.2 – Foundation typologies considered (Khatri, 2010)

The use of deep foundations elements for the reinforcement of shallow foundations of wind towers has also been proposed by some other authors such as Svensson (2010) who cited a work conducted by Ruukki, who analysed the impact of the reinforcement of a shallow foundation using eight steel pipe piles with 600mm of diameter, drilled for 10m to the bedrock and extended with smaller diameter pipes, injected in the bedrock for a few meters and observed a reduction of 1/3 in the concrete volume when compared with the equivalent shallow foundation with the same resistance properties. The cost of the reinforced foundation was reduced for about 10%. Aschenbroich (2010) proposed the use of micropiles or post-tensioned ground anchors as shown in Figure 4.3 and achieved reductions of 75% on the foundation area, 40% on the concrete volume and 70% on reinforcing steel volume leading to an estimated reduction of 20% to 30% in the foundation cost.

The wind towers foundations are constantly subjected to cyclic loading due to the wind induced vibrations and therefore the estimation of the cyclic behaviour of the system is relevant.

The effect of the cyclic loading induced on the foundation reinforced with micropiles has also been a subject of study by Kirsch and Richter (2011) who observed a reduction on the pile

axial capacity for cyclic load amplitudes above 10% of the static capacity of the pile. Cerato and Victor (2008; 2009) observed that high cyclic loads may increase the uplift capacity and minimize long-term creep and that the water table fluctuations after the installation can affect short and long-term uplift capacity of helical anchors, used as foundations of wind tower guy cables. Buhler and Cerato (2010) stated that these helical anchors, when subjected to large span dynamic loading, experienced reductions of their uplift capacity and that the value of the loading span had greater effect on the pile performance than the maximum load applied. The increase in the number of helix improved the behaviour of this foundation system.

Table 4.1 – Shallow and hybrid foundation comparison (Khatri, 2010)

	Advantages	Disadvantages	Cost factors	Soil issues
Conventional spread footing	Industry convention; can be designed to accommodate any tower height; no special approvals necessary; may be designed by any qualified engineering firm	Material quantities are excessive (steel + concrete); labor intensive; large footprint requiring excavation; becomes uneconomical beyond 30mx30m	Spread footings become expensive once they pass 20 m dimension, and the construction time is another parameter; difficult to construct in hilly terrain	Applicable for soils with reasonable bearing capacities; dynamic and frequency issues could be a problem
Cap with micropiles	Capacity is derived from the micropiles and groutable void form system; micropiles can be placed in practically any soil condition; small footprint and can be designed to accommodate any tower height; no shipping issues or site access problems	As the pile cap increases, so do the number of micropiles, and this become cost prohibitive; availability of materials could be an issue; requires a special patent permission from the developer and specialized crew for installation	Very competitive and may be installed in difficult site conditions; small footprint and equipment access is an advantage to the contractor	This option can be used in a variety of soils and deep piles can work on many site conditions; hard rock sites are not a problem because micropiles may be drilled through mast rock

Another way to improve the foundation geometry and their economic feasibility is to improve the shallow portion of the foundation. The use of hollow systems for foundations (filled with soil) or the adoption of low budget materials (ballast or levelling concrete) in non-resistant areas can be a solution to make the system less expensive but at the same time with a similar dead weight. As example, some manufactures propose the use of a precast concrete foundation as presented in Figure 4.4 with a cast in place concrete slab and central pedestal

with horizontal reinforcement and a plurality of radial reinforcing ribs extending radially outwardly from the central pedestal. Since most parts of the wind towers foundations are governed by the overturning resistance, unless the consideration of seismic loading that may become governing for concrete and hybrid towers, a solution consisting in the use of a shallow foundation with a hollow core and larger diameter is also presented as an economic viable solution due to the reduction of the concrete volume required.

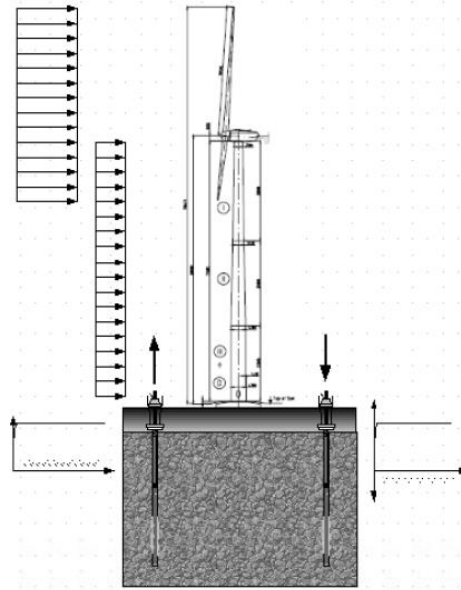


Figure 4.3 - Micropile application on wind turbine foundations (Aschenbroich, 2010)

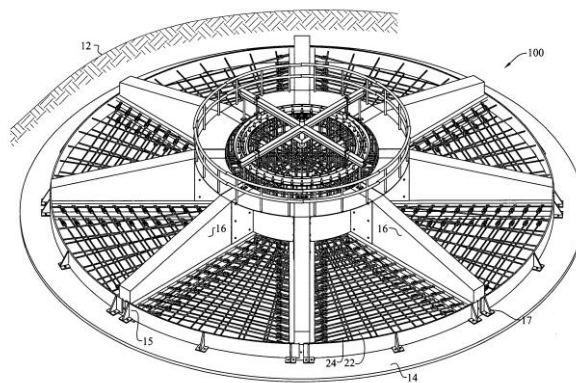


Figure 4.4 – Star foundation system (Phuly, 2011)

The design of shallow foundations for WT is highly dependent on the superstructure self-weight and, therefore, on the structural solution for the tower, mainly made of steel, concrete or hybrid steel-concrete. The vertical load eccentricity, resulting from the imposed horizontal loading from wind at hub height and from earthquake, is decisive for the design. In order to

cover a feasible range of turbine power and tower height three different combinations were considered. Therefore, hub heights of 80, 100 and 150 meters supporting multi-megawatt turbines of 2, 3.6 and 5MW respectively were considered for the design of the foundations. The tower in each of the three cases is considered to be built using either concrete, steel or hybrid steel-concrete tubular shell. The design of the towers is not addressed in this study. A description of the tower design and the loads at towers' base including the self-weight of the tower, which are used to design the case studies hereafter, are obtained from Rebelo et al. (2014). A detailed evaluation of the environmental impact of those tower solutions can be found in Gervásio et al. (2014).

4.2. Design of hybrid foundations

4.2.1. Description of the case studies

4.2.1.1. Geometry and materials

For each of the nine study cases current octagonal shallow foundations with and without micropiles are designed using the geometry sketched in Figure 4.5. In the design, equivalent circular foundations, with diameter B_{eq} , are considered. The materials adopted are concrete class C30/37, steel grade A500 for rebars and N80 steel grade for the micropile tubes.

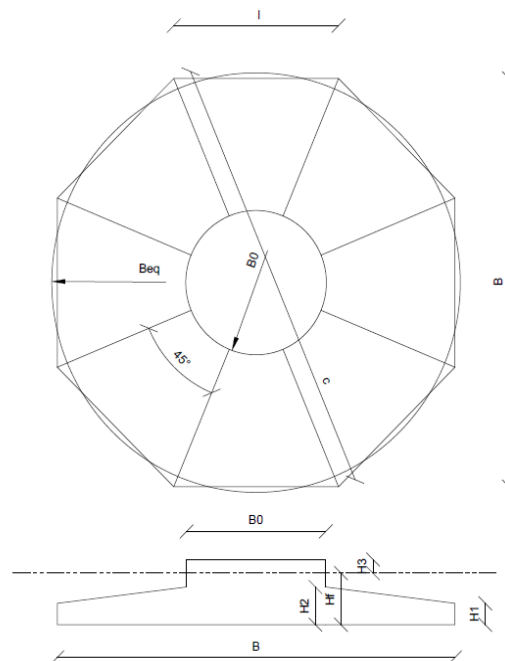


Figure 4.5 - Geometry of the octagonal foundation

The mechanical properties considered for the soil are: friction angle (ϕ'_k), cohesion (c'_k), unit weight (γ) and the low strain (dynamic) elastic modulus (E_s). The characteristic values are given in Table 4.2 and comply with ground type B for the seismic analysis according to Eurocode 8 (EN 1998-1, 2004) which represents a high density sand with good mechanical properties and where the equilibrium limit state is forecasted to be the design driving.

Table 4.2 - Soil properties

ϕ'_k [°]	c'_k [kPa]	γ [kN/m ³]	E_s [MPa]
42	0	18	675

4.2.1.2. Loading

Wind tower foundation loading is bound to the turbine type and power, to the dynamic characteristics of the tower (Rebelo et al., 2014) and to the load situations defined in the standard according to which the wind turbine is certified, e.g. IEC standards (IEC 61400-1, 2005). However, WT producers have restrict policies for the public use of proprietary loads to be used in structural design. In order to maintain the validity and generality of the present study the load calculation methodology proposed by LaNier (2005) was followed and the wind loads acting on the rotor and along the tower were obtained accordingly (Rebelo et al., 2014). Therefore, four different load situations are considered for the design of the foundations: i) extreme wind load in non-operating condition (EWM), ii) extreme wind load in operating condition (EO), iii) earthquake load (EQ) and iv) damage equivalent loads (DEL) for fatigue design.

Extreme wind load in operation or in non-operation includes loads on top of tower and wind load distributed along the tower height. Although both load situations have been evaluated for all case studies, only the EWM load case revealed to be design driving for the foundations. In this load case the turbine is in parked position and the steady wind speed at hub height is $V_{ref}=42.5\text{m/s}$, according to the definition of turbine class II (IEC 61400-1, 2005). The wind loads are calculated based on information collected from Veljkovic et al. (2012) for the 2.0MW/80m towers and extrapolated from simulations reported by LaNier (2005) for the 3,6MW/100m and 5,0MW/150m towers.

Seismic loading is defined using the response spectrum given in Eurocode 8 (EN 1998-1, 2004) for a region complying with the 475 years return period and peak ground acceleration of 0.25g. Behaviour factor was considered as $q=1$ for all towers, terrain type B, 2% damping for steel towers, 3% damping for hybrid and 5% for concrete towers. The load combination that includes earthquake (EQ) is approximated through superposition of the effect of this seismic load with 30% of determinant wind load on tower base calculated for operating condition.

Wind towers and respective foundations are prone to fatigue damage and must be checked for fatigue limit state. In general, the loading associated with this condition is based on S-N spectra describing the number of cycles N for each load effect range S , which are calculated according to the relevant load cases defined in IEC 61400-1 (2005). For the structural design of the foundation the fatigue loading considered consists on the approximation given by the concept of Damage Equivalent Load (DEL). This DEL induces in the structure the same damage as the S-N spectrum would induce and is obtained from the equation (4.1).

$$DEL = \left(\sum_{i=1}^n Range_i^m \frac{N_i}{N_{ref}} \right)^{1/m} \quad (4.1)$$

where $Range_i$ refers to the value of a certain load effect, e.g. bending moment, corresponding to N_i number of cycles in the fatigue spectrum. The parameters used in the calculation are $m=5$ and $N_{ref}=2 \times 10^6$ cycles, which are compatible with those values defined for the fatigue resistance of the steel rebars and micropiles.

In Table 4.3 the load values are given for the design driving extreme loads and for the damage equivalent loads for fatigue design considering 20 years lifetime. The resultants at the base of the foundation are the horizontal force (FH) and the bending moment (M), independent of the foundation type (hybrid or shallow foundation). The design governing extreme loading is the wind loading (EWM) for steel towers and the earthquake loading (EQ) for concrete and hybrid towers. The vertical forces (F_z) depend on the tower and foundation types since they are mostly due to the self-weight. The torsional moment (M_z) is taken into account in the interaction with the other load resultants following the methodology proposed by Hansen (1978) (cit. DNV/Risø (2002)). The DEL loads are given for predominant cyclic load effects which are the overturning moments (Rebelo et al., 2014).

Table 4.3 - Load resultants on the foundation base

Load		2.0MW	3.6MW	5.0MW
		80m	100m	150m
Design driving forces from extreme loading: EW, EO and EQ	FH [kN] – Steel (EWM)	871	1728	1515
	FH [kN] – Concrete (EQ)	2802	6047	6256
	FH [kN] – Hybrid (EQ)	1979	3678	4182
	FZ [kN] – Steel (Shallow) (EWM)	13699	29934	44347
	FZ [kN] – Concrete (Shallow) (EWM)	23635	56508	98073
	FZ [kN] – Hybrid (Shallow) (EWM)	19025	42090	74987
	FZ [kN] – Steel (Micropiles) (EWM)	6702	14545	30786
	FZ [kN] – Concrete (Micropiles) (EWM)	17104	44432	93963
	FZ [kN] – Hybrid (Micropiles) (EWM)	14015	30055	65731
	M [kN.m] – Steel (EWM)	63633	152598	266777
	M [kN.m] – Concrete (EQ)	178533	494790	803576
	M [kN.m] – Hybrid (EQ)	131191	324291	600570
	Mz [kN.m] – All types (EWM)	1218	5961	5834
	Damage equivalent overturning moments for $m=5$ and $N_{ref}=2 \times 10^6$	M [kN.m] – All types (DEL)	19853	80684

4.2.2. Foundation design criteria

4.2.2.1. Reliability concepts and design standards

The design of the supporting structures requires the application of different standards. Usually, the IEC 61400-1 (IEC 61400-1, 2005) is used to define load case sets and national standards (e.g. DIN, DNV) or CEN (Eurocodes) standards are used to assess resistances. The general principles of structural reliability provided by the Eurocodes (EN 1990, 2002) are in agreement with ISO 2394 (2015) which is also the reliability reference adopted by the IEC 61400-1 (2005) standard for the structural analysis of wind turbines. In most European countries the referred building codes are mandatory when design calculations are to be submitted for approval by local authorities, which is usually the case of wind towers foundation design. Furthermore, the procedure is also allowed by the IEC standard given that the reliability level is not lower than the one imposed by this standard, which is controlled by the safety factors applied to loads and resistances.

The design of the foundations is performed according to the concept presented above using the rules prescribed in Eurocode 7 (EN 1997-1, 2004) for geotechnical design, in Eurocode 8 (EN 1998-5, 2004) for geotechnical design under seismic loading, in Eurocode 2 (EN 1992-1-1, 2004) for reinforced concrete design and in Eurocode 3 (EN 1993-1-1, 2005) for steel micropiles design. The partial factors on actions (γ_F) and materials (γ_M) considered for the geotechnical design of the foundation (equilibrium and bearing capacity) are defined in EN 1997-1 (2004) and presented in Table 4.4. The comparable partial factors of EN 1997-1

(2004) are higher or equal to the specified by IEC 61400-1 (Table 4.5), therefore abiding to the recommendations of the later norm.

Table 4.4 - Partial factors on actions (γ_F) and soil parameters (γ_M) (EN 1997-1, 2004)

Combination	Source of loading	Unfavourable loads	Favourable loads	tgØ'
Bear 1	Permanent	1.35	1.00	1.00
	Variable	1.50	0.00	1.00
Bear 2	Permanent	1.00	1.00	1.25
	Variable	1.30	0.00	1.25
Overturning (EQU)	Permanent	1.10	0.90	-
	Variable	1.50	0.00	-
Seismic	-	1.00	1.00	1.10

Eurocode 7 refers to three possible design approaches for bearing capacity verification. Design approach 1 forces the designer to perform safety verifications for two sets of load combinations. The first set (Bear 1, in Table 4.4) uses the same (or higher, in the present case) partial factors that are used in the structural design of the structure (tower), the second set of partial factors (Bear 2, in Table 4.4) conditions the geotechnical design, thus the sizing of the footing. All three design approaches have similar structural reliability levels and in the present work design approach 1 was chosen. This design approach requires the use of two sets of combinations.

Fatigue may be the critical limit state for the internal (structural) design of the tower and foundation. It is explicitly considered in the structural design of the tower and the foundation using Eurocode requirements for steel and reinforced concrete structures (EN 1992-1-1, 2004), (EN 1993-1-9, 2005). But when it comes to the geotechnical design, the fatigue damage calculation for the soil is not performed explicitly. The same happens for the bond strength between the micropile grout and the surrounding soil. Neither IEC 61400 nor EC7 provide guidance on the geotechnical consideration of fatigue on the ground conditions. Even in the IEC 61400-1 addendum (IEC 61400-1/AMD1, 2010) there is not any fatigue design consideration.

The addendum only includes three paragraphs dealing with gravity foundations stating that a recognized standard shall be used for the limit states of overall stability and bearing capacity of soil and foundation. Eurocode 7 is one of such standards. It refers the partial safety factors for loads to be applied on the overall stability (which is the EQUilibrium limit state from EC7) and bearing capacity verifications. For overall stability (EQU), the addendum specifies

partial safety factors equal to $\gamma_F=1.1$ for unfavourable permanent loads and $\gamma_F=0.9$ for favourable permanent loads. These are equal to what is specified by EC7. The partial factors of safety for unfavourable variable (Normal) loads are equal to 1.35 in IEC 61400 and 1.50 in EC7.

Regarding bearing capacity, the factor of safety for permanent unfavourable and favourable loads is 1.0, if the weights and densities are estimated using the 5% and 95% fractiles. That same approach is followed in EC7 (Bear 2). The load factor to be applied for unfavourable variable (Normal) loads is 1.35 in IEC 61400 and 1.30 In EC7 (Bear 2), which is slightly less.

In the case where recognized design codes are available, such as the Eurocodes, IEC 61400 states that the combined partial safety factors for loads, materials and the consequences of failure, γ_F , γ_M and γ_n , shall not be less than those specified on IEC 61400. It should be noted that IEC 61400 does not provide partial safety factors specific for ground materials and the default value for materials ($\gamma_M=1.1$) is clearly lower than the 1.25 specified by EC7 for Bear2 and equal to what is specified by EC8.

The partial factors on actions (γ_F) used for the structural design of the reinforced concrete foundation are defined in IEC 61400-1 (2005) and are presented in Table 4.5. The partial factors on materials (γ_M) for resistance and fatigue analysis are given in Eurocodes 2 and 3 (EN 1992-1-1, 2004; EN 1993-1-9, 2005).

Table 4.5 - Partial factors on actions (γ_F) (IEC 61400-1, 2005)

Unfavourable loads			Favourable loads	Fatigue
Type of design situation			All design situations	
Normal (N)	Abnormal (A)	Transport and erection (T)		
1.35	1.1	1.5	0.9	1.0

For fatigue verification of the reinforced concrete components the partial factors for materials recommended by the Eurocode 2 are the same as those used for persistent design situations in ultimate limit states, i.e. 1.5 for concrete and 1.15 for steel rebars.

For fatigue verification of the steel micropiles the damage tolerant method may be applied since in the event of fatigue damage occurring in one pile a load redistribution between micropiles can occur. On the other hand, the consequence of failure is considered high and, therefore safety factor $\gamma_{Mf}=1.15$ (EN 1993-1-9, 2005) for the partial factor to be applied to the

nominal stress ranges of steel resistance $\Delta\sigma_c$ defined for the reference number of cycles $N_{ref}=2 \times 10^6$.

4.2.2.2. *Shallow foundation*

For the design of the shallow foundations the following cumulative verifications concerning stability and resistance must be performed. A detailed example of the application of this analytical design procedure considered for all cases considered is presented in Annex F of this document within the section regarding the shallow portion design.

- maximum applied stress in the base of the foundation for non-factored loads;
 - in this point it is considered a rectangular equivalent foundation with an effective area (A_{eff}), due to load excentricity, to determine the average stress in the bottom of the foundation (σ_{med}) and the maximum applied stress (σ_{max}) which is function of K obtained with the reference graph presented in Figure 4.6

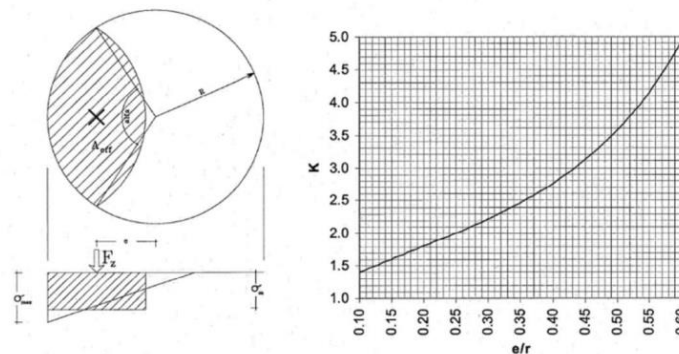


Figure 4.6 – Stress distribution in the foundation base

- effectively compressed area for characteristic wind loading where at least 50% of the base area must be under compression, which can be fulfilled imposing a limit for the load eccentricity $e < 0.59R$, where R is the foundation radius;
- limit state of equilibrium according to Eurocode 7 (EN 1997-1, 2004) where the equilibrium of the foundation when subjected to the overturning moment is verified;
 - comparison between the applied destabilising moment and the stabilising moment due to the vertical forces

- soil bearing capacity according to Eurocode 7 (EN 1997-1, 2004) where the maximum applied pressure in the foundation base is checked for three types of load combinations: ULS-GEO, ULS-STR and accidental combination for seismic loads;
 - definition of an effective rectangular foundation area and determination of the bearing capacity factors (N_q , N_c and N_γ), shape factors (s_q , s_c and s_γ), factors for the inclination of the foundation base (b_q , b_c and b_γ) and inclination factors for the load (i_q , i_c and i_γ) according to Annex D (D.4) of Eurocode 7 (EN 1997-1, 2004)
 - The bearing resistance for drained conditions is given by the expression (4.2) from Annex D (D.4) of Eurocode 7 (EN 1997-1, 2004)

$$\frac{R}{A} = c' N_c b_c s_c i_c + q' N_q b_q s_q i_q + 0.5 \gamma' B' N_\gamma b_\gamma s_\gamma i_\gamma \quad (4.2)$$

- bearing capacity according to Eurocode 8 (EN 1998-5, 2004) – in Annex F of EN 1998-5 it is presented a formulation for the assessment of the foundation stability taking into account the soil inertia (kinematic effect). This is particularly relevant for cohesionless soils, as found by Pender (2010), since their bearing capacity is more sensitive to the effect of inertia loading than in the case of cohesive soils;
 - application of general expression (4.3) for stability against seismic bearing capacity failure given by Annex F of Eurocode 8 (EN 1998-5, 2004)

$$\frac{(1 - e\bar{F})^{c_r} (\beta\bar{V})^{c_r}}{(\bar{N})^a \left[(1 - m\bar{F}^k)^{k'} - \bar{N} \right]^b} + \frac{(1 - f\bar{F})^{c'_m} (\gamma\bar{M})^{c_m}}{(\bar{N})^c \left[(1 - m\bar{F}^k)^{k'} - \bar{N} \right]^d} - 1 \leq 0 \quad (4.3)$$

- the parameters in the expression are presented in Annex F of Eurocode 8 (EN 1998-5, 2004) and in table F.1 for cohesionless soils
- additional soil bearing capacity verification for extremely eccentric loading ($e > 0.3B$) according to DNV/Risø (2002) which reflects the failure of the soil under the loaded part of foundation (Rupture 2 according to DNV/Risø (2002));

- general expression for bearing capacity according to (4.4) presented in point 8.2 of DNV/Risø (2002)) for extremely eccentric loading. Same shape and capacity factors as determined for the determination of bearing capacity according to Eurocode 7 (EN 1997-1, 2004) but with different inclination factors for loading presented in the same point

$$q_d = \gamma' b_{eff} N_{\gamma} s_{\gamma} i_{\gamma} + c_d N_c s_c i_c (1.05 + \tan^3 \phi) \quad (4.4)$$

- sliding ultimate limit state where the friction resistant forces under the foundation base are checked against the horizontal force and contribution of torsional moment M_z .
 - estimation of the horizontal force on the most loaded portion of the foundation (including torsional moment) and comparison with the resistant forces considering a sliding resistant angle $\delta=2/3.\phi'$

4.2.2.3. Hybrid foundation

The design of the hybrid foundations taking into account the contribution of the micropiles behaviour was carried out using a finite element model with shell elements considered for the modelling of the shallow portion of the foundation supported by bilinear springs to simulate both soil and micropiles. The soil bearing capacity according to EN 1997-1 (2004), EN 1998-5 (2004) and DNV (2002) was estimated by determining the percentage of load transferred by the active part of the shallow foundation and by the micropile elements.

This is a simplified method for the estimation of the foundation system behaviour, however a more accurate method involving a 3D simulation of both shallow and micropiles must be considered in order to obtain more realistic bearing capacity results and to properly simulate the changes of the stress state in the soil due to the load transfer caused by the micropiles.

For the internal resistance, considering an outer diameter of 88.9mm and thickness of 9.5mm pipe micropile ($A_s=2370\text{mm}^2$), of N80 steel ($f_y=562\text{MPa}$), the structural design resistance in tension is equal to 1066kN and in compression is 1550kN considering a borehole diameter of 200mm and $f_{ck,grout}=25\text{MPa}$.

The micropiles' external (geotechnical) resistance is checked considering Eurocode 7 (EN 1997-1, 2004) design approach 1 (D.A.1). The resistance's design values are computed with expressions (4.2) for compression and (4.3) for tension:

$$R_{c,d} = \frac{R_{s,k}}{\gamma_s \gamma_{Rd}} = \frac{q_s \times \pi \times D_b \times L_b}{\gamma_s \gamma_{Rd}} \quad (4.5)$$

$$R_{c,d} = \frac{R_{s,k}}{\gamma_{s,t} \gamma_{Rd}} = \frac{q_s \times \pi \times D_b \times L_b}{\gamma_{s,t} \gamma_{Rd}} \quad (4.6)$$

where q_s is the ultimate grout-to-ground shear resistance, D_b is the diameter of the bond length L_b , γ_s and $\gamma_{s,t}$ are the partial factors for the shear resistance in compression and tension (see Table 4.6) and $\gamma_{Rd}=1.5$ is the model factor (used to consider the uncertainty in the resistance model). Eurocode 7 does not define partial factors specific for micropiles, thus the values defined for driven piles were adopted. Boreholes with 200mm diameter, 12m bond length. The considered ultimate grout-to-ground shear resistance of 300kPa comply with soil dense sand type B ($N_{SPT}>50$) using IRS or IGU grouting techniques (Bustamante and Doix, 1985). For EQUilibrium and Combinations type 1 the compression resistance is 1508kN and 1206kN for the tension resistance. For Combinations type 2 the compression resistance value is 1160kN and the tension resistance is 942kN. In Seismic combination the compression resistance is 1311kN and the tension resistance 1160kN.

Table 4.6 - Partial resistance factors (γ_s) for driven piles (EN 1997-1, 2004)

	Symbol	EQU				Seismic
		Comb.1			Comb.2	
		R1	R2	R3	R4	
Side resistance (compression)	γ_s	1.00	1.10	1.00	1.30	1.15
Side resistance (tension)	$\gamma_{s,t}$	1.25	1.15	1.10	1.60	1.30

Two additional verifications were performed in the case of the hybrid foundations: the limit state of equilibrium of the foundation that was fulfilled if the applied forces to the micropiles never surpassed the resistant capacity and the spacing between adjacent micropiles, which should be higher than 3 times the micropiles diameter in order to reduce group effect phenomena (FHWA, 2005). The effect of the micropiles was neglected for the base sliding verification, since it was ensured that the base of the shallow foundation resisted the applied horizontal forces.

4.2.3. Foundation design

4.2.3.1. Numerical model for hybrid foundation

The finite element model (Figure 4.7) was developed in Autodesk Robot (Robot, 2015) considering shell elements with a behaviour of elastic foundation underneath (soil spring modelling) and the micropiles were modelled using spring supports in vertical direction with

different behaviour for tension and compression. These springs with a bi-linear behaviour condensate the micropile-soil interaction which is a simpler approach than the consideration of the full micropile model with skin friction and tip resistance springs.

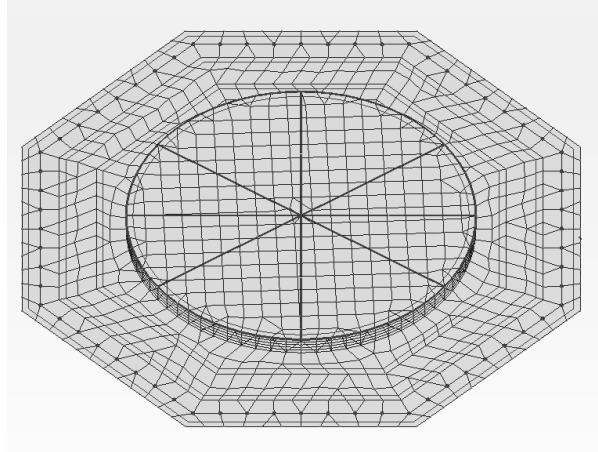


Figure 4.7 - Numerical model example - top view

Figure 4.8a presents the spring force-displacement behaviour with plateaus defined by the maximum resistance in tension and in compression according to what was described in the previous section. The spring stiffness was defined considering that a displacement of $\delta_u=20\text{mm}$ would be required to mobilize 1000kN, for both compression and tension forces, with the resulting spring stiffness equal to $K_z=50\text{MN/m}$.

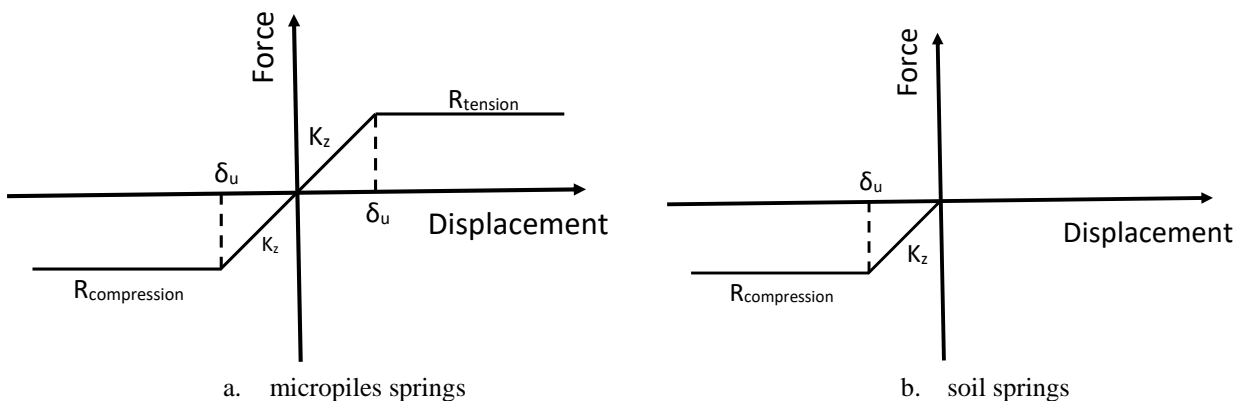


Figure 4.8 - Spring models

As described in Figure 4.8b, the soil-springs were defined as compression-only, linear-elastic, with a coefficient of vertical reaction computed with $E_s=675\text{MPa}$ and $\nu=0.30$, resulting on different k_z for each foundation dimension according to expression (4.4) (Vesic, 1961), where E_f and I_f are the foundation modulus and inertia, respectively.

$$k_z = \frac{0.65 \cdot E_s}{B(1-\nu_s^2)} \sqrt{\frac{E_s \cdot B^4}{E_f I_f}} \quad (4.7)$$

The value considered for the soil elastic modulus will influence the size of the foundation since it will be related with the percentage of force that is supported by the micropiles. The lower the elasticity modulus the higher the forces that are supported by the micropiles and therefore the higher the number of micropiles required and/or higher the shallow portion dimensions.

The loads applied in each model were presented in Table 4.3 and the micropiles were positioned at 0.5 m from the edge of the foundation. The inner line of micropiles was spaced 1m from the outer line (when applicable).

A design example of the application of the described numerical model is presented in Annex F where the obtained results can be found in the topic Numerical Results – micropile forces. By the model results presented in Annex F it is possible to observe that the soil springs are modelled to be activated only in compression (bending moment reactions) and by the reactions on the micropiles it is possible to conclude that the maximum allowed forces in the micropiles are never surpassed for the example considered.

This model allows the estimation of the percentage of forces (vertical axial force and bending moment) withstand by the micropiles while the remaining forces are to be withstand by the shallow portion of the foundation according to the procedure presented in section 4.2.2.2.

In order to respect the minimum center to center spacing of micropiles, four typologies of micropile row positioning were considered. The number of micropiles used was 32, 64 or 96. Figure 4.9 shows the arrangement (and the position of the micropile springs in the model) of each set of micropiles in the foundation geometry.

The resultant loads from the tower were applied in the central node of the foundation while the foundation weight was automatically considered equally distributed along the foundation and ballast weight is added over foundation surface. The model allows the verifications of bearing capacity of soil, overturning and rotational stiffness. The effect of the horizontal force on the sliding resistance was not considered.

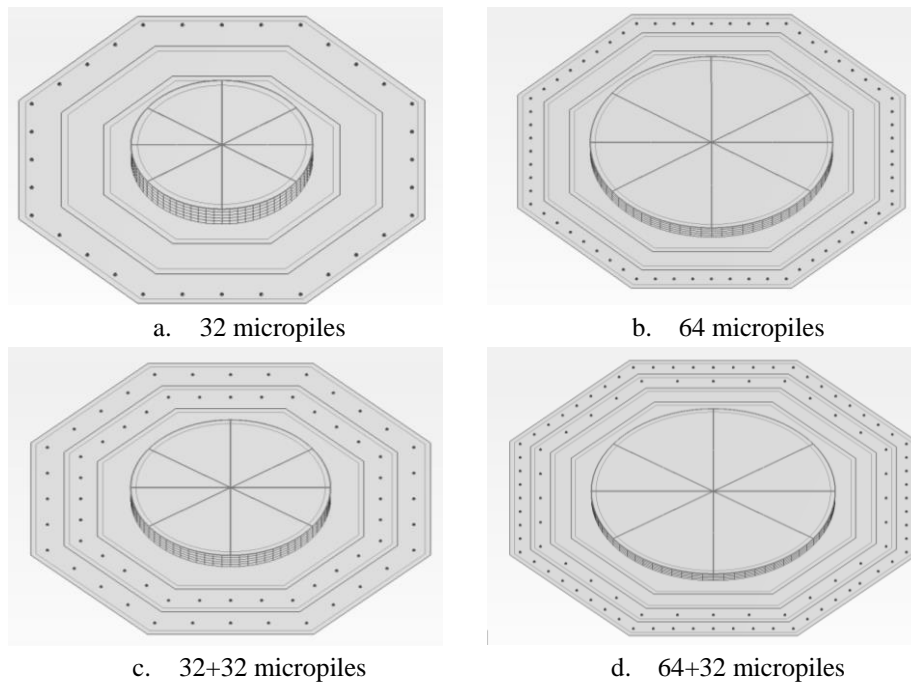


Figure 4.9 - Micropile locations

4.2.3.2. *Design results*

The design results obtained for dimensions and geometry of the foundations are presented in Table 4.7 and Table 4.9 for octagonal shallow and octagonal hybrid foundations respectively. It was observed, as expected, that the governing load case for the hybrid and concrete towers is the earthquake, independently of the type of foundation considered and height of the tower, because the mass of the system is much higher in those two cases. In the case of the steel tower, the governing load case is always the extreme wind. A detailed design example of the procedure considered is presented in Annex F.

Due to this fact, the foundation dimensions for the steel towers are always smaller than the other cases. Reductions between 27% and 54% on the concrete consumption were observed for the steel towers in comparison with the other structural solutions.

On the other hand, the concrete towers are, for all the cases, the most susceptible structures to earthquake loading since they have more mass than the other towers and consequently they present the largest foundation dimensions.

The hybrid foundations solutions required smaller dimensions and lower material consumption (concrete and rebar) however they required the use of micropiles tubes and grout.

Table 4.7 - Shallow foundations

Tower Type	80m 2.0MW			100m 3.6MW			150m 5.0MW		
	Steel	Concrete	Hybrid	Steel	Concrete	Hybrid	Steel	Concrete	Hybrid
H_f (m)	2.00	2.50	2.50	3.00	3.50	3.50	3.50	4.50	4.50
Governing load case	EWM	EQuake	EQuake	EWM	EQuake	EQuake	EWM	EQuake	EQuake
Governing design criteria	EQU								
H₁ (m)	0.95	0.95	0.95	1.20	1.20	1.20	1.20	2.00	2.00
H₂ (m)	2.00	2.50	2.50	3.00	3.50	3.50	3.50	4.50	4.50
H₃ (m)	0.50	0.50	0.50	0.50	0.50	0.50	0.50	0.50	0.50
I (m)	7.04	7.04	6.21	8.28	9.11	7.87	8.70	9.53	8.28
B_{eq} (m)	17.46	17.46	15.41	20.55	22.60	19.52	21.57	23.63	20.55
B (m)	17.00	17.00	15.00	20.00	22.00	19.00	21.00	23.00	20.00
B₀ (m)	5.60	8.00	7.20	8.00	11.00	10.80	11.00	14.00	13.80
C (m)	18.40	18.40	16.24	21.65	23.81	20.57	22.73	24.90	21.65
Concrete (m³)	359.0	458.9	373.6	729.3	1058.6	831.4	981.9	1664.1	1324.0
Rebar (Ton.)	30.5	54.4	44.35	53.0	114.0	62.7	65.4	152.6	62.8
Excavation (m³)	394.9	504.8	410.9	802.2	1164.4	914.5	1080.0	1830.6	1456.4

In this design, the position of the ground water table was considered to be below the depth of influence regarding bearing capacity, and the sand's dry unit weight was used in the calculations. The ratio between applied load and resistance obtained both for equilibrium and bearing capacity obtained by applying the design procedure of Annex F are presented in Table 4.8 for the shallow foundations examples.

Table 4.8 - Shallow foundations design ratio

Tower Type	80m 2.0MW			100m 3.6MW			150m 5.0MW		
	Steel	Concrete	Hybrid	Steel	Concrete	Hybrid	Steel	Concrete	Hybrid
EQU	0.91	0.89	0.92	0.83	0.80	0.87	0.92	0.71	0.85
Bearing	0.11	0.51	0.79	0.09	0.20	0.43	0.15	0.13	0.40

The consideration of the ground water table at the surface would lead to a reduction in the sand self-weight and consequently to a reduction in the bearing capacity of the soil. Given the values presented in Table 4.8, the ratio of the mobilization of the bearing capacity are low except for concrete and hybrid towers of 80m. The application of the design procedure described in the chapter and presented in Annex F showed that in only these two cases, the consideration of the water table at the ground surface would exceed the allowed bearing

capacity of the soil. For the hybrid towers with 100m and 150m the consideration of the water table level at the surface would make the bearing capacity the governing design criteria, however still within admissible values.

Table 4.9 - Hybrid foundations

Tower type	80m 2.0MW			100m 3.6MW			150m 5.0MW		
	Steel	Concrete	Hybrid	Steel	Concrete	Hybrid	Steel	Concrete	Hybrid
H_f (m)	2.00	2.50	2.50	3.00	3.50	3.50	3.50	4.50	4.50
Governing load case	EWM	EQuake	EQuake	EWM	EQuake	EQuake	EWM	EQuake	EQuake
Typology (according to Figure 4.9)	a	b	a	c	b	b	b	d	b
H₁ (m)	1.59	1.81	1.74	2.40	2.25	1.95	2.58	2.83	2.69
H₂ (m)	2.00	2.50	2.50	3.00	3.50	3.50	3.50	4.50	4.50
H₃ (m)	0.50	0.50	0.50	0.50	0.50	0.50	0.50	0.50	0.50
I (m)	4.14	4.97	4.56	4.97	7.04	5.80	6.21	8.28	7.04
B_{eq} (m)	10.27	12.33	11.30	12.33	17.46	14.35	15.41	20.55	17.46
B (m)	10.00	12.00	11.00	12.00	17.00	14.00	15.00	20.00	17.00
B₀ (m)	5.60	8.00	7.20	8.00	11.00	10.8	11.00	14.00	13.80
C (m)	10.82	12.99	11.91	12.99	18.4	15.15	16.24	21.65	18.40
Concrete (m³)	164.8	297.9	246.9	360.9	707.4	497.0	655.5	1410.6	1067.5
Rebar (Ton.)	14.1	19.2	13.8	20.3	56.3	21.0	30.7	66.3	31.2
Micropiles Steel (Ton.)	7.14	14.29	7.14	14.29	14.29	14.29	14.29	21.43	14.29
Micropile Grout (m³)	11.17	22.34	11.17	22.34	22.34	22.34	22.34	33.50	22.34
Excavation (m³)	181.3	327.7	271.5	397.0	778.1	546.7	721.1	1551.6	1174.3

The definition of the dimensions of the shallow part of the hybrid foundations is governed by the maximum allowable loads transferred to the micropiles. Both the equilibrium and bearing capacity mobilization coefficients are lower than the values obtained for the shallow foundation design (Table 4.8) according to the results obtained with the analytical procedure presented in Annex F and so the consideration of the water table level in ground surface is expected not to affect the presented design.

4.3. LCA and LCC analysis of hybrid foundations

4.3.1.1. *Life cycle environmental analysis*

A comparative Life-Cycle Analysis (LCA) was carried out in order to assess the potential environmental benefits of hybrid foundations in relation to shallow foundations.

LCA is the process of evaluating the potential environmental impacts of a given product in terms of material manufacturing, assembling/construction, maintenance and end-of-life (Gervásio et al., 2014).

The LCA presented in this section focuses on the foundations; it does not include the supporting structure of each tower. However, it is noted that foundations have usually a major contribution in the outcome of a complete LCA of a wind tower (i.e., foundations and supporting tower), particularly when seismic load is the governing load case (Gervásio et al., 2014).

The materials considered for the foundations are listed in Table 4.7 and Table 4.9, respectively for the shallow foundations and for the hybrid foundations.

A model for the LCA was developed in order to compare the two alternative type of foundations, i.e. simple shallow foundation and hybrid foundation, which includes micropiles, taking into account a lifespan of 20 years. The analysis was performed by the software GaBi (2012). The initial stage of the Life-Cycle Assessment includes the production of materials for the foundations, their transportation to the construction site, the excavation of soil for the foundations and its deposition into a landfill. For the hybrid foundations, the use of the drilling equipment and respective fuel consumption were also taken into account. Based on the information provided by a contractor, a drilling rate of 6 m/hour and a fuel consumption of 8 l/hour were considered.

During the service life of each tower, no maintenance is needed for the respective foundation. Therefore, in this stage no additional impacts were considered in the analysis.

Furthermore, in the end-of-life stage two scenarios were taken into account: in the 1st scenario it was assumed that the foundations of the towers are left in the ground, and in the 2nd scenario it was assumed that the foundations are demolished and demolition waste is recovered for recycling (for the hybrid solutions it was considered that the piles are not recovered since they are buried underground).

Hence, in the 1st scenario no materials are recovered for recycling or reuse and thus, no further emissions are considered due to the demolition process.

In the second scenario, the materials recovered from the demolition are recycled and credits are obtained since the recycled materials avoid the need to produce new ones from raw materials. The recycling rates for concrete and steel reinforcement were assumed to be 80% and 70%, respectively. All remaining materials were assumed to be sent to a landfill of inert materials. Apart from the credits obtained from the recycling process, this scenario takes into account the burdens due to the process of demolition and the transportation of materials to their final destination.

For the transportation of materials, a sensitivity analysis was performed in order to assess the importance of this process. A default distance of 100 km was initially considered for the transportation of materials to the construction site and from the construction site to the final destination of each material. By varying in $\pm 50\%$ the transportation distances, a variation of $\pm 12\%$ was obtained for the impact category of eutrophication and less than 10% for the remaining categories. Therefore, given the negligible importance of the process, the transportation distances were considered to be 100 km for all cases.

The life cycle analysis was carried out according to ISO standards 14040 (2006) and 14044 (2006). The CML methodology (Guinée et al., 2002) was used for the quantification of the following environmental categories: acidification potential, eutrophication potential, global warming potential, ozone depletion potential and photochemical ozone creation potential. In addition, an indicator expressing the total primary energy demand was considered. Hence, the environmental categories selected for the analysis are summarized in Table 4.10.

Table 4.10 - Environmental indicators considered for LCA

Indicator	Unit
Acidification Potential (AP)	kg SO ₂ -Equiv.
Eutrophication Potential (EP)	kg Phosphate-Equiv.
Global Warming Potential (GWP)	kg CO ₂ -Equiv.
Ozone Layer Depletion Potential (ODP)	kg R11-Equiv.
Photochem. Ozone Creation Potential (POCP)	kg Ethene-Equiv.
Primary energy demand (PED)	MJ

The results of the life cycle analysis, taking into account the environmental categories in Table 4.10 and both end-of-life scenarios, are indicated in Table 4.11 and Table 4.12 for the shallow and hybrid foundations, respectively. The lower values of Table 4.11 and Table 4.12 are highlighted in bold, for each environmental category and for each type of tower (80m, 100m and 150m).

It is observed from Table 4.11 and Table 4.12 that the difference between the results of the analysis, taking into account the 1st or the 2nd end-of-life scenarios, are negligible. This can be explained by the fact that the credits from the recycling of materials counterbalanced the burdens due to demolition and transportation processes. The main variations are for the impact categories of Eutrophication and Photochemical Ozone Creation. In the former category the results taking into account the 2nd scenario are increased in less than 20%; while in the latter the results are reduced in percentages up to 35% for the higher towers.

Due to the lightness of steel towers in comparison with the other towers and consequently the lower requirement in terms of materials, the shallow foundation of the steel towers achieved the best performance in most environmental categories (see Table 4.11), independently of the height of the tower. The only exception is for the tower with 150 m for the environmental category of Ozone Depletion (ODP).

Table 4.11 - Results of the environmental analysis for the shallow foundations

			AP [kg SO ₂ -Eq.]	EP [kg PO ₄ -Eq.]	GWP [kg CO ₂ -Eq.]	ODP [kg R11-Eq.]	POCP [kg C ₂ H ₄ -Eq.]	PED (MJ)
Tower 80 m	Steel tower	1 st	2.78E+02	3.82E+01	1.39E+05	3.83E-04	2.72E+01	1.18E+06
		2 nd	2.82E+02	4.45E+01	1.42E+05	4.37E-04	1.86E+01	1.20E+06
	Concrete tower	1 st	4.16E+02	5.37E+01	1.99E+05	6.79E-04	4.40E+01	1.80E+06
		2 nd	4.19E+02	6.18E+01	2.03E+05	7.75E-04	3.26E+01	1.83E+06
	Hybrid tower	1 st	3.39E+02	4.37E+01	1.62E+05	5.54E-04	3.59E+01	1.47E+06
		2 nd	3.42E+02	5.03E+01	1.65E+05	6.32E-04	2.66E+01	1.49E+06
Tower 100 m	Steel tower	1 st	5.30E+02	7.47E+01	2.69E+05	6.67E-04	4.98E+01	2.22E+06
		2 nd	5.37E+02	8.75E+01	2.76E+05	7.62E-04	3.26E+01	2.27E+06
	Concrete tower	1 st	9.15E+02	1.20E+02	4.44E+05	1.43E-03	9.46E+01	3.93E+06
		2 nd	9.23E+02	1.39E+02	4.52E+05	1.63E-03	6.87E+01	4.00E+06
	Hybrid tower	1 st	6.13E+02	8.59E+01	3.10E+05	7.89E-04	5.82E+01	2.57E+06
		2 nd	6.22E+02	1.01E+02	3.18E+05	9.01E-04	3.84E+01	2.63E+06
Tower 150 m	Steel tower	1 st	6.90E+02	9.87E+01	3.54E+05	8.25E-04	6.35E+01	2.87E+06
		2 nd	7.01E+02	1.16E+02	3.63E+05	9.42E-04	4.04E+01	2.95E+06
	Concrete tower	1 st	1.33E+03	1.81E+02	6.60E+05	1.91E-03	1.33E+02	5.67E+06
		2 nd	1.35E+03	2.10E+02	6.74E+05	2.18E-03	9.26E+01	5.78E+06
	Hybrid tower	1 st	8.30E+02	1.25E+02	4.42E+05	7.99E-04	7.03E+01	3.38E+06
		2 nd	8.47E+02	1.48E+02	4.55E+05	9.14E-04	3.98E+01	3.50E+06

In relation to the hybrid foundations, the environmental results for each type of tower are indicated in Table 4.12. Likewise, the hybrid foundation of steel towers achieved the best performance in all environmental categories, independently of the height of the tower. This is due to the same reason referred before, that is, the lightness of the steel towers in comparison with the other towers.

The global warming potential (GWP) aims to quantify the emission of greenhouse gases, such as CO₂ and CH₄, to the atmosphere. Due to its major influence in climate change, the results for the life cycle analysis, focusing on global warming, are illustrated in Figure 4.10 for the shallow foundations and for the hybrid foundations, considering the three types of towers (steel (S), concrete (C) and hybrid tower (H)) and for the three heights (80m, 100m and 150m).

Table 4.12 - Results of the environmental analysis for the hybrid foundations

			AP [kg SO ₂ -Eq.]	EP [kg PO ₄ -Eq.]	GWP [kg CO ₂ -Eq.]	ODP [kg R11-Eq.]	POCP [kg C ₂ H ₄ -Eq.]	PED (MJ)
Tower 80 m	Steel tower	1 st	2.20E+02	2.69E+01	9.73E+04	1.46E-03	2.46E+01	8.87E+05
		2 nd	2.21E+02	2.98E+01	9.87E+04	1.49E-03	2.06E+01	8.99E+05
	Concrete tower	1 st	3.90E+02	4.84E+01	1.73E+05	2.81E-03	4.30E+01	1.55E+06
		2 nd	3.94E+02	5.36E+01	1.76E+05	2.85E-03	3.60E+01	1.57E+06
	Hybrid tower	1 st	2.55E+02	3.33E+01	1.19E+05	1.46E-03	2.64E+01	1.02E+06
		2 nd	2.58E+02	3.76E+01	1.21E+05	1.49E-03	2.07E+01	1.04E+06
Tower 100 m	Steel tower	1 st	4.22E+02	5.38E+01	1.92E+05	2.83E-03	4.52E+01	1.67E+06
		2 nd	4.27E+02	6.01E+01	1.95E+05	2.87E-03	3.68E+01	1.70E+06
	Concrete tower	1 st	7.17E+02	9.27E+01	3.35E+05	3.28E-03	7.54E+01	2.93E+06
		2 nd	7.24E+02	1.05E+02	3.41E+05	3.38E-03	5.85E+01	2.99E+06
	Hybrid tower	1 st	4.85E+02	6.48E+01	2.29E+05	2.84E-03	4.89E+01	1.91E+06
		2 nd	4.92E+02	7.35E+01	2.34E+05	2.88E-03	3.75E+01	1.95E+06
Tower 150 m	Steel tower	1 st	5.93E+02	8.05E+01	2.85E+05	2.96E-03	5.87E+01	2.36E+06
		2 nd	6.01E+02	9.19E+01	2.92E+05	3.02E-03	4.36E+01	2.41E+06
	Concrete tower	1 st	1.16E+03	1.61E+02	5.70E+05	4.70E-03	1.11E+02	4.62E+06
		2 nd	1.18E+03	1.86E+02	5.84E+05	4.82E-03	7.82E+01	4.75E+06
	Hybrid tower	1 st	7.76E+02	1.13E+02	3.96E+05	2.98E-03	6.91E+01	3.04E+06
		2 nd	7.91E+02	1.32E+02	4.07E+05	3.04E-03	4.50E+01	3.14E+06

It is observed from Figure 4.10 that hybrid foundations achieve a lower value for the global warming potential, independently of the type and height of the tower. This was already expected from the comparison between Table 4.7 and Table 4.9, where the reduction of the mass achieved by hybrid foundations is evidenced. Although in the case of the hybrid foundations, additional equipment is necessary, as described before, the corresponding additional impacts are not enough to compensate the reduction of impacts due to the lower mass of the hybrid foundations.

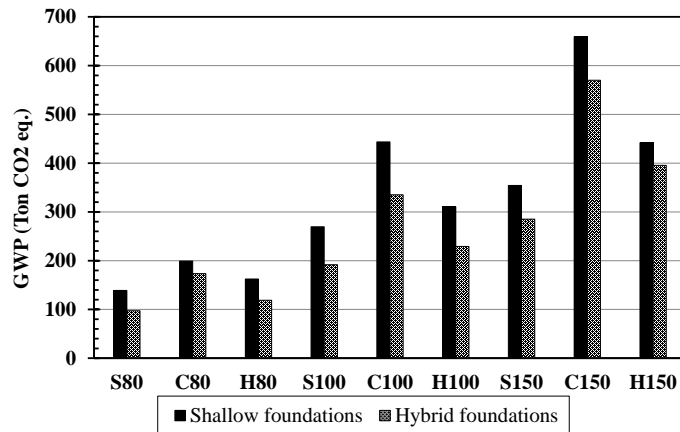


Figure 4.10 - Comparison of global warming potential (GWP) for shallow and hybrid foundations

In the case of Figure 4.10, the reduction of global warming potential for hybrid foundations varies from 10% to 30%, for the hybrid tower with a height of 150m (H150) and for the steel tower with a height of 80m (S80), respectively.

In addition, the comparative analysis between shallow and hybrid foundations, in terms of the total primary energy demand, is indicated Figure 4.11. Likewise, it is observed from Figure 4.11 that hybrid foundations achieve a lower value for the primary energy demand, independently of the type and height of the tower.

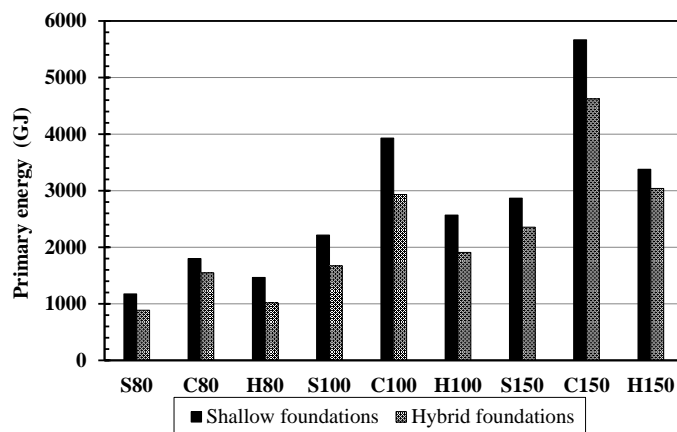


Figure 4.11 - Comparison of primary energy demand (PED) for shallow and hybrid foundations

In this case, the reduction of primary energy demand for hybrid foundations varies from 9% to 25%, for the hybrid tower with a height of 150m (H150) and for the concrete and hybrid towers with a height of 100m (C100 and H100), respectively.

It may be concluded from this analysis that by reducing the amount of materials for the foundation, hybrid foundations provide a better environmental performance, despite the need of additional material and construction equipment for the micropiles.

4.3.1.2. Life cycle cost analysis

The Life Cycle Cost (LCC) analysis of hybrid and shallow foundations takes into account the construction of the foundations and the demolition in year 20. Unit costs relative to the materials and construction processes are provided in Table 4.13.

Table 4.13 - Unit costs for the construction of hybrid and shallow foundations (prices valid for Portugal in year 2014)

Description	Unit	Unit cost (€)
Excavation in soil for foundations, including excavation, loading, transportation, unloading and levelling	€/m ³	6
Pipe micropiles (O.D. 88,9mm, t=9,5 mm) including steel supply, loading, transportation, unloading, placing with borehole drilling in rock	€/m	120
Provision and placing of levelling concrete on foundation base, including materials supply and transportation, preparation, loading, transportation, unloading, placing, vibration and cure	€/m ³	70
Provision and placing of concrete (C30/37) on foundation, including materials supply and transportation, preparation, loading, transportation, unloading, placing, vibration and cure	€/m ³	140
S500 reinforcing steel (S500), including steel supply and transportation, bending, assembly, connections, loading, transportation, unloading and placing	€/kg	1.2
Formwork for concrete modelling, including material supply, loading, transportation, unloading and assembly	€/m ²	15
Ballast on top of the footing, including materials supply, loading, transportation, unloading and placing	€/m ³	25
Demolition with the use of a backhoe loader with hammer and transportation of debris	€/m ³	175

The compilation of costs for the construction of shallow and hybrid foundations and respective demolition is illustrated in Figure 4.12. It is noted that the analysis was made based on current Portuguese unit costs, in year 2014. For hybrid foundations only the concrete cap was assumed to be demolished and transported to final destination.

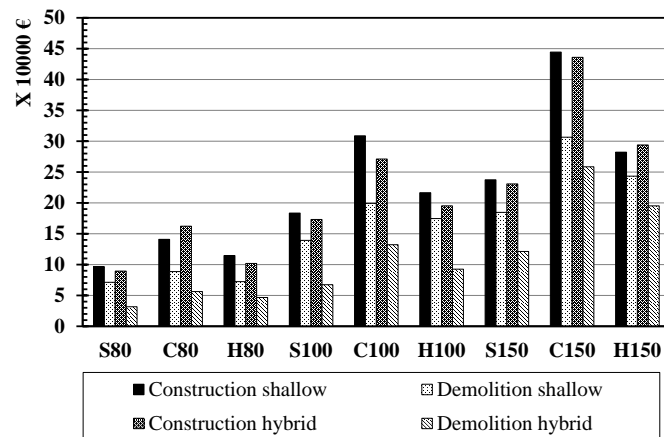


Figure 4.12 - Construction and demolition costs of shallow and hybrid foundations

It is observed from Figure 4.12 that the construction cost of hybrid foundations in comparison with shallow foundations, for the same tower, is in general lower, although the difference is not significant. The cost reduction in hybrid foundations enabled by the smaller dimensions is compensated by the cost of the micropiles. In all cases, the difference was below 15% and only in two cases (C80 and H150) the construction of the hybrid foundation was higher than the shallow foundation. In relation to the demolition, it may be concluded from Figure 4.12 that the costs for shallow foundations are generally higher than the costs for hybrid foundations, obviously because of smaller volume of concrete in hybrid foundation. It is also observed that the difference is reduced with the height of the tower. For the group of towers 80 m high the major difference is for the steel tower (S80) with a reduction of about 23%; while, for the group of towers 150m high the major difference is for the steel tower (S150) with a reduction of about 14%.

Finally, the results of the LCC are represented in Figure 4.13. In this case, the total present value of each foundation was quantified by discounting future costs (i.e. demolition costs) to the base year of the analysis with a discount rate of 2%. From Figure 4.13 it is observed that hybrid foundations are generally more beneficial than shallow foundations; although, even in the best cases (S80 and H100), the difference is lower than 25%. In addition, it may be concluded that the major differences are for the steel towers, independently of the height. On the other hand, smaller differences are observed for the concrete towers.

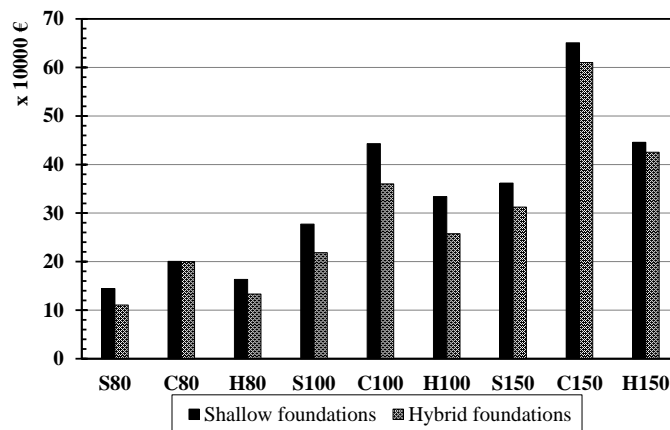


Figure 4.13 - Total present value (in €) of each foundation

4.4. Final comments

The expected increase in the height of the wind towers will consequently lead to an increase in the foundations diameter. The same influence is expected when additionally, to wind also seismic loading is considered in the design and becomes design driving. Hence an improvement in the foundation system was proposed and analysed in this paper and a feasibility assessment regarding the use of micropiles as a reinforcement of the actual shallow foundations of wind towers was performed.

Foundation design is based on typical wind loading defined for standard wind turbine class II as defined in IEC (IEC 61400-1, 2005) and moderate seismicity considering 0.25g peak ground acceleration as defined in Eurocode 8 (EN 1998-1, 2004). Nevertheless, conclusions can be considered also valid for lower seismicity regions, given that seismic forces do not condition the design. This is in general true for all the steel towers foundations considered. For concrete and hybrid towers there is a significant influence of the seismic forces in the dimensions of the foundations (Rebelo et al., 2014). Therefore, extrapolation to low or very low seismicity regions should be made with caution for those type of towers.

The results of the shallow and the hybrid foundations designs showed that the micropiles reinforcement is a very satisfactory solution both in terms of material consumption and in terms of potential environmental impacts, according to the presented LCA. In terms of costs, hybrid foundations may be beneficial when demolition costs are taken into account.

In relation to concrete consumption, it was observed that in the case of the hybrid foundations, a reduction between 15% and 54% was achieved when compared with the correspondent shallow foundations. The reduction in terms of steel reinforcement is between 50% and 69% (disregarding the micropile tube as rebar) and 30% to 53% (considering the micropile tube as

rebar). It is noted that in the case of the hybrid foundations, the materials related to the micropiles installation (micropiles and grout) were also considered in the analysis.

The results provided by the LCA pointed for a lower environmental impact in hybrid foundations in comparison with the correspondent shallow foundations, for every structure geometry and typology and for every environmental indicator considered in the analysis.

A reduction of 10% to 30% of the global warming potential was achieved by hybrid foundations in relation to shallow foundations, while for the primary energy demand a reduction of 9% to 25% was obtained. The main reason for the better environmental performance is due to the reduction of the mass achieved by hybrid foundations, in spite of the use of additional equipment.

The LCC showed that in terms of construction costs hybrid foundations and shallow foundations do not differ significantly. However, when demolition costs are considered, hybrid foundations became clearly more beneficial with a cost reduction of up to 25%.

5. HYBRID FOUNDATIONS – EXPERIMENTAL TESTS ON MICROPILES

5.1. Introduction

In order to analyze the improvement caused by the addition of micropiles to a shallow foundation in a foundation system as presented in chapter 4, load tests on steel pipe micropiles, installed in loose sand, were performed under controlled conditions, to access their resistance and stiffness.

The tests described in this chapter focus on the monotonic and cyclic behavior of the micropiles, both isolated and in groups, ungrouted and with pressure grout injection. The grouted micropiles considered in these tests are classified as type B according to FHWA (2005) according to the illustration of Figure 5.1. Schlosser and Frank (2004) propose an equivalent classification related to the grouting technique described as:

- Micropile type I: The micropile may or not be equipped with reinforcement and is filled with mortar placed with a guide pipe. The pipe is then closed at the top and the mortar is injected under pressure. The pipe is recovered while pressure is being applied.
- Micropile type II: These micropiles are equipped with reinforcement filled with grout injected with a guide tube by gravity or under very low pressure. This type is divided into two sub-types described as type II_h (refill of grout from the top) and type II_b (refill of grout from the bottom of the pile)
- Micropile type III: This type is equipped with reinforcement and a tube injection system placed inside the grout. The injection is conducted under pressure of at least 1MPa according to global and unitary injection.
- Micropile type IV: This type is equipped with reinforcement and a tube injection system placed inside the grout. The injection is conducted under pressure of at least 1MPa according to repetitive and selective injection using a shutter at different levels. The so called R-SOL type can be treated as this type.

The first tests were carried out under increasing monotonic loading, with constant rate of displacement until specimen failure. On other tests, quasi-static load cycles were applied prior

to the monotonic loading in order to check the influence of the cycle loading on the resistance and stiffness of the micropiles.

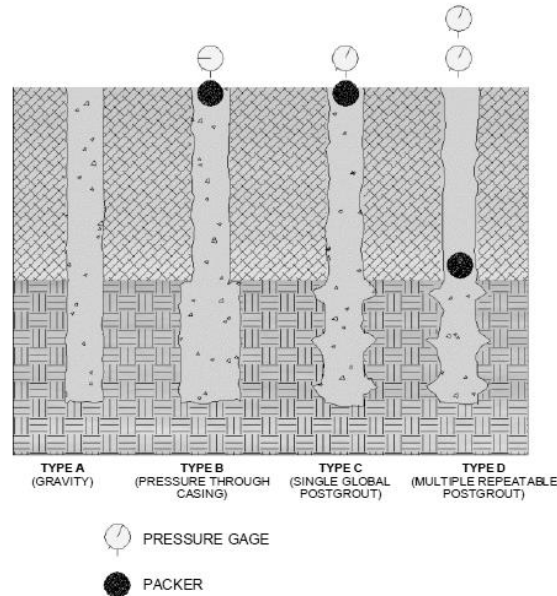


Figure 5.1 - Micropile Classification System Based on Type of Grouting (FHWA, 2005)

The influence of the grout injection in the resistance of the micropiles was studied. The load tests were conducted first on ungrouted specimens which were subsequently injected with pressured grout and retested.

Groups of 2x2 micropiles were also tested. Three layouts were assembled with different geometries in order to evaluate the effect of the micropile spacing.

5.2. Background information

The first references and studies about the use of micropiles were conducted and presented by Lizzi (1978). Most of the experimental data available was obtained with *in-situ* tests and the results achieved with laboratory work are somehow reduced, especially in the scale adopted in the present work.

The most extensive work presented on the behavior of micropiles was carried out in the scope of the FOREVER project (Schlosser and Frank, 2004). As examples of the results of this project may be cited works such as Francis (1997) and Le Kouby (2003) who thoroughly presented the procedure and the results of the tests conducted on a laboratory pressure chamber on reduced scale micropiles.

These deep foundation elements are sensitive to the type of installation and injection procedure. Grouting may be performed under gravity pressure (Type A), low pressure (Type B), low pressure followed by a single high pressure phase (Type C or IGU - *Injection Globale Unitaire*) or by multiple high pressure phases (Type D or IRS - *Injection Répétitive et Sélective*). The value for the unit skin friction is higher for IRS than for IGU as shown by Bustamante and Doix (1985). Other authors such as Russo (2004), who conducted experimental tests on full-scale micropiles placed in pre-drilled holes in a heterogeneous ground, confirmed those conclusions. The maximum values obtained for the unit skin friction on specimens injected with both techniques (95kPa for IRS and 69kPa for IGU) were comprised inside the boundaries provided by Bustamante and Doix (1985). Schlosser and Frank (2004) showed in their studies under the scope of FOREVER project that the side friction is largely dependent on the soil grains size, beyond the expected influence of the surface rugosity. The ground properties also influence the micropiles behavior since the static stiffness and limit loads increase with density index, in sand.

In the last few years an increase in the use of self-drilling hollow core micropiles has been registered. In spite of the hollow core micropile being typically classified as type B according to FHWA (2005) guidelines, Elaziz and El Naggar (2012) referred that this classification may be conservative and it should be classified as new type E. The reason pointed out by the authors is the underestimation of the interface bond strength, in non-reversal axial cyclic load tests under compression and tension, on micropiles installed on a stiff silty clay deposit.

An example of large scale laboratory tests is presented by Schwarz (2000) considering specimens with a geometry similar to the adopted in this study (5m long and 130mm of diameter) installed in boreholes drilled in sand, pressure grouted and subjected to monotonic and cyclic (one and two-way) axial loading. It was found that the cyclic loading tends to reduce the bearing capacity in comparison with static loads and it is dependent on the number of cycles and load cycle amplitude, in agreement with the works of Chan and Hanna (1980), Turner and Kulhawy (1990) and Briaud and Felio (1986) regarding the cyclic behavior of other types of deep foundations. The tests were conducted with force controlled cycles, with constant amplitude, at a given percentage (18 to 55%) of the tensile capacity. Results showed that more than 10000 cycles were required before failure was observed. For the sandy soil tested the authors proposed a factor to reduce the allowed peak-to-peak cyclic load range in function of the expected number of load cycles.

Boulon and Foray (1986) studied the behavior of single micropiles in sand, on a pressure chamber, under cyclic loading. The loading amplitudes varied between 30% and 45% of the monotonic tensile resistance and the results showed that about 25000 cycles were required to achieve micropile failure.

Cavey et al. (2000) applied reversed loads with increasing amplitude in micropiles installed in loose to medium sand and silt, reaching loads higher than the capacity determined by Davisson's method, and found that this capacity was reduced to as low as 60%, after only two load cycles. The results are in agreement with the ultimate capacity reduction of drilled shafts subjected to two-way cyclic loading observed by Turner and Kulhawy (1990).

The referred self-drilling hollow core micropiles tested by Elaziz and El Naggar (2012) on a stiff silty clay deposit and subjected to a cyclic loading (15 cycles with a half-amplitude of about 33% of the micropile design load) presented an increase in the accumulated pile head movement between 6 and 18% of the initial displacement throughout the cyclic loading and also showed a trend of constant stiffness during the applied cycles.

Considering the behavior of full scale helical pulldown micropiles, installed in stiff to very stiff clayey soils underlain by dense sand, it was observed by El Sharnouby and El Naggar (2011; 2012) that the cyclic resistance is very affected on the shaft contributions and the displacement during the cyclic loading during 15 cycles of one-way cyclic loading was less than 1.8 % of the shaft diameter. Those micropiles also experienced a slightly improvement of the ultimate axial stiffness and axial capacity in the cases of one-way cyclic loading with average and maximum values higher than 40% and 54% of the ultimate capacity.

The behavior of multiple micropiles was also studied. Those studies can be divided into two sub-groups according to the micropiles installation type: group specimens composed by vertical micropiles and reticulated network specimens for inclined micropiles.

Schlosser and Frank (2004) concluded from monotonic tests that both the limit load for 10 mm of deformation and the creep load are, in reticulated networks, 2/3 of the load obtained for groups. In terms of the initial deformability, it is very similar for all the reticulated network specimens but is higher for the groups (about 2 times). The same authors observed that the resistance of the groups is 8% to 15% higher than the reticulated networks for the same soil confinement, due to the system geometry divergence. Also, the geometry (inclination) of micropiles does not present any advantage in terms of vertical loading and groups with a small number of piles do not show any significant improvement to the single behavior, contradicting the observations in groups with a larger number of micropiles.

According to Juran et al. (2001) the behavior of reduced scale models micropile groups and reticulated networks subjected to dynamic (seismic) loading on centrifuge tests show that the dynamic stresses introduced to the micropiles are very low since the inertial forces of the superstructure are transferred to the soil through soil-structure interaction due to the flexible behavior of the micropiles. The group geometries also presented positive group effect which results in smaller bending moments for lower spacings while the reticulated networks resist

earthquake loading with higher axial stresses when compared with the group models showing also a reduction in pile bending moments and cap displacements.

One problem related to the current load-controlled testing procedure for micropiles is the required testing time. In order to overcome this problem it was proposed, by Juran and Weinstein (2009), a new strain-rate-controlled procedure which was compared with some model-scale tests conducted in a calibration chamber. The good agreement achieved for both monotonic and cyclic tests allows its recommendation for use in larger scale tests, as in the case of the current study.

The behavior of micropiles and piles installed on different grounds and under different types of loadings is well documented. However, the behavior of these elements subjected to cyclic loading has not been exhaustively presented. The main objective of the experimental program is to contribute to a better knowledge of such behavior.

5.3. Experimental layout and assembly procedure

A global view of the experimental layout is shown in Figure 5.2. The micropiles were installed in a cylindrical soil container with a 2m diameter and 3.5m high. Due to space constraints related to the available height inside the laboratory, the placement of the micropiles into the experimental layout was carried out before the filling of the container with sand.

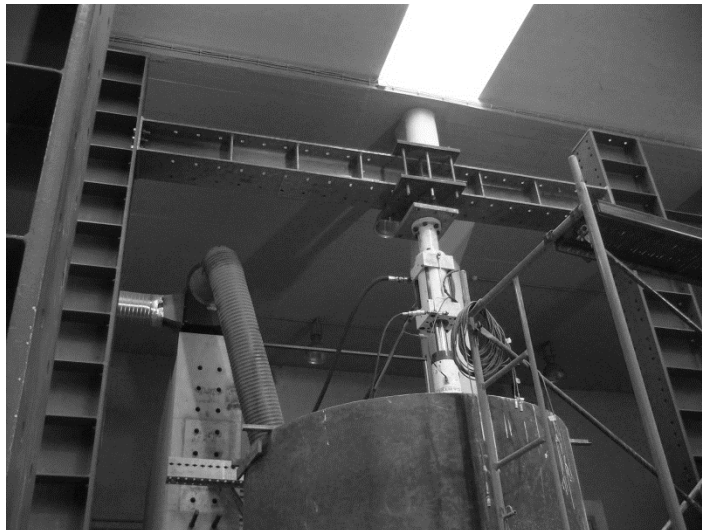


Figure 5.2 – Test layout

The soil container used for this work is composed by a tower segment (manufactured for HISTWIN project (Veljkovic et al., 2012) and improved to be used as a soil container. The

tube is composed by two different segments tightened together. The superposition of the plates is 0.3m.

Figure 5.3 shows the production geometry drawings of both sections and Figure 5.4 shows the final result of the soil container fully assembled.

The bottom plate is composed by normal round holes with a total height of 1.3m and a diameter of 2m. The steel used in that plate is S355 with a thickness of 14mm. In the bottom of this plate is welded a square plate also with a thickness of 14mm with 4 holes to allow the discharge of the soil.

The top plate is composed by long open slotted holes and also presents a 2m diameter and a thickness of 14mm with S355 steel. The height of this part is 2.5m.

The load was applied using a 20 tons Dartec actuator and a steel reaction frame. This actuator is provided with 2 unidirectional hinges, one on each end, placed orthogonally in order to simulate the behavior of a 3D hinge (see Figure 5.5).

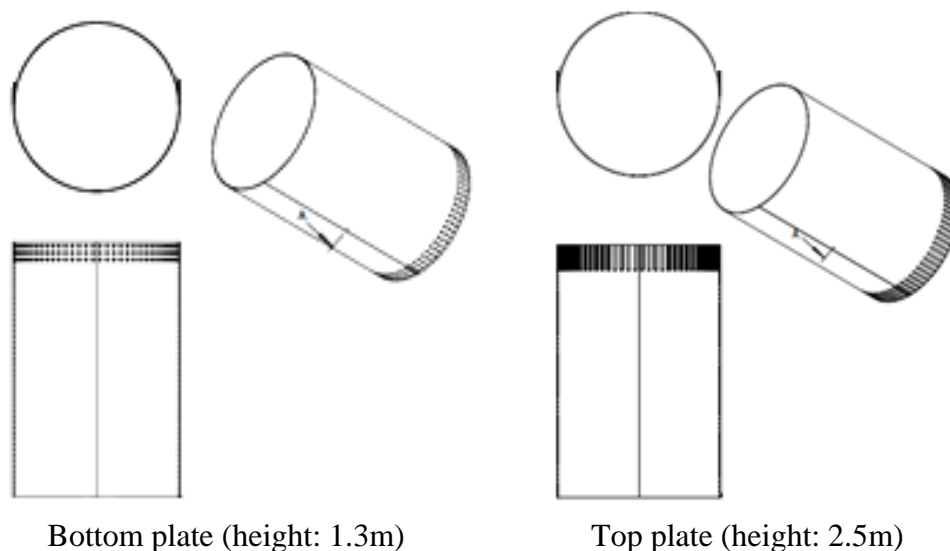


Figure 5.3 - Soil container geometry

The reaction frame considered for this layout is composed by 2 columns with a cross section of HEB500 and 6.5m high and a beam with a section of HEB300 with a length of 3.7m. All members are reinforced.

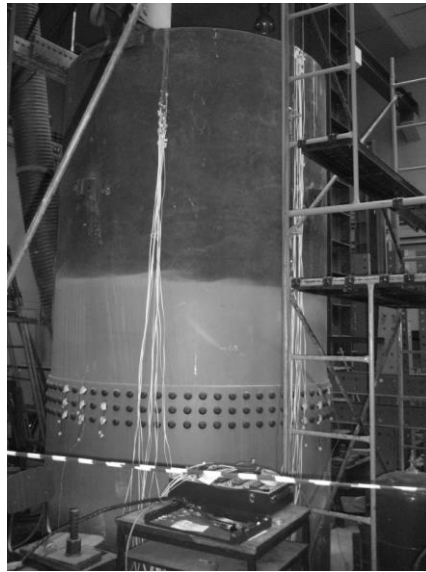


Figure 5.4 - Soil container



Figure 5.5 - 20 tons (200kN) actuator

The assembly procedure consisted on the following steps:

- Instrumentation of the micropiles (Figure 5.6) and placement of the grout exit holes protection rubber ring according to Figure 5.7;

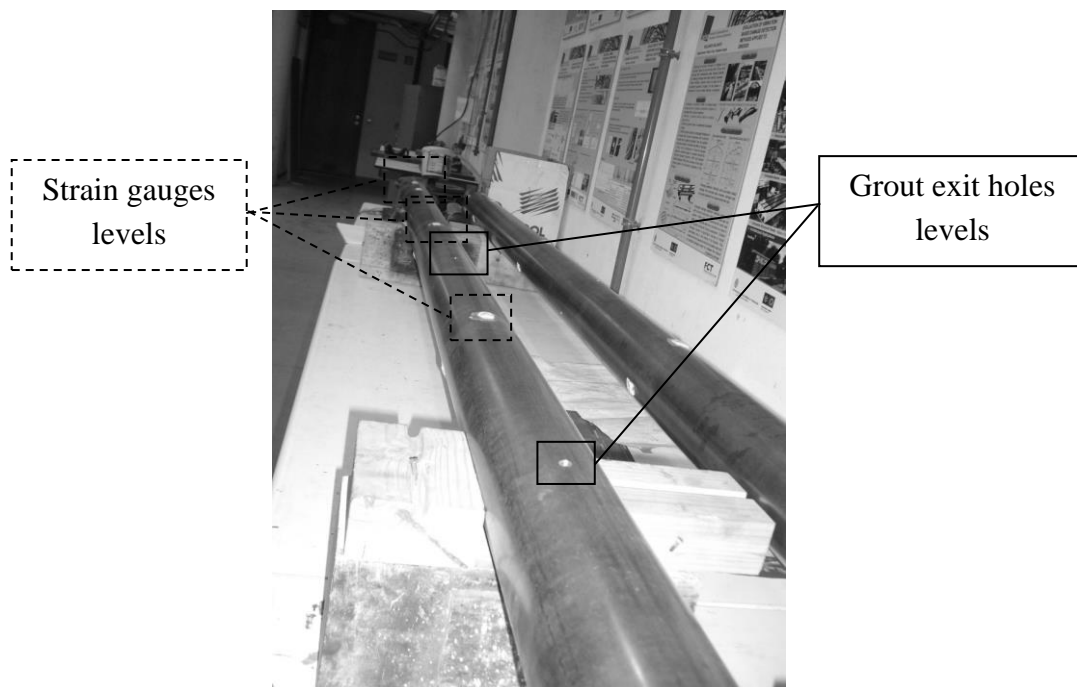


Figure 5.6 - Micropile preparation (instrumentation and drilling)

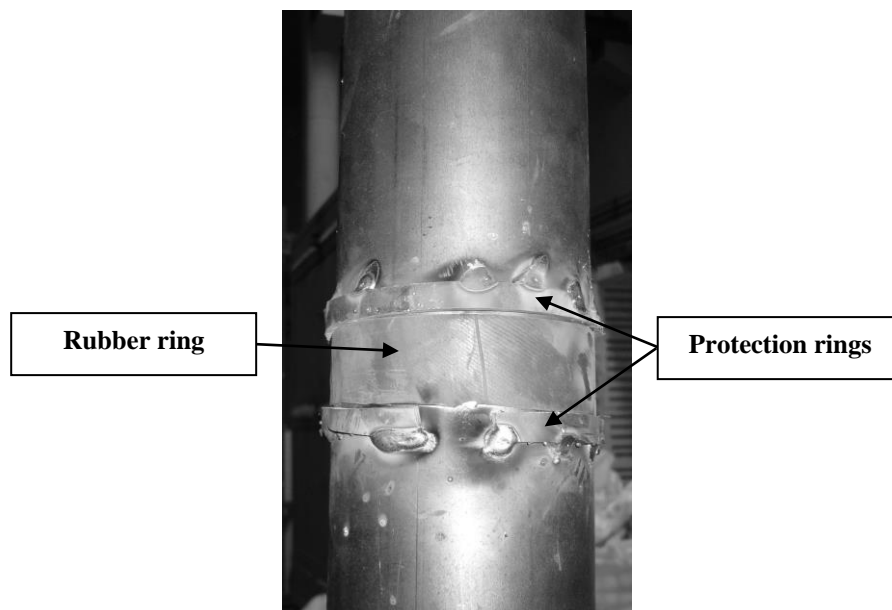


Figure 5.7 - Grout exit holes protection (tube à manchette)

- Placement of the micropiles into the soil container according to the positions of Figure 5.8;

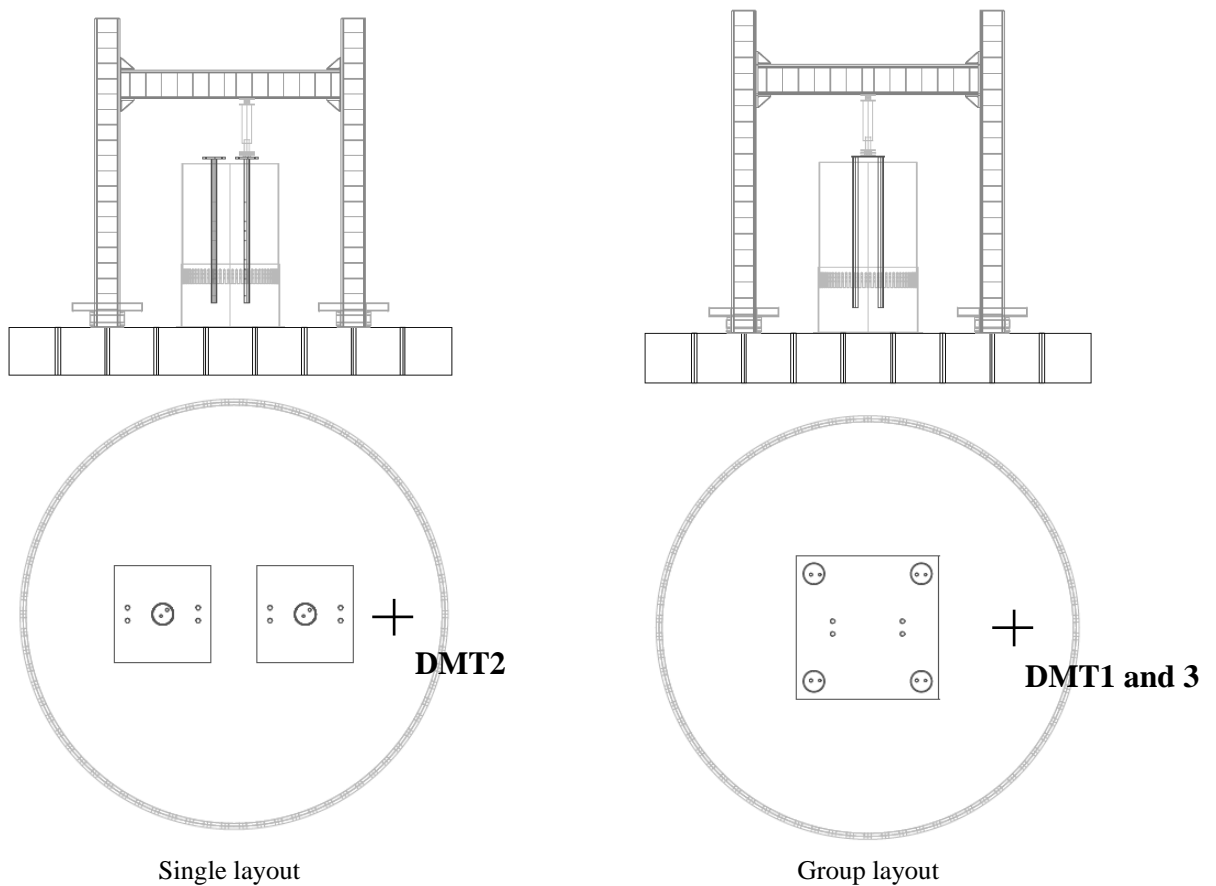


Figure 5.8 - Micropile positions in layouts – front and top view

The micropiles are placed and leveled into position in order to receive the sand around, into the soil container. Figure 5.9 shows the levelling and positioning procedure.

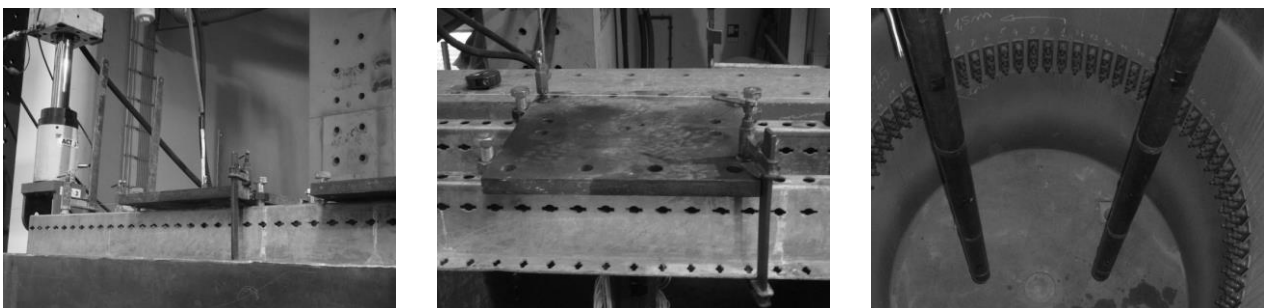


Figure 5.9 - Micropiles placing and levelling system

- Filling of the soil container including registration of the soil weight;

The sand is placed into the soil container around the pre-positioned micropiles by using bigbags to lift it. The bigbags are placed on the top of the soil container and are opened in order to allow the soil discharge.

The weight of the sand placed is known as well as the height of the sand and with it, it is possible to estimate the medium value of the soil density.

Figure 5.10 shows the soil loading procedure.



Figure 5.10 - Soil loading process

- Load tests of the ungrouted micropiles;

After the soil placement, the ungrouted tests are carried out on the placed micropiles.

The tests are monotonic (compression and tensile) or cyclic (cyclic + compression and cyclic + tension). The loading test apparatus is presented in Figure 5.11.



Figure 5.11 - Loading test apparatus

- Grout injection with the use of the prepared pressuring vessel presented in Figure 5.12, with injection pressure close to 0.2MPa. The injection process is illustrated by Figure 5.13;

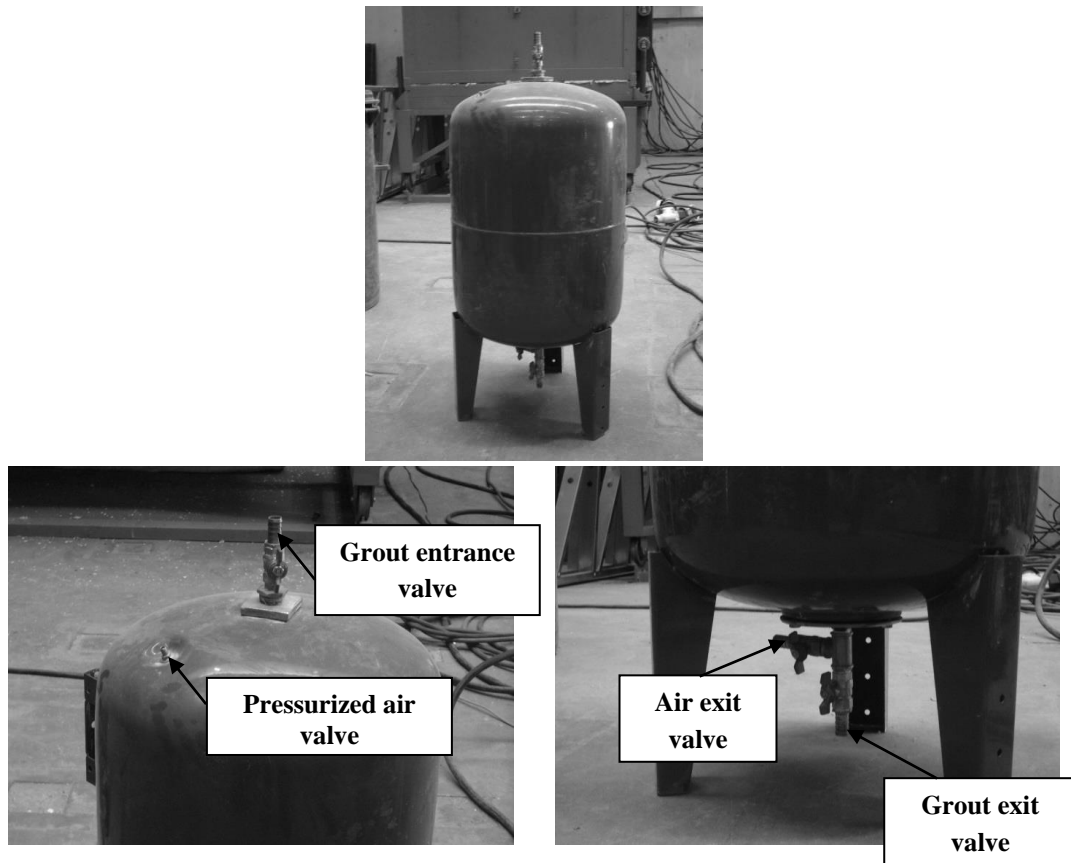


Figure 5.12 - Grout pressure system

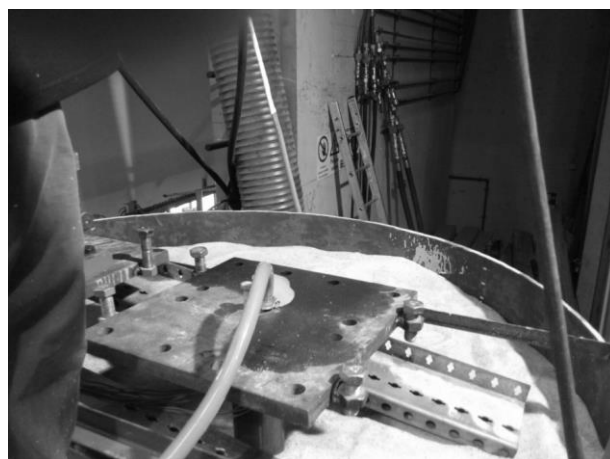


Figure 5.13 – Grout injection process

- Load tests of the grouted micropiles, 7 days after the grout injection;

- Soil discharging and storage for reuse.

When all the tests are accomplished, the soil is discharged from the soil container.

It is discharged by using the slab holes placed below the layout and then the sand is collected to the bigbags. The bigbags are stored into the laboratory and are ready, after the weighing, to be used for the sand loading of the soil container for the following layout.

Figure 5.14 shows one ongoing discharge process and Figure 5.15 illustrates the storage of the sand in bigbags in the end of the discharging.



Figure 5.14 – Soil discharging process



Figure 5.15 – Soil storing

Figure 5.16 and Figure 5.17 shows a Gant chart showing the duration for the assembly of, respectively, single and group tests specimens.

Table 5.1 presents a summary of the tests performed according to the type of micropile and loading protocol. The loading sequence was similar for each layout. UngROUTED specimens were loaded first in compression and then in tension. After the grout was injected, the test proceeded in compression followed by tension. In the designations M stands for single micropile while G stands for group. The mean index density of the sand was determined for each layout considering the measured weight as well as the mean volume occupied and the results obtained for each layout are presented in Table 5.2.

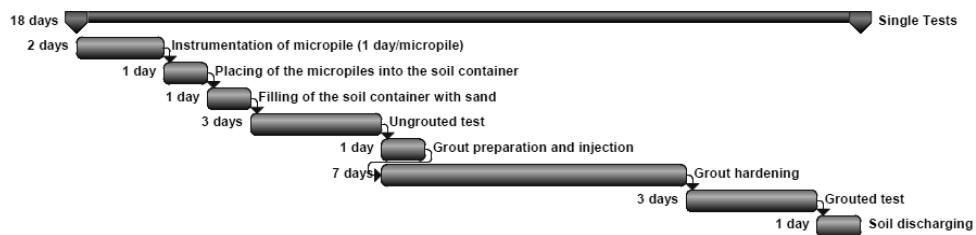


Figure 5.16 – Single tests assembly procedure and duration

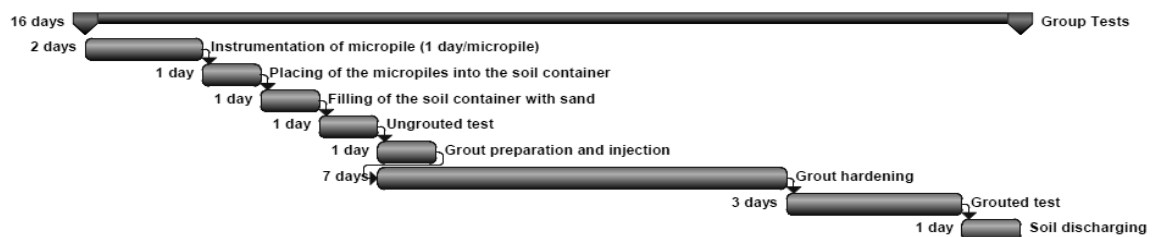


Figure 5.17 - Group tests assembly procedure and duration

In order to compare the behavior of the micropiles under monotonic and cyclic loading, micropiles from layout 2 were tested under monotonic conditions and the remaining layouts were submitted to cyclic loading with the specimen loaded to failure after the final cycle. The loading protocol was based on control of displacements as shown in Figure 5.18. The cycles had a period of 800 sec. each and amplitude of ± 1 mm. Five cycles were applied on all but the tests on micropile M8, where 10 load cycles were adopted to evaluate the effects of the additional cycles on micropile behavior. In the monotonic tests (or after the cyclic loading) the displacement rate was 0.01mm/s for the compression tests and 0.005mm/s for the tensile tests.

Table 5.1 - Experimental tests description

Layout	Micropile	Loading	Grout	Layout	Group	Loading	Grout
2	M3	Compression	No	5	G1 (3B)	Cyclic + Compression	No
		Tension	No			Cyclic + Tension	No
		Cyclic + Compression	Yes			Cyclic + Compression	Yes
		Cyclic + Tension	Yes			Cyclic + Tension	Yes
	M4	Compression	No	6	G2 (4B)	Cyclic + Compression	No
		Tension	No			Cyclic + Tension	No
		Compression	Yes			Cyclic + Compression	Yes
		Tension	Yes			Cyclic + Tension	Yes
3	M5	Cyclic + Compression	No	7	G3 (5B)	Cyclic + Compression	No
		Cyclic + Tension	No			Cyclic + Tension	No
		Cyclic + Compression	Yes			Cyclic + Compression	Yes
		Cyclic + Tension	Yes			Cyclic + Tension	Yes
	M6	Cyclic + Compression	No			Cyclic + Compression	No
		Cyclic + Tension	No			Cyclic + Tension	No
		Cyclic + Compression	Yes			Cyclic + Compression	Yes
		Cyclic + Tension	Yes			Cyclic + Tension	Yes
4	M7	Cyclic + Compression	No			Cyclic + Compression	No
		Cyclic + Tension	No			Cyclic + Tension	No
		Cyclic + Compression	Yes			Cyclic + Compression	Yes
		Cyclic + Tension	Yes			Cyclic + Tension	Yes
	M8	Cyclic + Compression	No			Cyclic + Compression	No
		Cyclic + Tension	No			Cyclic + Tension	No
		Cyclic + Compression	Yes			Cyclic + Compression	Yes
		Cyclic + Tension	Yes			Cyclic + Tension	Yes

Single tests

Group tests

Table 5.2 - Sand index density

Layout	Sand Weight (kg)	γ (kN/m ³)	Index Density (%)
2	15878	16.2	35.3
3	15828	16.0	31.8
4	15791	16.1	33.1
5	15583	15.9	28.1
6	15694	16.0	30.8
7	15953	16.0	31.4

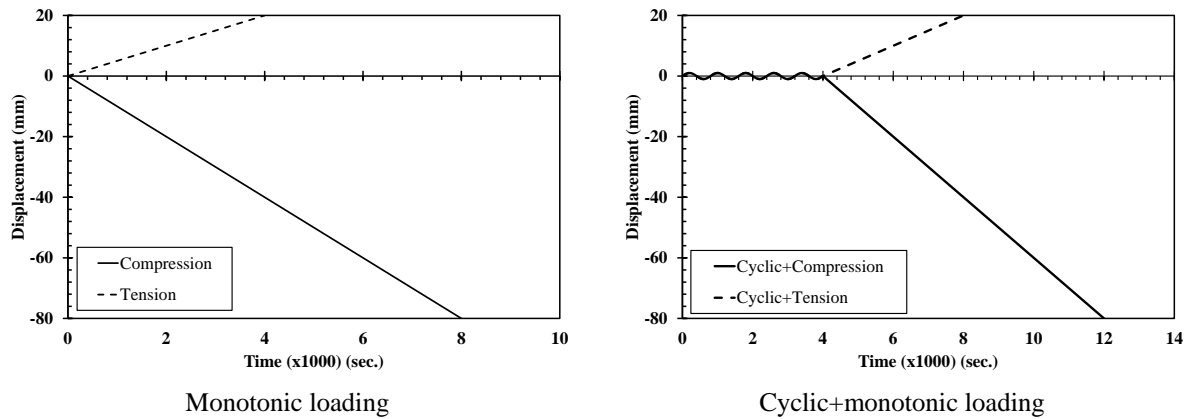


Figure 5.18 - Loading protocols

5.4. Test set-up

5.4.1. Specimen properties

In these tests a S355 steel circular tube with 101.6 mm of external diameter and a wall 3.6mm thick was used. The top plates for the single tests (layouts 2, 3 and 4) and for the G1 group were square, 450mm wide and 30mm thick. The G2 and G3 group top plates were 600x600x40mm³ and 675x675x30mm³, respectively.

The grout exit holes position, number and diameter changed between each layout, in order to obtain a uniform grout distribution along the micropile wall. The diameter on the lower levels was reduced because there was a higher grout flow on those sections. Figure 5.19 and Figure 5.20 show the considered geometry for each single and group layout, respectively.

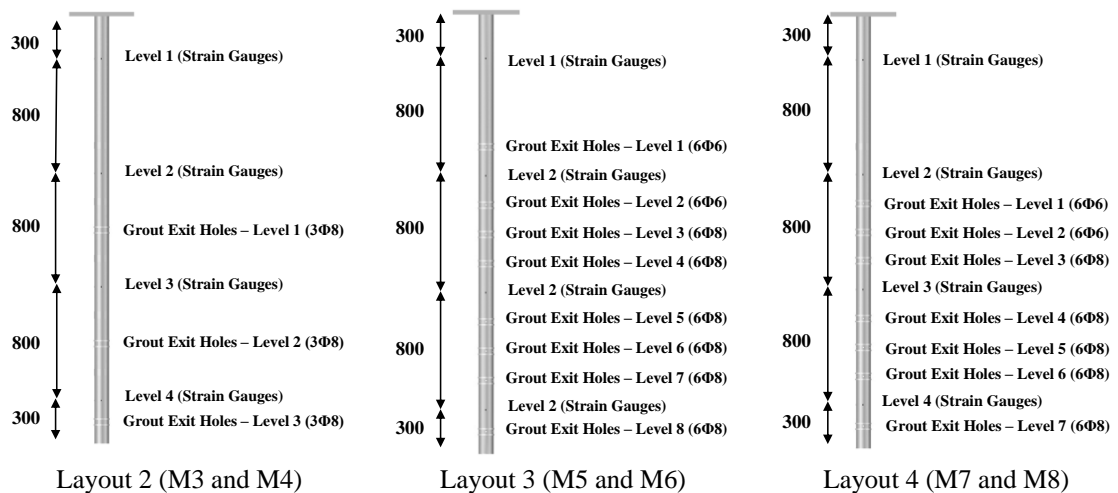


Figure 5.19 - Single specimens geometry

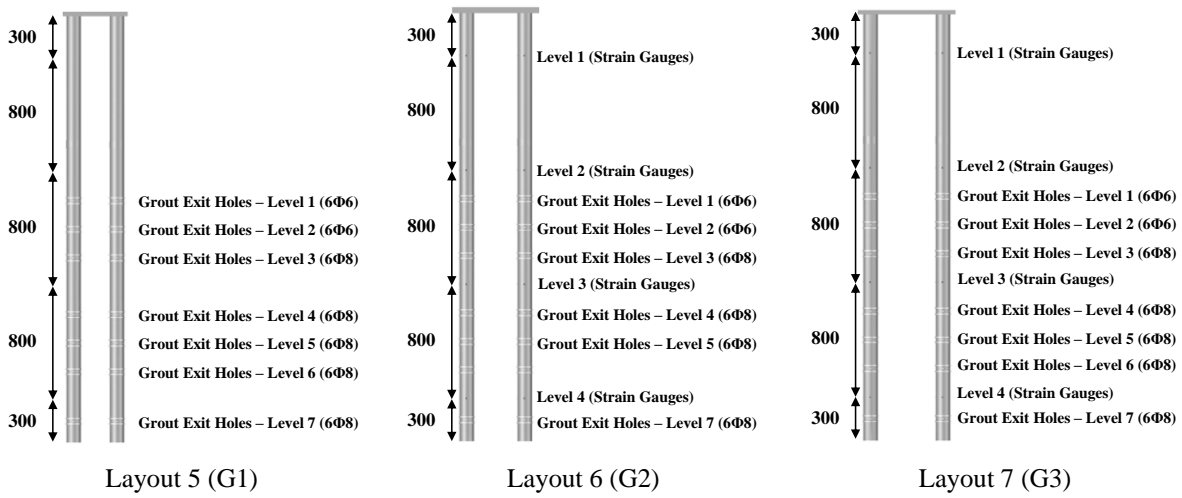


Figure 5.20 - Group specimens geometry

The position of each specimen in each layout as well as the orientation of the strain gauges in the correspondent specimen is presented in Figure 5.21.

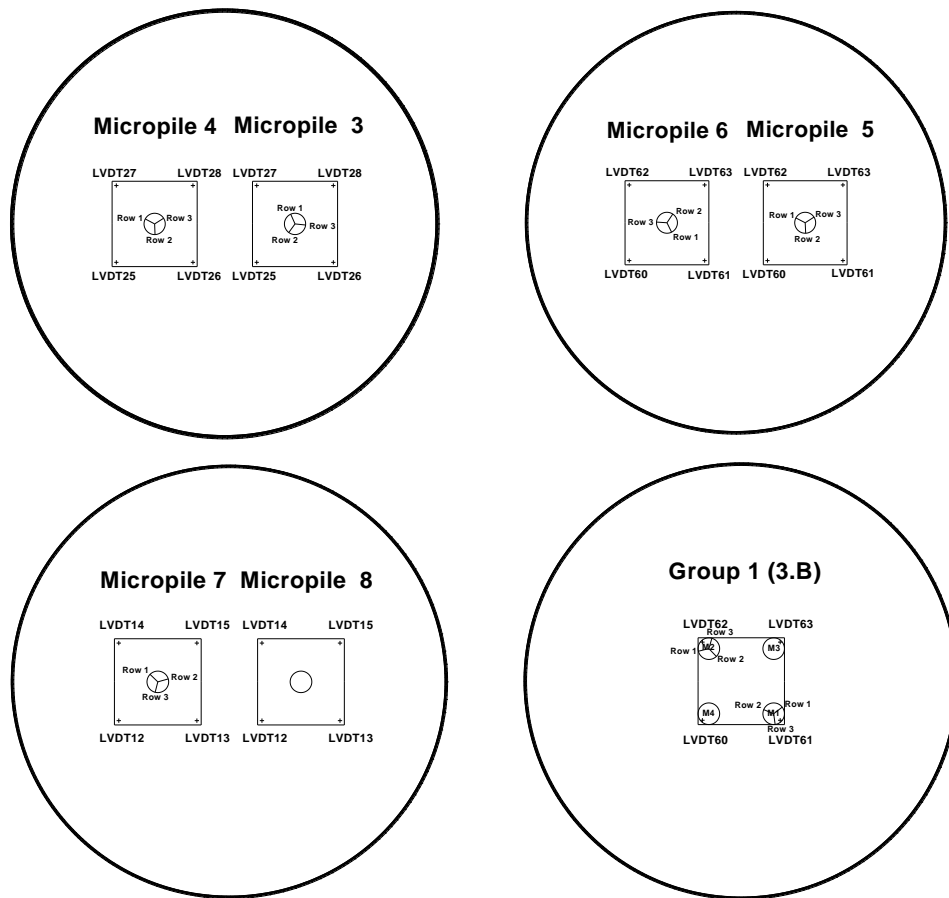


Figure 5.21 – Strain gauges and micropile positions

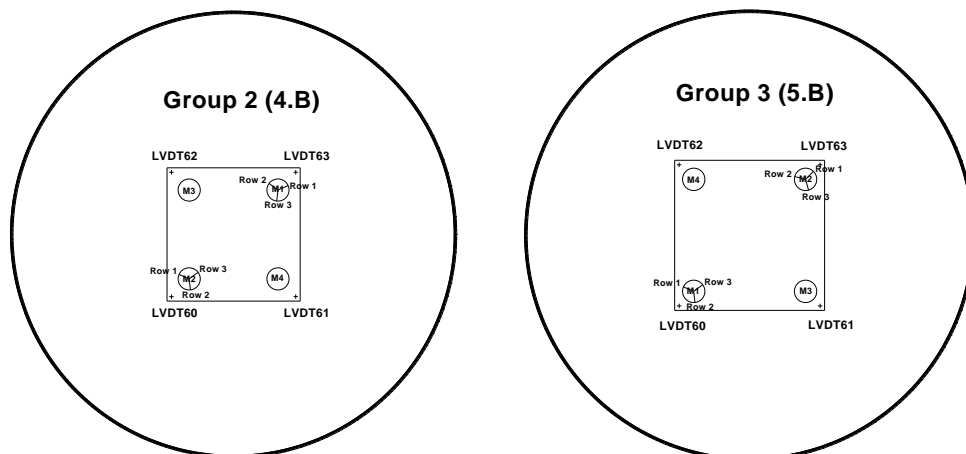


Figure 5.21 – Strain gauges and micropile positions (cont.)

5.4.2. Sand shear behaviour and stress-strain relation and experimental physical and mechanical properties

The soil used in the experimental tests on the micropiles (single and groups) presented in this chapter as well as for the numerical analysis of chapter 6, is a poorly graded sand.

In order to properly understand the behaviour of the micropiles installed in sandy soils it is indispensable to properly understand the stress-strain behaviour of the soil.

The shear strength of the soil can be determined with the well-known the Mohr-Coulomb failure criteria. A given point in the soil mass reaches failure when on a plane the shear stress τ_f is related to the normal stress σ'_f according to the expression (5.1), where c' is the cohesion and ϕ' is the angle of shear strength or friction angle.

$$\tau_f = c' + \sigma'_f \tan \phi' \quad (5.1)$$

Expression (5.1) describes the equation of a line tangent to the Mohr circles at failure according to Figure 5.22.

The shear strength of cohesionless soils depends only on the confining stresses and the friction angle. It should be pointed that for low confining stresses this angle (inclination of the material curve) tends to increase and therefore the proximity between the real envelope and the Mohr-Coulomb failure line is lower in the beginning of the curve, as presented in Figure 5.23. The approximation between the curves should take into consideration the stress range of the problem.

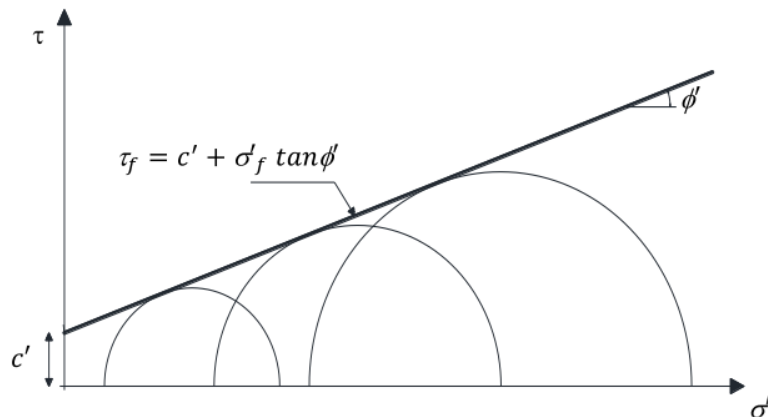


Figure 5.22 – Mohr-Coulomb failure envelope (Matos Fernandes, 2011)

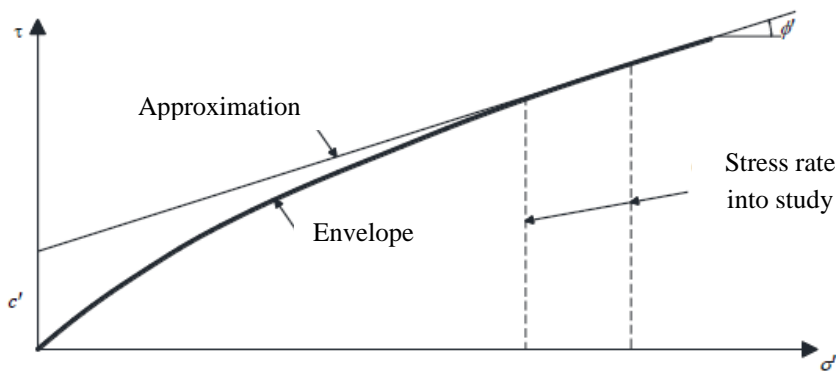


Figure 5.23 – Linear approximation to the rupture envelope (adapted from Matos Fernandes (2011))

The behaviour of sands under shear loading depends of the relative density of the soil and consequently of its void ratio. The characteristic curves for dense and loose sand are presented in Figure 5.24 in terms of deviatoric stress vs. axial strain. Due to the better particle arrangements in the dense sand, it is natural to obtain the higher peak strength depicted in the figure.

In the dense sand curve on Figure 5.24, is possible to observe a peak on the deviatoric stress, named peak strength. It is due to the higher interlocking of the particles and it is followed by a lower strength called residual strength in which the axial strain increases under constant load. For the loose sand there is no identified peak and the strength of the sand is similar to the residual strength of the dense sand. The strength of the loose sand increases with the increase of the axial loading due to the increase in the soil density while for the dense sand there is a reduction in the strength due to the “breaking” of the particles arrangement. This comments are illustrated in Figure 5.25 for the evolution of the volumetric strain where a small contraction can be found in the very beginning of the loading of the dense sample followed by a large expansion, while for the loose sample a contraction is found during the entire loading.

The void ratio also follows this pattern with a reduction in the loose sand and an increase in dense sample until the critical value (e_{crit}) is reached.

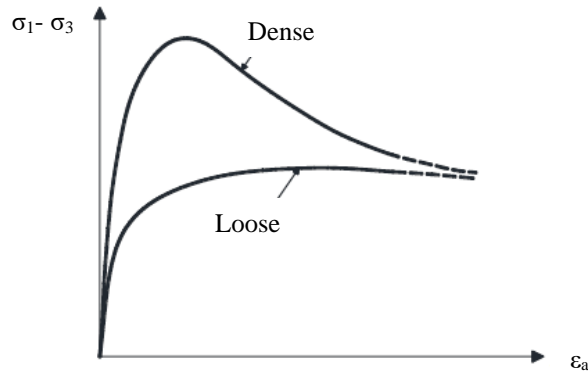


Figure 5.24 – Deviatoric stress evolution in triaxial tests (adapted from Matos Fernandes (2011))

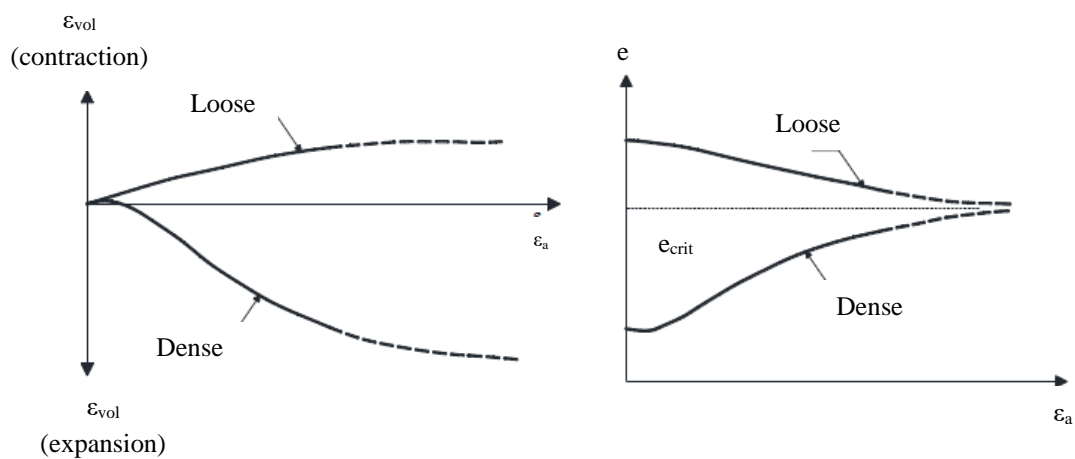


Figure 5.25 – Evolution of the volumetric strain and void ratio with the axial strain – drained triaxial test (adapted from Matos Fernandes (2011))

The behaviour represented in Figure 5.25 is related with the fact that the soils present a high deformation capacity when subjected to shear loading. This property is named dilatancy (ψ) and it is defined as the angle between the displacement vector and the shear plane (positive or negative). The definition of the dilatancy angle can be represented by the diagram of Figure 5.26.

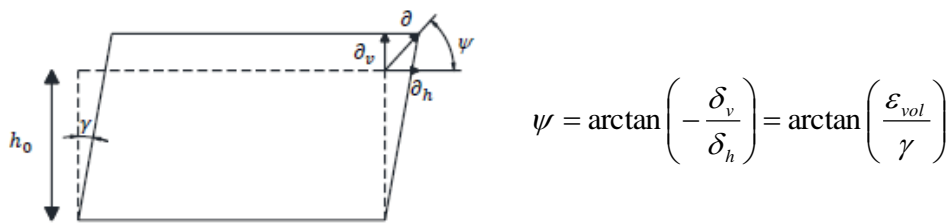


Figure 5.26 – Definition of the dilatancy angle (Matos Fernandes, 2011)

The dilatancy effect can be understood with an analogy proposed by Bolton (1986) and illustrated by Figure 5.27.

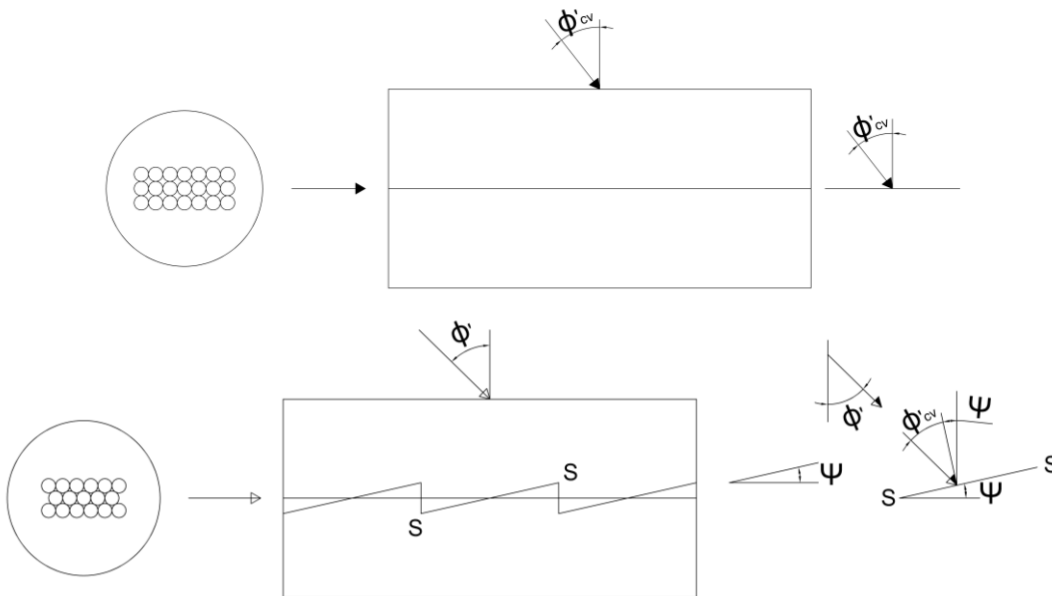


Figure 5.27 – Analogy for dilatancy (without and with positive dilatancy) (Bolton, 1986)

The value ϕ'_{cv} is the friction angle for constant volume (also known as critical friction angle) and it is obtained for the critical void ratio. It is obtained for the sand residual strength. According to the model presented in Figure 5.27, the value for the dilatancy is related with both friction angles according to expression (5.2).

$$\psi = \phi' - \phi'_{cv} \tag{5.2}$$

The last relevant parameter to define the behaviour of sands is the elasticity modulus. The modulus can be defined as initial tangent (E_i) or at any given point of the curve (E_t) and it is also common to define a secant stiffness to different stress levels (E_s), commonly 50% and 80% of the maximum stress. The representation of each one of the moduli is presented in Figure 5.28.

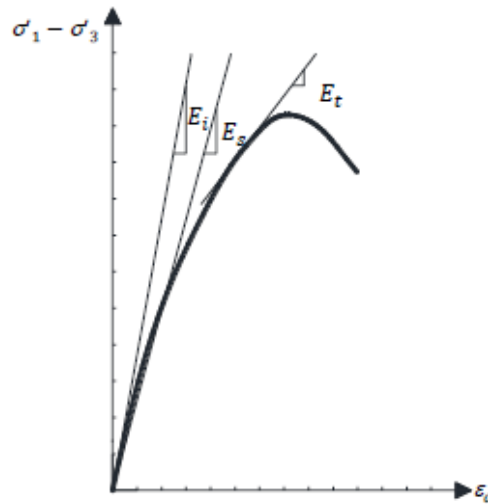


Figure 5.28 – Secant and tangential modulus (Matos Fernandes, 2011)

The Poisson coefficient ν is defined by the ratio between the axial and radial deformations $\nu = -\delta\epsilon_r/\delta\epsilon_a$. The relation between the elasticity modulus and the distortion modulus is dependent on the Poisson coefficient and it is given by equation (5.3).

$$G = \frac{E}{2(1 + \nu)} \quad (5.3)$$

The soil used in the tests is a poorly graded sand (SP). The particle size distribution curves, obtained for several samples, are shown in Figure 5.29. Minimum and maximum values for the unit weight were determined according to ASTM D4253-00 (2000). Specific gravity was also determined according to ASTM 854-05 (2005) and NP-83 (1965). The main physical properties obtained for the considered sand are presented in Table 5.3 and were determined by Coelho (2011). Triaxial tests were conducted by Coelho (2011) and Ferreira (2014) to determine the soil mechanical properties, considering four different soil densities and the results obtained are presented in Table 5.4 and Figure 5.30, superimposed to Schmertmann's (1978) chart.

The average density index (I_d) of the sand was determined considering the measured sand weight used in each layout divided by the correspondent volume occupied taking into account an average height of the soil inside the container. The interval confidence for the index density presented is $\pm 3\%$ for each test.

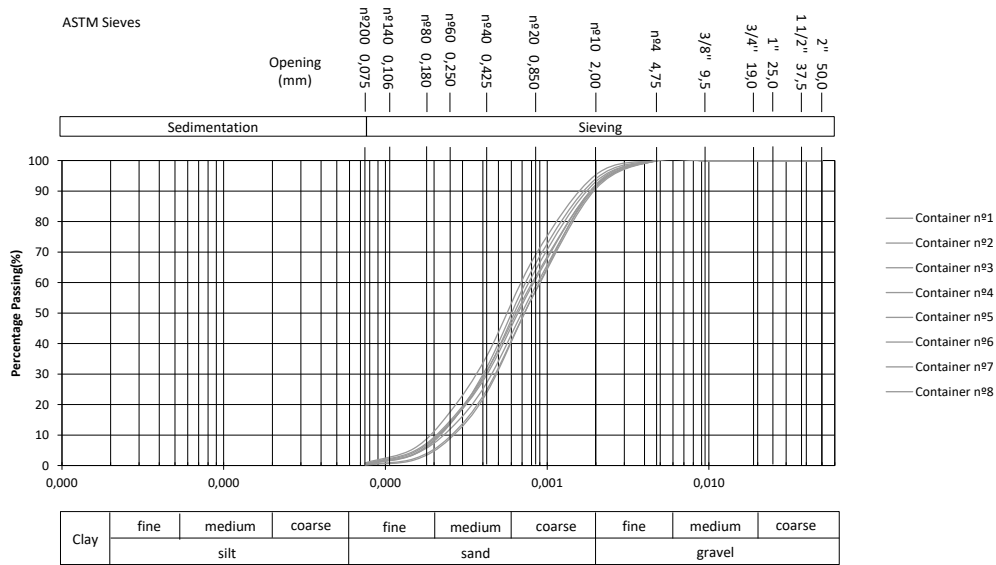


Figure 5.29 - Sieve analysis curves (Coelho, 2011)

Table 5.3 – Soil physical properties (Coelho, 2011)

$\gamma_{d,min}$ (kN/m ³)	$\gamma_{d,max}$ (kN/m ³)	ρ_{min} (gr/cm ³)	ρ_{max} (gr/cm ³)	ϵ_{max}	ϵ_{min}	G _s
14.7	18.9	1.50	1.93	0.76	0.37	2.64

Table 5.4 – Friction angle and elasticity modulus (triaxial tests)

ρ (g/cm ³)	ϕ (°)	Confining Stress (kPa)	E_{tan} (MPa)
1,58 ⁽¹⁾	33,8	50	10,26
		100	18,83
		200	33,85
1,63 ⁽²⁾	36,3	50	22,58
		100	46,74
		200	56,67
1,73 ⁽¹⁾	37,1	50	23,41
		100	51,15
		200	104,33
1,75 ⁽²⁾	44,0	50	37,12
		100	55,02
		200	87,59
1,88 ⁽¹⁾	44,7	50	77,70
		100	94,80
		200	158,21

⁽¹⁾ obtained by Coelho (2011)

⁽²⁾ obtained by Ferreira (2014)

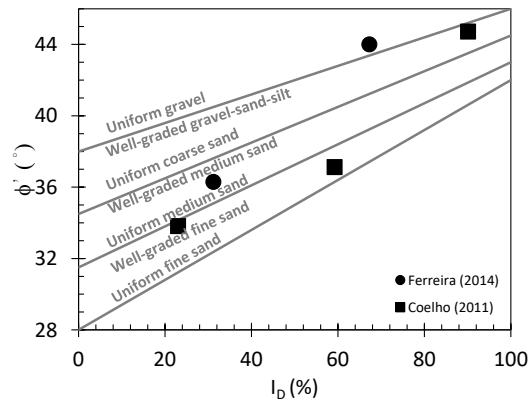
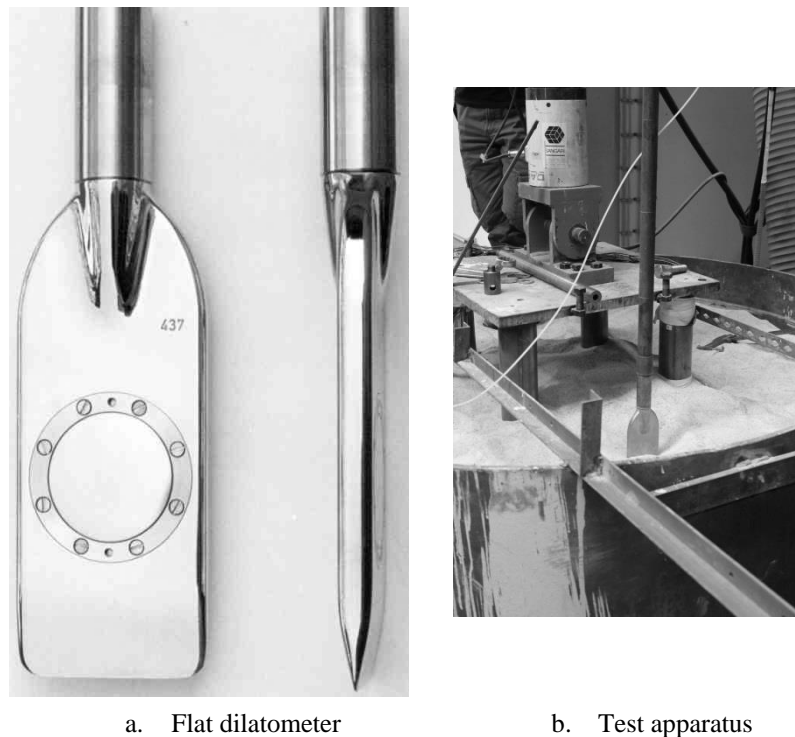


Figure 5.30 - Friction angle vs. density index (triaxial tests) (adapted from Schmertmann (1978))

Flat Dilatometer Tests (DMT) were performed in three layouts in order to better characterize the sand placed in the soil container. Figure 5.31b shows the application of the process on one of the layouts tested. The soil parameters estimation based on DMT tests is presented in Annex D.



a. Flat dilatometer

b. Test apparatus

Figure 5.31 - DMT tests

The DMT1 and DMT2 tests were performed in layouts 7 and 4 respectively, both after the grout injection. The DMT3 test was performed on layout 5 after the ungrouted tests on the G1 group and before grouting took place.

From what was observed during the tests and by the analysis of the results presented on Figure 5.32, it is possible to state that the sand properties improved after the grouting process, due to the increasing horizontal confining pressure. Test DMT3 was performed before grouting and presents lower readings (p_0 and p_1) and soil parameters than DMT1 and 2.

The DMTs carried out on grouted layouts allowed a measurement of the properties along all the height because of the confining pressure caused by the sand in the blade membrane. On the ungrouted layout that did not happen. It can be observed in Figure 5.32 that at some soil depths it was not possible to obtain readings because of the low confinement obtained.

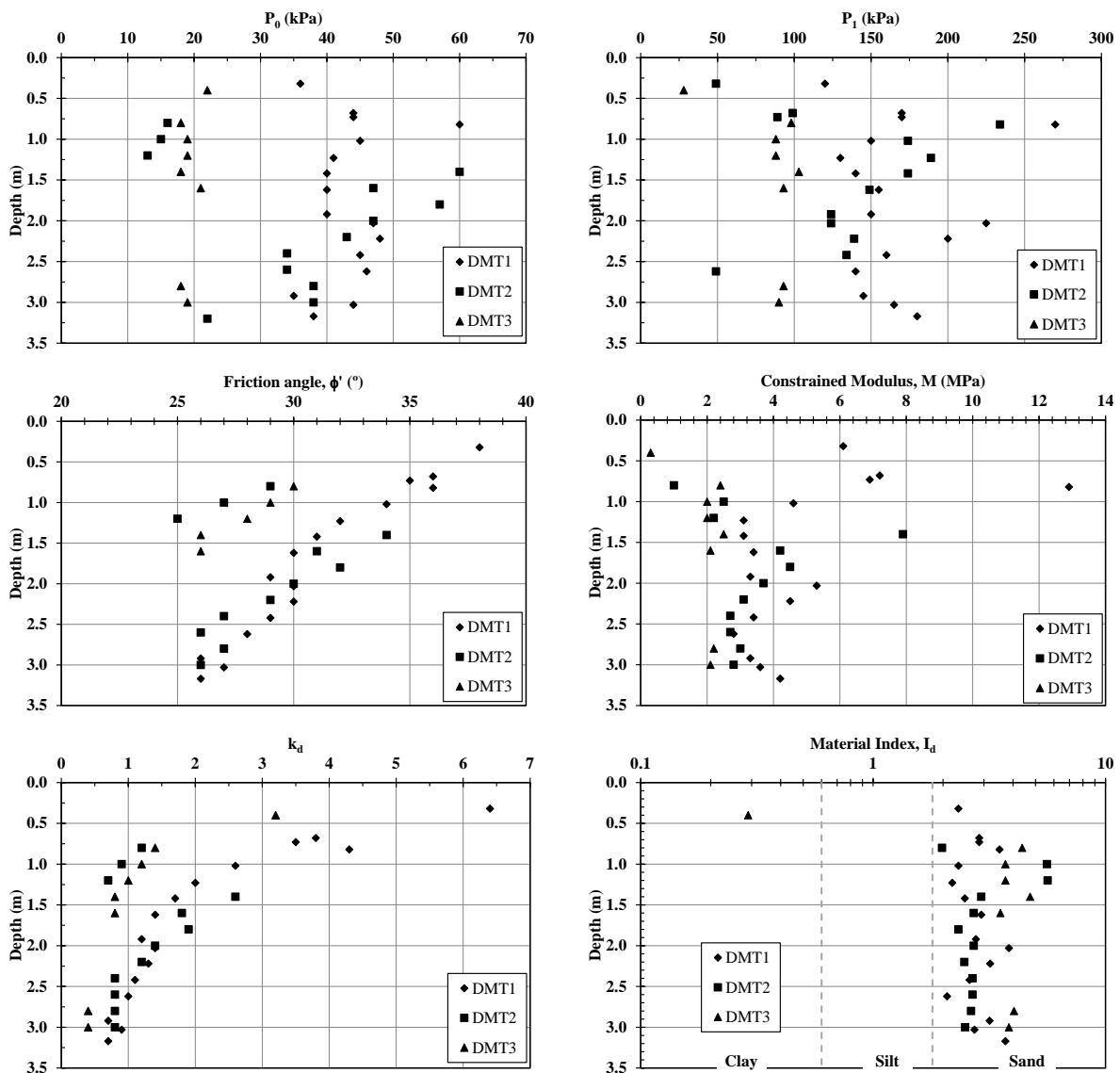


Figure 5.32 - DMT results

5.4.3. Grout properties

For these experimental tests, the grout composition was kept constant between each layout.

The following mix proportions were adopted, similarly to the composition adopted by Veludo et al. (2012): water/cement ratio 0.4, with type II: 32.5N Portland cement, 1% of modified polycarboxylate admixture (high range water reducer); and 1% of expansive admixture.

Tests were carried out in order to control some properties of the grout such as fluidity, exudation, volume variation and compression resistance. In Figure 5.33 are presented the results obtained for each test performed in each layout as well as the correspondent limit provided by the proper standard (NP EN 447, 2008).

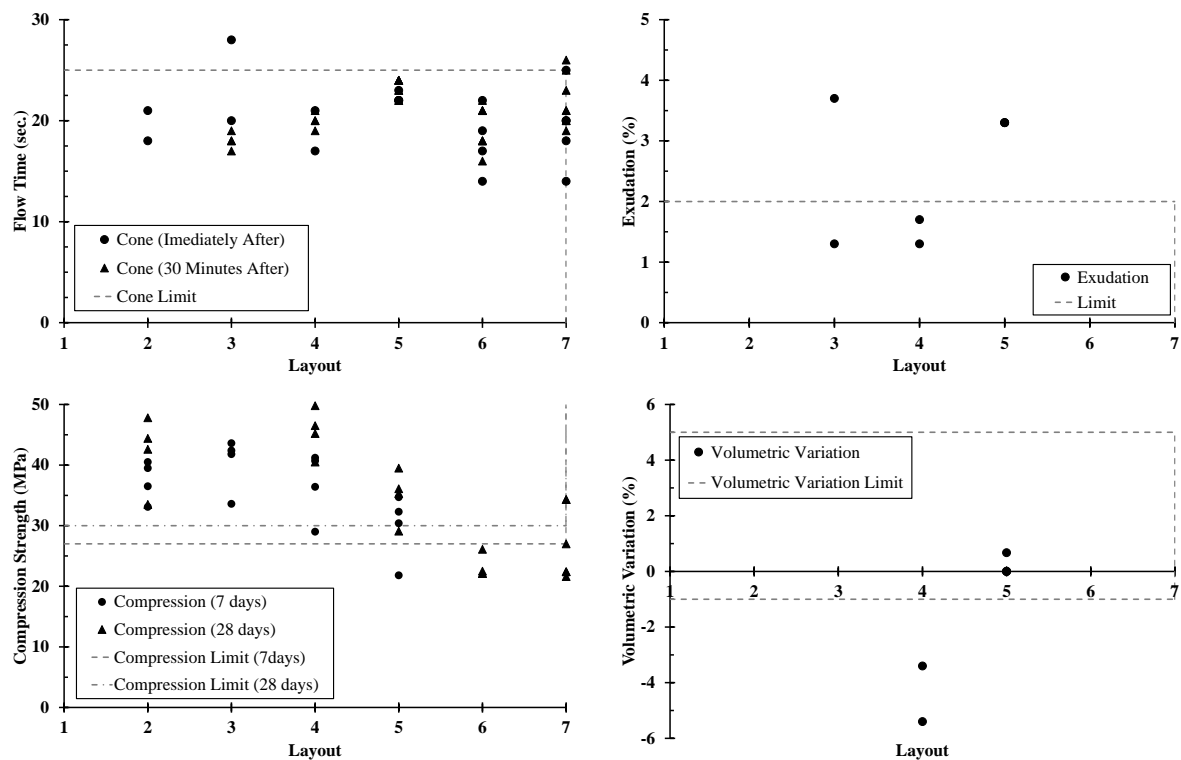


Figure 5.33 - Grout control tests results

In the fluidity tests it was used the cone method according to EN 445 (2008). From all the fluidity tests performed (54 tests), only two of them (one on M5 and another on one micropile of G3) presented results higher than 25 sec. (28 sec. and 26 sec. respectively).

The concept behind the cone test is to evaluate the grout fluidity. It is made using a standard funnel (Figure 5.34) and consists in measuring the time that takes to drop 1l of grout. The results of those tests are presented on each layout result. It is recommended to obtain a time less or equal than 25 sec.

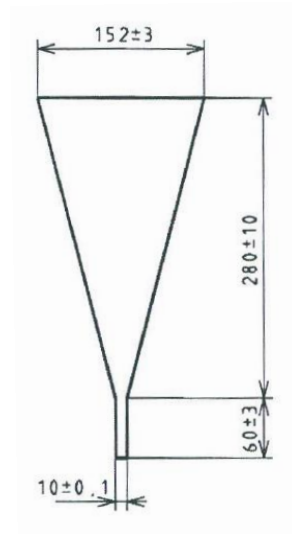


Figure 5.34 – Marsh cone standard measures

For the exudation test, a 50 mm diameter beaker was used, as specified by the EN 445 (2008). This test was considered only for layouts 3, 4 and 5 and the results were rather different between them. The results obtained for layout 3 were unsatisfactory for M5 (3.7%) and satisfactory for M6 (1.3%). For layout 4 the results were both satisfactory for M7 and M8 (1.7% and 1.3% respectively) and for layout 5 was unsatisfactory with 3.3% on the three mixtures measured.

The exudation test consists in measuring the drop of the level of cement related to the water for 3h (exudation). For those tests, graduated test tubes are used (in this case with 50mm of diameter). The recommended results are less than 0.3% of variation.

For the exudation tests the percentage of exudation is obtained by $h_1/h \times 100$, with h_1 being the height of the grout after 3h and h the initial height of grout.

The volume variation was controlled according to EN 445 (2008). The results of this test must be comprised between an interval of -1% and +5% according to the stated in EN 447 (2008). This test was carried out only on layouts 4 and 5. The results exceed the limits for layout 4 (-3.4% and -5.4%) and are within the limits for layout 5 (0% for all the 4 mixtures tested).

The volume variation test consists in measuring the drop of the level of grout for 24h. For those tests, some graduated test tubes were used (in this case with 50mm of diameter). The recommended results must stay between -1% to +5% variation.

For the volume variation tests, the percentage is given by $(h_2-h)/h \times 100$, with h_2 the height of the grout after 24h and h the initial height of grout.

Figure 5.35 shows a representation of the equipment for exudation and Marsh cone tests.

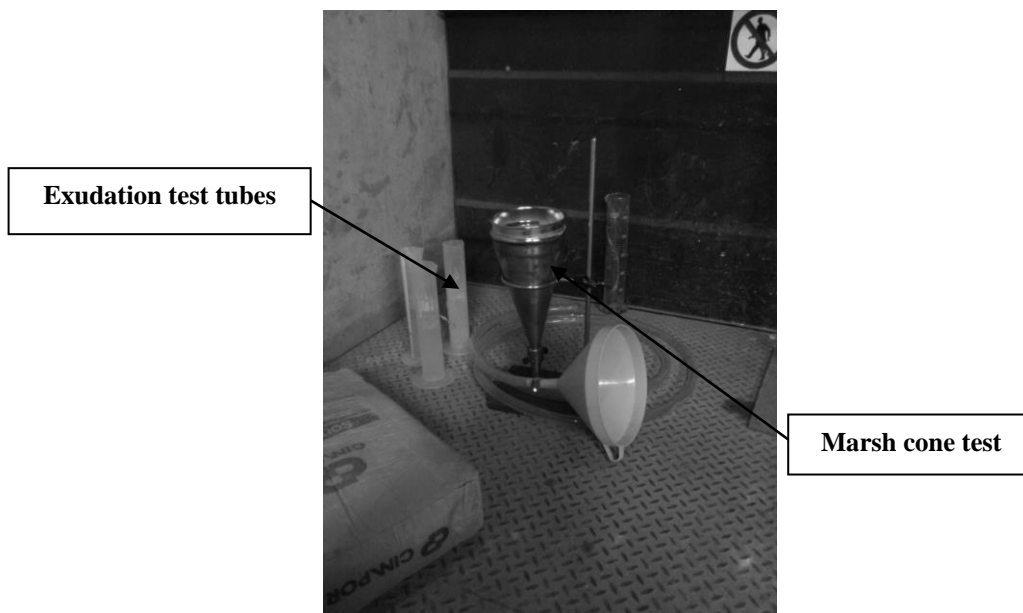


Figure 5.35 – Grout tests equipment

Finally, the compression resistance was determined, according to EN 447 (2008) and EN 196-1 (2006), for all the layouts assembled, both for 7 and 28 days after the mixture and injection. The results obtained were all satisfactory according to limits imposed by the standard (27 MPa and 30MPa respectively for 7 and 28 days), apart the results of layout 6 (22.3MPa and 24.1MPa for 28 days) and in one mixture of layout 7 (22MPa for 28 days). In these two cases it was considered the full cross-section of the mold (1600mm^2) (Figure 5.36) but the exudation was excessive on those specimens which conducted to a considerable soft layer on the top of the specimen (see Figure 5.37) which reduced the effective resistant area.

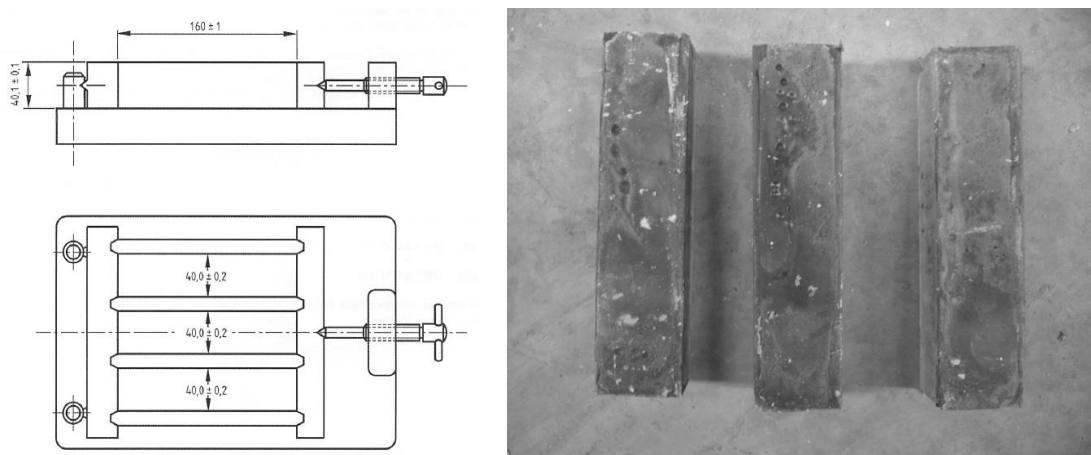


Figure 5.36 – Grout compressive test specimens

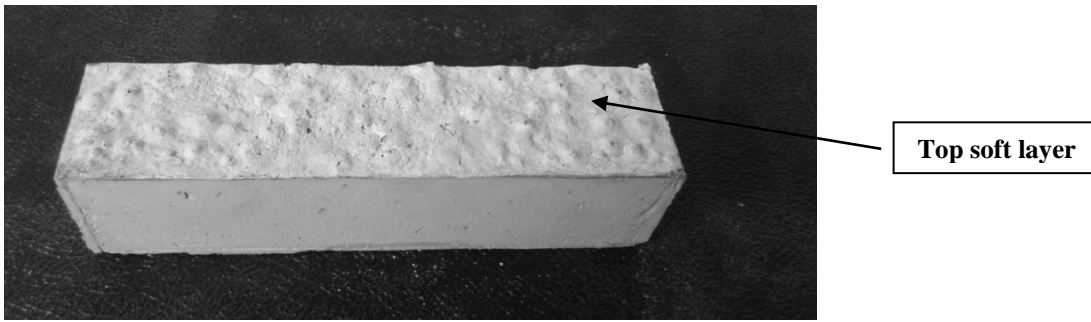
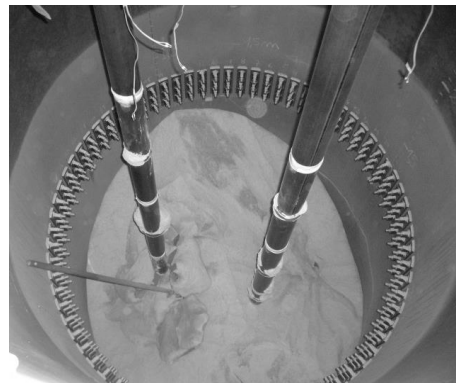
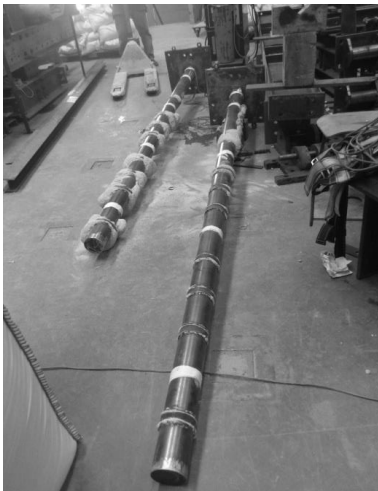


Figure 5.37 – Grout compression specimen appearance

After the tests, the sand was removed, the micropiles were exhumed and the grout distribution was measured and recorded. Similarly to what occurs to production micropiles, there is some scatter in the distribution of the grout from test to test. Figure 5.38 and Figure 5.39 shows an illustration of the obtained geometries for all the considered specimens.



Layout 2



Layout 3



Layout 4

Figure 5.38 - Single tests grout distribution

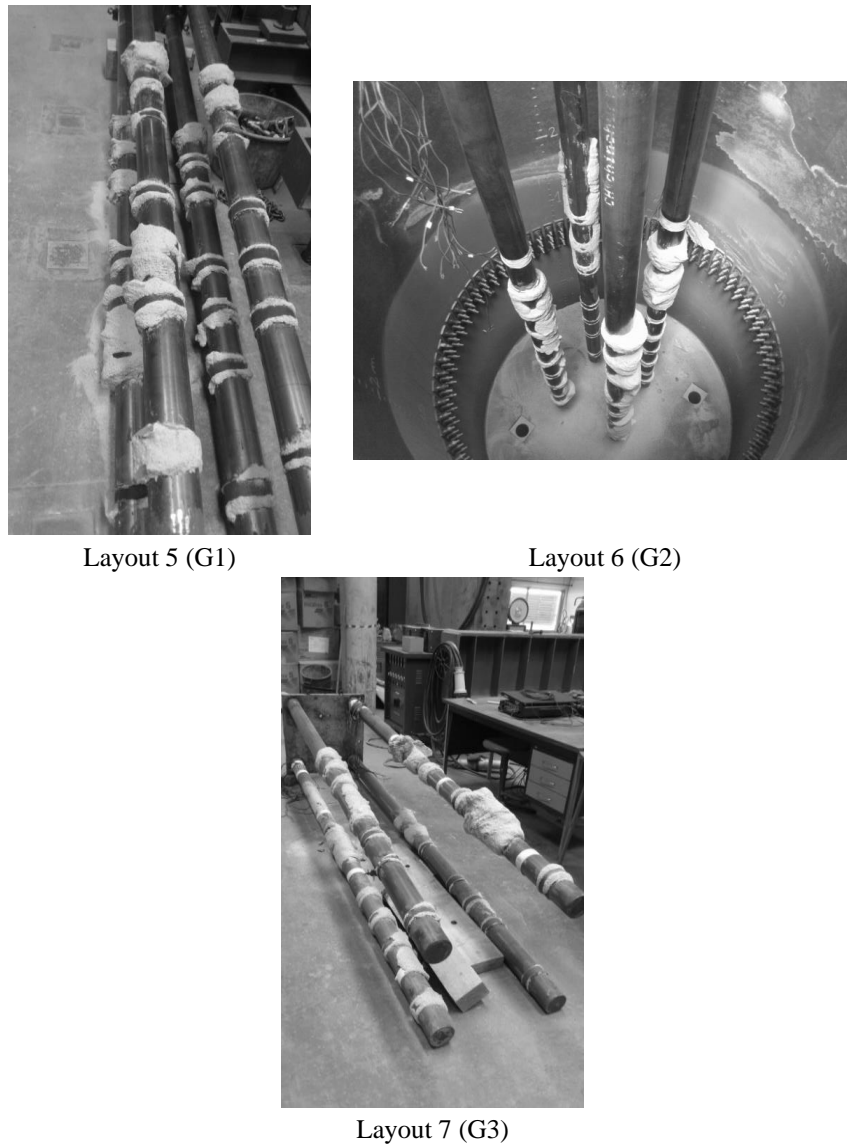


Figure 5.39 - Group tests grout distribution

It was observed that the grout did not come out of the tube in a uniform way. This happened because the sand is so loose that the grout spread more horizontally than vertically along the tube walls, as preferable. In Figure 5.38 and for layout 2, it is also possible to observe a horizontal grout plate that was formed between the two single micropiles.

By the end of the grouted tests and after the disassembling of the layouts, in some cases it was measured the grout placed around the micropile specimens. Table 5.5 resumes the results obtained both in terms of medium diameter for the grouted areas, as well as the total grouted length and the percentage of the grouted length related to the embedded length presented for each specimen before the pressure grouting.

Table 5.5 – Grout geometry

Specimen	Medium grout diameter (mm)	Grouted length (mm)	Embedded length (mm)	Grouted length (%)
M5	163	1010	2740	37
M7	158	1010	2670	38
M8	146	850	2700	31
G1 (3B)	140	725	2690	27
G2 (4B)	147	1123	2690	42
G3 (5B)	142	960	2700	36

5.5. Experimental results

5.5.1. Overview

The experimental results presented here correspond to the force-displacement curves, the resistance and the stiffness measured in each test, both cyclic and static/post-cyclic.

The test sequence was kept unchanged in all layouts prepared. All specimens were tested first without grout in compression (monotonic or cyclic+monotonic) and after in tension (monotonic or cyclic+monotonic). After that sequence, the pressured grout was applied and then compression tests with grouted specimens (monotonic or cyclic+monotonic) were carried out, followed by tension tests (monotonic or cyclic+monotonic).

As it may be observed in Figure 5.19 and Figure 5.20, most of the specimens assembled were instrumented with strain gauges, placed in 4 levels. The results obtained were not satisfactory because the induced strain level was low if compared with the noise level. Due to this fact, the strain results are not used in this analysis.

For the sake of results comparison, it was considered that the failure displacement was 10% of the micropile diameter (10.16mm) for tension tests and 20% of the pile diameter (20.32mm) for compression tests. The difference of the failure displacements is related to the shape of the force-displacement curves where it can be checked that for 10mm of displacement, the tensile capacity is basically fully mobilized while for the compression cases the full mobilization occurs for higher displacements, in the neighborhood of 20mm, due to the influence of the end bearing.

5.5.2. Resistance

Figure 5.40 and Figure 5.41 present, respectively, the global and the cyclic portion of the force-displacement curves obtained for the grouted and ungrouted compression tests.

Similarly, Figure 5.42 and Figure 5.43 show the global and the cyclic portion of the force displacement curves of the tensile tests. It may be clearly observed that the load amplitude during the cyclic phase of the loading is larger for the grouted micropiles which shows the benefit and the improvement due to the grout injection.

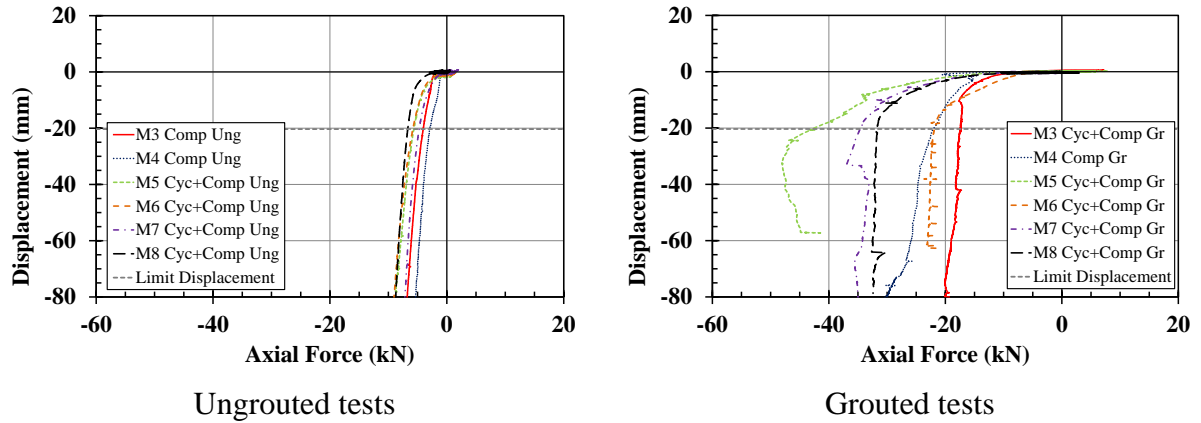


Figure 5.40 - Force-displacement curves (single tests – compression)

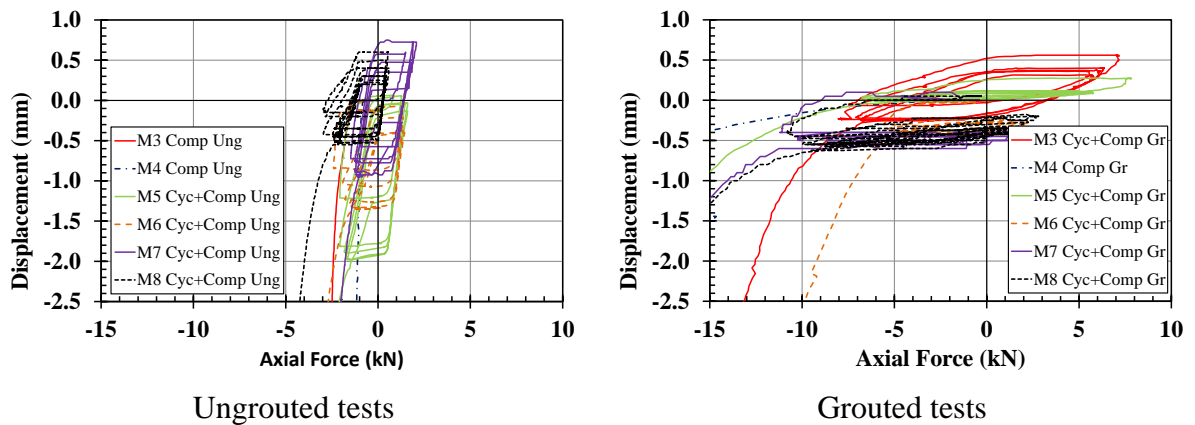


Figure 5.41 - Cyclic detail (single tests – compression)

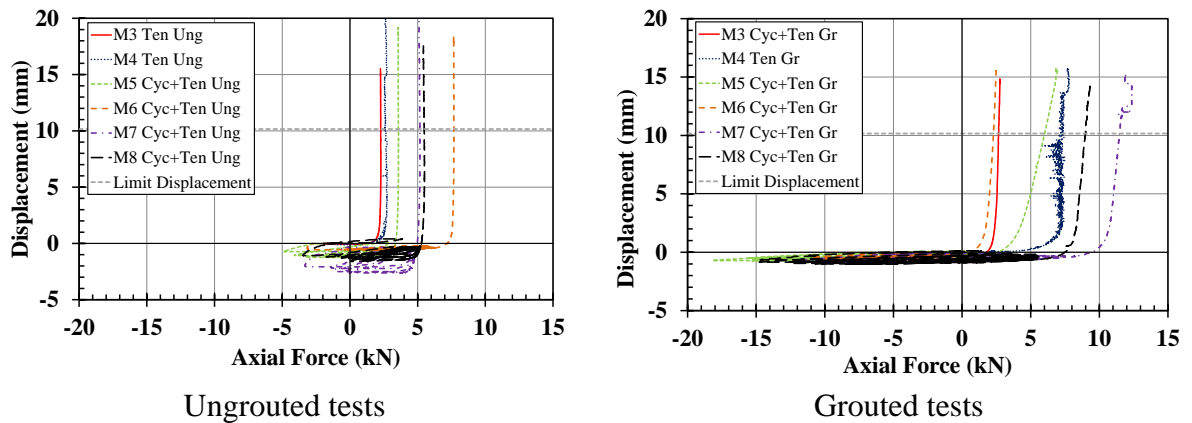


Figure 5.42 - Force-displacement curves (single tests – tension)

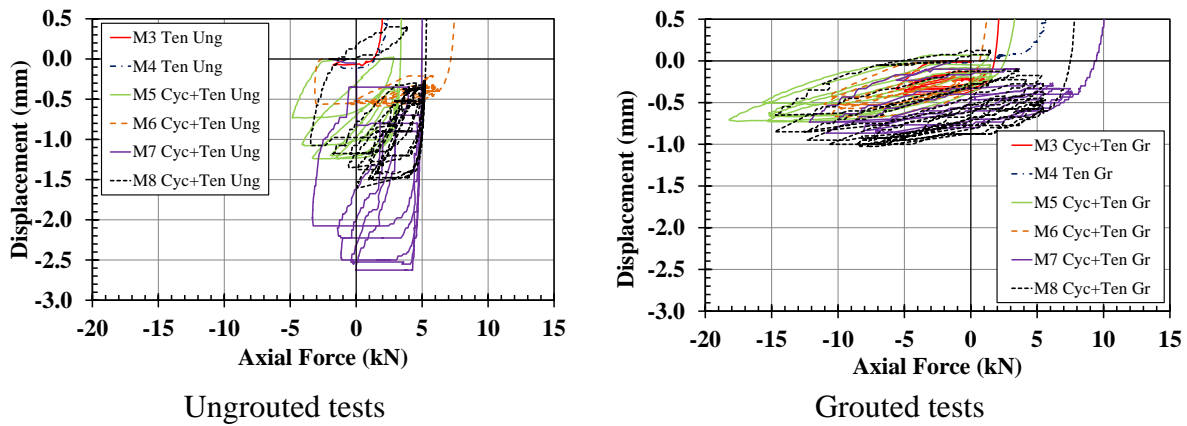


Figure 5.43 - Cyclic detail (single tests – tension)

The global and the cyclic portion of the force-displacement curves of the tests on group specimens are respectively presented on Figure 5.44 and Figure 5.45. The beneficial effects of the grouting may be observed, as the load amplitude during the cycles is, once again, higher for the grouted micropiles.

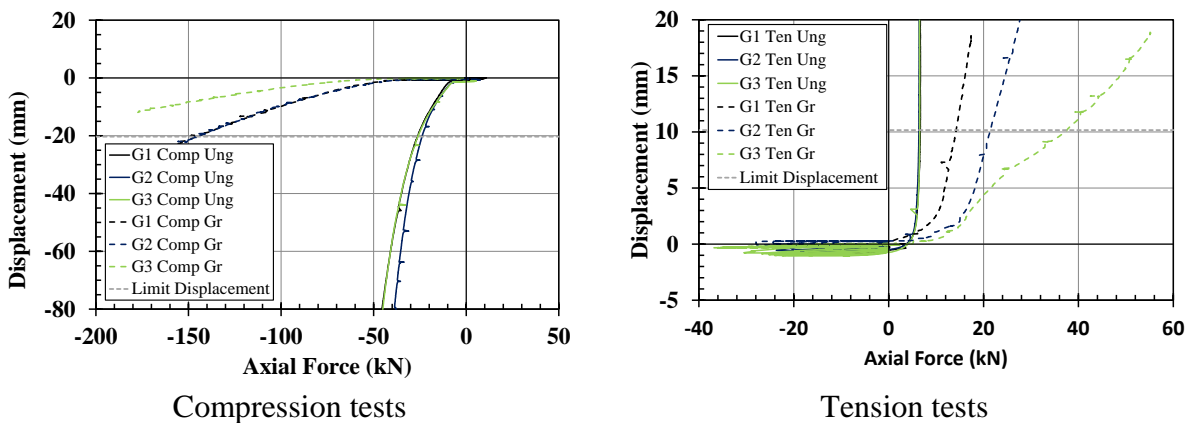


Figure 5.44 - Force-displacement curves (group tests)

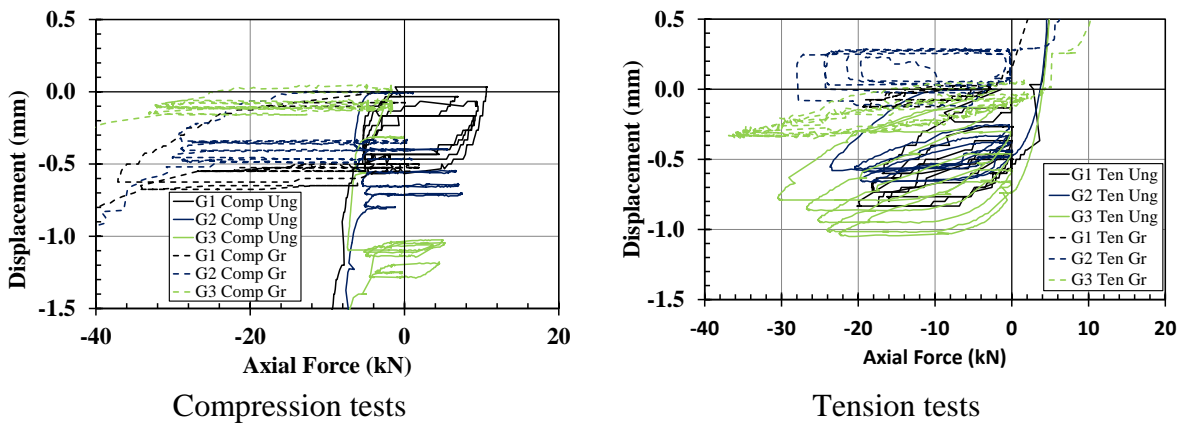


Figure 5.45 - Cyclic detail (group tests)

The results obtained, in terms of resistance and static (or post-cyclic when applicable) stiffness are presented in Table 5.6 and Table 5.7, respectively, for single and group tests. The resistance corresponds to the force obtained for the limit displacement considered for each test according to Figure 5.40, Figure 5.42 and Figure 5.44.

Table 5.6 – Single tests resistance and static/post-cyclic stiffness

Layout	Micropile	Loading	Grout	Resistance (kN)	Stiffness (kN/m)
2	M3	Compression	No	-4.04	662
		Tension	No	2.28	1053
		Cyclic + Compression	Yes	-17.37	8333
		Cyclic + Tension	Yes	2.66	7692
	M4	Compression	No	-2.92	114
		Tension	No	2.53	1220
		Compression	Yes	-22.07	885
		Tension	Yes	7.34	1176
3	M5	Cyclic + Compression	No	-5.66	1724
		Cyclic + Tension	No	3.58	2273
		Cyclic + Compression	Yes	-42.91	14286
		Cyclic + Tension	Yes	6.02	20000
	M6	Cyclic + Compression	No	-5.82	806
		Cyclic + Tension	No	7.68	3571
		Cyclic + Compression	Yes	-21.87	6250
		Cyclic + Tension	Yes	2.29	3448
4	M7	Cyclic + Compression	No	-4.73	1136
		Cyclic + Tension	No	5.17	495
		Cyclic + Compression	Yes	-34.63	6667
		Cyclic + Tension	Yes	11.47	7692
	M8	Cyclic + Compression	No	-6.68	1667
		Cyclic + Tension	No	5.49	1053
		Cyclic + Compression	Yes	-31.81	9091
		Cyclic + Tension	Yes	8.99	7143

According to Table 5.6, the comparison between the grouted and ungrouted specimens shows a substantial improvement on the resistance between 280% and 660% for compression tests on single micropiles. For the tension tests the improvement varies between 20% and 190% of the resistance found on the ungrouted tests (excluding micropile M6, where both the tensile resistances, ungrouted and grouted, are unreasonably different than expected).

Table 5.7 – Group tests resistance and static/post-cyclic stiffness

Layout	Group	Loading	Grout	Group resistance (kN)	Stiffness (kN/m)
5	G1	Cyclic + Compression	No	-26.26	11111
		Cyclic + Tension	No	6.67	12500
		Cyclic + Compression	Yes	-145.96	17544
		Cyclic + Tension	Yes	14.24	16129
6	G2	Cyclic + Compression	No	-23.91	20000
		Cyclic + Tension	No	6.36	20000
		Cyclic + Compression	Yes	-145.47	50000
		Cyclic + Tension	Yes	21.42	12500
7	G3	Cyclic + Compression	No	-26.14	10000
		Cyclic + Tension	No	6.54	7143
		Cyclic + Compression	Yes	(higher than) -177.35	50000
		Cyclic + Tension	Yes	37.57	50000

In the case of the group tests, the improvement on the resistance due to the grouting, varies between 460% and 580% for compression tests while for tension tests the improvement goes between 110% and 470% as it may be seen in Table 5.7.

Apart from M7 single specimen whose compression resistance is unreasonably low and M6 whose tension resistance is unreasonably high, the compression resistance is always higher, as expected, than the correspondent tension resistance. For ungrouted single tests, the compression resistance is 20% to 80% higher than the tensile resistance. For the grouted cases, that difference varies from 200% to 850% of the tensile resistance. It should be stated that for settlements higher than 20mm, the compression resistances on the ungrouted tests on M6 and M7 overcome the values obtained for the tension tests.

For the group tests, the compression resistance is higher from 280% to 300% of the tension resistances for ungrouted specimens, while for grouted it varies from 370% to 900%.

It was also found that for the conditions of these tests, the group spacing effect was not significant for the ungrouted tests. If the results for the G1 group (spacing of 3B) are used as reference, it was obtained, in compression, a reduction of 9% in the 4B spacing and a 0% reduction for 5B. In tension, a reduction of 5% was obtained for 4B spacing and of 2% for 5B spacing.

In the grouted tests the results present some differences but in these cases they are mainly due to the grout distribution along the pile length. In the compression cases, similar results were found for the 3B and 4B groups. For the 5B group, the equipment capacity was reached before the 20mm limit displacement was measured. shows that the load-displacement curve

is stiffer than the obtained for the 3B and 4B tests. For a 10mm displacement, a resistance increase of 61% was found. In the tension tests, an increase of 50% in 4B and 164% in 5B was obtained.

The group effect was observed by the comparison between the single and the correspondent group results. The mean value of resistance for the single compression ungrouted tests is $\bar{R}_{c,single}=5\text{kN}$, while the correspondent mean value for group is $\bar{R}_{c,group}=25\text{kN}$, which results on an efficiency of $\eta=125\%$. For the tension ungrouted cases, the single pile mean resistance was $\bar{R}_{t,single}=3.8\text{kN}$, while the group yielded $\bar{R}_{t,group}=6.5\text{kN}$ and the efficiency was only $\eta=43\%$. Excluding the results from the tests without cyclic prior the monotonic loading (M3 and M4) and M7 due to the unreasonable result, the mean value for the resistance for the single compression ungrouted tests is $\bar{R}_{c,single}=6\text{kN}$ which conducts to an efficiency of $\eta=104\%$, closer to an efficiency of $\eta=100\%$ expected for this situation.

The compression grouted tests provided $\bar{R}_{c,single}=28.5\text{kN}$, for the single specimens and $\bar{R}_{c,group}=145\text{kN}$ for groups G1 and G2 ($\eta=127\%$). The mean tensile resistance obtained for the single grouted tests was 7.3kN while for groups was 24.4 kN ($\eta=84\%$).

Taking into account the comparison between the compression and the respective tensile resistance, it may be observed that for the ungrouted specimens, the ratio $\bar{R}_{t,single}/\bar{R}_{c,single}$ varies between 0.6 and 0.9 (excluding specimens M6 and M7 for the reasons presented before) and between 0.1 and 0.3 for grouted specimens on the single micropiles. The larger differences between the tension and the compression grouted resistances are related to the fact that the tensioned specimens are tested after the compression tests which can lead to a detachment of some grout, reducing that way the tensile resistance.

For the group specimens, values of $\bar{R}_{t,group}/\bar{R}_{c,group}$ close to 0.3 were obtained for ungrouted specimens and of 0.1 to 0.2 for the grouted cases.

The resistances obtained are related to some singularities on the micropiles geometry. In the case of the ungrouted single micropiles it was observed that, the resistances for the layout 2 were lower than for the other two single ungrouted layouts, due to the reduced grout exit holes levels. Those levels and respective protections added extra side resistance to the micropiles. In terms of grouted specimens it was observed that the amount of grout measured, in the end of the tests, around the tube (Table 5.5) is related to the resistance obtained. The M5 micropile is clearly the specimen with more grout around and consequently it provided more resistance than the others. In the case of micropile M3, a horizontal grout plate was created which provided high compressive resistance, but it broke close to the end of the test and the subsequent tensile resistance was low. The M4 micropile presented more grout than the

others, close to the tip of the tube, which improved both the compressive and also the tensile resistance.

The grout distribution on the groups also influenced their resistance. On G1, the compressive resistance was high due to one horizontal plate formed in the middle of the micropiles. It broke after the test, leading to a relatively low tensile resistance. The G2 group presented a higher amount of grout around the piles which improved both the compression and the tensile resistances and G3 presented a grout layer connected to the soil container which improved substantially the compressive and tensile resistances.

Table 5.8 presents the values obtained for the unit skin friction on the tension tests. It is presented, for each test, the percentage of grouted length in comparison with the embedded length, the correspondent medium diameter of the grout and the mean unit skin friction (q_s) for each case. The value of mean unit skin friction presented for the grouted tests refers to the grouted length of the micropile while in the remaining portion it was assumed a value of unit skin friction similar to the value presented for the ungrouted tests.

Table 5.8 – Unit skin friction

Layout	Micropile/Group	Grout	Medium Diameter (mm)	Grouted Length (%)	q_s (kPa)
2	M3	No	101.6	0	2.6
		Yes	156.0 ^a	0 ^b	3.0 ^c
	M4	No	101.6	0	2.9
		Yes	156.0 ^a	35 ^a	11.7 ^c
3	M5	No	101.6	0	4.0
		Yes	163.0	37	7.0 ^c
	M6	No	101.6	0	-
		Yes	156.0 ^a	35 ^a	-
4	M7	No	101.6	0	6.0
		Yes	158.0	38	15.9 ^c
	M8	No	101.6	0	6.3
		Yes	146.0	31	12.9 ^c
5	G1	No	101.6	0	1.9
		Yes	140.0	27	7.1 ^c
6	G2	No	101.6	0	1.8
		Yes	147.0	42	8.5 ^c
7	G3	No	101.6	0	1.9
		Yes	142.0	36	19.3 ^c

^a value not measured – mean value from M5, M7 and M8 specimens

^b assumed value due to the low grout distribution along the pile outside wall

^c mean unit skin friction on the grouted length. The mean unit skin friction on the ungrouted length of the micropile is similar to the value of the ungrouted specimens

The mean unit skin friction ranged from 2.6 to 6.3kPa for the single ungrouted micropiles and from 3.0 to 15.9kPa for the grouted single specimens. For these soil properties, considering a medium density of 1.58 g/cm³, a friction angle of 33.8° and a friction angle between the soil and the ungrouted pile $\delta=20^\circ$, the resulting mean unit skin friction is $q_s=3.8\text{kPa}$. For the grouted micropiles, a value of $q_s=7.0\text{kPa}$ was obtained, considering the same soil properties except the friction angle between the soil and the ungrouted pile of $\delta=33.8^\circ$. Both values of the unit skin friction estimated for grouted and ungrouted tests are located in the interval obtained in the experimental tests.

In the same manner, the unit skin friction varies between 1.8 and 1.9kPa for ungrouted group specimens and between 7.1 and 19.3kPa on the grouted group cases.

The observation of Table 5.8 shows that the unit skin friction of the piles in the groups is lower than the determined for single micropiles and that is the reason why the group efficiency in tension is lower than 100%. The explanation to this fact lies on the pile installation procedure. As the groups were placed prior to the sand, the access to pluviated the sand on the central area between the piles was limited, and the sand was likely on a looser state, conducting to lower friction angles and consequently to lower values of the unit skin friction.

5.5.3. Stiffness

In terms of monotonic stiffness (k_m), measured after the cyclic phase as shown on Figure 5.46, it was observed in Table 5.6 and Table 5.7 that the values obtained are higher for grouted than for ungrouted tests, both for single and for group specimens, as expected. The estimation of the monotonic stiffness is based on the illustration of Annex E. The effect of the grouting on the stiffness of the single micropiles conducts to a variation between 1.0 and 15.4 between grouted and ungrouted. For the group tests, the same variation goes between 1.3 and 7.0 (excluding G2 where the tensile grouted stiffness is unexpectedly lower than the correspondent ungrouted). The improvement caused by the grout is more prominent on the single micropiles than in the group.

Considering the mean value of the monotonic stiffness of the single micropiles without cyclic loading and comparing it with the mean value of the monotonic stiffness of the single micropiles with cyclic loading, a lower value for the tests without cyclic loading was obtained. The values obtained for the ratio of stiffness's were comprised in the interval of 0.1 to 0.6. However it is important to refer that the specimens without cyclic loading were the specimens from layout 2 (M3 and M4) which had less grout exit hole levels and consequently less resistance and stiffness than the rest of the specimens.

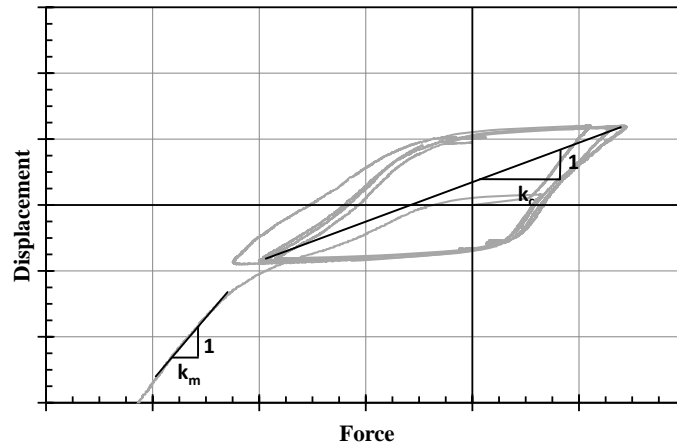


Figure 5.46 - Cyclic and monotonic stiffness estimation procedure (generic curve)

The cyclic stiffness (k_c) was determined using the method presented in Figure 5.46. In this generic representation of a cyclic loading, the cyclic stiffness is defined as the inverse of the slope of the line connecting the two cycle extremes.

The values obtained for each test where the cyclic loading was considered are presented in Figure 5.47 for the single tests and on Figure 5.48 for the group tests.

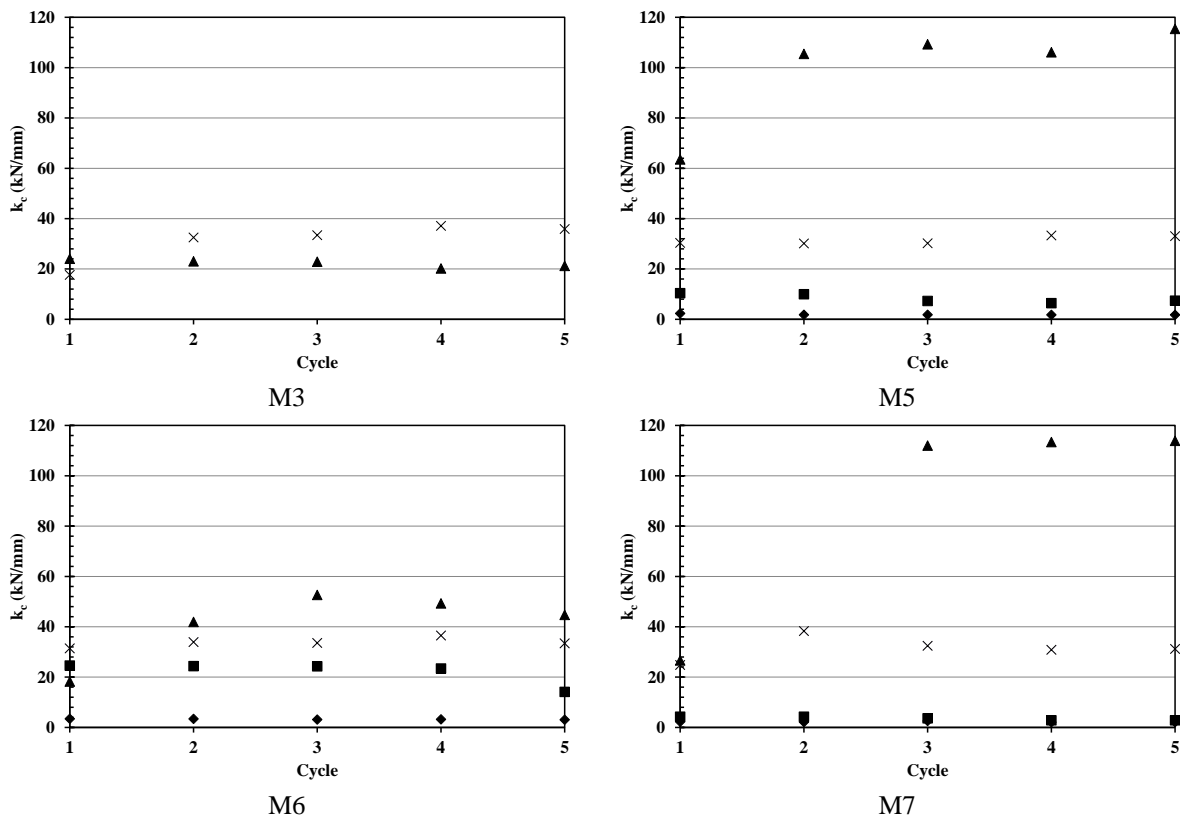
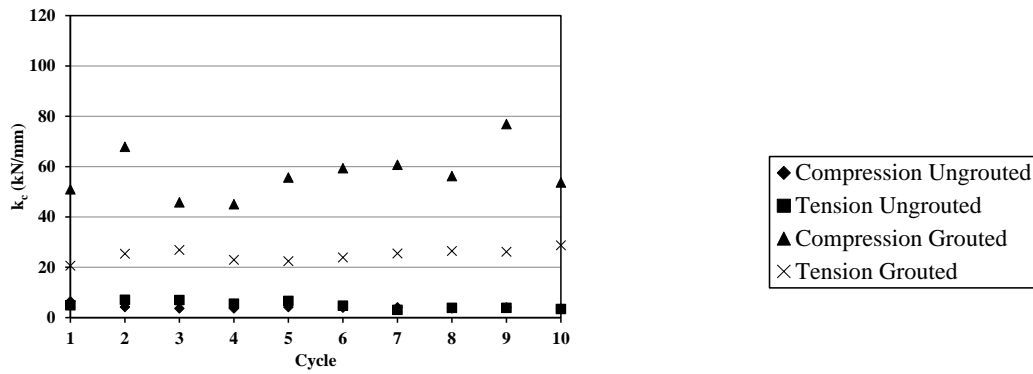
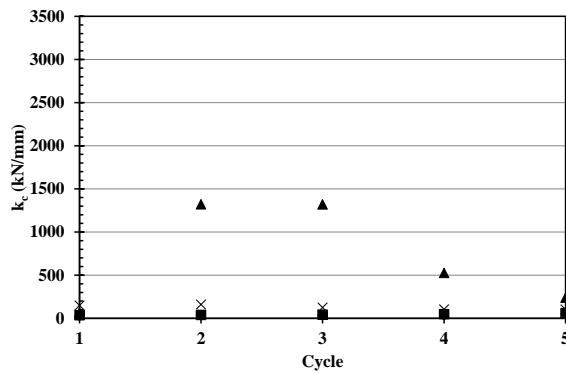


Figure 5.47 - Single tests cyclic stiffness

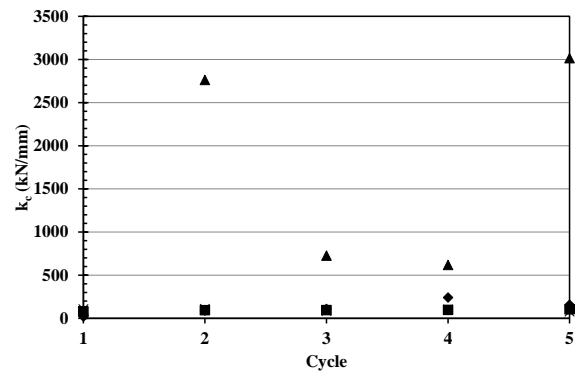


M8

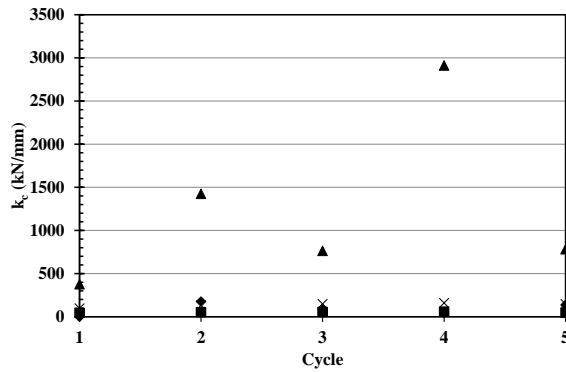
Figure 5.47 - Single tests cyclic stiffness (cont.)



G1



G2



G3

Figure 5.48 - Group tests cyclic stiffness

From the analysis of Figure 5.47 and Figure 5.48 it is possible to observe, as expected and in the same manner as in the static/post-cyclic stiffness, that the grouted specimens presented a higher cyclic stiffness than the correspondent ungrouted specimen, both for single and group tests. For this analysis, the mean value for the stiffness of the 5 cycles (or 10 cycles in the case of M8 micropile) was considered.

On the single tests, the improvement caused by the grout in the cyclic stiffness varies from 12.7 to 52.7 times for the compression tests and between 1.5 and 8.9 for the tension cases. The respective results for the groups vary from 11.6 to 19.3 for compression tests and around 1.0 to 2.8 for the tensile tests.

It was observed, in Figure 5.47 and Figure 5.48, that the cyclic stiffness variation from cycle to cycle is quite small including the variation obtained for M8 specimens where a higher number of cycles (10 cycles) was applied.

5.6. Final comments

The grouted specimens show higher resistances than the corresponding ungrouted cases. This improvement is more emphasized in compression than in tension tests.

The gain in the resistance is expected and it is due to the increase of grout-to-ground bond strength, the micropile diameter and the improvement of the soil characteristics as was observed in the DMT tests.

In both the single and the group tests, it was observed that the grout causes improvement in the specimens' resistances, as the larger cycles (higher force amplitudes) were obtained. This was expected because of the force required to mobilize an imposed displacement was higher in grouted specimens.

In the large majority of the tests, with exception of M6 and M7, the compression resistances are higher than the correspondent tension resistance due to the influence of the tip effect. Both for single and group tests, the differences are higher for grouted than for ungrouted specimens. For higher displacements of M6 and M7, higher compression than tension resistances were obtained, which was in agreement with the rest of the tests.

The spacing effect is not significant for the ungrouted tests because the increase in the micropiles spacing lead to very reduced differences between the ungrouted sets. The differences observed for grouted specimens are higher but in this case it is not possible to state that the tests conditions are similar from each layout because, as it was presented, there are differences between the grout distributions from test to test.

A comparison between the mean values of resistance of the single specimens and the correspondent group specimens (group effect) showed that the efficiency coefficient is higher than 100% for the compression tests, in the case of the ungrouted tests. If the results from the

specimens without cyclic loading, prior the monotonic were neglected, the efficiency coefficient is close to 100%.

The values obtained for the mean unit skin friction on single micropiles, both grouted and ungrouted, fall quite well within the analytical estimations performed ahead of the tests. The values for the unit skin friction for the single micropiles when compared with the group specimens were, in average, higher 132% for ungrouted tests and 29% for grouted tests. The looser sand in the middle of the group specimens may have conducted to lower friction angles.

The obtained static monotonic stiffness (or post-cyclic when applicable) is, in average, 490% higher for the grouted than for the ungrouted specimens. The improvement of the grout is more relevant on the single micropiles where an average improvement of 630% was obtained against an improvement of 200% for the group cases.

The monotonic stiffness of the specimens with cyclic loading was in average 476% higher than the obtained for specimens without cyclic loading, unlike expected.

In the case of the cyclic stiffness it was concluded that, for every case studied, the grouted specimens provided higher stiffness than the correspondent ungrouted, both for compression and tension loadings with an average improvement of 1280%. The improvement is much more evident on the compression tests than on the tensile as it was obtained, respectively, average values of 1820% and 270% of improvement.

The comparison between the compressive and the tensile cyclic stiffness shows that for the ungrouted single tests, the tensile cyclic stiffness is in average 250% higher than the respective compressive, while for the grouted tests an average improvement of 150% was observed between the compressive and tensile tests. This is due probably to an increase in the sand density after the compression ungrouted tests resulting in higher tensile ungrouted cyclic stiffness, while in the grouted cases it may occur a detachment of some grout after the compression grouted tests conducting to lower tension grouted cyclic stiffness values.

On the group tests, taking as the exception the G1 group, the compressive stiffness is higher, 570% on average, both for ungrouted and grouted tests.

As the relevance of the grouting in both strength and stiffness of the micropiles was shown, it is therefore very important to achieve the best grouting procedure in order to optimize use of the micropile and promote the highest ground-to-grout bond strength.

6. HYBRID FOUNDATIONS – NUMERICAL ANALYSIS

6.1. Introduction

The behaviour of small scale micropiles placed in loose sand was estimated according to the experimental procedure presented in the previous chapter. The results obtained are used for the calibration of finite element models to allow the prediction of their behaviour when installed on soils with better mechanical properties and for micropiles with different length.

The improvement caused by the installation of micropiles in dense sand will be analysed and compared with the results obtained for the sand with a density index $I_D=30\%$.

The simulation of the experimental tests presented in chapter 5 was done using a finite element software (Plaxis, 2006) where the stress-strain behaviour of the soil was modelled by the use of the non-linear Mohr-Coulomb and Hardening Soil material models. The main goal of the analysis presented in this chapter is to ensure about the accuracy and fitness of the numerical method to estimate the behaviour of micropiles and to understand their behaviour when installed in hybrid foundations. A comparison (vantages and disadvantages) of both soil models considered in the assessment of the micropiles will also be presented.

Along with the mechanical properties of the sand estimated by Ferreira (2014) and obtained with triaxial tests, it was also performed a numerical calibration of the obtained results for the sand with the two different index densities of $I_D=30\%$ and $I_D=70\%$. The values obtained by Ferreira (2014) with this calibration procedure will be presented and will be considered in the analysis. The soil elastic modulus E in the case of MC model and E_{50}^{ref} , E_{UR}^{ref} and E_{oed}^{ref} for the case of HS model will be estimated for each confining stress conditions. In order to understand the effect of each parameter in the behaviour of the micropile, a sensitive analysis was considered and presented.

The calibration of the experimental tests of chapter 5 was done with the objective of determining a proper value for the elastic modulus of the soil for both models along with a proper value for R_{inter} on the interface between the soil and the micropile. Based on the results and procedure considered during the calibration process, an extrapolation of the results was done for micropiles with more realistic dimensions (12m long and grouted diameter of 250mm) installed both in loose and dense sand.

Considering the results obtained with the extrapolation process (resistance and stiffness) an upgraded analysis of the results presented in the design of chapter 4 is presented along with a proposal of a bilinear behaviour for the springs of micropiles grouted considering the same technique and installed in sand with similar mechanical properties and densities as considered in the study. A detailed analysis of the micropile behaviour under the wind induced vibration in the tower and foundation will be addressed and commented.

6.2. Material Models

6.2.1. Overview

Plaxis (Plaxis, 2006) is the finite element software applied for this analysis. In this software it is possible to find different material models available for different soil and *in-situ* ground conditions such as the Jointed Rock Model to simulate rock and the Soft-Soil-Creep and the Soft Soil models are considered for soft soil.

According to Plaxis (Plaxis, 2006) the most appropriate model to simulate the soil-pile interaction in sands considering FEA is the Hardening-Soil model (HS), however there are more available material models.

Linear elastic model is the simplest available with a linear stress-strain relationship given by Hooke's law, however it is not suited in this case because the soil presents a strongly inelastic behavior. It will be considered for the simulation of the micropile.

The Mohr-Coulomb model (MC) is elastic perfectly-plastic considering a fixed yield surface. It is a good first order approximation, providing a trustfull first insight in the soil behavior and consequently in the micropile properties. Its main advantage is the capability to adopt a constant modulus for each soil depth (or linear variable in depth if required), thus decreasing the computational effort, making it quite fast, but on the other hand it can be excessively simple and not representative of the actual soil behavior.

The main characteristic of the HS model is the advanced hyperbolic soil model formulation, in the framework of hardening plasticity and it is defined by 3 different elastic moduli, which is one of the differences with MC model which is defined by only 1. The value of the elasticity modulus of the soil is also dependent on the confining stress at the considered point. The main advantages of the model are therefore the more accurate stiffness definition versus the MC model, the consideration of the dilatancy and the yield surface that can expand. The shortcomings are the high computational costs and the non inclusion of the viscous effects and the softening of the soil.

For the reasons presented, the HS model is the most appropriate model available in Plaxis (Plaxis, 2006) for the simulation of the given problem however in this case the results provided by this model will be compared with the results provided by the MC model. The micropile will be simulated considering a linear elastic model according to Figure 6.1.

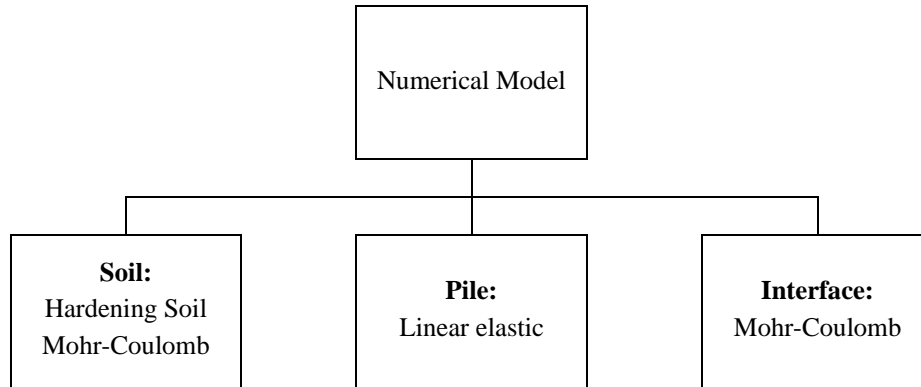


Figure 6.1 – Numerical modelling strategy

The interface of the model is simulated according to the Mohr-Coulomb behavior law (Eq. (6.1)) and the level at which (plastic) slipping occurs is directly controlled by the strength properties of the soil and the inputted R_{inter} value of the relevant material set. R_{inter} value relates the interface strength to the soil strength (friction angle and adhesion) (Plaxis, 2006). According to the reference manual of Plaxis, the strength reduction factor for the friction angle should be given by $R_{inter} \cdot \tan(\phi')$ however, and after several tests, the shear strength of the interface should be estimated according to the expression (6.1).

$$\tau = c' + \sigma'_N \times \tan(R_{inter} \phi') \quad (6.1)$$

The scope of each geotechnical problem in terms of shear strain is presented in Figure 6.2, which is in accordance also with the comments of Herold and von Wolffersdorff (2009). The HS small strain model is presented as an upgraded version of HS standard model in order to handle the commonly observed phenomena of strong stiffness variation and hysteretic, nonlinear elastic stress-strain relationship applicable in the range of small strains (Obrzud 2010). HS small strain model can be useful for dynamic applications or for unloading-conditioned problems and it is suited to simulate the most part of the existing soils however it is not implemented in the version of Plaxis (Plaxis, 2006) used in this thesis.

The material model recommended for each design situation can be found according to the diagram of Figure 6.3. Obrzud (2010) presented recommendations based on the material models available in the software Z Soil. The behaviour of both MC (Drucker-Prager) and HS-Standard are equivalent to MC and HS models available in Plaxis. The range of validity of HS model is higher than MC.

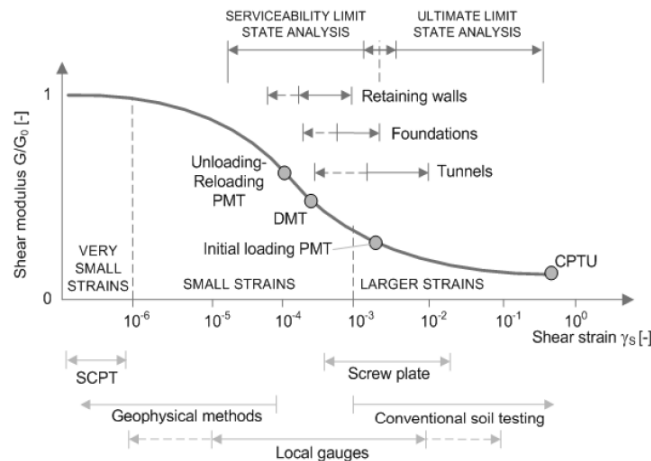


Figure 6.2 - Typical representation of stiffness variation in as a function of the shear strain amplitudes; comparison with the ranges for typical geotechnical problems and different tests (Obrzud, 2010)

Selected soil models implemented in Z_Soil	Type of analysis	SANDS	SILTS		CLAYS		
			Dilatant, Low compressible	Non-dilatant, Compressible	Degree of Overconsolidation		
					High Stiff clays	Low	Normal, Soft clays
Mohr-Coulomb (Drucker-Prager)	SLS						
	ULS	—	- - - -				
CAP	SLS	- - - - -					
	ULS	—					—
Modified Cam-Clay	SLS			- - - -			—
	ULS			—			—
HS-Standard HS-Small Strain	SLS	—					
	ULS	HS-Small Strain					HS-Std

Figure 6.3 - Recommendations for the soil model choice for soil type and types of analysis. Dashed line: may be used but not recommended in terms of quality of results; Solid line: can be applied; HS models: recommended (Obrzud, 2010)

6.2.2. Mohr-Coulomb model

Mohr-Coulomb model is usually considered for a first approximation of the behavior of soils although it doesn't represent their non-linear behavior. The MC model is a very suited solution for a limit state analysis (bearing capacity, slope, wall stability...) (Obrzud, 2010) since it provides good approximation to the failure loads with low computational requirements.

It is an elastic and perfectly plastic model in which the soil present a linear behavior until failure, given by the Mohr-Coulomb failure criteria. After the failure there is no stiffness and there is an increase in the plastic deformations even without an increase in the stress.

Figure 6.4 shows a comparison between the curves obtained in a triaxial tests and the approximation provided by the Mohr-Coulomb model.

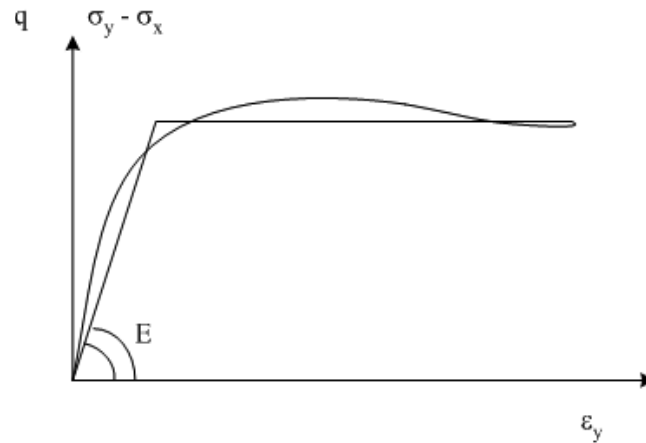


Figure 6.4 – Approximation of MC model result to a triaxial test curve

For the use of this model it is required to define the soil friction angle (φ), cohesion (c), Poisson's ration (ν), dilatancy angle (ψ) and the Young's modulus (E).

6.2.3. Hardening Soil model

The Hardening Soil model is an advanced material model since it allows the modeling of the non-linear properties of the soil due to the advanced hyperbolic soil model formulation in the framework of hardening plasticity.

The HS model is suited for a deformation analysis (pile or retaining wall deflection, supported deep excavations, tunnel excavations, consolidation...) (Obrzud, 2010).

The characteristic stress strain curve of the HS model are presented in Figure 6.5 along with the initial (E_{50}) and unloading/reloading (E_{UR}) elastic moduli.

The HS model is defined by 3 different elastic parameters including the two parameters defined in Figure 6.5 added to the oedometer modulus obtained in the oedometer test (axial loading without radial expansion). All the moduli in this model are function of the effective confining stress σ'_3 .

Expressions (6.2), (6.3) and (6.4) define, respectively, the values for the secant stiffness at 50% of the failure load, the unload/reload modulus and the oedometer modulus for a reference confining stress (p_{ref}) usually taken as 100kPa.

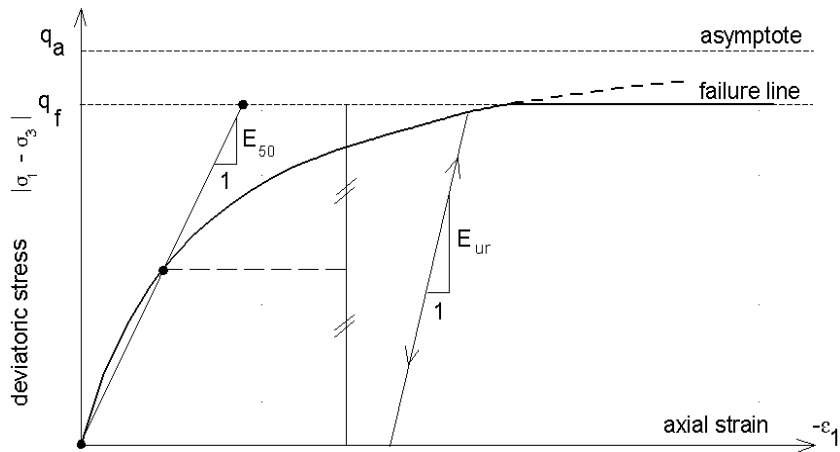


Figure 6.5 – HS characteristic stress-strain curve and parameter definition (Plaxis, 2006)

$$E_{50} = E_{50}^{ref} \left(\frac{\sigma_3' + c \cot \varphi}{p^{ref} + c \cot \varphi} \right)^m \quad (6.2)$$

$$E_{ur} = E_{ur}^{ref} \left(\frac{c \cot \varphi - \sigma_3'}{c \cot \varphi + p^{ref}} \right)^m \quad (6.3)$$

$$E_{oed} = E_{oed}^{ref} \left(\frac{\sigma_1' + c \cot \varphi}{p^{ref} + c \cot \varphi} \right)^m \quad (6.4)$$

The value for E_{oed}^{ref} is commonly taken as similar to the E_{50}^{ref} for design purposes and according to Schanz and Vermeer (1998) it is a valid assumption however keeping in mind that the normalization of the oedometer modulus is given by σ_1' while for the initial modulus is given by σ_3' . For this analysis is considered a value $E_{oed}^{ref} = E_{50}^{ref}$.

In this model there are two different surfaces that can generate plastic deformation when they are reached. They are designated hardening and cap surface and their representation is presented in Figure 6.6. The position of the cap and the hardening surfaces are numerically controlled, respectively, by the parameters OCR (overconsolidation ratio) and POP (pre-overburden pressure).

If the numerical parameters are set as default (OCR=POP=1), the initial point is coincident with the cap surface, so after any loading of the soil, there will be plastic deformation along with elastic deformation. Figure 6.7 shows the graphical definition of OCR and POP.

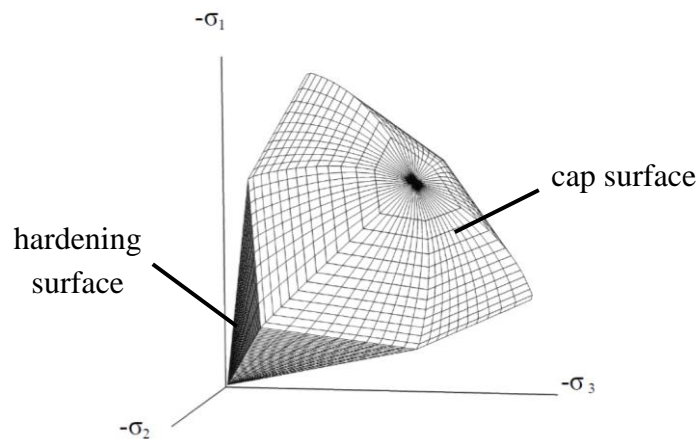


Figure 6.6 – Principal stress space representation of HS model surfaces (Plaxis, 2006)



Figure 6.7 – Illustration of vertical preconsolidation stress in relation to the in-situ vertical stress using OCR and POP (Plaxis, 2006)

Figure 6.8 shows the evolution of the stress state, the referred surfaces and the failure line in the p - q' plan along with common loading trajectories.

The effect of the POP value on the behaviour of the model was studied in a model performed to simulate a constrained specimen under pure shear according to the geometry presented in Figure 6.9. A prescribed variable displacement between 0 and ± 1 mm was applied on the side surface while on the top surface it was applied a constant vertical displacement of -1mm and a horizontal displacement equal to the maximum displacement at the side surface at each load step. The model is $5 \times 2 \text{m}^2$ square with very fine mesh and the displacements of the base of the model are fixed both in vertical and horizontal directions. The presented results were obtained in the center area region in order to avoid any numerical problems related with the side edges.

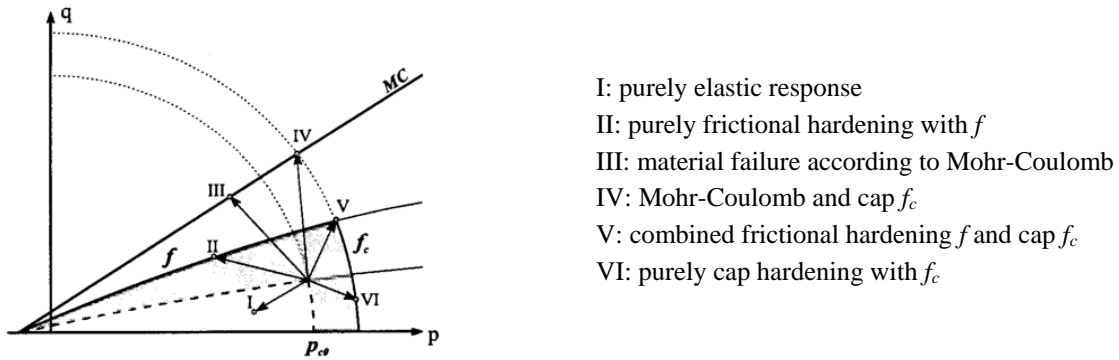


Figure 6.8 - Evolution of the stress state and yielding surfaces of HS model (Sture, 2004)

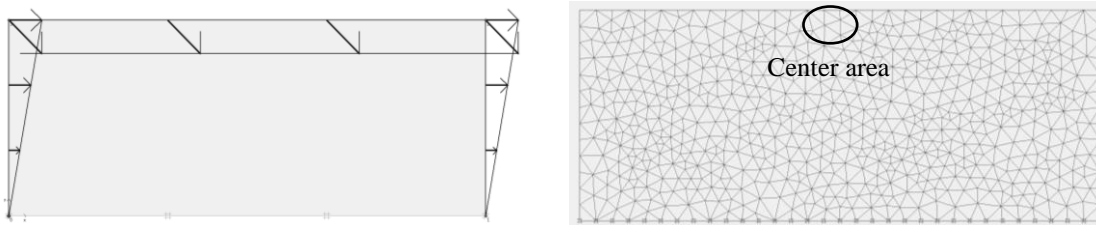


Figure 6.9 – Shear model geometry

In this analysis, a displacement pattern was applied to simulate 5 cycles in a model with HS material model. According to the results presented on Figure 6.10a in terms of force-displacement curves it is possible to understand a decrease in the cycle hysteresis with the increase in the POP value (moving of the cap surface) which shows a reduction of the plastic deformation in the soil as expected according to the formulation presented. For the s^t - t graphic in Figure 6.10b it is possible to understand that all the models follow the K_0 line of loading and the plastic deformation occurs latter in the loading pattern with the increase in the cap position.

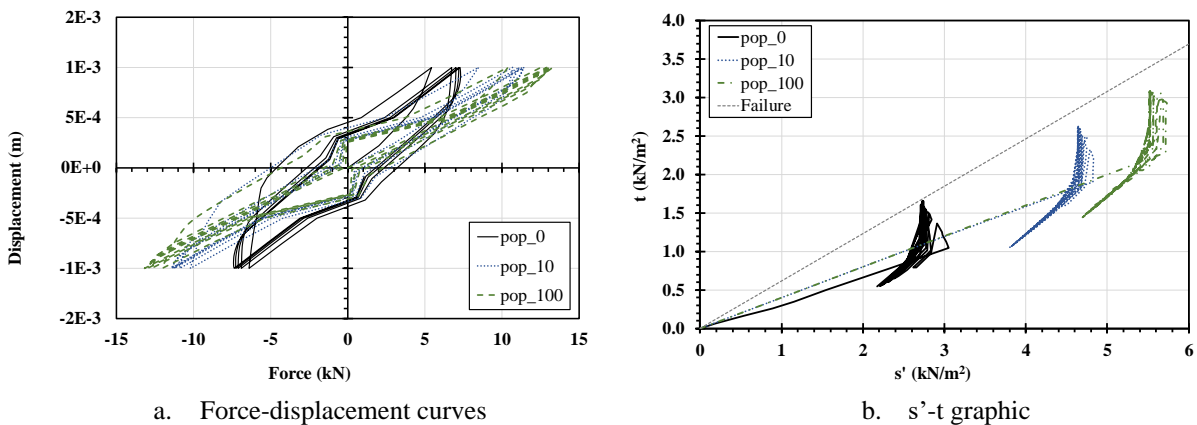


Figure 6.10 – Cap position influence (5 cycles)

6.3. Numerical parameters – soil properties and numerical model values

The soil physical and mechanical properties were evaluated by Coelho (2011) and Ferreira (2014). Ferreira (2014) also performed a numerical calibration of the triaxial tests in order to obtain the relevant numerical parameters to properly simulate the material behaviour considering the use of Mohr-Coulomb and Hardening Soil material models implemented in Plaxis (Plaxis, 2006) software.

The results for the characterization tests carried out are presented in chapter 5.4.2. The detailed properties obtained in the triaxial tests carried out by Ferreira (2014) for the 3 different confining stresses (50, 100 and 200kPa) are presented in Table 6.1.

Table 6.1 – Soil mechanical properties – triaxial tests (Ferreira (2014))

	σ'_c (kPa)	E_{50} (MPa)	ν	ψ' (°)	c' (kPa)	ϕ' (°)
Low Density ($I_D=31,2\%$)	50	15	0,3	4,3		
	100	27	0,3	3,8	0	37
	200	42	0,3	3,5		
High Density ($I_D=67,3\%$)	50	25	0,2	15,7		
	100	36	0,2	14,8	0	45
	200	68	0,2	12,5		

In the scope of the work carried out by Ferreira (2014), a numerical calibration of the presented triaxial tests was accomplished. The material behaviour parameters obtained for the considered sand are presented in Table 6.2 and are available both for Mohr-Coulomb and Hardening Soil material models. The elastic parameters presented in Table 6.2 for the MC model were obtained by the calibration of the triaxial tests of the specimens with 50kPa of confining stress.

According to the Plaxis formulation of the HS material model, some combinations of values of K_0 and $E_{\text{ref}}^{\text{oad}}$ are not possible to be considered by the software. By the observation of Table 6.2, Ferreira (2014) opted to change the value of K_0 to allow the use of a fixed value of $E_{\text{ref}}^{\text{oad}}$. In this study it was assumed to use $E_{\text{ref}}^{\text{oad}}=E_{50}^{\text{ref}}$ and a fixed value of K_0 given by Jaki's expression ($K_0=1-\sin(\phi)$) since K_0 influences directly the shear resistance of the system. The considered value for K_0 in HS model is, therefore similar to the value used in MC model and presented in Table 6.2.

In the present study, the mechanical properties of the sand determined by Ferreira (2014) will be considered and the calibration procedure presented following will be focused only on the

determination of the values for the elastic properties of both MC (E) and HS (E_{50}^{ref} , E_{oed}^{ref} , E_{ur}^{ref}) as well as the resistance parameter R_{inter} that fits better to the results of the experimental tests presented on chapter 5.

Table 6.2 – Calibration parameters for MC and HS models

Parameter	Unit	Model					
		DR30 MC E50	DR30 MC E80	DR30 HS E50	DR70 MC E50	DR70 MC E80	DR70 HS E50
γ	(kN/m ³)	15.95	15.95	15.95	17.3	17.3	17.3
Φ'	(°)	38.0	38.0	38.0	46.1	46.1	46.1
Ψ	(°)	4.3	4.3	4.3	15.7	15.7	15.7
C_{ref}	(kN/m ²)	0.10	0.10	0.11	1.00	1.00	1.00
ν/ν_{ur}	-	0.3	0.3	0.3	0.2	0.2	0.2
E	(kN/m ²)	15 000	8 000	-	25 000	16 000	-
E_{oed}	(kN/m ²)	20 192	10 769	-	27 778	17 778	-
G_{ref}	(kN/m ²)	5 769	3 077	-	10 417	6 667	-
E_{50}^{ref}	(kN/m ²)	-	-	27 000	-	-	36 000
E_{oed}^{ref}	(kN/m ²)	-	-	36 346	-	-	40 000
E_{ur}^{ref}	(kN/m ²)	-	-	81 000	-	-	108 000
p_{ref}	(kN/m ²)	-	-	100	-	-	100
k_0/k^{nc}_0	-	0.384	0.384	0.403	0.279	0.279	0.322
m	-	-	-	0.7	-	-	0.5

6.4. Numerical model description and calibration

6.4.1. Numerical model description

The values of the mechanical properties of the sand considered for the analysis are presented in Table 6.2. The goal of this calibration is to obtain feasible values for the friction coefficient between the micropile pipe and the soil (R_{inter}) and for the elastic parameters of both adopted soil models. A sensitivity analysis is presented in order to expose the influence of each relevant parameter of the soil models in the behavior of the micropiles.

The calibration was conducted in order to allow an extrapolation of the small scale experimental tests results to micropiles with realistic dimensions (12m long and 250mm of diameter) installed both in loose and dense sand. The results obtained are used for a comparison with the considered values (resistance and stiffness) in the design of the hybrid

foundations presented in chapter 4. A comparison between soil models (HS and MC) is presented (advantages and disadvantages of each one).

The general configuration of each finite element model developed is presented in Figure 6.11. An axisymmetric model was used to simulate only half of the set-up of Chapter 4 (1m radius and 3.5m high). The mesh was defined with triangular 15-node elements. Two layers of the same soil were considered in order to allow the proper simulation of the two different friction interfaces (soil-soil in the bottom part ($R_{inter} = 1$) and soil-pipe (or soil-grout when applicable) in the top part). The mesh was set to fine in all cases.

The boundary conditions adopted were standard fixities, corresponding to sliders in the vertical direction (tube wall and axis of symmetry) and a full fixity in the horizontal direction (container base).

In order to understand the effect of the modelling of the interface, a second model (model 2) was compared with model 1. The geometry was similar to what was presented before but the interface was considered also at the micropile base as presented in Figure 6.12.

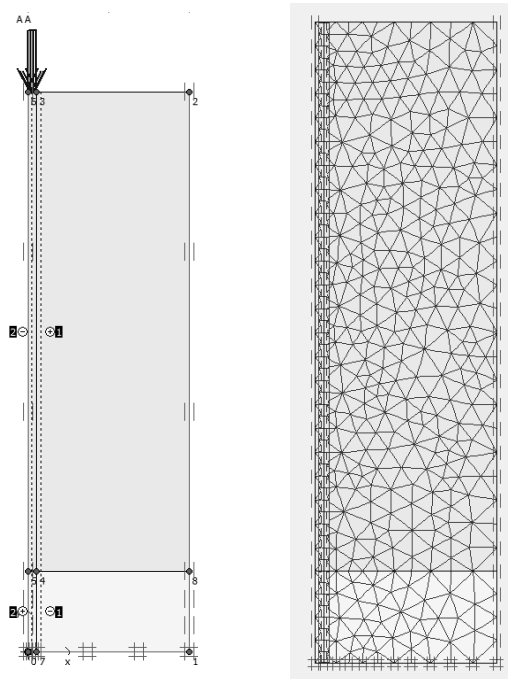


Figure 6.11 – Numerical model geometry and elements mesh (model 1)

For the pile properties, an auxiliary calculation is needed to determine the value of the equivalent elasticity modulus to be considered in the model. The axial stiffness of the model must be equal to the real micropile stiffness, however as the micropile was modelled with continuous elements, the calculation according to expression (6.5) was performed.

$$E_{tube} \times A_{tube} = E_{model} \times A_{model} \Leftrightarrow E_{model} = E_{tube} \times \frac{A_{tube}}{A_{model}} \quad (6.5)$$

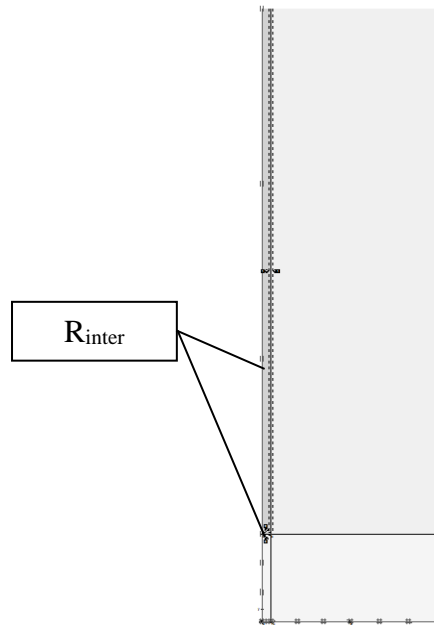


Figure 6.12 – Interface position and description (model 2)

Considering 1108.4mm^2 for the area of the real pile, 8107.3mm^2 for the area of the model and 210GPa for the elasticity modulus of the tube, the value obtained for the equivalent elasticity modulus to be considered in the model is 29GPa .

By comparing the results from both models, each using three different soil densities, it was concluded according to the Figure 6.13, that force-displacement curves are quite similar. Having this conclusion in mind, model 1 was adopted to continue the study.

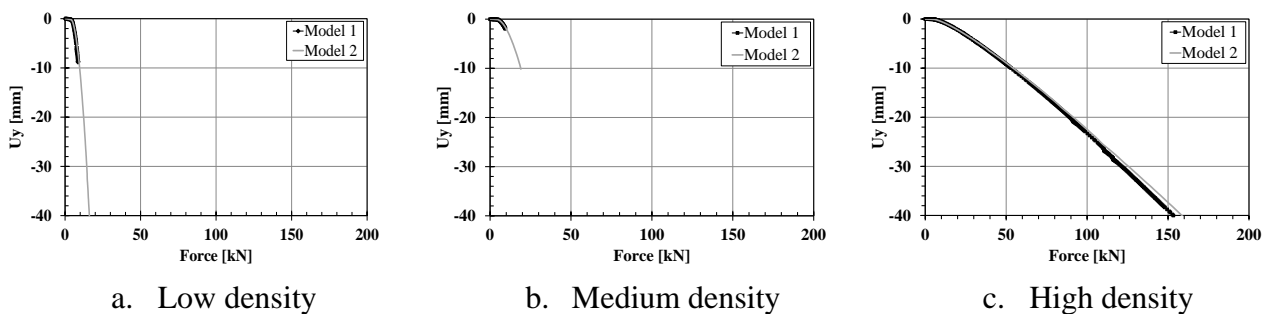


Figure 6.13 – Compression force-displacement curves (different soil densities)

The main difference in the response of the model observed in the force-displacement curves is located after the full mobilization of the shear strength of the micropile where the tip resistance plays an important role. The only difference between the models is in the modelling of the tip. In model 1 the tip contribution is simulated as rigid for shear strength along the pile tip (x direction) while for model 2 the shear effect in the tip of the micropile is simulated with given value for friction between pile and soil. Since the most predominant stresses in this analysis are normal stresses, the effect of the shear behaviour of the tip do not lead to any major differences in the results between both models evaluated.

The comparison of the tension behaviour of both models is presented in Figure 6.14. In the case of tension, where the side resistance is the only active component in the resistance of the foundation, there is a complete similarity in both models.

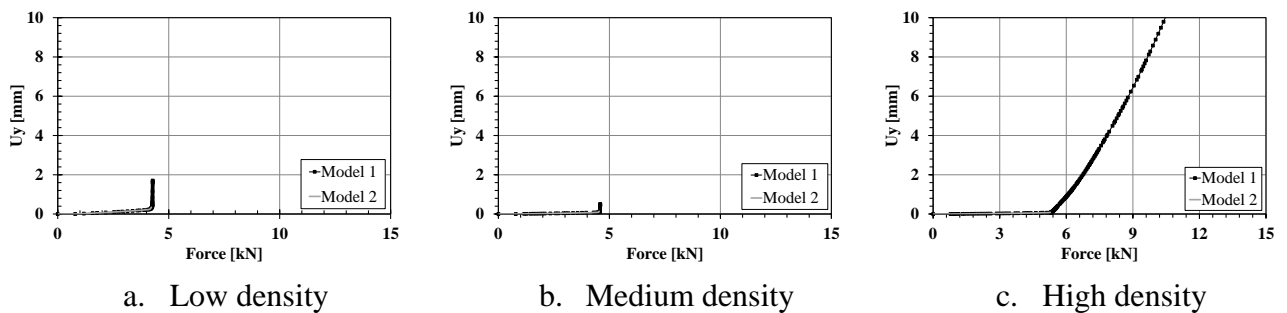


Figure 6.14 – Tension force-displacement curves (different soil densities)

In order to evaluate the effect of the rigid boundaries of the model, an analysis was performed by increasing the distance between the micropile and the rigid edges of the model. An increase in 4m in the height and 6m in width was carried out and the results obtained (force-displacement curves) are presented in Figure 6.15 and plotted against the corresponding results for the real geometry presented before and used in the experimental tests presented in Chapter 4.

As expected, the results provided by the increased geometry conduct to lower resistances since the confinement of the sand is lower in these models due to the higher distance between the micropile tip and the rigid boundaries in the bottom of the model. The main difference in the curves can be observed mainly in the tip resistance “component” of the curves.

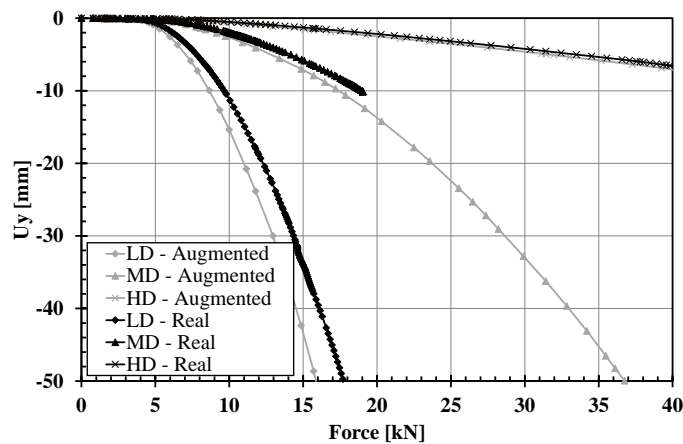


Figure 6.15 – Compression force-displacement curves comparison between real (experimental) and augmented model dimensions

6.4.2. Sensitivity analysis

The parameters that were evaluated in this procedure were E_{OED} , E_{UR} , ν , ψ and K_0 values. Each one of these parameters was analysed independently in different models and with different geometric dimensions. In each case, all the numerical model parameters and geometries were kept constant and it was changed only the parameter analysed.

The effect of the oedometer modulus E_{OED} , adopted on the HS model, on the response of the model is presented in Figure 6.16. This evaluation was done for a compression example and considering the same geometry and the same soil parameters except E_{OED} value. It is possible to understand by the analysis of Figure 6.16 that the value of E_{OED} does not affect the force-displacement behaviour of the micropile on the elastic portion of the curve when the side friction is the dominant resistance of the micropile. On this compression example, the only difference occurs in the tip resistance behaviour after the mobilization of the side friction resistance as there is an increase in the isotropic stress at the micropile tip whereas near the pile side the stress increase is mainly due to shear.

The effect of the unloading-reloading modulus E_{UR} , on the behaviour of the micropile was also considered in this calibration analysis. The effect of this parameter was studied both for tension and compression cases in order to understand the differences. The obtained behaviour is presented on Figure 6.17 for the compression and tension cases.

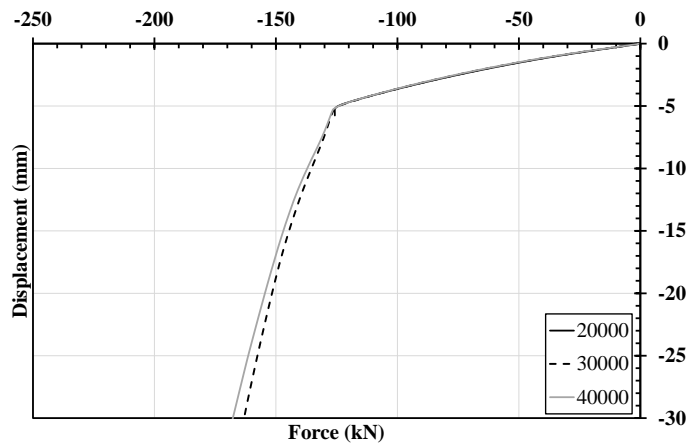
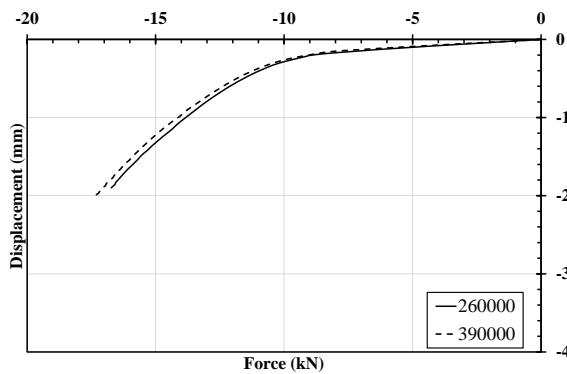
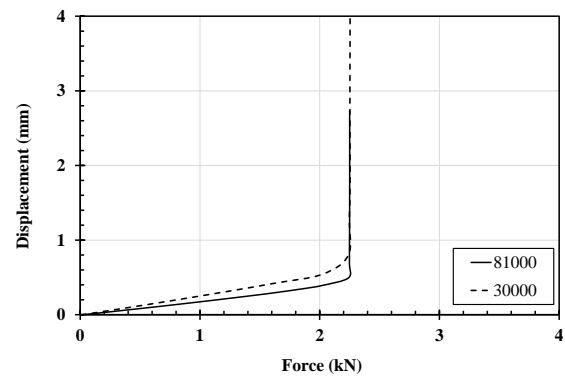


Figure 6.16 – Effect of the E_{OED} (kPa) value on the response of a 12m long micropile (HS model with $R_{inter}=0.9$)



a. Compression (HS – $R_{inter}=1.0$)



b. Tension (HS – $R_{inter}=0.3$)

Figure 6.17 – Effect of the E_{UR} (kPa) value on the response of a 3m long micropile

In this case it is possible to observe that the variation of value of E_{UR} does not lead to any change in the initial stiffness of the micropile under monotonic compression while for monotonic tension there is a slight change.

Having the formulation of the HS model in mind, this means that in the monotonic tension model some elements of the finite element mesh have a reduction effective isotropic stress (p') in which leads to the use of this value for calculation purposes both for unloading and/or reloading of those points. This effect does not occur in the monotonic compression example since the initial stiffness obtained is the same regardless of the value of E_{UR} inputted in the model. For the sake of comparison, the initial stiffness of the compression model with $E_{UR}=81000$ kPa on Figure 6.17a is 2500kN/m while for the correspondent tension model of Figure 6.17b is 3600kN/m showing the different influence of the elasticity parameters in the initial stiffness of the system.

The dilatancy angle also plays a very important role in the micropile behaviour. A variation of this angle was performed both for compression and tension cases. A variation of this parameter was considered in some cases and the obtained results are presented in Figure 6.18 both for tension and compression.

In this case, tests under different dilatancy conditions were tested. For the compression cases, examples with the obtained dilatancy of the loose sand presented in Table 6.2 were considered ($\psi=4.3^\circ$), cases without dilatancy in all the soil and only under the micropile (base) and also one case with the cut-off option activated. The analysis was replicated for the tensile models except for the cut-off example.

The first conclusion to be drawn from this analysis is that the dilatancy angle only plays some role in the tip resistance behaviour. The initial stiffness and the shear resistance are not influenced by this parameter.

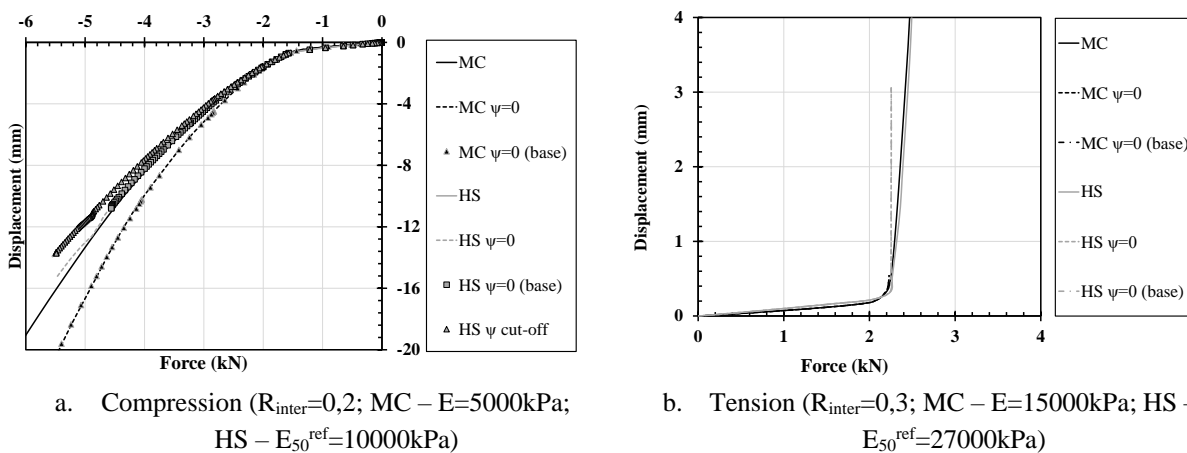


Figure 6.18 – Effect of the dilatancy angle value on the response of a micropile

It was also observed that there is no difference in considering a null dilatancy angle in all the model or only in the soil under the micropile. This conclusion is logical since the dilatancy angle only influences the tip resistance which is assured by the underlying soil and so the dilatancy of the soil on the side of the micropile which influences only the side resistance of the foundation does not affect the micropile response.

The final conclusion of this analysis is that the inclusion of the dilatancy cut-off option does not affect the micropile behaviour if it is compared with the same model without cut-off. This means that in these simulations the plateau of the dilatancy is not achieved and the dilatancy of the soil follows the same path both in cases with full dilatancy and cut-off dilatancy.

The effect of the at-rest coefficient of horizontal earth pressure K_0 was also studied. Figure 6.19 presents the results of two analyses where only the value of K_0 varied. As expected, the higher K_0 results on a higher resistance.

According to the equation (6.6), the shear resistance at the soil-micropile interface is directly dependent on the value of K_0 . For an increase in the value of K_0 there is an increase in the confining stress leading therefore to an increase in the value of the shear resistance of the micropile.

$$\begin{aligned}\tau &= c' + \sigma'_h \times \tan(\phi' \cdot R_{inter}) \\ \sigma'_h &= K_0 \cdot \gamma \cdot h\end{aligned}\quad (6.6)$$

The last parameter to be analysed was the Poisson's Coefficient (ν). The analyses were conducted for a generic compression ungrouted model by changing only the value of ν for both soil models considered. The force-displacement curves obtained are presented in Figure 6.20.

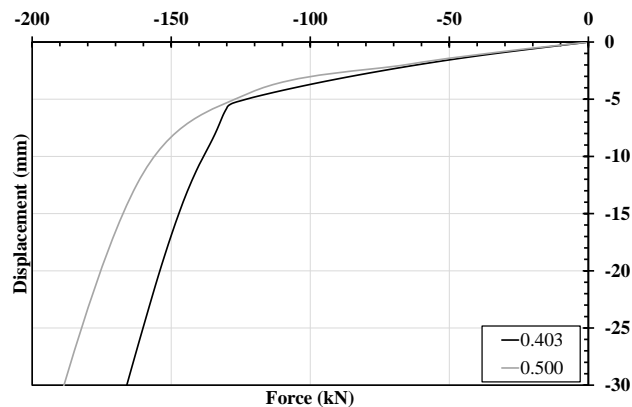


Figure 6.19 - Effect of the K_0 value on the response of a micropile

The difference in the models occurs only in the area of the curve after the full mobilization of the side friction for the MC model because a higher value of ν should provide lower volumetric deformations leading therefore to lower vertical displacements as obtained in this case. HS model conducted to similar results both for models with $\nu=0.3$ and $\nu=0.5$ (incompressible soil).

The parameters that directly affect the initial stiffness of the micropiles are the values of E (MC model) and $E_{50}^{ref}/E_{UR}^{ref}$ (HS model) as it can be concluded from the sensitivity analysis presented. The variation of the other parameters tested influence the behaviour after the full mobilization of the shear resistance. The most relevant conclusion of this analysis is that the initial stiffness of the micropile in the HS model is governed by the value of E_{50}^{ref} for the

compression cases while for the tension there is also a mobilization of the value of E_{UR}^{ref} . Having the conclusions of the previous analysis in mind, for the sake of the analysis of the HS models, the value of $E_{OED}^{ref}=E_{50}^{ref}$ was adopted following the procedure of Schanz and Vermeer (1998) and the value of $E_{UR}^{ref}=3 \times E_{50}^{ref}$ as considered by default in Plaxis (Plaxis, 2006).

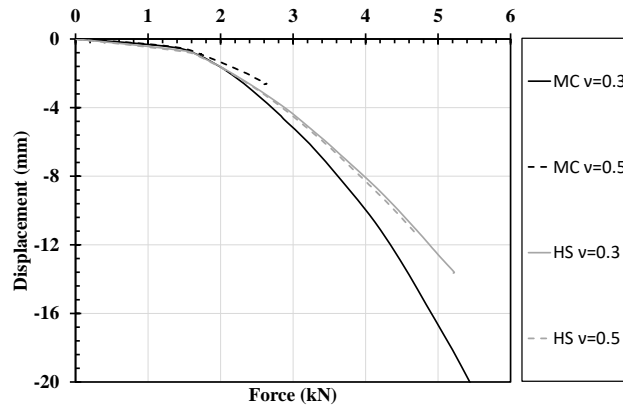


Figure 6.20 - Effect of the ν value on the response of a micropile ($R_{inter}=0,2$; MC – $E=5000\text{kPa}$; HS – $E_{50}^{ref}=10000\text{kPa}$)

6.4.3. Numerical model calibration

For the legend of the figures in this calibration section as well as in the rest of the document, the parameters presented are the values inputted on Plaxis to provide the results presented. For instance, the value of E of MC refers to the constant elastic modulus of the soil inputted while for the HS E stands for the inputted E_{50}^{ref} while the remaining elastic parameters are set according to the conclusions of section 6.4.2. The legend value of E is always in kPa. The values that are not mentioned in the legends are the same as presented in Table 6.2.

In the calibration process it was not considered the value of the self-weight of the experimental specimens (micropile pipe (and grout when applicable) and top plate). The numerical results were compared with the correspondent experimental force-displacement curves presented in chapter 5 removing the value of the self-weight.

6.4.3.1. Monotonic tests on single specimens

Taking into consideration the comments and conclusions presented in section 6.4.2, some models were prepared in order to calibrate (back-analyse) the results from the experimental tests presented in chapter 4.

The force-displacement curves for models M3 and M4 of chapter 5 are presented in Figure 6.21.

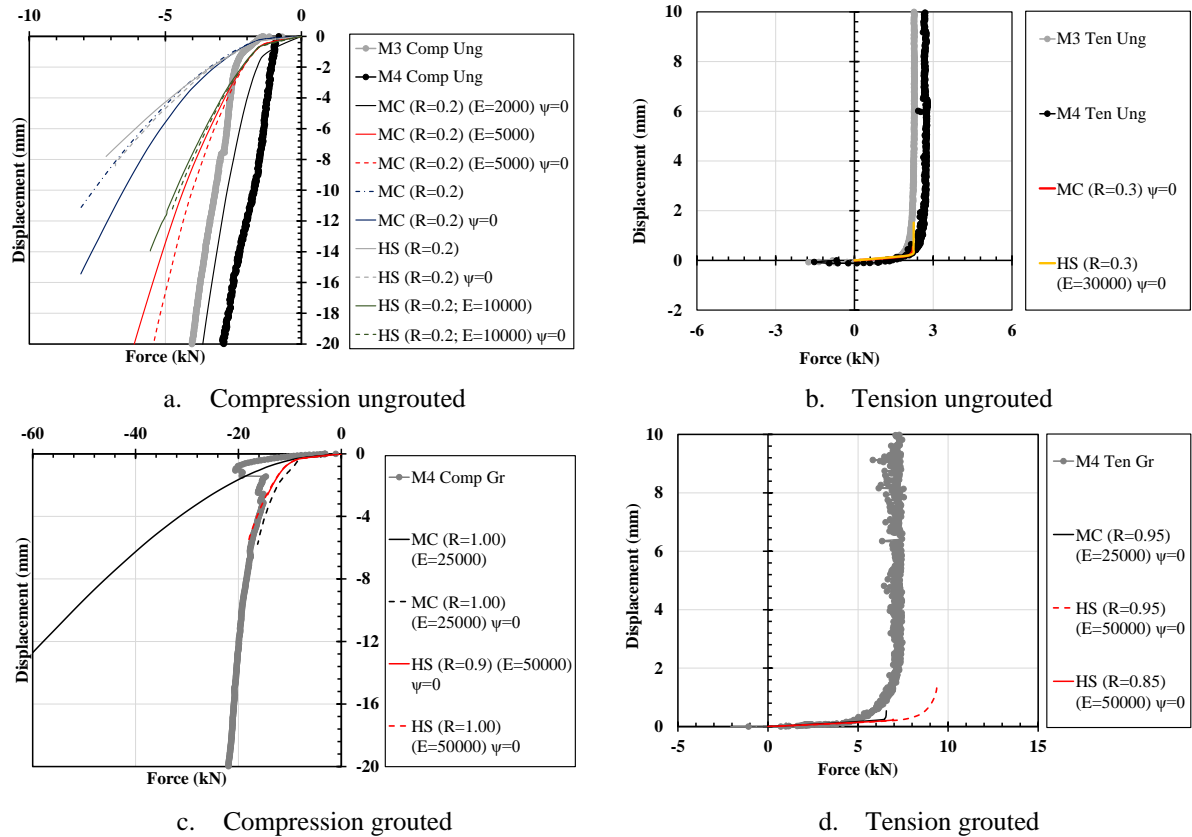


Figure 6.21 – Calibration force-displacement curves for monotonic tests

For the calibration of the monotonic compression tests on ungrouted single specimens, some assumptions were made to estimate a proper value for the elasticity modulus to be considered for the numerical simulation. The elasticity modulus of the soil will influence the initial stiffness of the micropile and also the tip behaviour (in the case of the compression tests).

In this case, three different assumptions were tested for the MC model.

First it was tested the elasticity modulus obtained in the triaxial test with a confining effective stress of 50kPa (even though the value of 9.19kPa of confining (horizontal) stress at mid-depth is considerably lower in these tests), then it was tested an approximate elasticity modulus based on the results of the DMT tests presented in section 5.4.2 and finally it was assumed the value obtained using a regression of the values obtained in the triaxial tests for the three different confinement stresses and for loose sand ($I_D=30\%$).

For the MC model and for a confining stress of 50kPa, the calibration of the triaxial tests performed by Ferreira (2014) provided a value for $E=15\text{MPa}$ (Table 6.2).

In the case of the DMT tests and applying the expression (6.7) that relates the value of E and the measured value of the constrained modulus M, considering an average value of 2.2 MPa for M and a value of 0.3 for ν , the value obtained for E is 2.2MPa.

$$M = E \cdot \frac{(1 - \nu)}{(1 + \nu)(1 - 2\nu)} \quad (6.7)$$

The values of the deformability modulus determined in the triaxial tests for 3 confining stresses (50, 100 and 200kPa) are presented in Figure 6.22. They were used to determine the parameters of the hyperbolic model (Duncan and Chang, 1970) in a power law similar to the used in the HS model ($E=k \cdot (\sigma'_3)^m$). The values for E obtained for each confining stress and considered in this interpolation are presented in Table 6.3. The resulting equation was used to determine the modulus for the confining effective stress representative of the model.

Table 6.3 – E values for MC model (triaxial tests calibration) – loose sand

Confining stress, σ'_3 (kPa)	E (MPa)
50	15
100	27
200	42

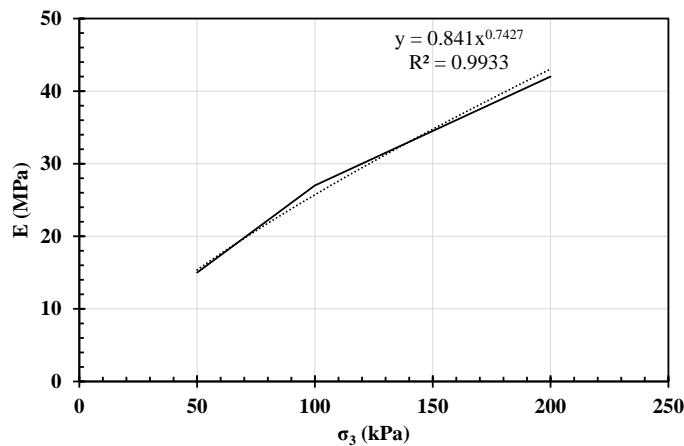


Figure 6.22 – Power regression for E value (low density sand)

The value for the horizontal stress at 1.5m depth (half length of the micropile) is, in this case, 9.19kPa which leads to a value for E=4.4MPa. For the sake of modelling it was considered E=5MPa. The obtained value is similar to what would be obtained using the common procedure proposed by Janbu (1963) where the dependency of the soil elastic modulus in relation to the confining stress is given by $E=k \cdot p_a (\sigma'_3 / p_a)^n$ where k and n are dimensionless

and obtained according to the procedure of Figure 6.23 and p_a is the atmospheric pressure in the same units as the confining stress.

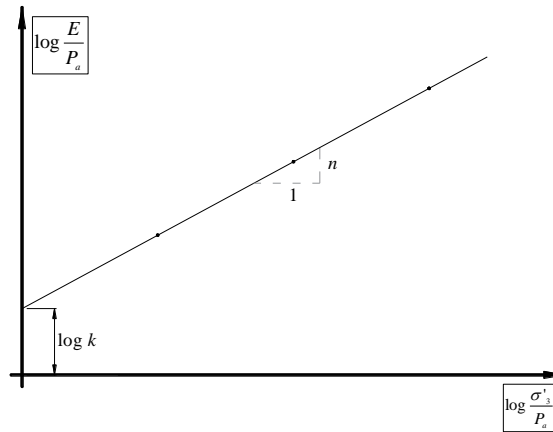


Figure 6.23 – Dependency of the elastic modulus and the effective confining stress (adapted from Matos Fernandes (2011))

For the calibration of the monotonic tension tests on ungrouted specimens, the modulus determined in the triaxial test with a confining stress of 50kPa was used.

According to the observation of Figure 6.21a it can be stated that for the MC model, the value for E that best suits the experimental curves is $E=5\text{MPa}$. The value of $E=2\text{MPa}$ proved to be too low in comparison with the experimental results and the value of $E=15\text{MPa}$ is too high. The value of 15MPa is also very high to simulate the tip behaviour after the mobilization of the side resistance.

The experimental tests present a sudden drop in the resistance after the mobilization of the side shear resistance presenting a behaviour in accordance with the consideration of null dilatancy in the model. The results presented in the sensitivity analysis shows that the dilatancy angle numerically influences the behaviour of the micropile after the full mobilization of the shear resistance. For this reason, no dilatancy was assumed in the model and it was proven to be a good approach to the experimental results, however it was not possible to simulate such a marked drop even without numerical dilatancy as it can be observed in Figure 6.21a.

For the HS model the goal was to obtain an initial stiffness similar to the MC model since it is in a good agreement with the experimental results. In this case, the agreement was obtained considering an input value for $E_{50}^{\text{ref}}=10\text{MPa}$, 2 times higher than the input modulus for the MC model. Even though, for the mean confining stress of 9.19kPa, the obtained value of E_{50} is much lower than the MC value of 5MPa, the initial stiffness behaviour of the micropile both for MC and HS models is similar due to an increase in the value of minimum principal stress σ_3 under the micropile which will lead to an increase in the computed value of E_{50} in that region according to the expression (6.2).

In terms of input value for R_{inter} for this models, it was assumed 0.2 as the best value to obtain the plastic load of the micropiles. This value proved to be valid for both soil models.

In the case of Figure 6.21b the approximation of the numerical curves is acceptable considering the values provided for the MC model in the calibration of the triaxial tests with a confining stress of 50kPa according to the values presented in Table 6.3.

For tensile situation, in the same manner as for compression, the dilatancy was assumed as equal to 0 since there is a sudden drop in the resistance after the full mobilization of the side friction and it was proved to be a very good approach in terms of resistance. If the dilatancy angle would have been considered different than 0, the resistance of the micropile after the full mobilization of the shear resistance would have been increasing.

For the value of E_{ref}^{50} for the HS model, it was assumed, as in the MC model 2 times the input value for E for MC model and it was obtained a very good approach for the initial stiffness of both MC and HS models. Similarly to the compression case, the inputted value of E_{ref}^{50} provide a lower value for E_{50} than the value considered in the MC model however the stiffnesses obtained with both models are very similar. In the tension cases there is not a big change in the value of the confining stress throughout the loading process however, and as it is presented in the sensitivity analysis presented, the tensile models are influenced also by the unload/reload modulus which is 3 times higher than the initial modulus leading therefore to a higher stiffness similar to the MC model.

The value that suits better for the R_{inter} for the soil-micropile interface is 0.3, slightly higher than the 0.2 obtained for the compression cases.

It is very important for this stage to recall that the compression ungrouted tests were conducted prior to the tension tests as described and presented in chapter 4. This can explain the reason why the R_{inter} value is bigger in tension than in compression. It is very likely that a rearrangement and improvement of the soil particles in the vicinity of the micropile occurred from one test to the following.

The improvement in the soil elasticity modulus can also be explained by this factor. If the tension test is assumed as a reload of the compression test, the assumption of the value of E is 3 times larger is likely. For sake of comparison, Plaxis (Plaxis, 2006) considers, by default, the unload/reload value for the elasticity modulus in HS model as 3 times the value of the reference value for E^{50} which is in accordance with the values obtained.

For the modelling of the grouted tests, an estimation of an equivalent diameter to be considered in the analysis was carried out in order to deal with the non-uniform increase in the diameter caused by the grouting of the specimens. The shear resistance of each part of the specimen (grouted and ungrouted) was estimated and the equivalent diameter considering the full length of the micropile properly grouted is then determined, according to the procedure presented in Figure 6.24.

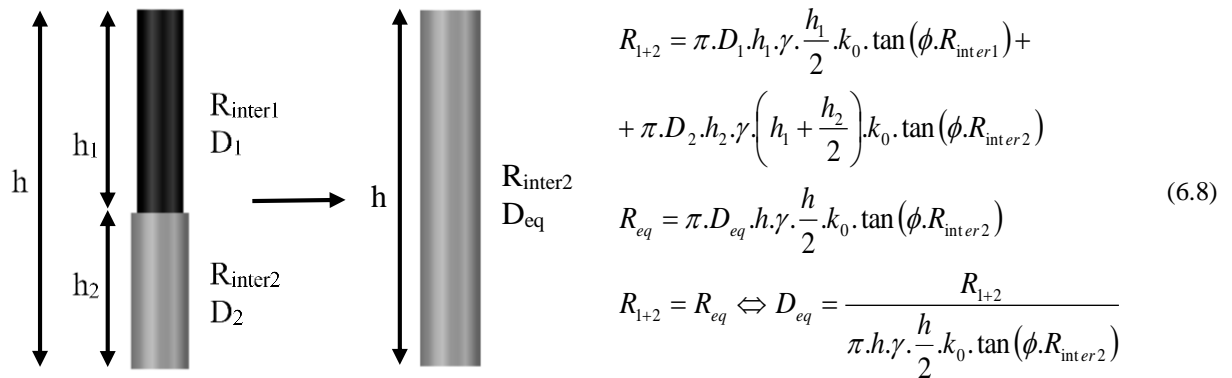


Figure 6.24 – Equivalent grouted diameter estimation procedure

The soil properties were estimated in the triaxial tests for the specimens with density index of 30%, the mean diameter of the grouted portion is 156mm and 35% of the total length of the micropile as grouted (both values according to the measurements of Table 5.5) and $R_{inter1}=0.2$ and $R_{inter2}=1$. Taking these values into consideration and applying the procedure presented, a value of $D_{eq}=97\text{mm}$ was obtained. For the sake of modelling and calibration of the grouted specimens a diameter of 101.6mm will be used. This calculation is valid for the combination $R_{inter1}=0.2$ and $R_{inter2}=1.0$ however since the value of R_{inter1} will be shifted from test to test, it is required an iterative procedure to get a value of R_{inter2} to match the required resistance for a micropile with a diameter of 101.6mm.

The values considered for both models and used in the calibration of the experimental compression test on the grouted specimen are presented in Figure 6.21c along with the correspondent force-displacement experimental curves.

For the calibration of the tension tests on grouted specimens (carried out after the end of the compression tests on grouted specimens), it was considered a slight reduction on the value for R_{inter} for both soil models (0.95 for MC and 0.85 for HS) due to some detachment and/or breaking of the grouting after the compression tests.

In terms of values for the elasticity modulus, it was observed that keeping the same values adopted for the calibration of the compression tests, the agreement between the experimental and the numerical results is very acceptable and so these values will be considered in the following analysis.

The results of this calibration procedure is presented in Figure 6.21d.

According to Figure 6.21c it is possible to understand that an increase of 5 times in the elasticity modulus of the compression ungrouted examples is a good approach for both models between numerical and experimental results.

The reference value for E_{50}^{ref} of the HS model is once again twice the input value E of the MC model. This approximation generates a good agreement between the initial stiffness of both MC and HS models.

As in the previous examples for the calibration, it was considered a value of 0 for the soil dilatancy angle which is shown to be a good agreement between experimental and numerical curves in the tip resistant branch.

For these tests on grouted specimens it was concluded that it is required a lower value for the R_{inter} on HS model than in the MC model to provide the same full mobilization of the shear stress in both models. In order to understand the reason of this difference a detailed analysis was performed. The shear strength is given by the Mohr-Coulomb expression (6.9).

$$\tau = c' + \sigma'_N \times \tan(R_{\text{inter}} \cdot \phi') \quad (6.9)$$

It should be stated that, although Plaxis' reference manual (Plaxis, 2006) explains that the interface parameter R_{inter} should be applied to the value of $\tan(\phi)$, in the version of the program used it was found that it is applied to the friction angle, as presented in expression (6.9).

In the initial state prior to the loading, the value of the normal stress σ_N is coincident with the horizontal stress σ_3 . However this value of σ_N tends to increase with the loading due to the rotation of the principal directions. When the value of σ_3 is not reduced, a higher angle of rotation of the principal directions implies an increase of σ_N .

According to classic material mechanics, the principal stress rotation and value are given by equation (2.1) and (2.3) respectively according to Figure 2.21.

Figure 6.25 shows a comparison, for the same load levels, between the rotation in principal directions for both MC and HS models while Figure 6.26 represents the principal stresses σ_1 and σ_3 intensities obtained for the elements in the vicinity of the interface and for both models in comparison with the analytical value.

In Figure 6.27 it is possible to observe the shear stress in the vicinity of the micropile (interface soil-micropile) for different values of R_{inter} on both MC and HS models in comparison with the analytical values provided by expression (6.9). The presented analysis was done considering load steps where the full mobilization of the shear stress occurred. The analytical (theoretical) value was determined considering $\sigma_N = \sigma_3$ for all cases and all depth.

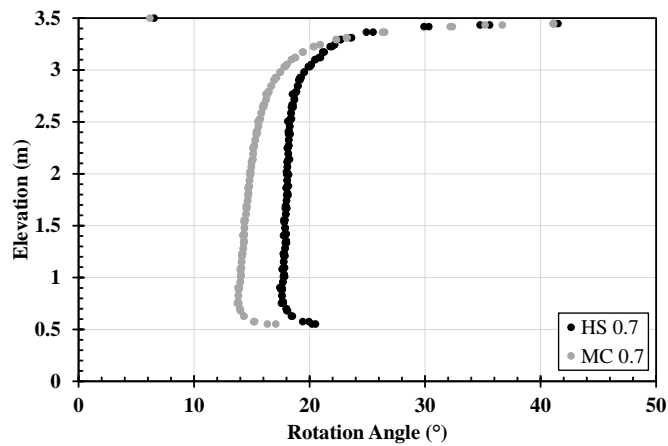


Figure 6.25 – Principal stress directions

It is possible to observe by Figure 6.27 that the HS model results in higher shear stresses when compared with the correspondent value for MC, especially for higher values of R_{inter} . This is the reason why it is required a lower value for R_{inter} for HS models for grouted specimens in order to achieve the same resistance for the full mobilization of the shear stress than the MC model.

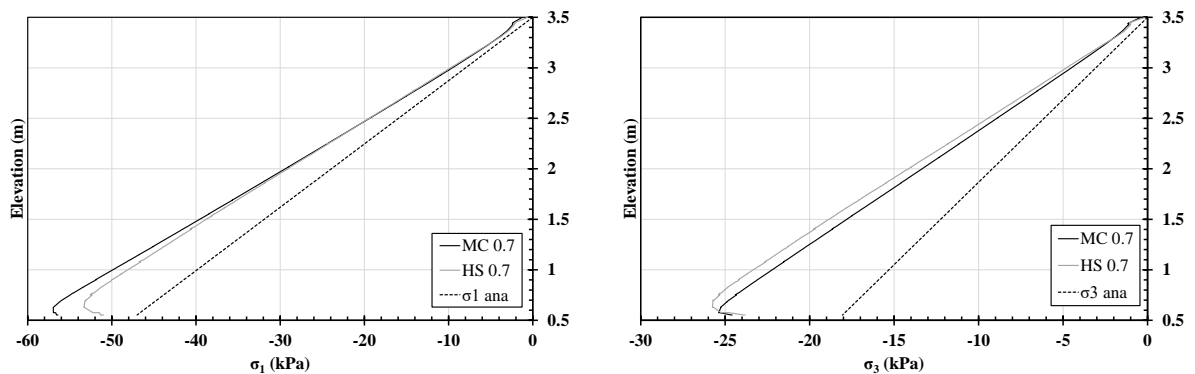


Figure 6.26 – Principal stress intensity

It was also observed that this difference between the analytical stresses (initial stress state) and the numerical stresses (stresses determined for a loading step after full mobilization of the shear stress) is higher in the vicinity of the micropile and tends to stabilize around the theoretical stress value for the given depth as it gets further the micropile. An HS model with $R_{inter}=0.9$ was used to illustrate this comment as depicted in Figure 6.28.

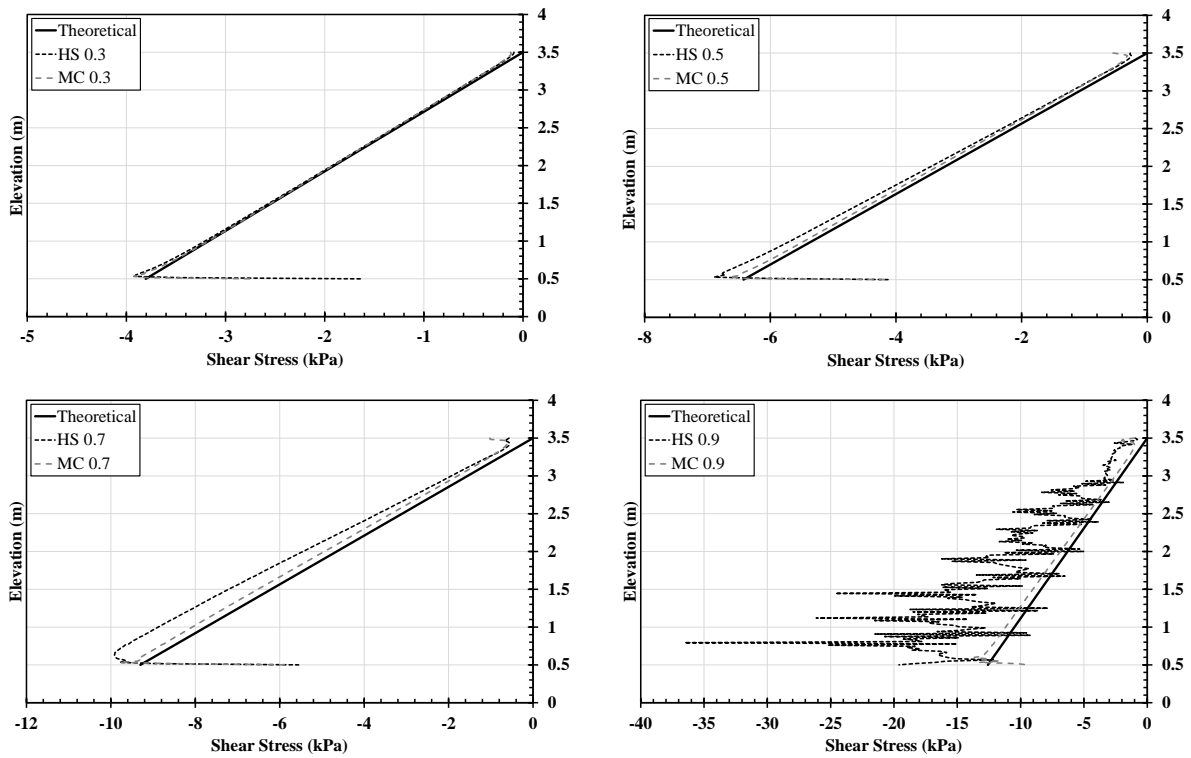


Figure 6.27 – Shear stress comparison

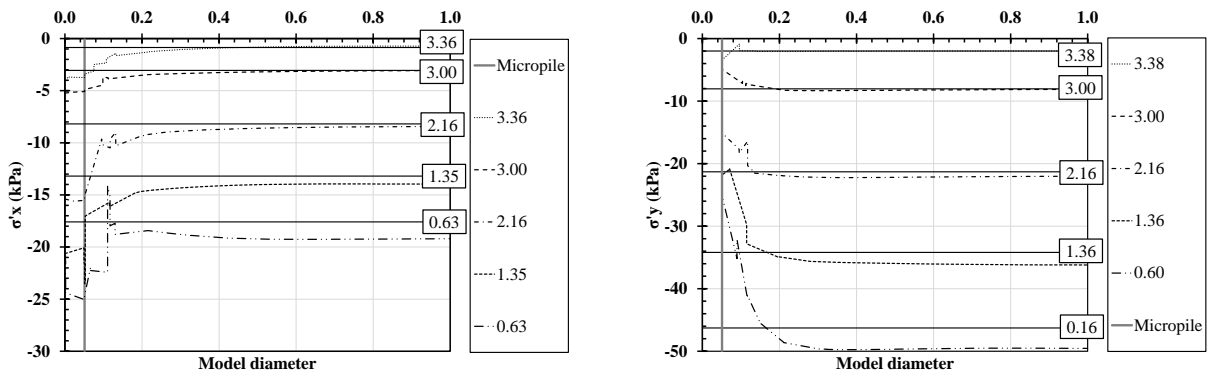


Figure 6.28 – σ_x and σ_y variation along the radial distance (HS model with $R_{inter}=0.9$)

6.4.3.2. Cyclic tests on single specimens

In order to calibrate the numerical parameters to be used in the cyclic models, a representative experimental curve was chosen for each type of loading according to the results presented on chapter 4.

For the calibration of the cyclic compression tests on ungrouted specimens the M7 test was considered to be representative of the considered case, for cyclic tension tests on ungrouted specimens M5, cyclic compression tests on grouted specimens M3 and finally cyclic tension

tests on grouted specimens M7. The values obtained for each case studied are presented in Figure 6.29.

A similar procedure to the calibration of the monotonic tests was executed for the calibration of the cyclic models. Regarding the elastic modulus of the soil, the value considered for the monotonic loading was concluded to be a good approximation to the experimental results, for the case of the ungrouted tests.

The displacement amplitude modelled was the same as obtained in the experimental tests considered for each simulation according to the values presented in Chapter 4. For the tests on ungrouted specimens, a displacement amplitude considered of $\pm 0.7\text{mm}$ was considered in the case of the cyclic+compression test (amplitude obtained in M7 specimen) and $+1.15/-0.4\text{mm}$ for the cyclic+tension test (as obtained in M5 specimen).

As for the monotonic cases, the values for the R_{inter} are similar to the monotonic tests for the compression loading and are slightly higher for the tension loading. This is likely to be related with a rearrangement of the particles due to the cyclic loading applied prior to the monotonic loading. The secant stiffness of the cyclic part is very similar both on numerical and experimental results presented in Figure 6.29 even though the hysteresis is lower in the numerical results.

For the tests on grouted specimens, the parameters considered for elasticity of the soil and for the resistance of the interface were similar to the values tested for the monotonic results. The displacement amplitude considered for the grout cyclic+compression test was $+0.4/-0.2\text{mm}$ (similarly to the obtained amplitude of M3 specimen) and $-0.35/-0.85\text{mm}$ (obtained amplitude in M7 specimen) for the grout cyclic+tension test. The values considered for the interface resistance are also similar for the monotonic and cyclic compression. In the grouted cyclic+tension case, the values for the resistance of the interface remained the same as grouted cyclic+compression, in opposite to the slight reduction verified in the case of monotonic loading. The numerical curves obtained are in very good agreement with the experimental results, both in terms of resistance as in terms of initial (post cyclic) and secant cyclic stiffness both for tension and compression.

In summary, the parameters (elastic modulus and R_{inter}) obtained by this calibration procedure are presented in Table 6.4 and Table 6.5 both for monotonic and cyclic loading. All the calibration models were considered with $\psi=0$ for loose sand.

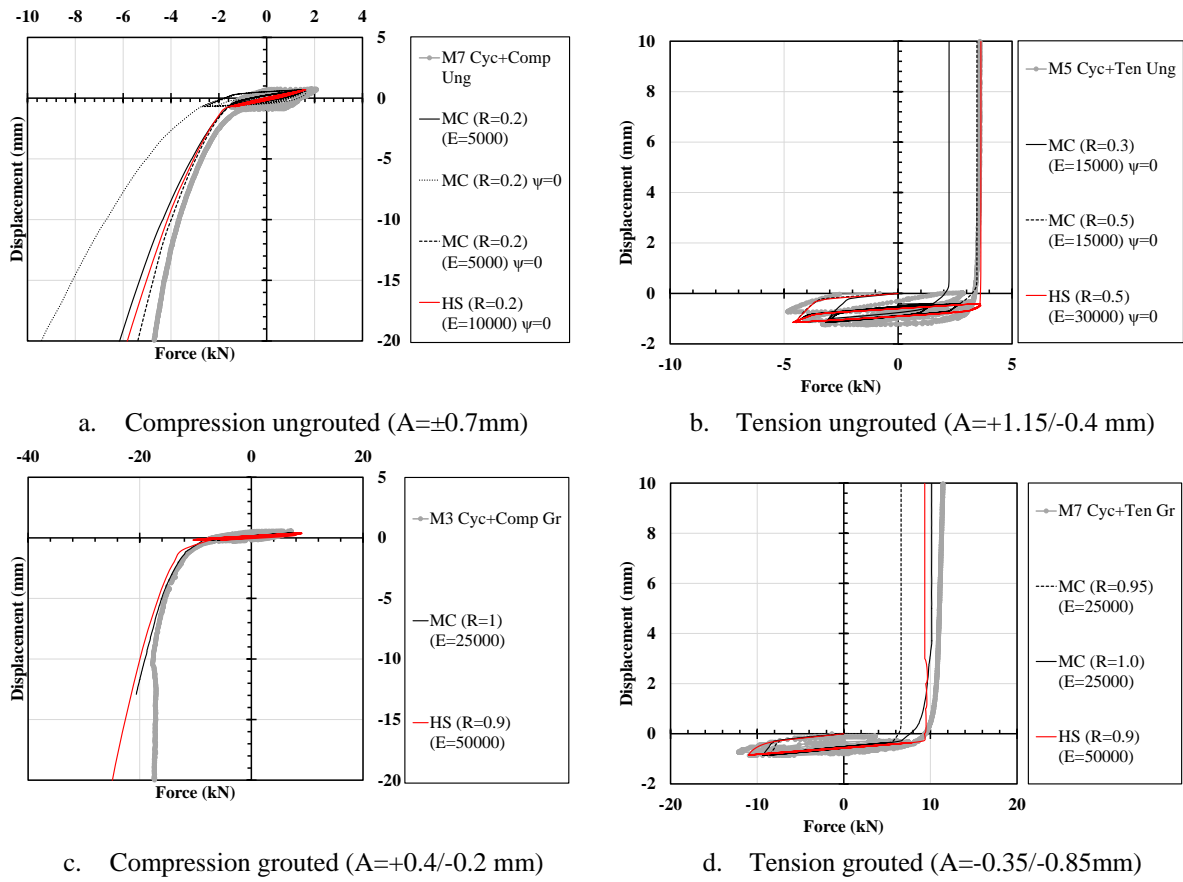


Figure 6.29 – Calibration force-displacement curves for cyclic+monotonic tests

Table 6.4 – Calibration parameters (monotonic tests)

	Comp. Ung.		Tens. Ung.		Comp. Gr.		Tens. Gr.	
	MC	HS	MC	HS	MC	HS	MC	HS
$E_{MC}/E_{50}^{ref} = E_{EDO}^{ref}$ (MPa)	5	10	15	30	25	50	25	50
E_{UR}^{ref} (MPa)	-	30	-	90	-	150	-	150
R_{inter}	0.2	0.2	0.3	0.3	1	0.9	0.95	0.85

Table 6.5 – Calibration parameters (cyclic+monotonic tests)

	Comp. Ung.		Tens. Ung.		Comp. Gr.		Tens. Gr.	
	MC	HS	MC	HS	MC	HS	MC	HS
$E_{MC}/E_{50}^{ref} = E_{EDO}^{ref}$ (MPa)	5	10	15	30	25	50	25	50
E_{UR}^{ref} (MPa)	-	30	-	90	-	150	-	150
R_{inter}	0.2	0.2	0.5	0.5	1	0.9	1	0.9

6.5. Real-scale micropile behaviour

An extrapolation of the results obtained in the calibration process will be addressed in the current section. The results for 3m long micropiles will be extrapolated for ground conditions and micropile geometry (12m length and 250mm diameter) closer to real installation conditions. In this analysis, the complete finite element model of Figure 6.11 was increased 4 times including the distance from the boundaries to the origin.

Both for monotonic and cyclic loading, the parameters obtained from the calibration of the compression tests will be used as standard parameters for the following analysis because the experimental specimens under compression were under undisturbed test conditions. The calibration of the ungrouted tests allowed an estimation for the improvement of the soil properties due to the grouting and throughout this section the obtained value of increase of 5 times in the elastic modulus after grouting will be considered for the MC model. The value secant modulus for HS

The analysis in this section is focused only on the behaviour of grouted micropiles under monotonic and cyclic loading because this is the only viable solution for structural purposes both in terms of stiffness and resistance. A comparison between the behaviour of micropiles installed in loose sand ($I_D=30\%$) and in dense sand ($I_D=70\%$) is also addressed later on.

6.5.1. Loose sand ($I_D=30\%$)

6.5.1.1. Monotonic models

- **Resistance**

The force-displacement curves are presented both for compression and tension loading cases for micropiles with 12m in models considering both MC and HS models. The main goal of this analysis is to estimate the properties of real-scale micropiles installed in loose sand and grouted under the conditions presented in chapter 5. The obtained curves are presented in Figure 6.30. For illustration purposes, the results obtained for 3m long micropiles during the calibration process is also presented.

The definition of the failure load was based in displacement limitation. Both for tension and compression loading it was assumed a displacement of 10% of the diameter of the micropile for the micropiles with $D=250\text{mm}$.

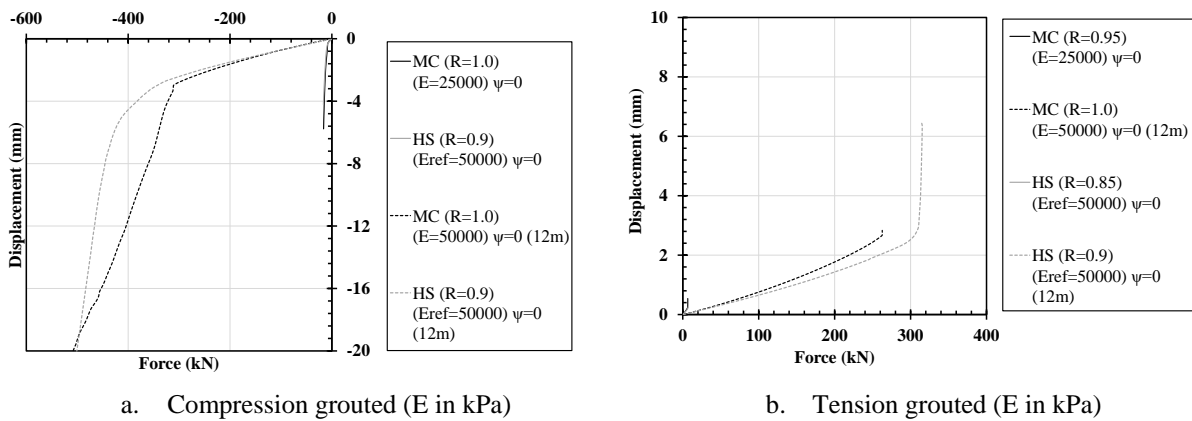


Figure 6.30 – Force-displacement curves for 12m long micropile and comparison with 3m long results (monotonic loading on grouted specimens)

For the estimation of the elasticity modulus of the soil to be inputted on MC model in the case of the 12m long micropile model the expression of Figure 6.22 was used and for a mean confining stress of 37kPa at 6m of depth. A modulus of $E=12\text{MPa}$ was obtained and for the sake of simulation a value of 10MPa was adopted. Since the value of E_{50}^{ref} is independent of the confining stress, this value was kept constant for this 12m long micropile analysis. In the case of the presented analysis of the grouted micropiles, an improvement in the elastic modulus of the soil is considered leading therefore to values of 50MPa for MC model and 50MPa for HS model.

As expected, the resistance and the stiffness for longer micropiles is, obviously, much higher than the correspondent values for the 3m long micropiles. The correspondent values for the 12m long micropile are presented in Table 6.7.

Table 6.6 – Initial stiffness and resistance (monotonic compression grouted) – D30

MC	L (m)	D (mm)	R_{inter}	E (MPa)	ψ (°)	Stiffness (MN/m)	Resistance	
							Load (kN)	Disp. (mm)
	12	250	1	50	0	106	563	25
HS	L (m)	D (mm)	R_{inter}	E (MPa)	ψ (°)	Stiffness (MN/m)	Resistance	
							Load (kN)	Disp. (mm)
	12	250	0.9	50	0	128	521	25

Even with a lower value of inputted R_{inter} , the HS model provides higher resistances than the correspondent MC model. This point is due to the higher stress rotation in the HS model leading to an increase in the confining stress and consequently to an increase in the shear resistance of the system as pointed out in the calibration procedure presented.

The ratio R_{ten}/R_{comp} for the MC model is 0.47 and for HS is 0.60.

Table 6.7 – Initial stiffness and resistance (monotonic tension grouted) – D30

MC	L (m)	D (mm)	R_{inter}	E (MPa)	ψ (°)	Stiffness (MN/m)	Resistance		
							Load (kN)	Disp. (mm)	q_s (kPa)
	12	250	1	50	0	100	263 ^a	2.72	28

HS	L (m)	D (mm)	R_{inter}	E (MPa)	ψ (°)	Stiffness (MN/m)	Resistance		
							Load (kN)	Disp. (mm)	q_s (kPa)
	12	250	0.9	50	0	128	315 ^b	6.37	33

^a last converged value – 271kN obtained with a linear extrapolation to 25mm

^b last converged value – 321kN obtained with a linear extrapolation to 25mm

- **Initial Stiffness**

The values obtained for the initial stiffness of each considered model are presented in Table 6.6 and Table 6.7.

The ratio $S_{j,ini_ten}/S_{j,ini_comp}$ is 0.94 for the MC model and 1.0 for HS. The value for MC is expected since in this case the tip resistance is improving the stiffness in the compression case leading to a higher value however in the HS model the stiffnesses are similar both for tension and compression because of the contribution of the value of the higher unload/reload elastic modulus.

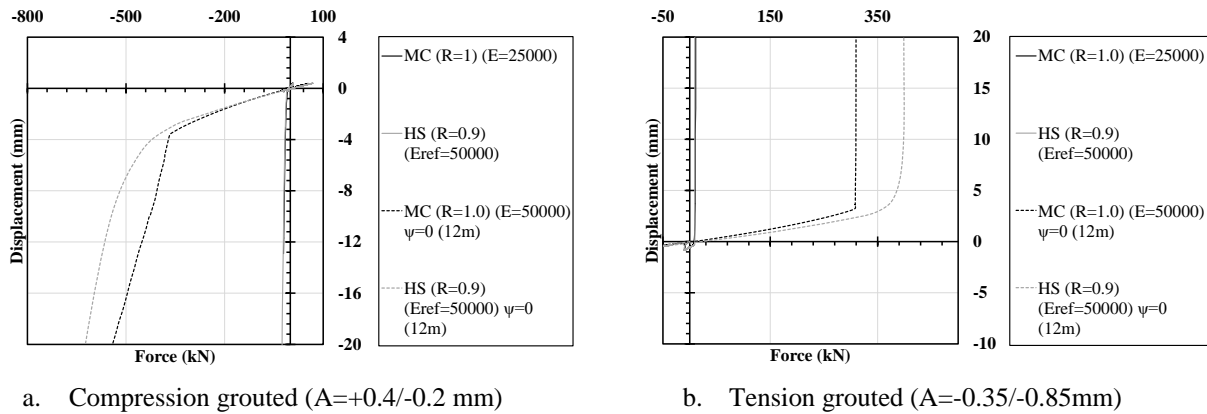
6.5.1.2. Cyclic models

- **Resistance**

For the sake of comparison, in this analysis it will be considered a cyclic loading prior to the monotonic loading with the same amplitude as in the calibration procedure (3m micropile). The results, in terms of force-displacement curves, are presented in Figure 6.31 for all the considered results. The 3m long micropile results are presented for sake of comparison.

The properties used in these models are in accordance with the correspondent properties used in the monotonic modelling presented before

The resistance and initial stiffness for the grouted tests are presented on Table 6.8 and Table 6.9.



a. Compression grouted (A=+0.4/-0.2 mm) b. Tension grouted (A=-0.35/-0.85mm)

Figure 6.31 – Force-displacement curves for 12m long micropile and comparison with 3m long results (cyclic+monotonic loading)

The ratio R_{ten}/R_{comp} for the MC model is 0.52 and for HS is 0.61 which is close to the same ratio obtained in the monotonic tests even though the last step of convergence occurred before the adopted failure displacement in the monotonic analysis.

Table 6.8 – Initial stiffness and resistance (cyclic+monotonic compression grouted) – D30

MC	L (m)	D (mm)	Disp. amp. (mm)	Load amp. (mm)	R_{inter}	E (MPa)	ψ (°)	Stiff. (MN/m)	Resistance	
									Load (kN)	Disp. (mm)
	12	250	0.6	86.87	1	50	0	120	599	25

HS	L (m)	D (mm)	Disp. amp. (mm)	Load amp. (mm)	R_{inter}	E (MPa)	ψ (°)	Stiff. (MN/m)	Resistance	
									Load (kN)	Disp. (mm)
	12	250	0.6	93.45	0.9	100	0	128	649	25

Table 6.9 – Initial stiffness and resistance (cyclic+ monotonic tension grouted) – D30

MC	L (m)	D (mm)	Disp. amp. (mm)	Load amp. (mm)	R_{inter}	E (MPa)	ψ (°)	Stiff. (MN/m)	Load (kN)	Disp. (mm)	Resistance
											q_s (kPa)
	12	250	0.5	74.12	1	50	0	112	310	25	33

HS	L (m)	D (mm)	Disp. amp. (mm)	Load amp. (mm)	R_{inter}	E (MPa)	ψ (°)	Stiff. (MN/m)	Load (kN)	Disp. (mm)	Resistance
											q_s (kPa)
	12	250	0.5	80.14	0.9	100	0	137	399	25	42

6.5.1.3. Cyclic and Initial (post-cyclic) stiffness

The values obtained for the initial stiffness of each considered model are presented on Table 6.8 and Table 6.9.

The ratio $S_{j,ini_ten}/S_{j,ini_comp}=0.93$ for the MC model and 1.1 for HS which is very similar to the results obtained for the monotonic analysis and so the comments are still valid for this section.

The cyclic secant stiffness, determined in the same way as for the experimental tests using the same procedure of Figure 5.46 is presented on Figure 6.32.

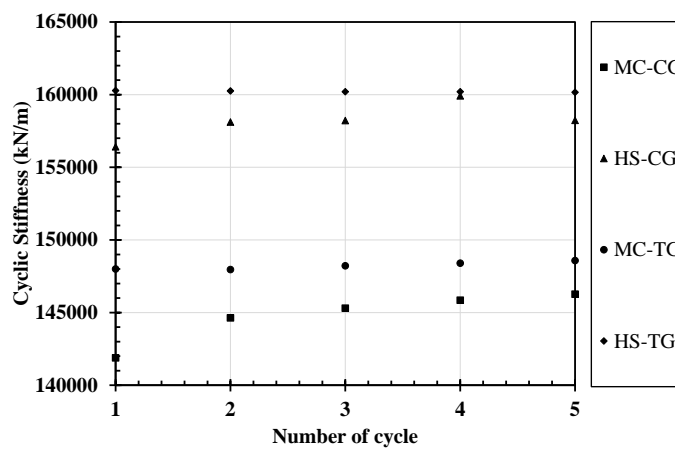


Figure 6.32 – Cyclic secant stiffness on grouted specimens – D30

The values obtained for cyclic secant stiffness are very similar both for tension and compression cases (ratio of mean value of $S_{cyc_ten}/S_{cyc_comp}=1.0$ for both soil models) which is completely expected since the numerical models have the same properties.

The cyclic stiffness is, for all the considered cases, higher for the HS model in comparison with the MC correspondence which is foreseen since the HS model provides and higher unload/reload elastic stiffness in comparison with the MC model, which considers the same module for unload/reload and for primary loading.

6.5.2. Dense sand ($I_D=70\%$)

Taking into consideration the results presented in section 6.5.1, it is possible to understand that the resistances obtained are not feasible for a use on practical situations such as the reinforcement of foundations to support wind towers. Considering the design example of chapter 4, where micropiles with characteristic compressive resistances of 2262kN are used, the study of these elements installed in dense sand is very relevant.

In the following sections, the results obtained for micropiles installed in a dense sand with $I_D=70\%$, characterized by Ferreira (2014), are presented. The mechanical properties of the sand as well as the calibrated parameters for both MC and HS models are presented in Table 6.2.

Both the displacement failure (10%D) and the improvement caused by the grouting (increase 5 times of the secant modulus) is followed in the same manner as for the loose sand.

6.5.2.1. Monotonic models

- **Resistance**

The numerical results obtained, in terms of force-displacement curves, are presented in Figure 6.33. The parameters considered for the analysis of the micropiles installed in loose sand where considered for this analysis.

For the estimation of the elastic modulus of both models to be used in this analysis, a similar procedure to the considered in the loose sand analysis was used. Considering the values obtained with the triaxial tests performed by Ferreira (2014) and presented on Table 6.10, a power regression was obtained and the correspondent elastic modulus was retrieved for the mean confining stress of the analysis.

The obtained expression for the power regression is presented in Figure 6.34 and for a confining stress 28.96kPa obtained at mid depth (6m) leads to a value for $E=15\text{MPa}$. Assuming the same improvement in the soil as obtained in the calibration procedure (improvement of 5 times in the elasticity modulus), the value to be considered is then $E=75\text{MPa}$ for grouted conditions.

Excluding the commented behaviour of the HS model detected in the previous analysis (increase in the elastic modulus due to the increase of the horizontal stress under the micropiles for compressive tests and unload of the isotropic effective stress leading to a consideration of the E_{UR}^{ref} in the analysis) the value to be considered for the E_{50}^{ref} should be 36MPa (value for a confining stress of 100kPa) incremented 5 times due to the grouting effect (180MPa), however in this case, and in order to obtain a similar initial stiffness for both MC and HS models, it was obtained a value for the E_{50}^{ref} of 120MPa and will be used in the subsequent analysis.

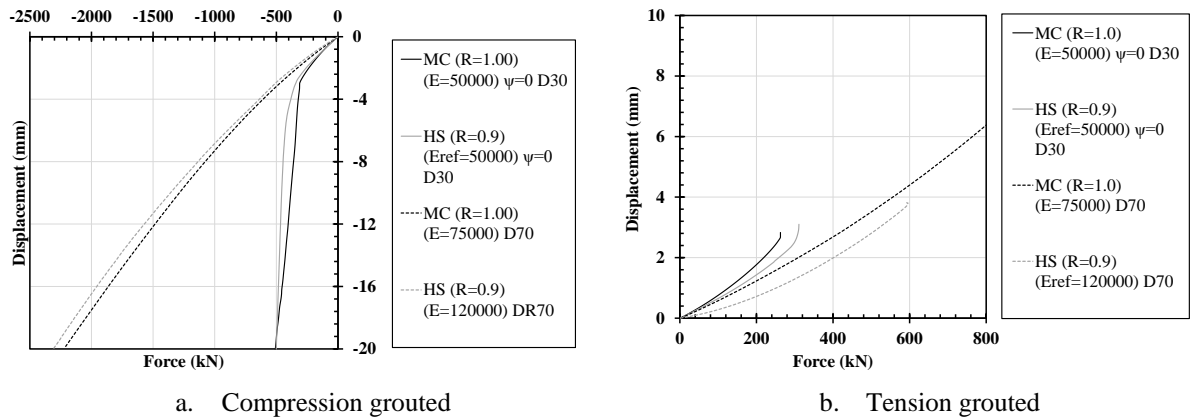


Figure 6.33 - Force-displacement curves for 12m long micropile in high density and comparison with 12m long micropiles in low density sand (monotonic loading)

Table 6.10 – E values for MC model (triaxial tests calibration) – high density sand

Confining stress (kPa)	E (MPa)
50	25
100	36
200	68

Even though the friction angle is considerably higher for the high density sand, the mobilization of the full shear strength of the side resistance occurs for the same load because the horizontal stresses (σ'_3) are lower due to the lower value of K_0 . Considering equation (6.9), the shear resistance is governed by the value of friction angle but also for the value of σ'_3 .

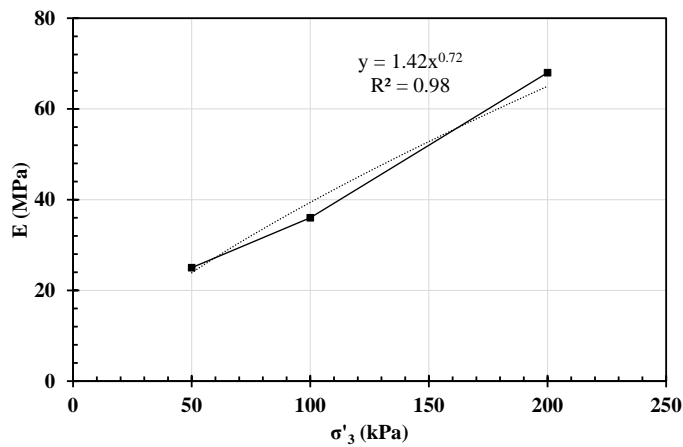


Figure 6.34 – Power regression for E value (high density sand)

The resistance and initial stiffness for the compression grouted tests are presented in Table 6.11.

Table 6.11 – Initial stiffness and resistance (monotonic compression grouted) – D70

MC	L	D	R_{inter}	E (MPa)	ψ (°)	Stiff. (MN/m)	Resistance	
	(m)	(mm)					Load (kN)	Disp. (mm)
	12	250	1	75	15.7	166	2657	25

HS	L	D	R_{inter}	E (MPa)	ψ (°)	Stiff. (MN/m)	Resistance	
	(m)	(mm)					Load (kN)	Disp. (mm)
	12	250	0.9	120	15.7	181	2715	25

Table 6.12 – Initial stiffness and resistance (monotonic tension grouted) – D70

MC	L	D	R_{inter}	E (MPa)	ψ (°)	Stiff. (MN/m)	Resistance		
	(m)	(mm)					Load (kN)	Disp. (mm)	q_s (kPa)
	12	250	1	75	15.7	155	1402 ^a	13.9	149

HS	L	D	R_{inter}	E (MPa)	ψ (°)	Stiff. (MN/m)	Resistance		
	(m)	(mm)					Load (kN)	Disp. (mm)	q_s (kPa)
	12	250	0.9	150	15.7	202	596 ^b	3.8	63

^a last converged value – 2207.3kN obtained with a linear extrapolation to 25mm

^b last converged value – 1124.6kN obtained with a linear extrapolation to 25mm

The ratio R_{ten}/R_{comp} for the MC model is 0.53 and for HS is 0.19. In this case the conclusions cannot be definitive since the convergence occurred for lower displacements. It is likely that an increase in the strength would occur. Considering the tensile resistances obtained via linear extrapolation the same ration will take the values 0.83 for MC and 0.37 for HS.

- **Initial Stiffness**

The values obtained for the initial stiffness of each considered model are presented in Table 6.11 and Table 6.12.

The ratio $S_{j,ini_ten}/S_{j,ini_comp}$ is 0.93 for the MC model and 1.0 for HS. Similarly to the monotonic results in the loose sand, the value for MC is expected since in this case the tip resistance is improving the stiffness in the compression case leading to a higher value however in the HS model the stiffnesses are similar both for tension and compression because of the contribution of the value of the higher unload/reload elastic modulus.

6.5.2.2. Cyclic models

- **Resistance**

In the current analysis, the parameters for the soil models are the same as in the monotonic analysis. For sake of comparison, both micropile models with $I_D=30\%$ and $I_D=70\%$ were subjected to a cyclic loading of $\pm 1\text{mm}$ followed by the monotonic loading (compression or tension).

The results obtained are presented on Figure 6.35 for the considered cases.

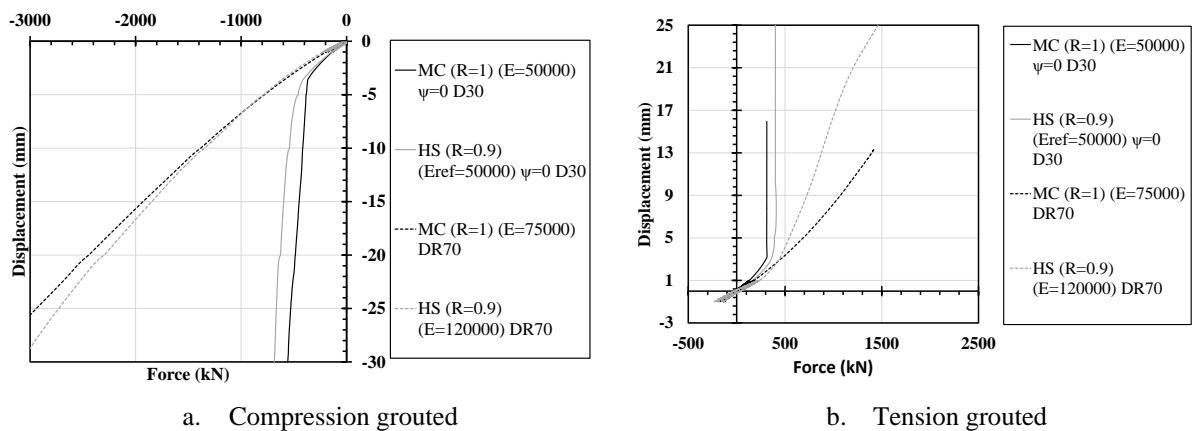


Figure 6.35 - Force-displacement curves for 12m long micropile in high density and comparison with 12m long micropiles in low density sand (cyclic+monotonic loading)

The trend of the curves obtained is in agreement with the results obtained only for monotonic loading. Even though the friction angle of the soil is bigger for the high density sand, the value of K_0 is smaller and therefore the confining stress is smaller leading to a close shear strength. The main differences between both densities are given by the consideration of dilatancy in the high density sand leading to an increase in the side resistance after full mobilization of the shear strength.

The values obtained for resistance and stiffness are presented, for the grouted specimens installed in sand with $I_D=70\%$, in Table 6.13 and Table 6.14.

For MC models the ratio R_{ten}/R_{comp} is 0.79 while for the HS takes the value 0.53. The values cannot be directly compared with the monotonic results due to the early lack of convergence in the monotonic tensile tests.

Table 6.13 – Initial stiffness and resistance (cyclic+monotonic compression grouted) – D70

MC	L (m)	D (mm)	Disp. amp. (mm)	Load amp. (mm)	R_{inter}	E (MPa)	ψ (°)	Stiff. (MN/m)	Resistance	
									Load (kN)	Disp. (mm)
	12	250	2	370.9	1	75	15.7	177	2940	25

HS	L (m)	D (mm)	Disp. amp. (mm)	Load amp. (mm)	R_{inter}	E (MPa)	ψ (°)	Stiff. (MN/m)	Resistance	
									Load (kN)	Disp. (mm)
	12	250	2	399.3	0.9	120	15.7	191	2727	25

Table 6.14 – Initial stiffness and resistance (cyclic+monotonic tension grouted) – D70

MC	L (m)	D (mm)	Disp. amp. (mm)	Load amp. (mm)	R_{inter}	E (MPa)	ψ (°)	Stiff. (MN/m)	Load (kN)	Disp. (mm)	q_s (kPa)

HS	L (m)	D (mm)	Disp. amp. (mm)	Load amp. (mm)	R_{inter}	E (MPa)	ψ (°)	Stiff. (MN/m)	Load (kN)	Disp. (mm)	q_s (kPa)

^a last converged value – 2312.25kN obtained with a linear extrapolation to 25mm

- **Cyclic secant and initial (post-cyclic) stiffness**

The values obtained for the initial stiffness of each considered model are presented in Table 6.13 and Table 6.14. The ratio $S_{j,ini_ten}/S_{j,ini_comp}$ is 0.91 for the MC model and 0.93 for HS and are in accordance with the monotonic results with an expected higher compressive initial stiffness.

The cyclic secant stiffness, determined in the same way as for the experimental tests using the same procedure of Figure 5.46 is presented on Figure 6.36.

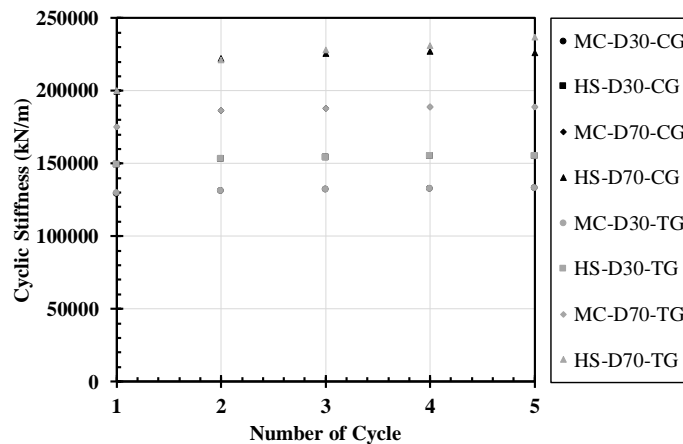


Figure 6.36 – Cyclic secant stiffness

The values obtained for cyclic secant stiffness are coincident both for tension and compression cases which is completely expected since the numerical models have the same properties. A comparison between MC and HS results shows that the HS models provide higher (1.17 for D30 and 1.19 in D70) secant stiffness due to the mobilization of the higher E_{UR} modulus instead of MC which consider the same module for unload/reload and for primary loading and the stiffness for the dense sand is also higher (1.41 for MC and 1.44 for HS model) than the stiffness for the loose sand.

6.6. Design review of hybrid foundations – detailed analysis of micropiles installed in hybrid foundations for wind towers

Shallow foundations reinforced with micropiles present a behaviour governed by both foundation elements, the ground conditions and the applied loads.

The procedure for the design of this foundation system is presented in Chapter 4 along with some practical design examples for different wind tower foundations. In the referred design, the micropiles considered were 12m long, 200mm of diameter and a shear resistance (grout-to-ground bond resistance) of 300kPa. These properties led to a characteristic resistance of 2262kN in tension. For the distribution of the micropiles under the foundation, a distance equal or higher than 3.D was assumed in order to reduce the group effect according to Federal Highway Administration (2005) and according to the results obtained experimentally in the test on groups of ungrouted specimens.

In the current section, a review on the numerical results (micropile properties) presented in section 6.5 is addressed in order to obtain a representative bilinear curve for each of the micropile and ground conditions tested which are going to be used in the update of the numerical models for the design of the hybrid foundation considered in chapter 4. The main

idea of this section is to update the chapter 4 model with representative behaviour of the micropiles with real behaviour of the soil and valid for the grouting conditions considered. The micropiles tested experimentally can be classified, in terms of grouting technique, approximately as Type A or B according to FHWA manual (FHWA, 2005). The grout-to-ground bond resistance values provided by this guide for Type A or B micropile are much smaller than the 300kPa adopted in the design example. This value of $q_s=300\text{kPa}$ is common for Type C or D, respectively IGU or IRS according to Bustamante and Doix (1985) method) for a soil with good properties. Given the results obtained for the micropiles installed in loose sand, it is possible to conclude that it is not a feasible solution for the reinforcement of foundations for wind towers since it will require a very high number to withstand with the applied load turning this into a non-viable solution. Following, the behaviour of micropiles installed in dense sand to be used in as reinforcement of shallow foundations is addressed.

The numerical analysis presented in the previous sections proved to be valid for the estimation of the behaviour of micropiles based on the experimental tests. The results are valid only for this specific test conditions (micropile type, grouting conditions, density and mechanical properties of the sand) however the numerical approach is valid for other conditions.

The estimation of the value of grout-to-ground bond strength (q_{s_gr}) is presented both for loose and dense sand considering the procedures presented by Bustamante and Doix (1985), FHWA manual (FHWA, 2005) and CLOUTERRE abacus (Presses de l'Ecole Nationale des Ponts et Chaussées, 2002).

The abacus for sands proposed for Bustamante and Doix (1985) can be found in Figure 6.37 with the obtained results both for low and high density sand at half depth of the micropiles (6m). Considering the abacus, an estimation for the value of q_{s_gr} is possible based on the use of the number of blows in SPT test. To achieve a 300kPa shear resistance it would be required a number of blows in SPT test of 60 or higher for IGU technique and 50 for IRS technique.

For the estimation of the number of blows for the SPT test it was considered the correlation proposed by Mayne et al. (2001) with a correlation between density index and number of blows normalized for atmospheric pressure ($(N_1)_{60}$) given by equation (6.10).

$$I_D = 100 \sqrt{\frac{(N_1)_{60}}{60}} \quad (6.10)$$

For a density index of 30% the value for $(N_1)_{60}$ is 5 while for 70% is 29. In order to correct the value for the vertical stress at the level of the measurement, the normalized value should

be affected by C_N coefficient given by equation (6.11) according to Liao and Whitman (1986).

$$C_N = \sqrt{\frac{p_a}{\sigma'_{v0}}} \quad (6.11)$$

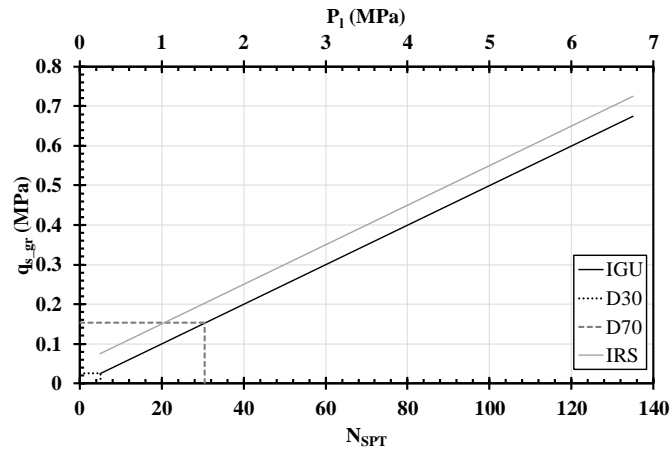


Figure 6.37 – Abacus for the estimation of the value of q_s for sands including the estimations for the considered D30 and D70 sand (adapted from Bustamante and Doix (1985))

Table 6.15 – Estimated values for q_s for IGU considering the method proposed by Bustamante and Doix (1985)

	Depth (m)	σ'_v (kPa)	C_N	N_{60}	q_s (kPa)
D30 ($\gamma=15.95$ kN/m ³)	0	0.0	2.00	0	0
	-6	-95.7	1.04	5	26
	-12	-191.4	0.52	10	52
D70 ($\gamma=17.3$ kN/m ³)	0	0.0	2.00	0	0
	-6	-103.8	0.96	31	153
	-12	-207.6	0.48	61	305

The values obtained are graphically presented in Figure 6.38.

According to FHWA (2005) the typical values of shear resistance for micropiles type A or B are respectively 70-145kPa or 70-190kPa for low density sand and 95-215kPa or 120-360kPa for high density sand.

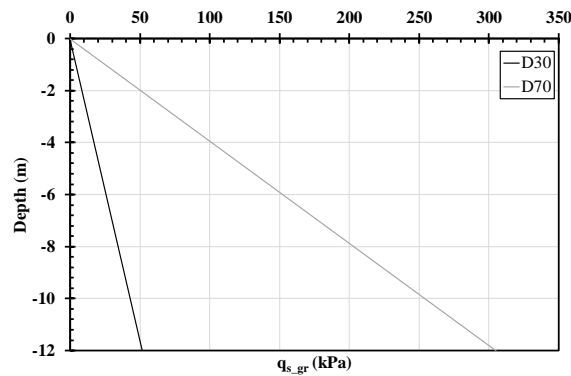


Figure 6.38 – Grout-to-ground bond strength variation in depth for IGU grouting

The maximum grout-to-ground bond resistance with soil nailing technique should be around 25kPa for low density sand and 100kPa for high density sand according to Presses de l'Ecole Nationale des Ponts et Chaussées (2002) using the abacus of Figure 6.39.

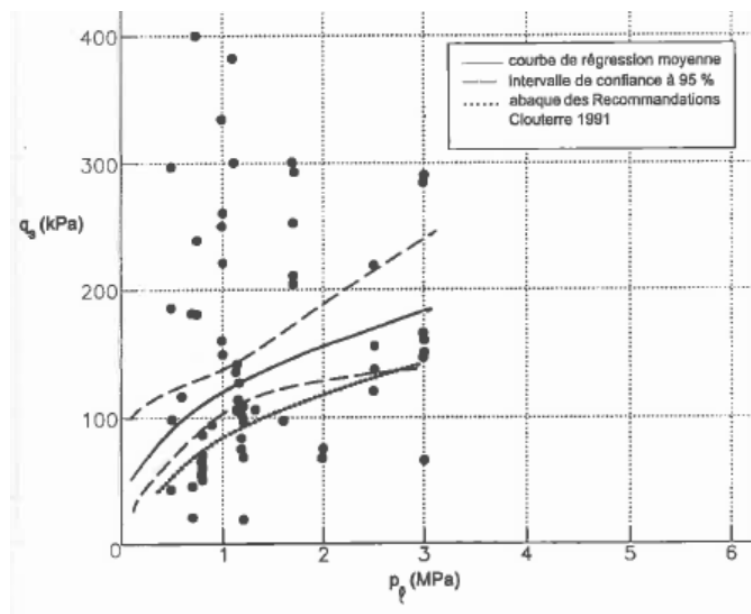


Figure 6.39 – Abacus for the estimation of the value of $q_{s,gr}$ on soil nailing technique with gravitic grout injection (Presses de l'Ecole Nationale des Ponts et Chaussées, 2002)

The grouting technique used on the experimental tests presented on Chapter 5 should lead to results close to the values provided by the soil nailing techniques due to the similarities of both, however for the loose sand the shear resistances given by the soil nailing technique is the same as the IGU technique proposed by Bustamante and Doix (1985). This conclusion is valid also for the 3m long micropiles where a mean value of $q_s=6$ kPa is obtained from a value of $p_1=0.06$ MPa. For this range of values of p_1 ($p_1 < 0.25$ MPa) the estimation of q_s is harder, nevertheless it is forecasted a value considerably lower than $q_s=25$ kPa as obtained for 12m

micropiles on loose sand and so the value of $q_s=6\text{kPa}$ obtained using the abaqus of Bustamante and Doix (1985) is a good approach for this specific case. The differences are bigger for a soil with better mechanical properties such as the high density sand considered.

The value of $q_s=150\text{kPa}$ is in accordance with the value proposed by the FHWA guide (FHWA, 2005) for micropiles installed in high density sand using a grouting technique type A or B. According to the same document, the value of 300kPa is viable also for micropiles in the same conditions but grouted according the recommendations for type C or D which makes it feasible the value considered for the shear resistance in the design example of Chapter 4.

In terms of stiffness, in the models considered in Chapter 4, it was assumed a stiffness of 50MN/m (1000kN resistance for 20mm displacement) however this is a low stiffness in comparison with the numerical values obtained in the analysis presented.

A representation of the bilinear curves representing each studied case compared with the micropile behaviour of Robot (2015) model of Chapter 4 is presented in Figure 6.40. The values considered are presented in section 6.5 for each correspondent case, only for the grouted examples.

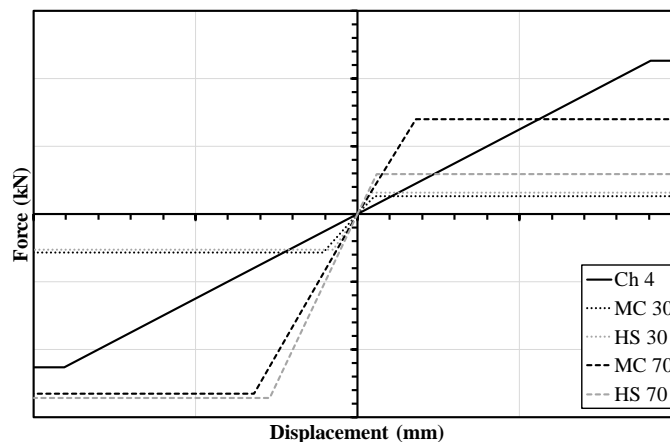


Figure 6.40 – Bilinear curve comparison between the behaviour assumed for the design examples and the results obtained for each considered soil model on low and high density sand

The resistances obtained for the high density sand and the chapter 4 curves are very similar, however the diameter considered in the numerical analysis was 250mm versus the 200mm of the Robot (2015) model micropile. In terms of shear strength, the numerical values obtained are close to 30kPa for D30 sand. For the high density sand models under monotonic loading $q_s=63\text{kPa}$ and $q_s=149\text{kPa}$ for HS and MC respectively, versus the $q_s=300\text{kPa}$ considered in chapter 4. Even that the convergence has stopped before the limit displacement, the path should be similar to obtained in the models with cyclic loading. Considering the results for the

models under cyclic+monotonic loading the correspondent shear strength is 154kPa and 245kPa respectively for HS and MC soil models.

The stiffness values are higher in the numerical models than what was considered in the earlier model. For the case of the high density sand, the average stiffness is 170MN/m against the value of 50MN/m considered in chapter 4. If compared with real scale tests on micropiles with a grouted diameter of 210mm and 8m of grouting length with the IRS technique (pipe with 210mm of diameter and 10m of length) the numerical stiffness for the high density sand is similar even grouted with a different technique. According to the results of an *in-situ* test presented in Figure 6.41, the obtained stiffness of this micropile is close to 200MN/m.

For sake of comparison with the results of chapter 4 it was modelled (with MC model) a micropile with 12m long and with a diameter of 200mm in dense sand and a value of 200kPa of shear stress and a stiffness around 100MN/m was obtained. The effect of the reduction of the shear stress and the increase of the stiffness was evaluated for the case of the steel towers foundations.

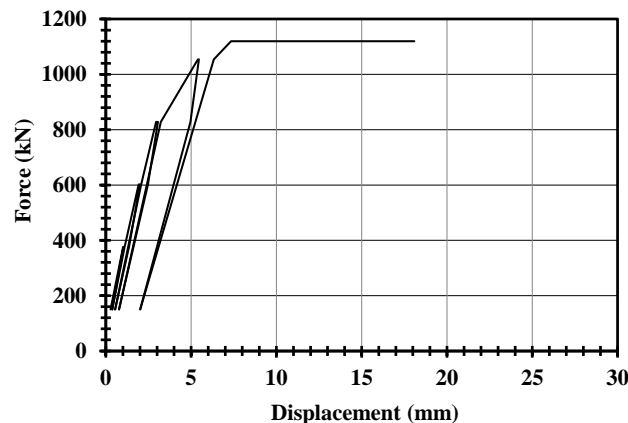


Figure 6.41 – Real tests on micropile with IRS grouting technique (Tecnasol, 2010)

The design procedure of chapter 4 was considered as well as the foundation geometry in order to allow a proper comparison. The obtained results for the geometry of the hybrid foundation under the loading considered in chapter 4 are presented in Table 6.16 which should be compared with the values presented in Table 4.9. The detailed design analysis considered is presented in Annex F.

The increase in the stiffness of the micropiles will lead to an increase of the foundation dimensions and/or in the micropile dimensions. According to the results presented in Table 6.16, the required concrete volume for the hybrid foundations is higher in comparison with the examples of the micropiles with the properties presented in chapter 4 (Table 4.9). In the example of the hybrid foundation for the steel tower with 150m, the obtained dimensions for

the hybrid foundations are the same as the shallow foundation considering the same micropile distribution as in chapter 4 (64 micropiles - Figure 4.9b). The allowed resistance of the micropiles under this grouting conditions is relatively low and so a feasible solution for this structure would be the use of micropiles with higher shear strength given by better grouting techniques like IRS or IGU.

Table 6.16 - Hybrid foundation geometry with grouted micropiles under very low pressure grout

Tower type	80m	100m	150m
	2.0MW	3.6MW	5.0MW
	Steel	Steel	Steel
H_f	2.00	3.00	3.50
Governing load case	EW	EW	EW
Typology (according to Figure 4.9)	a	c	b
H_1 (m)	1.23	1.65	1.20
H_2 (m)	2.00	3.00	3.50
H_3 (m)	0.50	0.50	0.50
I (m)	5.80	7.04	8.70
B_{eq} (m)	14.38	17.46	21.57
B(m)	14.00	17.00	21.00
B_0 (m)	5.60	8.00	11.00
C (m)	15.15	18.4	22.73
Concrete (m ³)	276.2	599.8	981.9

A parametric study was carried out in order to evaluate the effect of the micropile stiffness on the design of the foundation. For the sake of comparison, it was considered a square foundation with constant thickness of 2m under constant loading (bending moment and axial loading) and changing the studied parameters. The design procedure presented in Chapter 4 was followed. The micropiles were assumed to have 12m of length, 250mm of diameter and 300kPa of shear strength. The micropiles were placed with a distance from the edge of the foundation of 0.5m. Thirty-two micropiles along the edges were considered except in the analysis of the influence of the number of micropiles.

The results obtained in the parametric study are presented in Figure 6.42 by changing the following parameters: stiffness of the micropiles, number of micropiles and elastic modulus of the soil.

As it is possible to conclude by the analysis of Figure 6.42, an increase in the stiffness of the micropiles will lead to an increase in the foundation geometry in comparison with the results of Chapter 4 because these elements are going to withstand higher forces. The increase in the

number of micropiles will naturally reduce the foundation geometry as well as the improvement in the soil properties.

Foundations for wind towers are mainly subjected to high vibrations both due to ultimate limit states such as starting/stopping of the turbine, extreme winds, etc. but also due to the vibration induced by the normal wind.

The highest wind tower considered in the study of Chapter 4 is 150m high. In order to have the characteristic wind load along with the variable component of the load, a simulation using the software Ashes (2016) was carried out for a wind speed of 12m/s which leads to the highest stresses in the tower as concluded in Chapter 2. NWM model according to IEC 61400-1 should be estimated for a reference wind speed of 25m/s however the stresses due to 12m/s and 25m/s are similar due to the pitch angle control of the wind turbine blades.

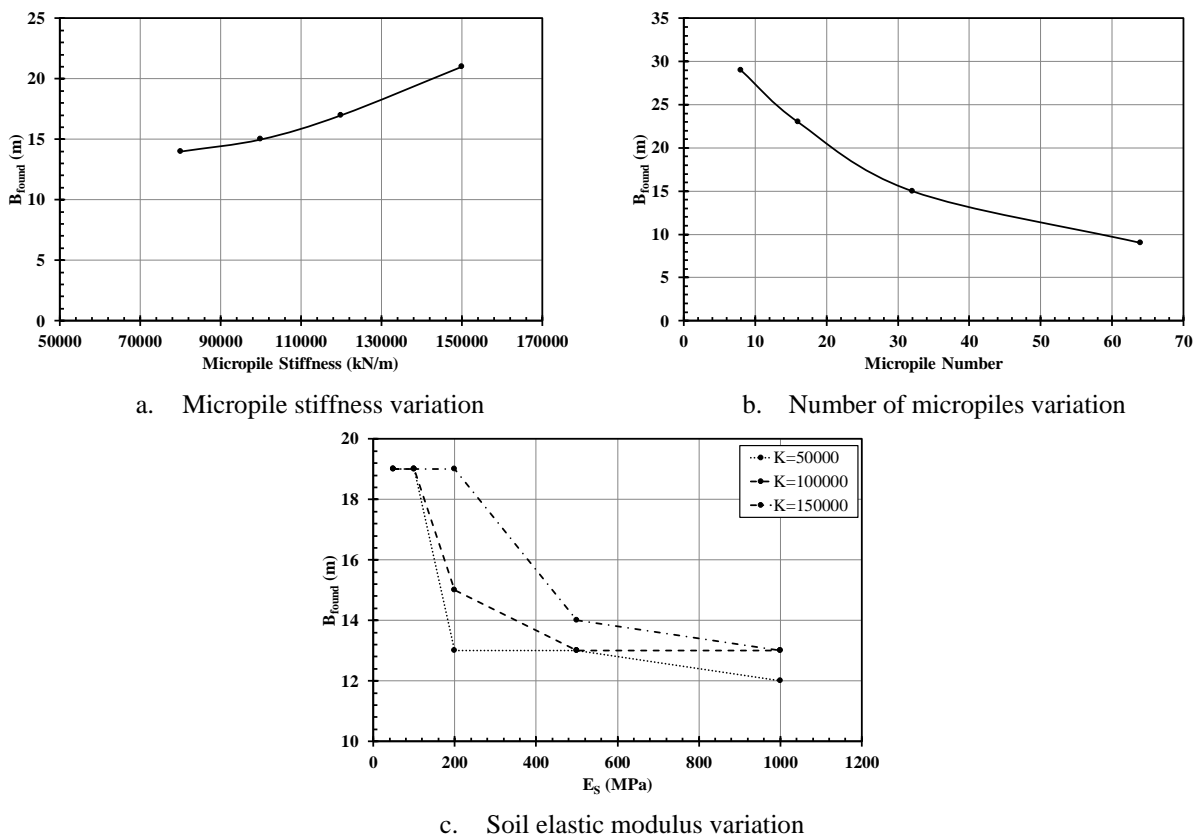


Figure 6.42 – Parametric analysis on the influence of relevant parameters for the behaviour of the foundation

The results obtained for the 150m high steel tower under 12m/s of wind speed are presented in Figure 6.43 in terms of base bending moment.

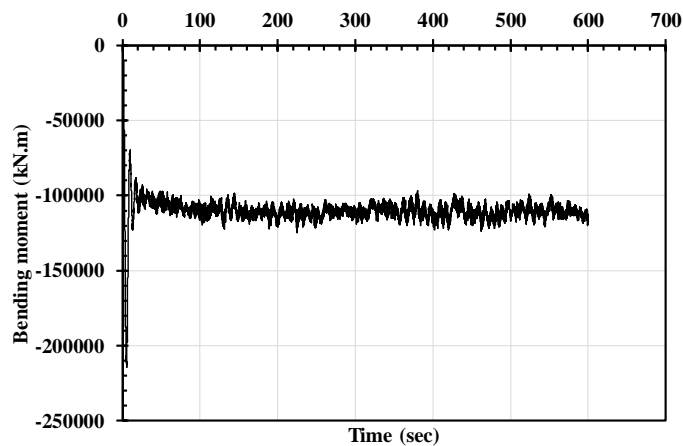


Figure 6.43 – Characteristic base bending moment induced by wind loading on a 150m high wind tower – 12m/s wind speed

The initial part of the curve is sparser than the end because this simulation is based on the premises that the wind tower is standing still before the analysis and in the beginning is suddenly stroke by a gust of 12m/s. After the stabilization of the response it is possible to extract the required results.

The mean value of the bending moment (after 100sec) is close to 111000kN.m. The variation around this value is around $\pm 13\%$. This value is close to the turbulence defined by IEC 61400-1 for class A (0.16) or class B (0.14) wind towers.

According to IEC standard (IEC 61400-1, 2005), the normal turbulence model (NTM) is obtained using a safety factor of 1.35 providing therefore a value for the bending moment of 150000kN.m. This value is 55% of the value considered in the analysis of the foundations in Chapter 4 for extreme wind model (EWM). In order to have a good approximation for the NWM should be therefore considered a load of $55\% \pm 13\%$ of the values for EWM.

The modelling and analysis of the influence of the wind induced vibration due to the service load will be presented for the micropiles placed in the most stressed area of the foundation assuming a full mobilization of the micropile capacity for EWM loading. Considering the procedure presented in the previous sections, the micropiles were monotonically loaded (under prescribed displacement) up to a load of 55% of their full capacity under monotonic loading followed by a 5 cycle loading of $\pm 13\%$ of the mean NTM load (55% of the maximum capacity)

In Figure 6.44 it is represented both the cyclic force-displacement curves ($\pm 1\text{mm}$ before the monotonic loading) presented in section 6.5 the force-displacement curves of the cases with the vibration loading (SLS).

The force-displacement curves and the respective approximate bilinear model are presented in Figure 6.45. Both initial stiffness and resistances of the bilinear approximation presented are in accordance with the values obtained and presented in Table 6.13 and Table 6.14. Since for the tensile MC model for dense sand it was not reached a displacement of 25mm, a resistance value considering a linear extrapolation from the last converged values was adopted.

The approximation between the bilinear and the real force-displacement curves is better when the ratio between full mobilization strength and strength for the maximum allowed displacement is close to 1.0 as in the tensile models of micropiles installed in loose sand.

The cyclic stiffness obtained in this analysis is presented in Figure 6.46.

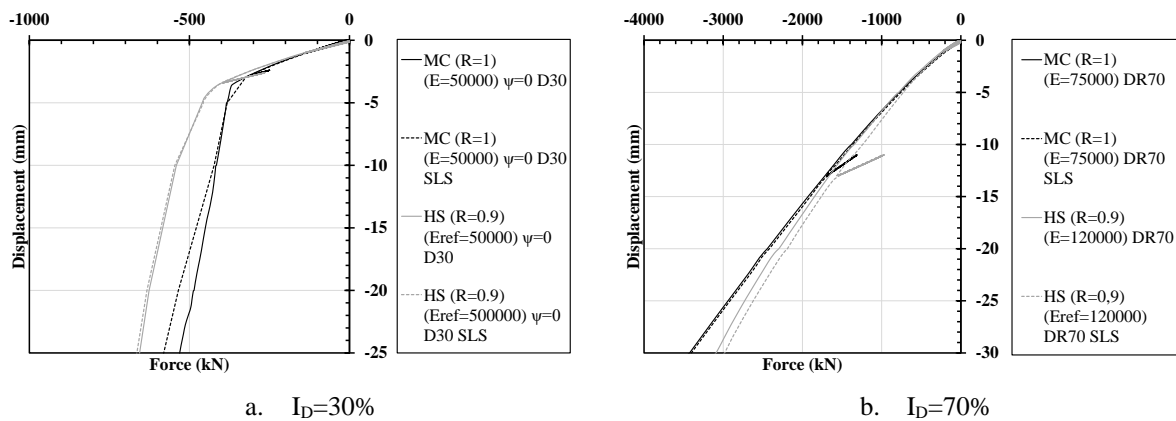


Figure 6.44 – Compressive force-displacement curves comparison between the response micropiles under wind induced vibration loading (NTM) and micropiles under initial cyclic loading

The cyclic stiffness of the MC models is always lower than the correspondent HS stiffness. This is due to the fact that, during the cyclic loading the material behaviour follows the path of EUR and not E50 leading therefore to a higher stiffness regarding MC model where the loading and unloading elastic modulus are equivalent.

The use of micropiles as a reinforcement of the shallow foundation will lead to an improvement in the global foundation rotational stiffness which should comply more easily with the requirements of the turbine manufacturers in terms of excessive vibrations. The requirements of the manufacturers are very restrictive in order to ensure proper working conditions of the turbine, especially by keeping the position of the turbine shaft of the generator. Even for SLS induced vibrations, it is forecasted to have a better dynamic behaviour of the wind tower global structure by reducing the displacements due to the wind induced vibrations.

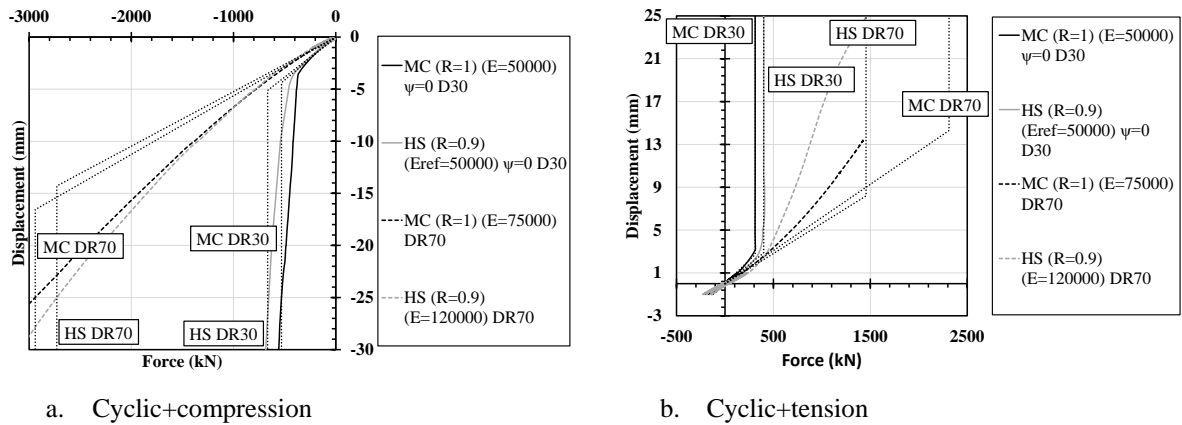


Figure 6.45 – Tensile force-displacement curves including bilinear spring model approximation

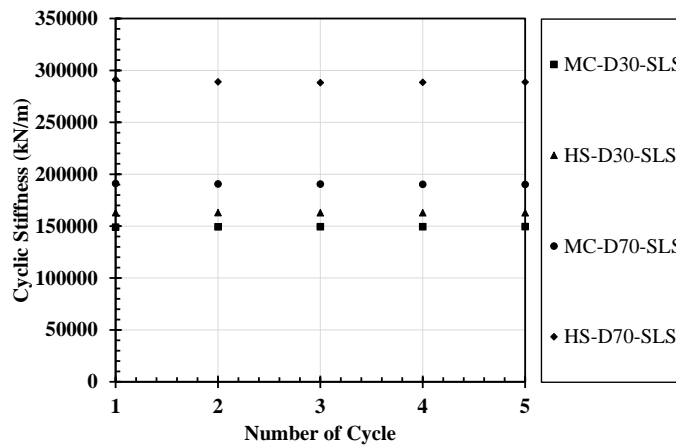


Figure 6.46 – Cyclic stiffness due to the wind induced vibration loading

6.7. Final comments

The calibration of the experimental tests of chapter 5 proved to be acceptable both for MC and HS models. The cyclic calibration was also possible in terms of cyclic secant stiffness, however the hysteresis obtained in the numerical models is much more reduced than in the experimental tests.

In the experimental tests, it was also obtained a strong reduction of stiffness after the side failure that was possible to simulate numerically with models without dilatancy, however the final results were not an exact match.

The HS model simulates more accurately the real behaviour of the soil and it is more adequate for the problem raised in this study according to the relevant bibliography. However the MC

model provides a good first approach to the problem as it provides results close to the HS with the advantage of requiring less computational costs.

Apart from the increase in the resistance, a difference between the consideration of a high density and a low density sand occurs in the value of the initial stiffness. The mobilization of a higher stiffness will reduce the wind induced vibrations in the tower improving its global behaviour for the working conditions of the turbine.

The numerical shear strength obtained for both soil densities is very similar in the presented analysis under the considered test conditions, however this conclusion may not be valid for real conditions. In this analysis, a value of $K=K_0$ was assumed (and it was valid to calibrate the experimental results in the loose sand) both for loose and dense sand but for real grouted micropiles this equivalence is not valid since $K>K_0$. This increase due to the grouting should be estimated with experimental tests. On the other hand, the values given by empirical charts shows a significant difference depending on the ground density.

The considered soil models (MC and HS) are not accurate to estimate the behaviour of a foundation under cyclic loading. These models do not take into account the change of resistance due to the cyclic loading. In the cyclic stage, the path followed is the path given by the unload/reload modulus (equal to primary loading modulus for MC model and higher in HS model) returning after the cyclic loading to the monotonic path. Regardless the number of cycles applied, the final resistance and initial stiffness will not change drastically due to the imposition of cyclic loading.

Taking into account that in the design example of Chapter 4 it was considered a shear resistance of 300kPa considering a grouting technique equivalent to IRS or IGU (Bustamante and Doix 1985), the considered stiffness is lower than the obtained with the FEA analysis, for the considered soil. The obtained results in the analysis provide stiffnesses of around 100MN/m against the considered 50MN/m in the design example. Techniques such as IRS or IGU will mobilize even higher stiffnesses than the one obtained in this analysis for micropiles type A or B (FHWA 2005).

As a summary of the results obtained in this analysis carried out for a specific soil and for specific grouting conditions, the parameters for a 250mm micropile with 12m is 200MN/m of initial stiffness and 150kPa of shear strength (type A or B). The values obtained in this study should be taken as a lower limit for both stiffness and shear resistance given the considered grouting conditions.

The bilinear approximation proved suited for the low density soil numerical results (without numerical dilatancy) while for the high density sand results a bilinear curve with two different slopes (or even three in the case of the tension cases) should be considered to take into

account the increase in the resistance after the full mobilization of the shear strength. This gain of resistance in the dense sand is due to the gradual plastification of the points in the vicinity of the interface elements to reach the equilibrium of the model. It is important to highlight again that this curves are valid only for the given test conditions and, in order to proper implement the model, real scale tests are advised for a suited estimation of the micropile properties. The comments provided for the analysis of the bilinear curves for dense sand should not be taken as conclusive due to the lack of tests under this ground conditions and due to direct use of the soil mechanical properties obtained with the triaxial tests (namely dilatancy) considered in the analysis.

7. CONCLUSIONS

7.1. General conclusions and final remarks

The increase in the exploitation of renewable energies, namely wind energy, has led to the need of improving the current generators in order to become more efficient.

The most effective way to improve the wind energy generators is by increasing the supporting tower height allowing the use of more powerful and more stable wind shear profiles which will allow the increase of the energy generation. This increase in the height of the structure is therefore conditioned by three of the issues that must be solved, which are:

- Transportation requirements – maximum allowable diameter to be transported in public roads;
- Fatigue problems related to the welded connections;
- Foundation cost.

Nowadays, the maximum allowed diameter to be transported in public roads is 4.5m and, considering the typical structural system used for the 80m high steel wind tower, the required bottom diameter is 4.2m, pointing out to the need of improving the construction technique of the tower.

A feasible study on a segmented tower inspired in the segment concrete tower technology was addressed and it was concluded that it is a valid option for these structures. This modular solution with longitudinal bolted shear connections was studied along with a new proposed friction connection for the transversal joints. This system with longitudinal shear connections and friction transversal connections will overcome both the problem of the transportation requirements and the fatigue problems in the welded connections.

The design of the current steel tubular towers with flange connections is commonly governed by the fatigue problems both in the welded connections as well as in the bolts in tension. An increase in the height of the towers will require the use of higher strength steel, in order to reduce the maximum required diameter. The use of both friction and longitudinal shear connections will withdraw both the welds and the bolts in tension of the structure.

Within the specifications of this connection geometry is the use of bolts that allow the tightening only from the inner side of the tower. Some solutions are available in the market and their behaviour was evaluated in this study. The friction resistance is highly dependent on the value of the installed bolt force and so the estimation of the installed force is fundamental during the lifetime of the tower (20 years).

The free maintenance bolts under study are the TCB bolts and the BobTail and both presented installation forces close to the values provided by the manufacturer, with losses around 7% for adjacent bolts and 1% in non-adjacent bolts. A long term monitoring (around 1 year) carried out in the BobTail pointed out to a stabilization of the forces for a time of around 1.5 years after the installation and a total loss of around 5% during the 20 years of lifetime for the case of the isostatic bolts.

The foundation systems for higher towers should be reviewed and redesigned since they present a considerable percentage in the total cost of the solution. The design of the current and more common shallow foundations is governed mainly by the overturning capacity. In order to improve the overturning capacity of foundations, a hybrid solution was presented, adding micropiles to the shallow foundation, together with the design steps to be considered according to the relevant standard.

The design examples of hybrid foundations considering micropiles with a high grout-to-ground bond strength in accordance with high quality grouting techniques considered for different heights (80, 100 and 150m) and different tower types (steel, tubular and hybrid steel+concrete) led to a reduction between 15% and 54% in concrete consumption. Along with the geotechnical design, an LCA and LCC analysis were conducted leading to a reduction of 10% to 30% of the global warming potential and 9% to 25% in the primary energy demand with a reduction in the foundation cost up to 25%.

In order to provide a feasible tool to estimate the behaviour of micropiles, a set of experimental tests was conducted on micropiles under monotonic and cyclic loading and under very low pressure grouted and ungrouted conditions. It was observed an improvement both in the ground conditions and the micropile resistance after the grouting. The compression resistance was higher than the respective tensile due to the tip contribution. In the group tests it was observed that the spacing effect is not significant for tests under the same conditions.

An increase in the stiffness was observed between grouted and ungrouted single specimens, especially for single specimens. For the specific ground and grout conditions the increase was around 490%. The cyclic stiffness is also higher for grouted specimens than for the correspondent ungrouted. The same tendency was obtained between tensile and compressive tests with higher values for tensile.

Based on the experimental tests conducted on micropiles, a finite element model was developed in order to be calibrated using the software Plaxis and considering two different soil material models (MC and HS). The model was properly calibrated both for monotonic and cyclic loading for the single tests results (grouted and ungrouted) which makes this a viable procedure to estimate the behavior of micropiles under different conditions (loading, ground conditions, micropile geometry). HS model is more accurate to reproduce the soil nonlinear behavior, however MC model proved to be a valid option for a first approximation for the micropile load-displacement behavior due to the lower computational costs.

The sudden increase in the displacements and reduction of the micropile stiffness observed in the experimental tests after the full mobilization of the shear strength on the micropile-soil interface was numerically achieved by considering a null dilatancy in the soil material models.

The higher foundation stiffness will reduce the wind induced vibrations in the tower improving its global behaviour for the working conditions of the turbine.

Both soil models considered conducted to numerical resistance close to the values determined by the experimental tests however this numerical model and the procedure is not accurate to estimate the behaviour of a micropile under cyclic loading because the effect of the reduction in the resistance due to the cyclic loading is not obtained.

Under the grouting conditions considered in the experimental tests (very low pressure), the determined shear strength for dense sand is around 150kPa which is a characteristic value for low pressure grouting conditions like soil nailing technique. The obtained stiffness is lower than the stiffness obtained in real conditions tests on micropiles with IRS techniques.

The bilinear spring model to be considered in the full foundation design was proven to be a good approximation for micropiles in low density sand (with a marked drop in the resistance after full mobilization of the side friction) however the conclusions for the dense sand should be considered with some caution.

Solutions have been proposed and analysed for the three problems raised with the required increase in height. This increase in height will be feasible for tubular steel towers by withdrawing the need of welding (friction and longitudinal shear connections) improving that way the fatigue behaviour of the structure and allowing the use of higher strength steel to reduce the required diameter. The bolt requirements for the friction connections are met with free maintenance bolts like TCB or BobTail with losses during the tower lifetime of around 5% of the total applied force. The use of shallow foundations proved to be a feasible solution both environmentally and economically leading to a reduction of the required diameter. The

numerical estimation of the behaviour of the micropiles is feasible however real scale tests are required to allow a proper calibration of the model for each specific case.

7.2. Future work

After the conclusion of this work, some questions are still possible to be discussed and analysed. The most relevant topics are listed below:

1. Evaluation of the availability and cost of cranes to allow the installation of the higher towers and/or the analysis of a self-raising system for the segment lifting;
2. Long-term monitoring of free-maintenance bolts (preferably BobTail bolts) installed in plates with different thicknesses than the prototype presented in chapter 3 in order to compare and to conclude about the influence of the thickness of the plates in the bolt force losses. The connection of the strain gauges should now be done with a full-bridge wire to avoid the influence of the wire length in the results;
3. Numerically simulate the experimental tests carried out in groups of micropiles in order to understand the group effect phenomena in these elements and to conclude about the effect of the micropile spacing;
4. Use of a material model that allows the simulation of the reduction of the resistance of the micropiles due to the cyclic loading;
5. Detailed structural analysis and estimation of the required rebars of a hybrid foundation for the transfer of the load to the micropiles and comparison with the correspondent shallow solution;
6. Evaluation of the dynamic behaviour of the full hybrid foundation under cyclic loading and under wind induced vibration.

7.3. Personal contributions and publications

- **Personal contributions**

The main personal contributions performed in the scope of the presented thesis are listed below:

1. Presentation and description of a monitoring strategy system for full functional wind towers. Detailed description of the behaviour of a wind tower in terms of stress distribution, accelerations and dynamic displacements.
2. Description of the procedure for estimation of the fatigue spectra and fatigue design requirements. Estimation of the fatigue spectra based on the vertical stresses on the shell.
3. Presentation of a connection geometry proposed to improve the fatigue resistance of the wind tower and therefore allow the use of higher strength steel. Monitoring of free-maintenance bolts and estimation of their behaviour during the lifetime span of the structure (20 years).
4. Detailed design description of shallow and hybrid foundations for support of different wind towers. Estimation of the required foundation geometry along with detailed LCA and LCC analysis to compare each solution.
5. Description of an experimental technique to test ungrouted and grouted micropiles. The experimental tests were conducted on micropiles installed in very loose sand, with and without low pressure grout and in setups with single or groups of 4 micropiles with varying spacing. They were tested under cyclic and monotonic loading. The resistance, monotonic and cyclic (when applicable) stiffnesses were determined and compared for each tested specimen.
6. Presentation and calibration, with the experimental tests, of a numerical 2D method to determine the resistance and stiffness by the force-displacement curves using Plaxis software considering non-linear soil models (Mohr-Coulomb and Hardening Soil). Description of the advantages and disadvantages of each model for the determination of the micropile properties.
7. Estimation of real dimension micropiles properties installed in dense sand and grouted using the same technique adopted for the experimental tests.

- **Publications**

On the scope of the presented study, some publications were published and are listed in the current section.

Project Reports

HISTWIN – Final project report – national project funded by FCT with the reference PTDC/ECM/64217/2006

HISTWIN - Final project report – national project funded by RFCS with the reference RFSR-CT-2006-00031

HISTWIN2 - Final project report – national project funded by RFCS with the reference RFSR-CT-2010-00031

HISTWIN+ - Final project report – national project funded by RFCS with the reference RFS2-CT-2014-00023

Journal Papers

Rebelo, C., Veljkovic, M., Matos, R., Simões da Silva, L., 2012. Structural Monitoring of a Wind Turbine Steel Tower – Part II: monitoring results, *Wind and Structures*, 15(4), pp.301-311

Jesus, A., Matos, R., Fontoura, B., Rebelo, C., Simões da Silva, L., Veljkovic, M., 2012. A comparison of the fatigue behavior between S355 and S690 steel grades, *Journal of Constructional Steel Research*, 79, pp.140-150

Matos, R., Pinto, P., Rebelo, C., Gervásio, H., Veljkovic, M., 2016. Improved design of tubular wind tower foundations using steel micropiles, *Structure and Infrastructure Engineering*, 12

International and National Conference Papers

Matos, R., Rebelo, C., Simões da Silva, L., Veljkovic, M., Simões, R., 2009. Ensaaios de Fadiga de Ligações Metálicas por Atrito para Torres Eólicas Metálicas, *VII CMM*, Lisbon

Matos, R., Correia, J., Jesus, A., Rebelo, C., Simões da Silva, L., 2010. Avaliação da Resistência à Fadiga de Ligações Metálicas Recorrendo aos Modelos de Aproximação Local, *Reabilitar 2010*, Lisbon

Fontoura, B., Matos, R., Jesus, A., Rebelo, C., Correia, J., Silva, A., Silva, L., 2011. Comparação da resistência à fadiga entre o aço S355 e o aço de alta resistência S690, 2º *ASCP*, Coimbra

Matos, R., Fontoura, B., Rebelo, C., Jesus, A., Veljkovic, M., Silva, L., 2011. Fatigue Behavior of Steel Friction Connections: Experimental and Numerical Results, *Eurosteel 2011*, Budapest

Fontoura, B., Matos, R., Jesus, A., Rebelo, C., Silva, L., Veljkovic, M., 2011. Avaliação da resistência à fadiga de ligações por atrito em aço estrutural de alta resistência S690, *VIII CMM*, Guimarães

Rebelo, C., Simões, R., Matos, R., Silva, L., Veljkovic, M., Pircher, M., 2012. Structural Monitoring of a Wind Turbine Steel Tower, *Experimental Mechanics - New Trends and Perspectives*, Porto

Matos, R., Rebelo, C., Silva, L., Veljkovic, M., 2013. Dynamic Measurements of a Steel Wind Tower, *ICOVP2013*, Lisbon

Matos, R., Cruz, J., Rebelo, C., Veljkovic, M., 2013. Feasibility Tests on Single Shear Lap Friction Connections for Wind Towers, *IX CMM*, Matosinhos

Matos, R., Pinto, P., Rebelo, C., Veljkovic, M., 2013. Laboratory Testing of Single Micropiles, *IX CMM*, Matosinhos

Matos, R., Rebelo, C., Silva, L., Veljkovic, M., 2014. Behaviour of pre-stressed BobTail bolts: Application in tubular wind towers, *Eurosteel2014*, Naples

Matos, R., Rebelo, C., 2014. Monitoring and assessment of the behavior of prestressed BobTail bolts, *CNME2014*, Aveiro

Matos, R., Pinto, P., Rebelo, C., Silva, L., Veljkovic, M., 2015. Cyclic performance of single and group micropiles on loose sand, *IFCEE 2015*, San Antonio, Texas

REFERENCES

- Adhikari, S. and Bhattacharya, S., 2011. Vibrations of wind-turbines considering soil-structure interaction. *Wind and Structures*, 14(2), pp.85–112.
- Almeida, J., 2015. *Hybrid Lattice-Tubular Steel Onshore Wind Towers : Conceptual Design of Tower and Transition Segment*. University of Coimbra.
- Andresen Towers, 2011. Next Generation Wind Turbines. Available at: <http://andresen-towers.com/andresen-media>.
- Aschenbroich, H., 2010. A Real Root Pile (Pali Radici) - Support of Vancouver 's Hollow Tree - Parallels to Wind Turbine Foundations. In *10th ISM Workshop*. Washington, DC.
- Ashes, 2016. Ashes 2.3.1 - Reference Manual.
- ASTM D4253-00, 2000. Standard Test Method for Maximum Index Density and Unit Weight of Soils Using a Vibratory Table.
- ASTM D854-05, 2005. Standard Test Methods for Specific Gravity of Soil Solids by Water Pycnometer.
- ASTM E1049-85, 2011. Standard practices for cycle counting in fatigue analysis.
- Beer, F.P., Johnston Jr., E.R., DeWolf, J.T. and Mazurek, D.F., 2012. *Mechanics of Materials* 6th Ed., McGraw-Hill.
- Bendat, J. and Piersol, A.G., 1993. *Engineering application of correlation and spectral analysis*, John Wiley & Sons.
- Bolton, M., 1986. The strength and dilatancy of sands. *Géotechnique*, 36(1), pp.65–78.
- Boulon, M. and Foray, P., 1986. Physical and numerical simulation of lateral shaft friction along offshore piles in sand. In *3rd Conference Numerical Methods in Offshore Piling*. Nantes, France.
- Bowles, J.E., 2001. *Foundation Analysis and Design* 5th Ed., McGraw-Hill.
- Briaud, J.-L. and Felio, G.Y., 1986. Cyclic axial loads on piles: Analysis of existing data. *Canadian Geotechnical Journal*, 23, pp.362–371.
- Brincker, R., Zhang, L. and Andersen, P., 2000. Modal Identification from Ambient

- Responses using Frequency Domain Decomposition. In *18th International Modal Analysis Conference*. San Antonio, TX, USA.
- Buhler, R. and Cerato, A.B., 2010. Design of Dynamically Wind-Loaded Helical Piers for Small Wind Turbines. *Journal of Performance of Constructed Facilities*, 24(4), pp.417–427.
- Burton, T., Sharpe, D., Jenkins, N. and Bossanyi, E., 2001. *Wind Energy Handbook*, West Sussex, England: John Wiley & Sons, Ltd.
- Bustamante, M. and Doix, B., 1985. *Une méthode pour le calcul des tirants et des micropieux injectés*, Bulletin de liaison des laboratoires des Ponts et Chaussées, Paris, France.
- Cavey, J.K., Lambert, D. V, Miller, S.M. and Krhounek, R.C., 2000. Observation of minipile performance under cyclic loading conditions. *Ground Improvement*, 4, pp.23–29.
- Cerato, A.B. and Victor, R., 2008. Effects of Helical Anchor Geometry on Long-Term Performance of Small Wind Tower Foundations Subject to Dynamic Loads. *DFI Journal*, 2(1), pp.30–41.
- Cerato, A.B. and Victor, R., 2009. Effects of Long-Term Dynamic Loading and Fluctuating Water Table on Helical Anchor Performance for Small Wind Tower Foundations. *Journal of Performance of Constructed Facilities*, 23(4), pp.251–262.
- Chan, S. and Hanna, T., 1980. Repeated loading on single piles in sand. *Journal of the Geotechnical Engineering Division*, 6(GT2), pp.171–187.
- Coelho, N., 2011. *Caracterização Laboratorial do Comportamento de um Solo Arenoso para a Previsão de Resistência Axial de Microestacas*. University of Coimbra.
- Dally, J.W., Riley, W.F. and McConnell, K.G., 1993. *Instrumentation for engineering measurements* 2nd Editio., John Wiley & Sons.
- DNV/Risø, 2002. Guidelines for Design of Wind Turbines - 2nd Edition. *Wind Engineering*, 29.
- Downing, S.D. and Socie, D.F., 1982. Simple rainflow counting algorithms. *International Journal of Fatigue*, 4(1), pp.31–40.
- Duncan, J. and Chang, C.-Y., 1970. Nonlinear Analysis of Stress and Strain in Soils. *Journal of the Soil Mechanics and Foundations Division*, 96(5), pp.1629–1653.
- Earth Systems Global Inc., 2009. P&H Foundations for Wind Turbine Support. Available at: http://www.chinawind.org.cn/cwp2012/czs/uploadpdf/9902_english.pdf.

- Elaziz, A.Y.A. and El Naggar, M.H., 2012. Axial Behaviour of Hollow Core Micropiles Under Monotonic and Cyclic Loadings. *Geotechnical Testing Journal*, 35(2).
- EN 1990, 2002. Eurocode - Basis of structural design.
- EN 1992-1-1, 2004. Eurocode 2: Design of concrete structures - Part 1-1: General rules and rules for buildings.
- EN 1993-1-1, 2005. Eurocode 3: Design of steel structures - Part 1-1: General rules and rules for buildings.
- EN 1993-1-8, 2005. Eurocode 3 - Design of steel structures, Part 1-8: Design of joints.
- EN 1993-1-9, 2005. Eurocode 3: Design of steel structures - Part 1-9: Fatigue.
- EN 1997-1, 2004. Eurocode 7: Geotechnical Design - Part 1 : General Rules.
- EN 1998-1, 2004. Eurocode 8: Design of structures for earthquake resistance - Part 1: General rules, seismic actions and rules for buildings.
- EN 1998-5, 2004. Eurocode 8: Design of structures for earthquake resistance - Part 5: Foundations, retaining structures and geotechnical aspects.
- Engström, S., Lyrner, T., Hassanzadeh, M., Stalin, T. and Johansson, J., 2010. Tall tower for large wind turbines - Elforsk rapport 10:48.
- EWEA, 2014. Wind energy scenarios for 2020.
- EWEA, 2015. Wind in Power: 2014 European Statistics.
- Ferreira, C., 2014. *Modelação Numérica de Ensaios de Carga em Placa em Modelos à Escala Reduzida*. University of Coimbra.
- FHWA, 2005. *Micropile Design and Construction - Reference Manual (Publication No. FHWA NHI-05-039)*, Washington, D.C.
- Francis, R., 1997. *Etude du comportement mécanique de micropieux modèles en chambre d'étalonnage. Application aux effets de groupe*. L'École Nationale des Ponts et Chaussées.
- GaBi 6, 2012. Software-System and Databases for Life Cycle Engineering. Version 5.56.

- General Electric, 2014. Space Frame Tower. Available at: https://renewables.gepower.com/content/dam/gepower-renewables/global/en_US/documents/GEA31082_SF_FS_R2.pdf.
- Gervásio, H., Rebelo, C., Moura, A., Veljkovic, M. and Simões da Silva, L., 2014. Comparative life cycle assessment of tubular wind towers and foundations - Part 2: Life cycle analysis. *Engineering Structures*, 74, pp.292–299.
- GL-Germanischer Lloyd, 2003. Guideline for the Certification of Wind Turbines.
- Guinée, J.B., Gorrée, M., Heijungs, R., Huppes, G., Kleijn, R., Koning, A. de, Oers, L. van, Wegener Sleeswijk, A., Suh, S., Udo de Haes, H.A., Bruijn, H. de, Duin, R. van and Huijbregts, M.A., 2002. Handbook on Life Cycle Assessment. Operational Guide to the ISO Standards. I: LCA in Perspective. IIA: Guide. IIB: Operational Annex. III: Scientific Background. Available at: www.cml.leiden.edu/research/industrialecology/researchprojects/finished/new-dutch-lca-guide.html.
- Guo, F., 2004. *A New Identification Method for Wiener and Hammerstein Systems*. University of Karlsruhe. Available at: www.ubka.uni-karlsruhe.de/volltexte/fzk/6955/6955.pdf
- GWEC, 2015. *Global Wind Report - Annual Market Update*, Brussels, Belgium.
- Hau, E., 2013. *Wind Turbines - Fundamentals, Technologies, Application, Economics* 3rd Ed., Berlin, Germany: Springer.
- Heistermann, C., 2011. *Behaviour of Pretensioned Bolts in Friction Connections - Towards the Use of Higher Strength Steels in Wind Towers*. Luleå University of Technology.
- Heistermann, C., 2014. *Resistance of Friction Connections with Open Slotted Holes in Towers for Wind Turbines*. Luleå University of Technology.
- Herold, A. and von Wolffersdorff, P.-A., 2009. The Use of Hardening Soil Model with Small-Strain Stiffness for Serviceability Limit State Analyses of GRE Structures. In *GeoAfrica 2009*. Cape Town, South Africa.
- Husson, W., 2008. *Friction Connections with Slotted Holes for Wind Towers*. Luleå University of Technology.
- IEC 61400-1, 2005. Wind Turbines - Part 1: Design Requirements.
- IEC 61400-1/AMD1, 2010. Wind Turbines – Part 1 Design requirements, Amendment 1.
- INNEO Torres, 2008. Precast Concrete Wind Towers. Available at: <http://inneotorres.es/web/index.php/en/installation-process.html>.

- IRENA (International Renewable Energy Agency), 2012. Renewable Energy Technologies: Cost Analysis Series – Issue 5/5 Wind Power, Vol. 1: Power Sector, United Arab Emirates.
- ISO 14040, 2006. Environmental management - Life cycle assessment - Principles and framework.
- ISO 14044, 2006. Environmental management - Life cycle assessment - Requirements and guidelines.
- ISO 2394, 2015. General principles on reliability for structures.
- Janbu, N., 1963. Soil compressibility as determined by oedometer and triaxial tests. In *European Conference on Soil Mechanics and Foundation Engineering*. pp. 19–25.
- Jesus, A.M.P. de, Matos, R., Fontoura, B.F.C., Rebelo, C., Simões Da Silva, L. and Veljkovic, M., 2012. A comparison of the fatigue behavior between S355 and S690 steel grades. *Journal of Constructional Steel Research*, 79, pp.140–150.
- Juran, I., Benslimane, A. and Hanna, S., 2001. Engineering Analysis of the Dynamic Behavior of Micropile Systems. *Journal of the Transportation Research Board*, 1772, pp.91–106.
- Juran, I. and Weinstein, G.M., 2009. Long-Term Performance Assessment of Micropiles Under Monotonic and Cyclic Axial Loading. *9th ISM Workshop*.
- Kelly, S.G., 2000. *Fundamentals of mechanical vibrations* 2nd Ed., Singapore: McGraw-Hill.
- Khatri, D., 2010. Economics of Taller Wind Towers. Available at: <http://www.renewableenergyworld.com/rea/news/article/2010/02/economics-of-taller-wind-towers>.
- Kirsch, F. and Richter, T., 2011. Cyclic degradation of pile foundations for offShore wind turbines. In *36th Annual Conference on Deep Foundations*. Boston, MA, USA.
- Ko, H., Jhung, M. and Choi, J., 2012. A study on the stress cycle determination using an optimization technique. In *Transactions of the Korean Nuclear Society Spring Meeting*. Jeju, Korea.
- Le Kouby, A., 2003. *Etude du comportement mécanique de micropieux sous chargements monotones et cycliques verticaux. Application aux effets de groupe*. L'École Nationale des Ponts et Chaussées.
- LaNier, M.W., 2005. LWST Phase I Project Conceptual Design Study: Evaluation of Design and Construction Approaches for Economical Hybrid Steel/Concrete Wind Turbine

Towers.

- Lavassas, I., Nikolaidis, G., Zervas, P., Efthimiou, E., Doudoumis, I.N. and Baniotopoulos, C.C., 2003. Analysis and design of the prototype of a steel 1-MW wind turbine tower. *Engineering Structures*, 25, pp.1097–1106.
- Liao, S. and Whitman, R., 1986. Overburden Correction Factors for SPT in Sand. *Journal of Geotechnical Engineering*, 112(3), pp.373–377.
- Lizzi, F., 1978. Reticulated Root Piles to Correct Landslides. In *ASCE National Convention*.
- LNEC NP-83, 1965. Determinação da Densidade das Partículas (portuguese version).
- LUSAS, 2006a. Element Reference Manual - version 14.
- LUSAS, 2006b. Modeller Reference Manual - version 14.
- Marchetti, S., Monaco, P., Totani, G. and Calabrese, M., 2001. The Flat Dilatometer Test (DMT) in Soil Investigations - A Report by the ISSMGE Committee TC16. In *The second international flat dilatometer conference*.
- Matos Fernandes, M. de, 2011. *Mecânica dos Solos - Conceitos e Princípios Fundamentais* 2nd Ed., Porto, Portugal: FEUP Edições.
- Mayne, P.W., Christopher, B.R. and DeJong, J., 2001. *Manual on Subsurface Investigations - National Highway Institute (Publication No. FHWA NHI-01-031)*, Washington, D.C.
- Moayed, R.Z. and Naeini, S.A., 2012. Improvement of Loose Sandy Soil Deposits using Micropiles. *KSCE Journal of Civil Engineering*, 16(3), pp.334–340. Available at: <http://link.springer.com/10.1007/s12205-012-1390-2>.
- Moura, A., 2012. *Análise comparativa de torres eólicas em aço e híbridas aço-betão para alturas e potências variáveis*. University of Coimbra.
- NI - National Instruments, 2006. Labview full development system - version 8.2.
- NP EN 196-1, 2006. Métodos de ensaio de cimentos - Parte 1: Determinação das resistências mecânicas (portuguese version).
- NP EN 445, 2008. Caldas de injeção para armaduras de pré-esforço - Métodos de ensaio (portuguese version).
- NP EN 447, 2008. Caldas de injeção para armaduras de pré-esforço - Requisitos básicos (portuguese version).

- Obrzud, R.F., 2010. On the use of the Hardening Soil Small Strain model in geotechnical practice. In *Numerics in Geotechnics and Structures*. Elmepress International.
- Pender, M., 2010. Seismic Assessment and Improvement of Building Foundations.
- Phuly, A., 2011. Fatigue resistant foundation system.
- Plaxis, 2006. Plaxis 2D - Reference Manual - Version 8.
- Presses de l'Ecole Nationale des Ponts et Chaussées, 2002. *Additif 2002 aux recommandations CLOUTERRE 1991 – pour la conception, le calcul, l'exécution et le contrôle des soutènements réalisés par clouage des sols*, Paris, France.
- Rebello, C., Moura, A., Gervásio, H., Veljkovic, M. and Simões da Silva, L., 2014. Comparative life cycle assessment of tubular wind towers and foundations - Part 1: Structural design. *Engineering Structures*, 74, pp.283–291.
- Rebello, C., Veljkovic, M., Matos, R. and da Silva, L.S., 2012. Structural monitoring of a wind turbine steel tower-Part II: monitoring results. *Wind and Structures*, 15(4), pp.301–311.
- Rebello, C., Veljkovic, M., Matos, R. and Simões da Silva, L., 2012. Structural Monitoring of a Wind Turbine Steel Tower - Part II: monitoring results. *Wind and Structures*, 15(4), pp.301–311.
- Rebello, C., Veljkovic, M., Simões Da Silva, L., Simões, R. and Henriques, J., 2012. Structural Monitoring of a Wind Turbine Steel Tower - Part I: system description and calibration. *Wind and Structures*, 15(4), pp.285–299.
- Robot, 2015. Autodesk Robot Structural Analysis Professional 2016 - Reference Manual.
- Russo, G., 2004. Full-scale load tests on instrumented micropiles. *Proceedings of the Institution of Civil Engineers, Geotechnical Engineering*, 157(GE3), pp.127–135.
- Schanz, T. and Vermeer, P.A., 1998. On the stiffness of sands. *Géotechnique*, (January 1998), pp.383–387.
- Schijve, J., 2009. *Fatigue of Structures and Materials* 2nd Ed., Springer.
- Schlosser, F. and Frank, R., 2004. *FOREVER - Synthèse des résultats et recommandations du Projet national sur les micropieux*, Paris, France.
- Schmertmann, J., 1978. *Guidelines for Cone Penetration Test Performance and Design. Report FHWA-TS-78-209*, Washington DC, USA.
- Schwarz, P., 2000. Axial Cyclic Loading of Small Diameter Injection Piles in Sand. In *10th*

ISM Workshop. Washington DC, USA.

- Seidel, M. and Schaumann, P., 2001. Measuring Fatigue Loads of Bolts in Ring Flange Connections. In *European Wind Energy Conference Exhibition, EWEC 2001*. Copenhagen, Denmark.
- El Sharnouby, M.M. and El Naggar, M. H., 2011. Monotonic and cyclic axial full-scale testing of reinforced helical pulldown micropiles. In *2011 Pan-Am CGS Geotechnical Conference*. Toronto, Ontario, Canada.
- El Sharnouby, M.M. and El Naggar, M.H., 2012. Field investigation of axial monotonic and cyclic performance of reinforced helical pulldown micropiles. *Canadian Geotechnical Journal*, 49(5), pp.560–573.
- Sture, S., 2004. Non-Linear Hyperbolic Model & Parameter Selection.
- Svensson, H., 2010. *Design of foundations for wind turbines*. Lund University.
- SVS, 2007. ARTeMIS Extractor pro - release 4.1 - Structural Vibration Solutions.
- Tecnasol, 2010. Relatório Final - 1º Ensaio de Carga à Tração em Microestaca - I.C.17 – CRIL – Sublanço Buraca/Pontinha - Túnel De Benfica.
- The MathWorks Inc., 2010. MATLAB version2010.
- Turner, J. and Kulhawy, F., 1990. Drained uplift capacity of drilled shafts under repeated axial loading. *Journal of Geotechnical Engineering*, 116(3), pp.470–492.
- Veljkovic, M., Feldmann, M., Naumes, J., Pak, D., Rebelo, C. and Da Silva, L.S., 2010. Friction connection in tubular towers for a wind turbine. *Stahlbau*, 79(9), pp.660–668.
- Veljkovic, M., Feldmann, M., Naumes, J., Pak, D., Simões da Silva, L. and Rebelo, C., 2011. Wind turbine tower design, erection and maintenance. In J. D. Sørensen & J. N. Sørensen, eds. *Wind energy systems: Optimising design and construction for safe and reliable operation*. Cambridge, UK: Woodhead Publishing Limited, pp. 274–300.
- Veljkovic, M., Heistermann, C., Garzon, O., Limam, M., Tran, A.T., Pavlovic, M., Feldmann, M., Möller, F., Richter, C., Baniotopoulos, C.C., Gerasimidis, S., Zygomalas, I., Matos Silva, A., Simões da Silva, L., Rebelo, C., Pinto, P.L., Matos, R., Moura, A., Gervásio, H. and Siltanen, J., 2015. HISTWIN2 - High steel tubular towers for wind turbines (Grant Agreement RFSR-CT-2010-00031 1).
- Veljkovic, M., Heistermann, C., Husson, W., Limam, M., Feldmann, M., Naumes, J., Pak, D., Faber, T., Klose, M., Fruhner, K.-U., Krutschinna, L., Baniotopoulos, C.C., Lavassas, I., Pontes, A., Ribeiro, E., Hadden, M., Sousa, R., Simões da Silva, L., Rebelo, C., Simões,

-
- R., Henriques, J., Matos, R., Nuutinen, J. and Kinnunen, H., 2012. HISTWIN - High-strength tower in steel for wind turbines (Contract No RFSR-CT-2006-00031).
- Veludo, J., Dias-da-Costa, D., Júlio, E.N.B.S. and Pinto, P.L., 2012. Bond strength of textured micropiles grouted to concrete footings. *Engineering Structures*, 35, pp.288–295.
- Vesic, A.S., 1961. Bending of Beams Resting on Isotropic Elastic Solid. *Journal of the Engineering Mechanics Division, ASCE*, 87(2), pp.35–54.
- Wills, A., Schön, T., Ljung, L. and Ninnes, B., 2013. Identification of Hammerstein–Wiener models. *Journal of Automatica*, 49, pp.70–81.

ANNEX A – CALIBRATION ERRORS FOR STRAIN GAUGES

cFP1 (Levels 0 and 1) – software version 2

Equip.	L1R15D	L1R15H	L1R15V	L1R16D	L1R16H	L1R16V	L1R17D	L1R17H	L1R17V	L1R18D	L1R18H
Mean Val.	-197.777	68.80983	-252.745	218.1761	106.4281	360.1397	-3.62166	37.61173	-3.95738	-55.3491	23.09337
Equip.	L1R18V	L1R19D	L1R19H	L1R19V	L1R20D	L1R20H	L1R20V	L1B1	L1B2	L1B3	L1B4
Mean Val.	-417.08	34.06635	113.3786	-155.862	-84.4992	53.69987	-234.566	39.86979	-9.00664	-484.27	76.73744
Equip.	L1B5	L1B6	L0R21D	L0R21H	L0R21V	L0R22D	L0R22H	L0R22V	L0R23D	L0R23H	L0R23V
Mean Val.	-23.6121	-105.759	283.9887	-76.7921	120.9536	168.8409	190.504	227.0831	-5.41783	72.10135	90.44558
Equip.	L0R24D	L0R24H	L0R24V	L0R25D	L0R25H	L0R25V	L0R26D	L0R26H	L0R26V	L0B1	L0B2
Mean Val.	-53.5488	34.20478	-171.498	-23.6417	303.3024	192.9476	201.8546	-55.903	1109.42	16.86545	-203.855
Equip.	L0B3	L0B4	L0B5	L0B6							
Mean Val.	159.3648	-387.313	-486.513	-487.664							

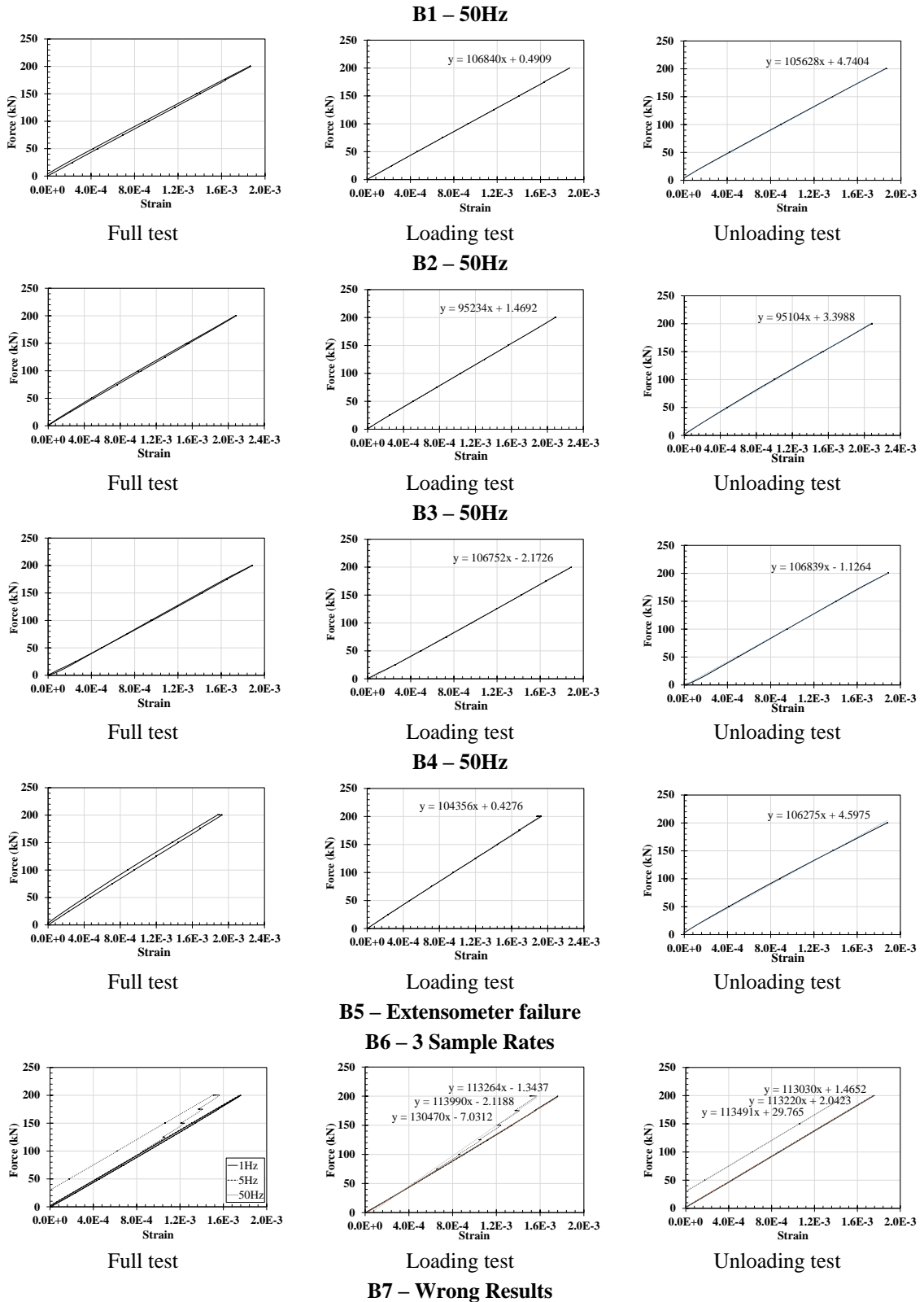
cRIO2 (Level 2) – software version 2

Equip.	L2R06V	L2R06H	L2R06D	L2R05V	L2R05H	L2R05D	L2R04V	L2R04H	L2R04D	L2R03V	L2R03H
Mean Val.	-300.234	-28.3901	-242.774	-347.412	-366.798	-220.377	-357.441	-631.132	-186.613	-196.76	-15.8391
Equip.	L2R03D	L2R02V	L2R02H	L2R02D	L2R01V	L2R01H	L2R01D	L2B6	L2B5	L2B4	L2B3
Mean Val.	-503.993	-524.679	-124.889	-330.869	-325.788	-120.043	-506.275	9390.428	-495.938	-324.836	-707.952
Equip.	L2B2	L2B1									
Mean Val.	-278.737	-556.177									

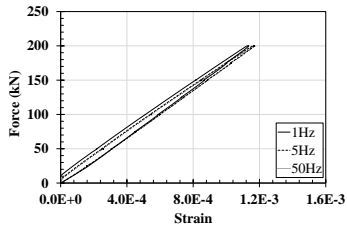
cRIO3 (Level 3) – software version 2

Equip.	L3R07V	L3R07H	L3R07D	L3R08V	L3R08H	L3R08D	L3R09V	L3R09H	L3R09D	L3R10V	L3R10H
Mean Val.	-301.694	-256.109	-261.197	-169.831	-28.7939	-61.8436	-83.4078	-378.283	-260.905	-166.562	-108.97
Equip.	L3R10D	L3R11V	L3R11H	L3R11D	L3R12V	L3R12H	L3R12D	L3R13V	L3R13H	L3R13D	L3R14V
Mean Val.	9402.982	-9395.33	-377.569	-264.8	4327.535	-474.555	-127.236	-516.158	-484.82	-9.86542	-21.9001
Equip.	L3R14H	L3R14D									
Mean Val.	-193.564	-130.951									

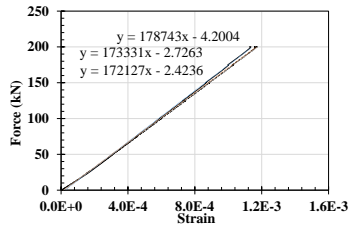
ANNEX B - INDIVIDUAL RESULTS OF BOLT STRAIN GAUGES CALIBRATION TESTS



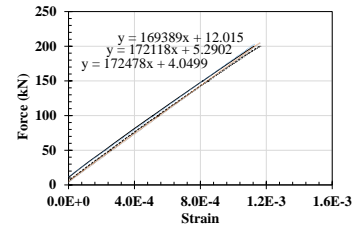
B8 – 3 Sample Rates



Full test

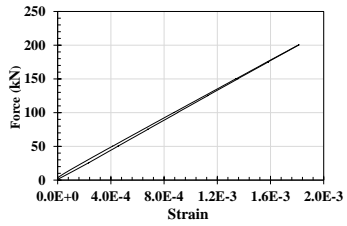


Loading test

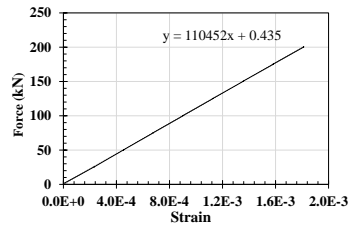


Unloading test

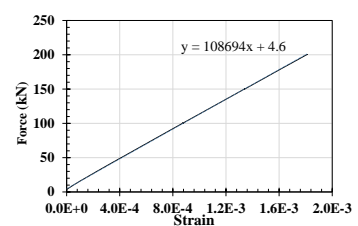
B9 – 5Hz



Full test

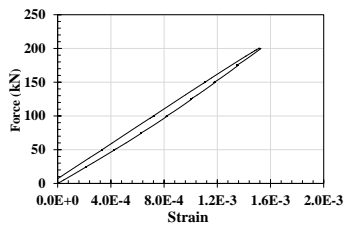


Loading test

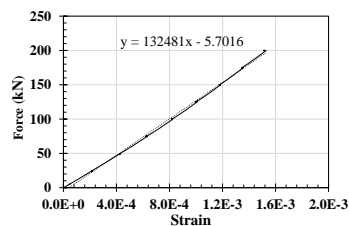


Unloading test

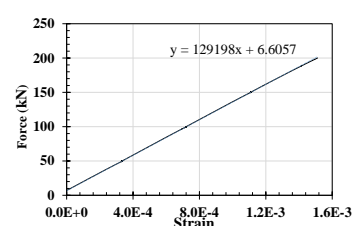
B10 – 50Hz



Full test

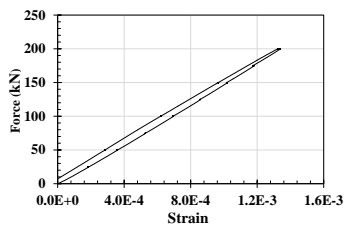


Loading test

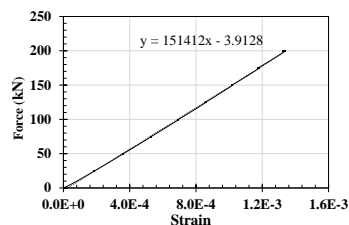


Unloading test

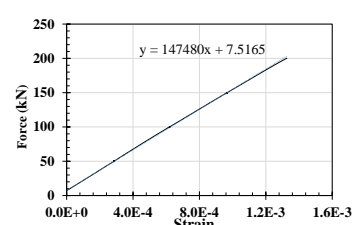
B11 – 50Hz



Full test



Loading test

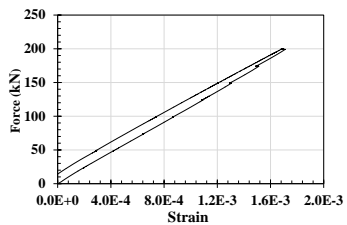


Unloading test

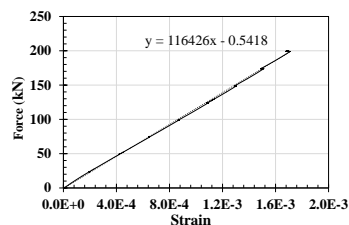
B12 – Wrong Results

B13 – Wrong Results

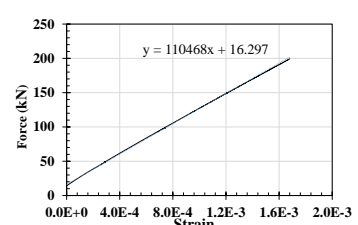
B14 – 50Hz



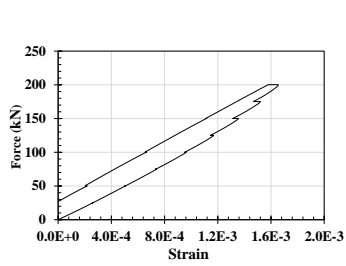
Full test



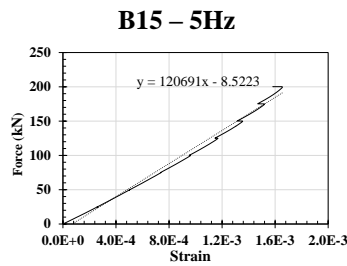
Loading test



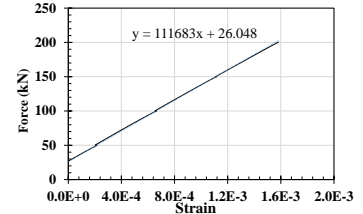
Unloading test



Full test



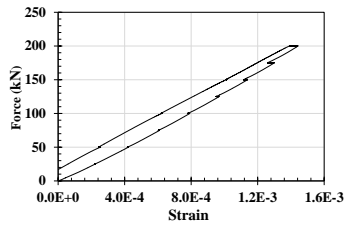
Loading test



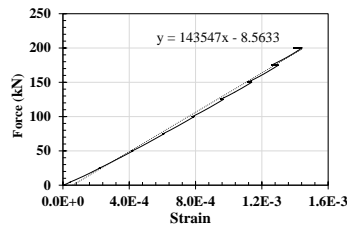
Unloading test

B16 – Extensometer Failure

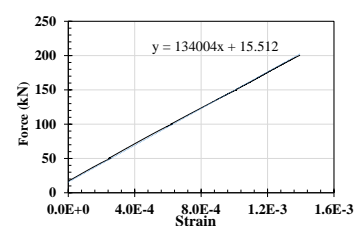
B17 – 50Hz



Full test

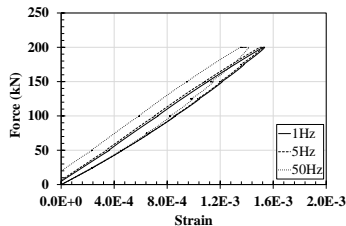


Loading test

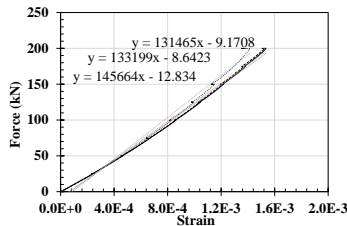


Unloading test

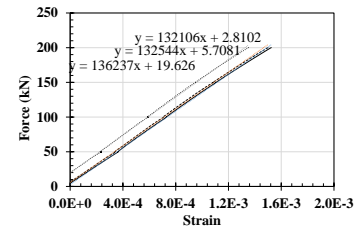
B18 – 3 Sample Rates



Full test

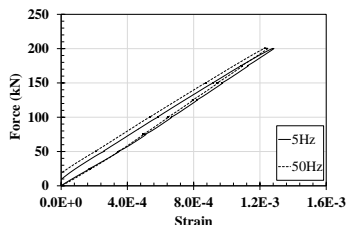


Loading test

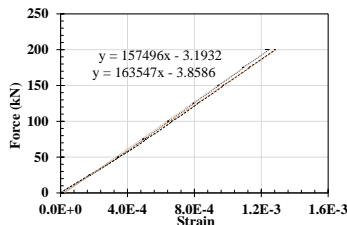


Unloading test

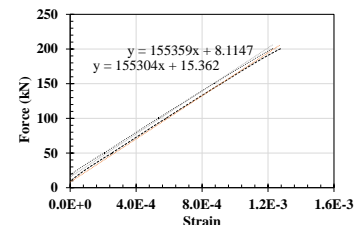
B19 – 2 Sample Rates



Full test

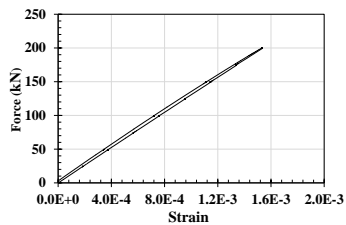


Loading test

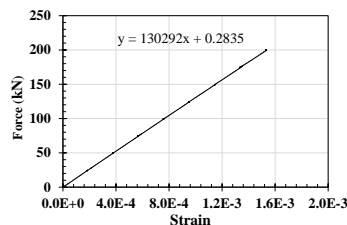


Unloading test

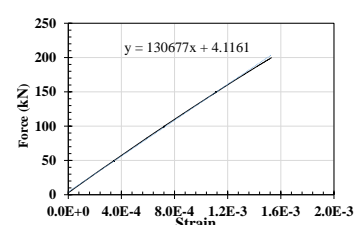
B20 – 50Hz



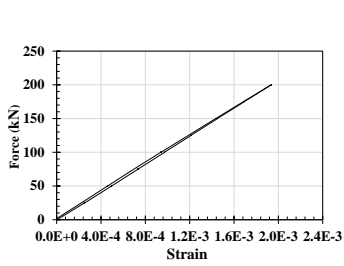
Full test



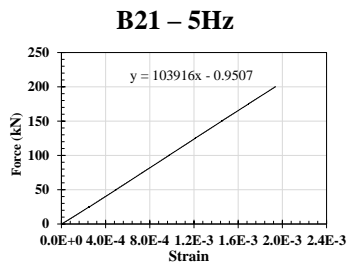
Loading test



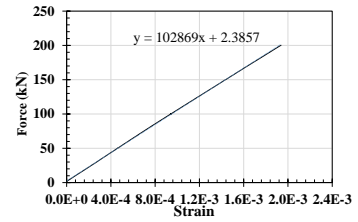
Unloading test



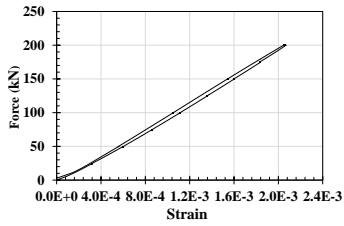
Full test



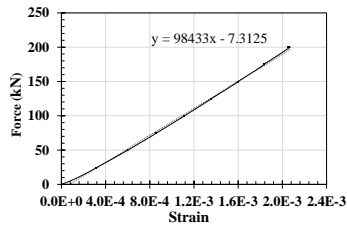
Loading test
B21 – 5Hz



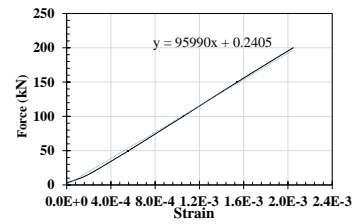
Unloading test



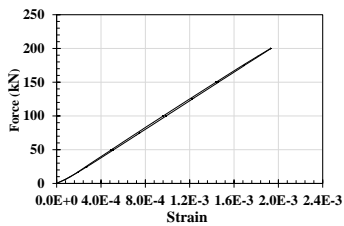
Full test



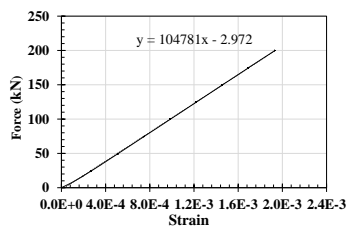
Loading test
B22 – 50Hz



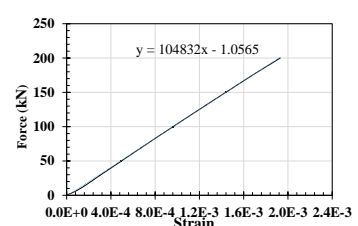
Unloading test



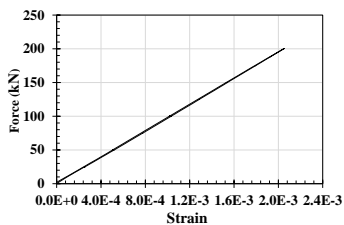
Full test



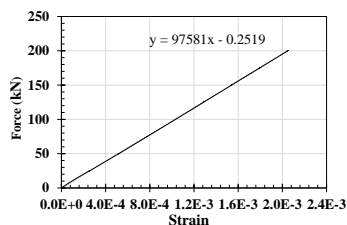
Loading test
B23 – 50Hz



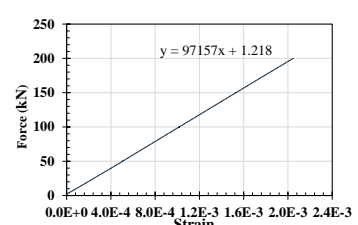
Unloading test



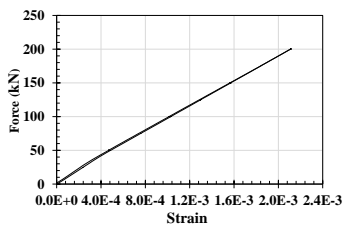
Full test



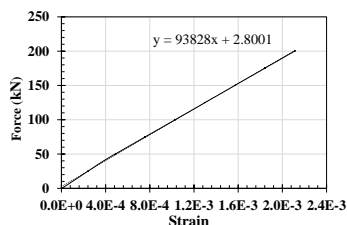
Loading test
B24 – 5Hz



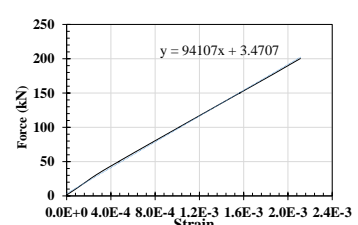
Unloading test



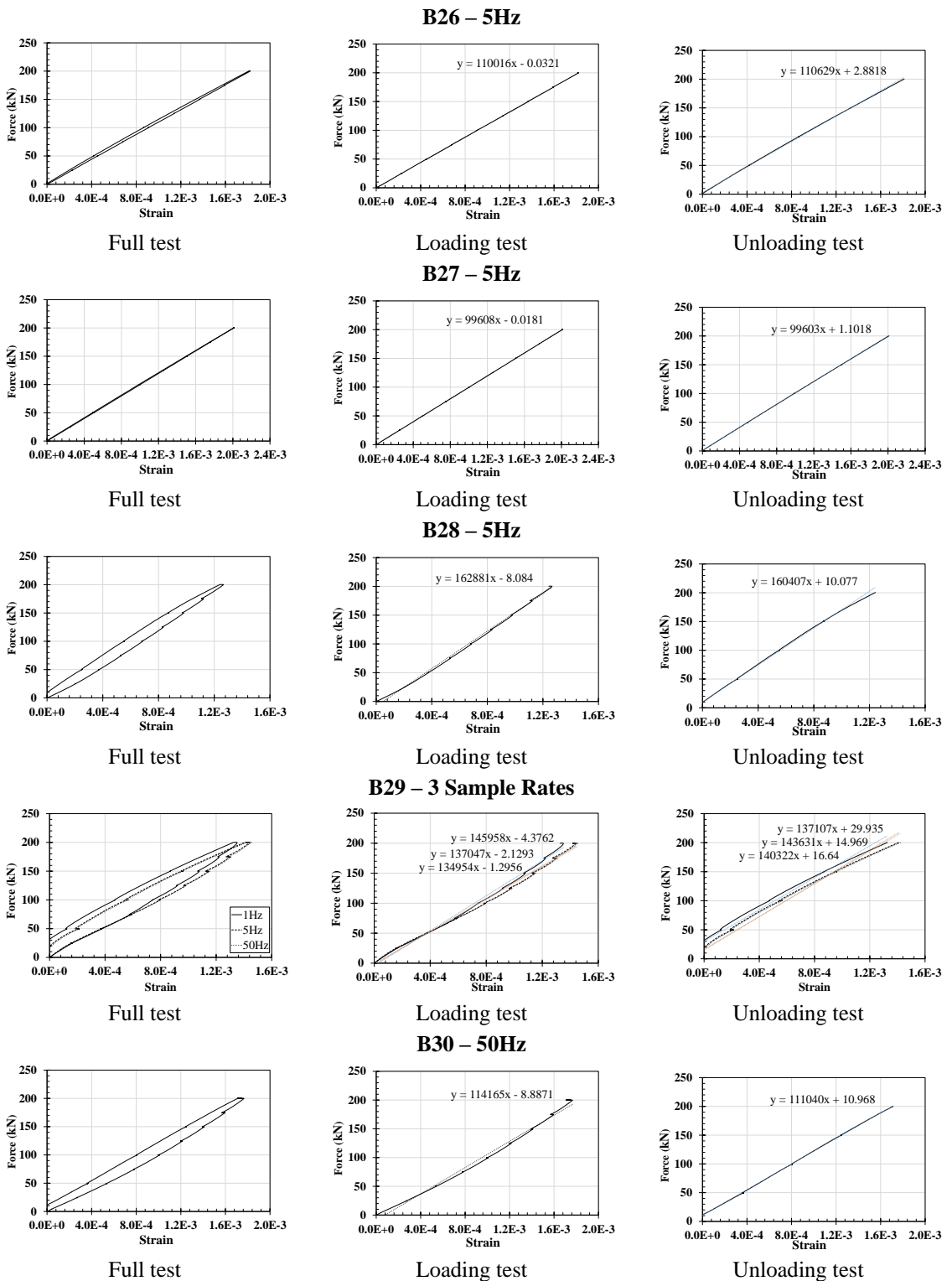
Full test



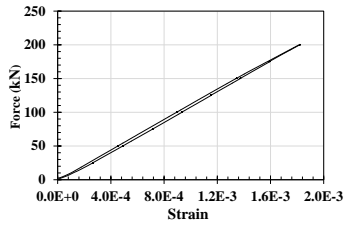
Loading test
B25 – 5Hz



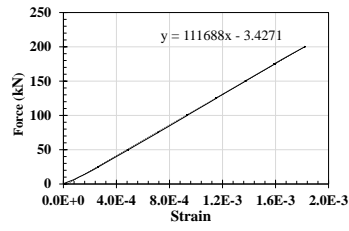
Unloading test



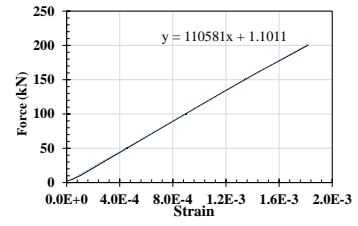
B31 – 50Hz



Full test

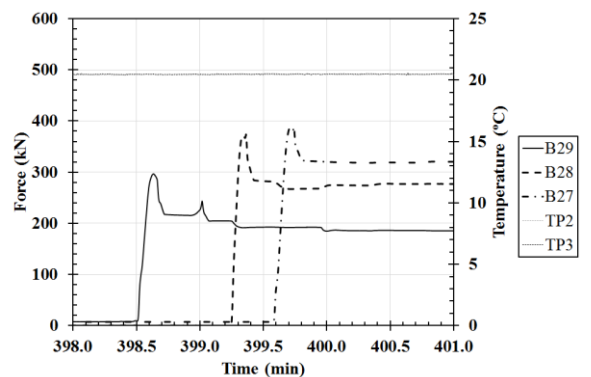
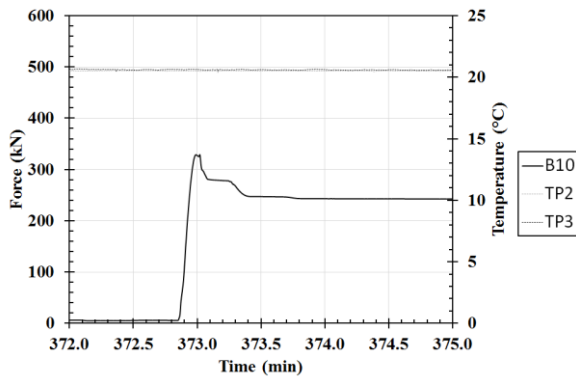
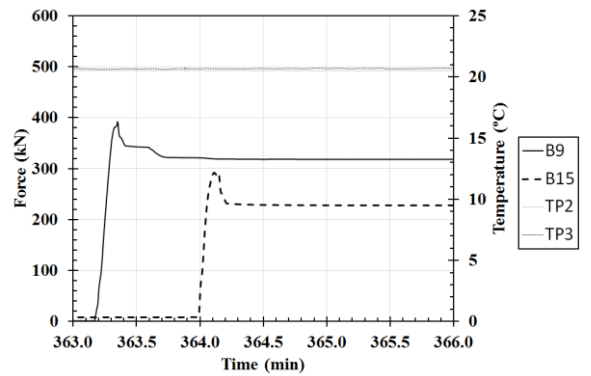
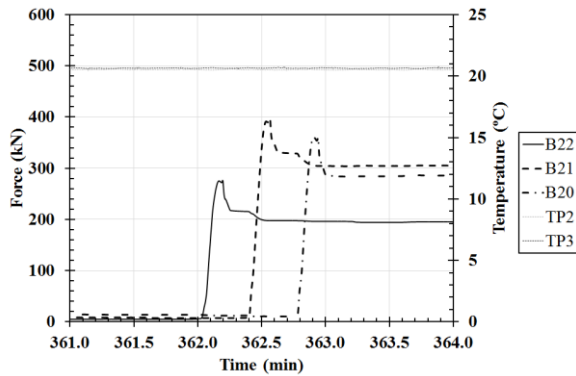
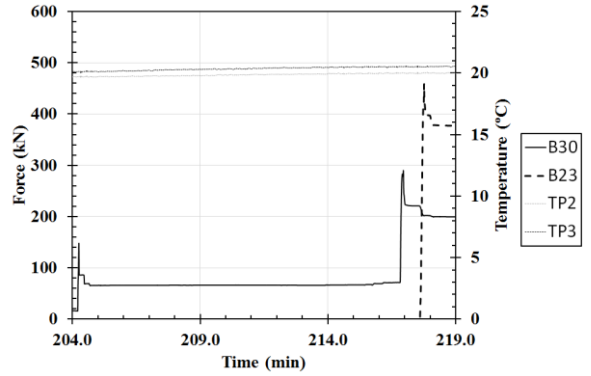
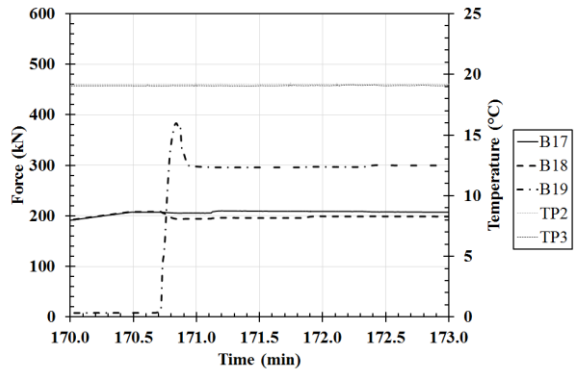
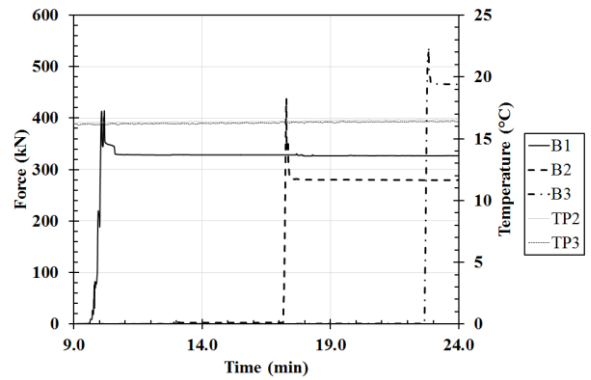
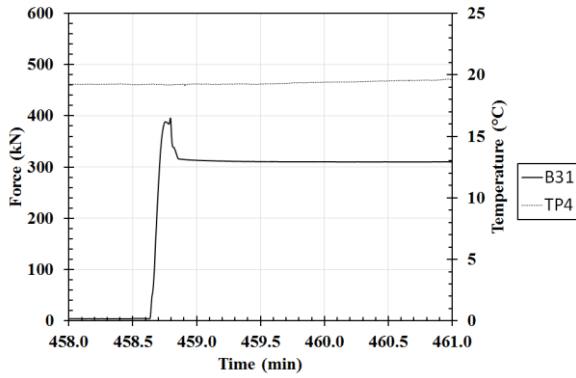


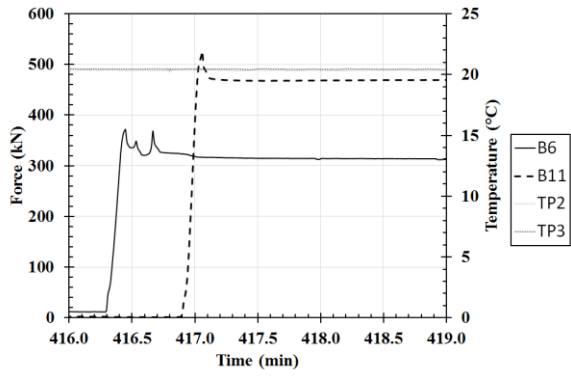
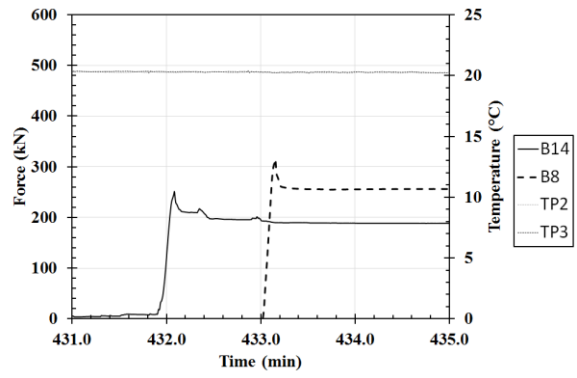
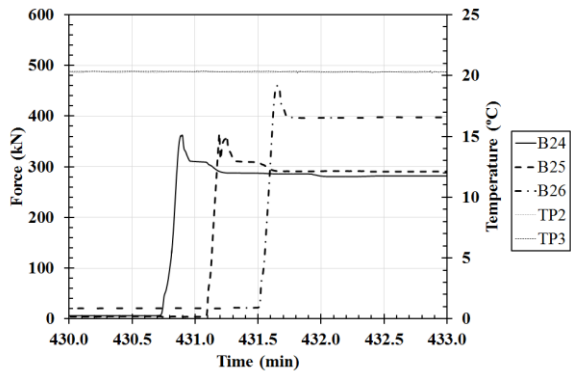
Loading test



Unloading test

ANNEX C - APPLIED FORCE VARIATION CURVES (BY ROW) – PROTOTYPE 2





ANNEX D - DMT CALCULATION PROCEDURE (MARCHETTI ET AL. 2001)

General layout of the dilatometer test

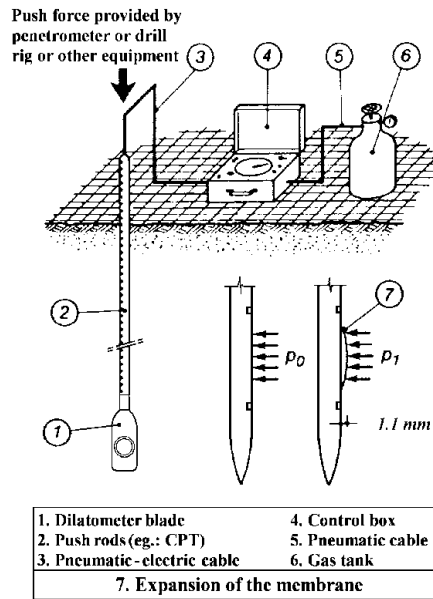
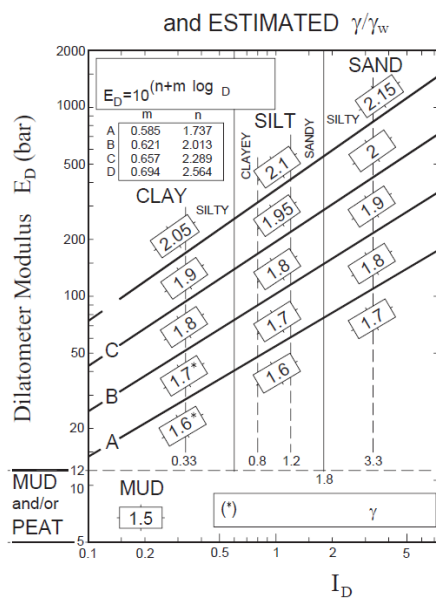


Chart for estimating soil type and unit weight γ (normalized to $\gamma_w = \gamma_{\text{water}}$)



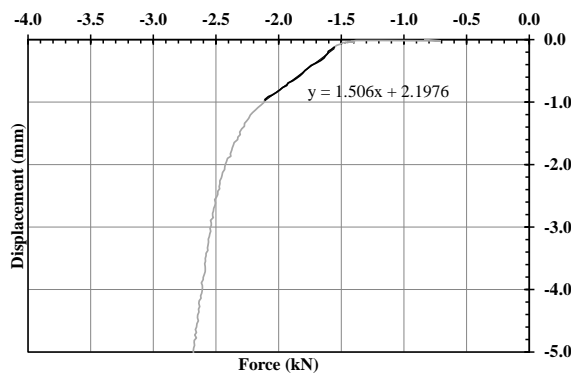
Basic DMT reduction formulae

SYMBOL		DESCRIPTION	BASIC DMT REDUCTION FORMULAE
p_0	Corrected First Reading	$p_0 = 1.05 (A - Z_M + \Delta A) - 0.05 (B - Z_M - \Delta B)$	$Z_M =$ Gage reading when vented to atm.
p_1	Corrected Second Reading	$p_1 = B - Z_M - \Delta B$	If ΔA & ΔB are measured with the same gage used for current readings A & B, set $Z_M = 0$ (Z_M is compensated)
I_D	Material Index	$I_D = (p_1 - p_0) / (p_0 - u_0)$	$u_0 =$ pre-insertion pore pressure
K_D	Horizontal Stress Index	$K_D = (p_0 - u_0) / \sigma'_{v0}$	$\sigma'_{v0} =$ pre-insertion overburden stress
E_D	Dilatometer Modulus	$E_D = 34.7 (p_1 - p_0)$	E_D is NOT a Young's modulus E. E_D should be used only AFTER combining it with K_D (Stress History). First obtain $M_{DMT} = R_M E_D$, then e.g. $E_s \approx 0.8 M_{DMT}$
K_0	Coeff. Earth Pressure in Situ	$K_{0,DMT} = (K_D / 1.5)^{0.47} - 0.6$	for $I_D < 1.2$
OCR	Overconsolidation Ratio	$OCR_{DMT} = (0.5 K_D)^{1.56}$	for $I_D < 1.2$
c_u	Undrained Shear Strength	$c_{u,DMT} = 0.22 \sigma'_{v0} (0.5 K_D)^{1.25}$	for $I_D < 1.2$
Φ	Friction Angle	$\Phi_{safe,DMT} = 28^\circ + 14.6^\circ \log K_D - 2.1^\circ \log^2 K_D$	for $I_D > 1.8$
c_h	Coefficient of Consolidation	$c_{h,DMTA} \approx 7 \text{ cm}^2 / t_{flex}$	t_{flex} from A-log t DMT-A decay curve
k_h	Coefficient of Permeability	$k_h = c_h \gamma_w / M_h$ ($M_h \approx K_0 M_{DMT}$)	
γ	Unit Weight and Description	(see chart)	
M	Vertical Drained	$M_{DMT} = R_M E_D$	
	Constrained Modulus	if $I_D \leq 0.6$ $R_M = 0.14 + 2.36 \log K_D$ if $I_D \geq 3$ $R_M = 0.5 + 2 \log K_D$ if $0.6 < I_D < 3$ $R_M = R_{M,0} + (2.5 - R_{M,0}) \log K_D$ with $R_{M,0} = 0.14 + 0.15 (I_D - 0.6)$ if $K_D > 10$ $R_M = 0.32 + 2.18 \log K_D$ if $R_M < 0.85$ set $R_M = 0.85$	
u_0	Equilibrium Pore Pressure	$u_0 = p_2 = C - Z_M + \Delta A$	In free-draining soils

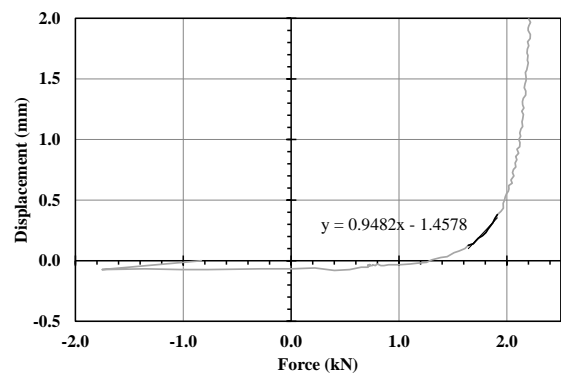
ANNEX E – STATIC/POST-CYCLIC STIFFNESS (EXPERIMENTAL TESTS ON MICROPILES)

The value of the initial stiffness (in kN/mm) is obtained by considering 1/m, with m being the inclination of the line, for each test presented.

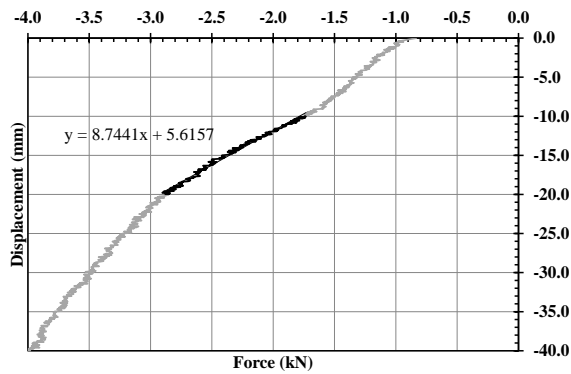
- Layout 2



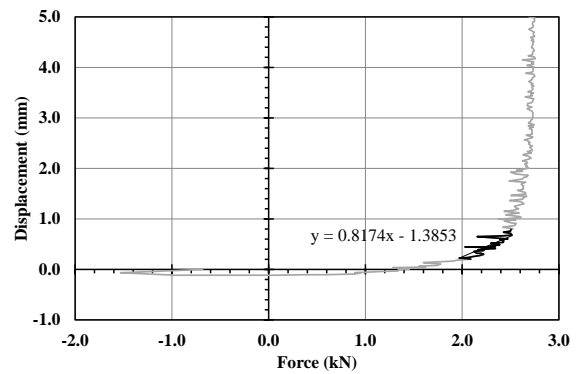
M3 Compression Ungrouted



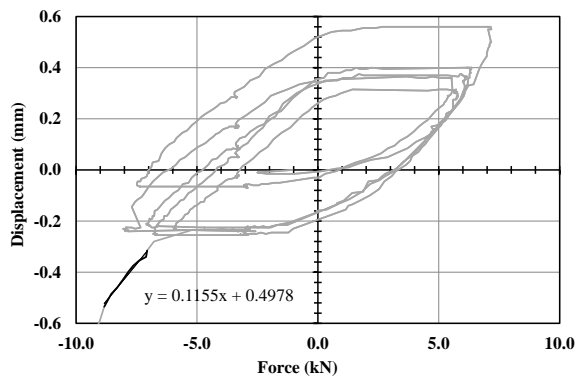
M3 Tension Ungrouted



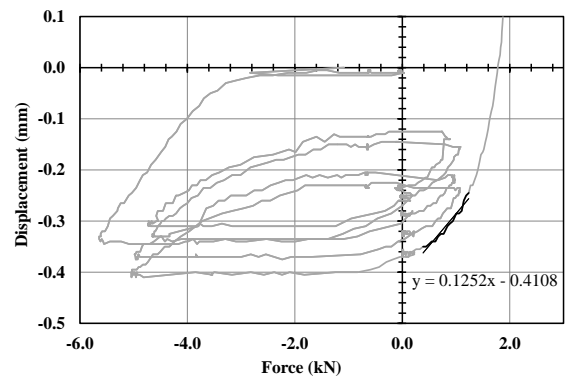
M4 Compression Ungrouted



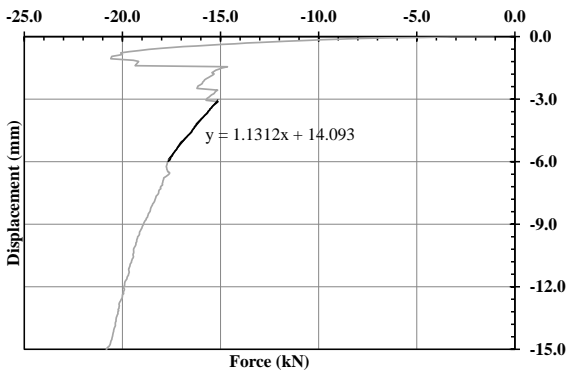
M4 Tension Ungrouted



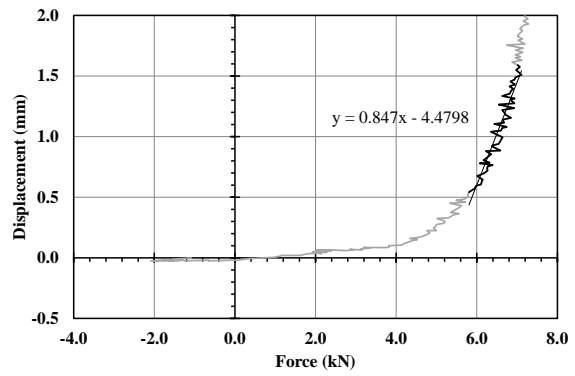
M3 Compression Grouted



M3 Tension Grouted

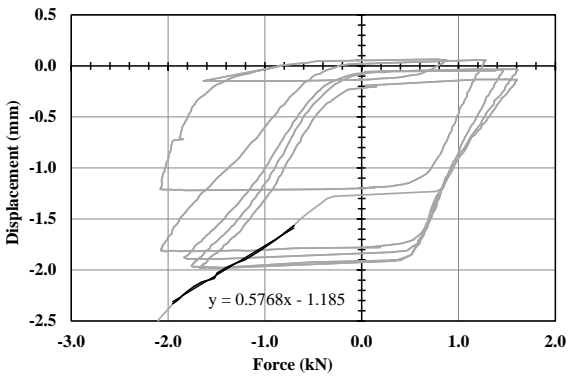


M4 Compression Grouted

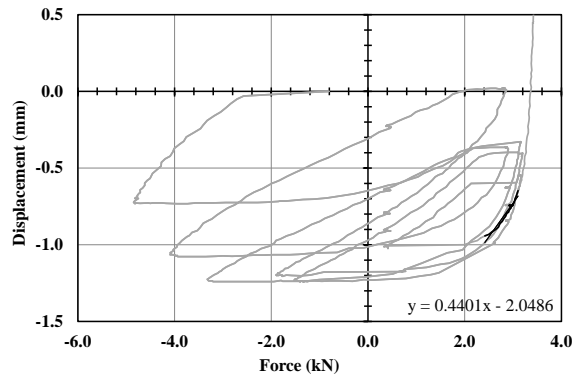


M4 Tension Grouted

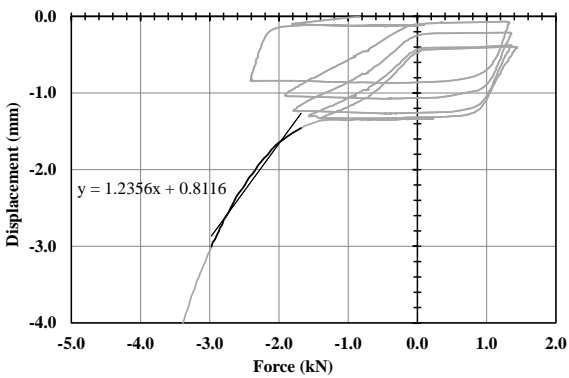
• Layout 3



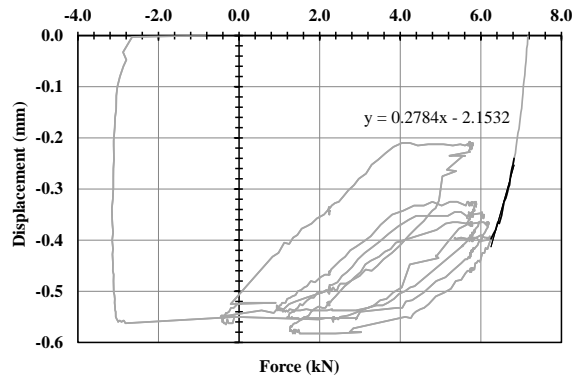
M5 Compression Ungouted



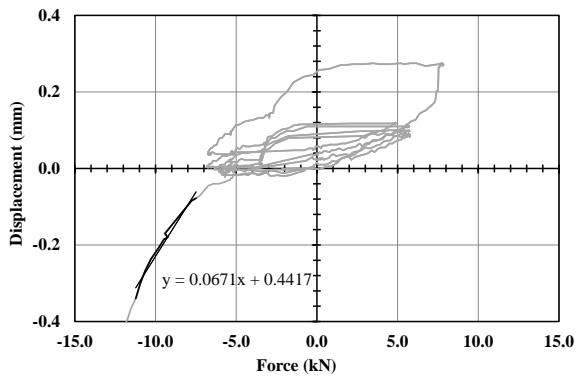
M5 Tension Ungouted



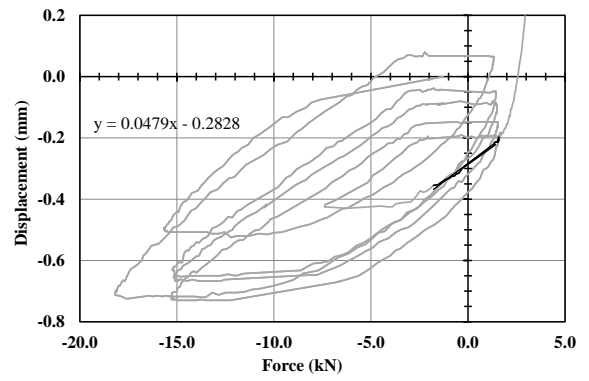
M6 Compression Ungouted



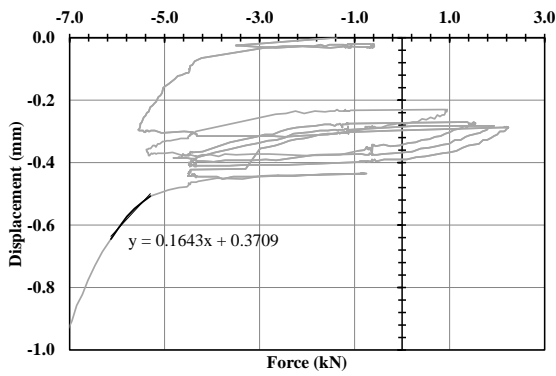
M6 Tension Ungouted



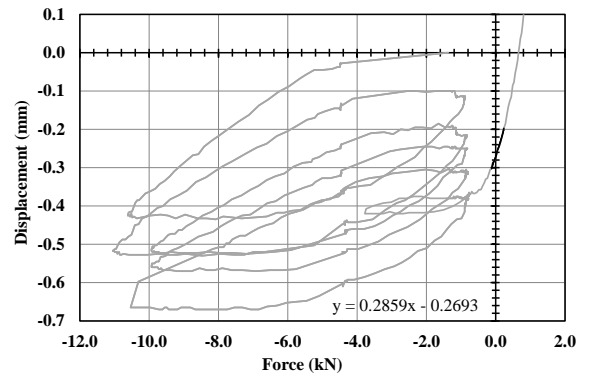
M5 Compression Grouted



M5 Tension Grouted

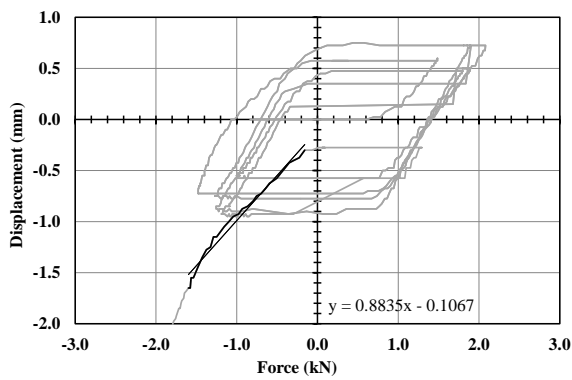


M6 Compression Grouted

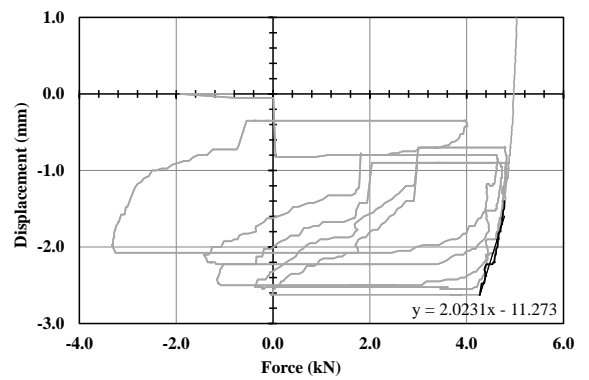


M6 Tension Grouted

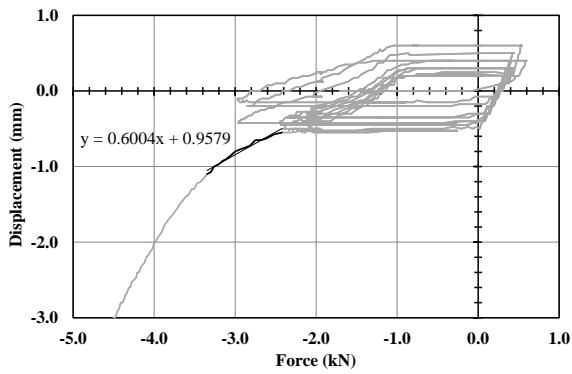
- Layout 4



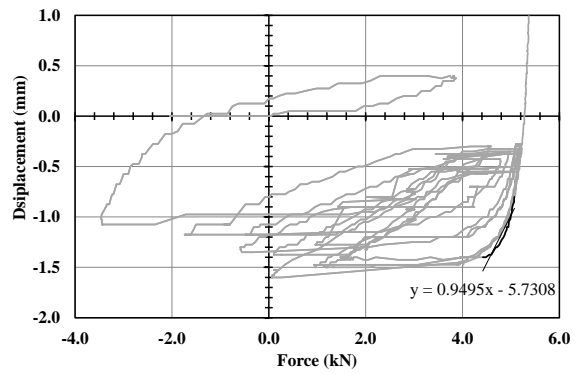
M7 Compression Ungouted



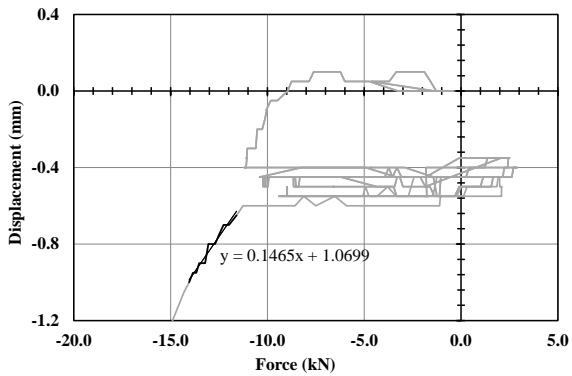
M7 Tension Ungouted



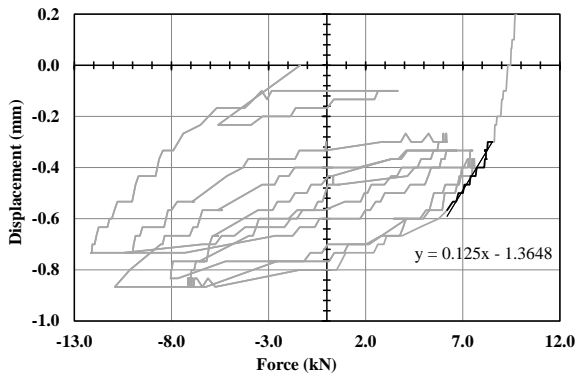
M8 Compression UngROUTed



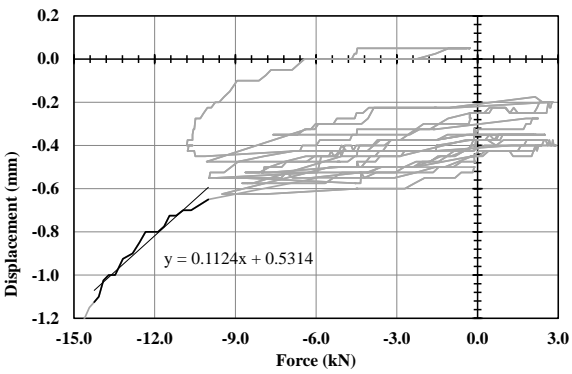
M8 Tension UngROUTed



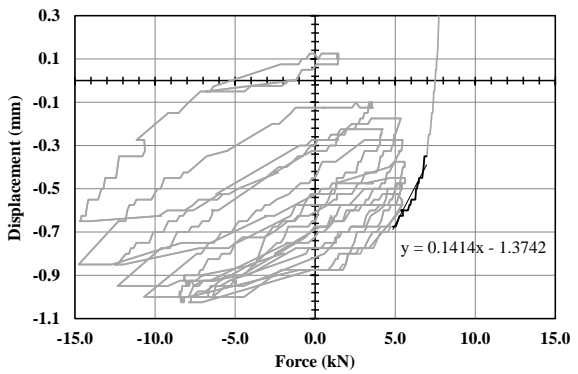
M7 Compression GROUTed



M7 Tension GROUTed

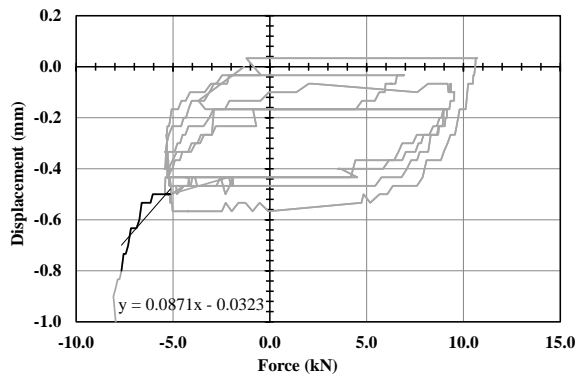


M8 Compression GROUTed

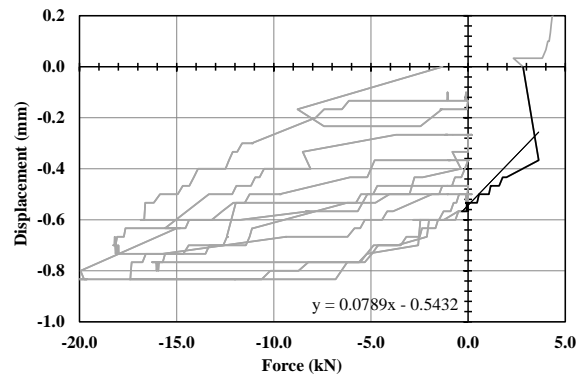


M8 Tension GROUTed

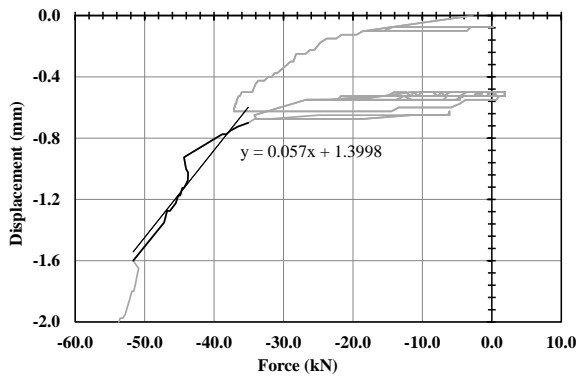
- Layout 5



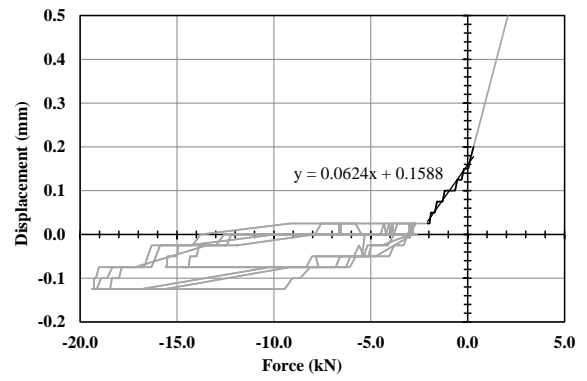
G1 Compression UngROUTED



G1 Tension UngROUTED

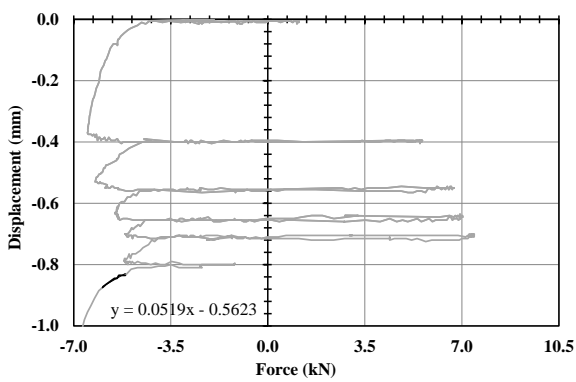


G1 Compression GROUTED

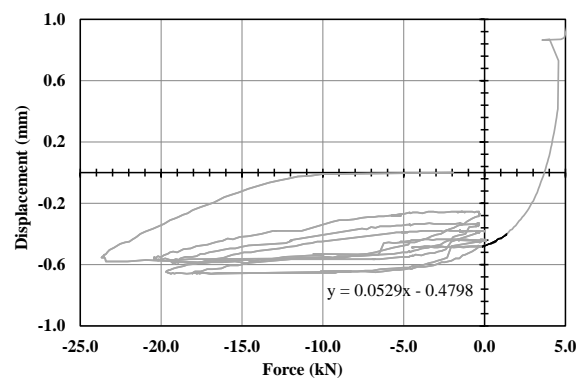


G1 Tension GROUTED

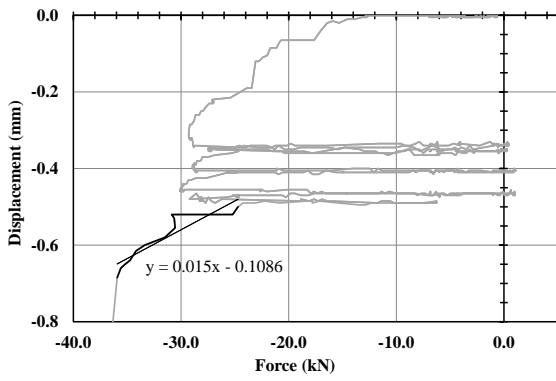
- Layout 6



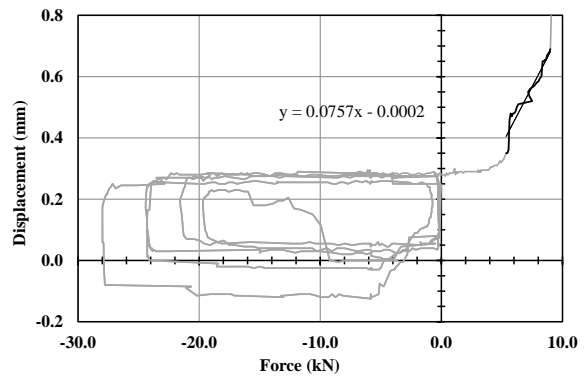
G2 Compression UngROUTED



G2 Tension UngROUTED

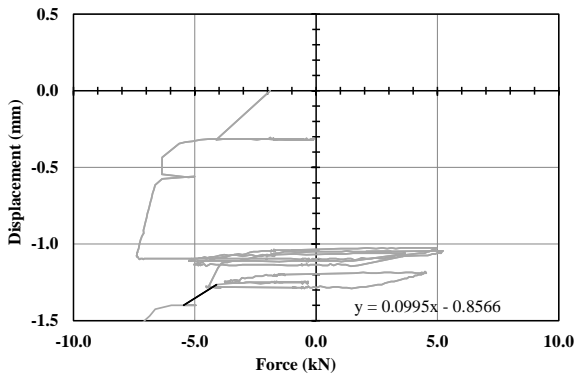


G2 Compression Grouted

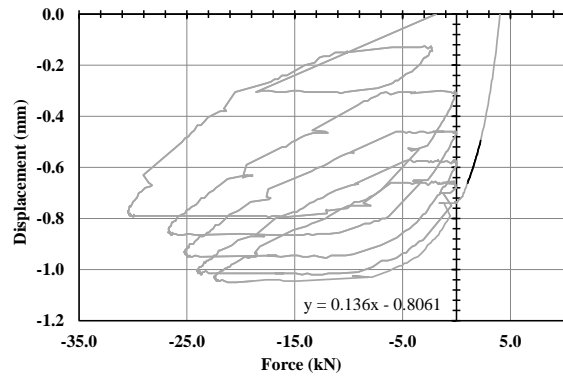


G2 Tension Grouted

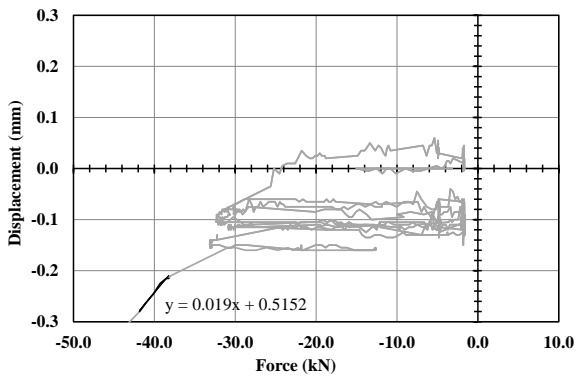
• Layout 7



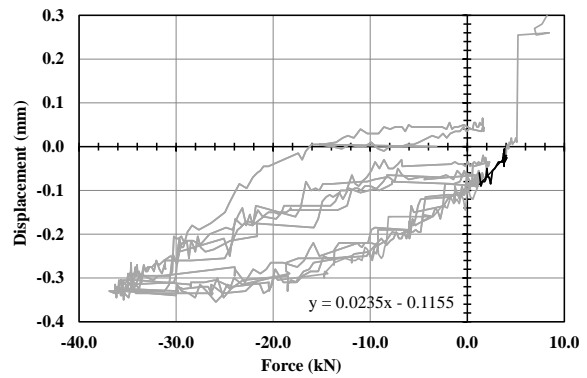
G3 Compression UngROUTed



G3 Tension UngROUTed



G3 Compression Grouted



G2 Tension Grouted

ANNEX F – HYBRID FOUNDATION DESIGN EXAMPLE (80M HIGH TUBULAR STEEL WIND TOWER)

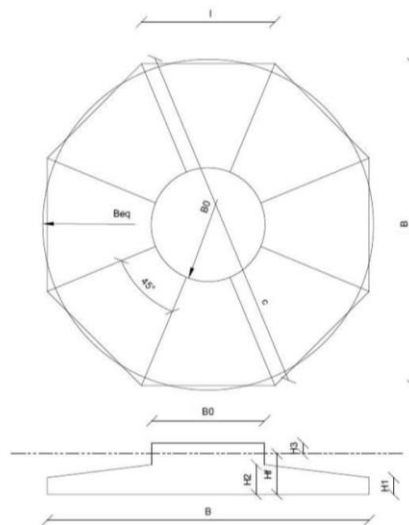
• Soil information:

$\nu_{so} := 0.30$	Soil poisson ratio
$E_{so} := 675 \cdot MPa$	Soil elastic modulus
$G_{so} := \frac{E_{so}}{2 \cdot (1 + \nu_{so})} = 259.615 \cdot MPa$	Soil shear modulus

• Loading (tower base - non factored):

$Fz_{total} := 2346 \cdot kN$	Vertical axial loading
$Fb_{total} := 870.9 \cdot kN$	Horizontal axial loading
$MbI := 60150 \cdot kN \cdot m$	Bending moment
$Mzb_{total} := 1218 \cdot kN \cdot m$	Torsional moment

• Foundation configuration:



$B_{eq} := 14.38 \cdot m$	$R := \frac{B_{eq}}{2} = 7.19 \cdot m$	$l2 := 5.8 \cdot m$	$n := 8$
$H_1 := 2.00 \cdot m$	$B := 14 \cdot m$	$\theta := 22.5 \cdot ^\circ$	$c := 15.15 \cdot m$
$H_1 := 1.23 \cdot m$	$H_2 := 2.00 \cdot m$	$H_3 := 0.50 \cdot m$	$B_0 := 5.60 \cdot m$

$$Area := \frac{12 \cdot \sqrt{\left(\frac{c}{2}\right)^2 - \left(\frac{12}{2}\right)^2}}{2} \cdot n = 162.351 \text{ m}^2$$

$$Area2 := \pi \cdot R^2 = 162.408 \text{ m}^2 \quad \text{Area circular foundation (Beq)}$$

$$Volum_{found} := Area \cdot H_1 + \frac{1 \cdot \pi}{3} \cdot \left(R^2 + R \cdot \frac{B_0}{2} + \left(\frac{B_0}{2} \right)^2 \right) \cdot (H_2 - H_1) + \pi \cdot \left(\frac{B_0}{2} \right)^2 \cdot H_3 = 276.247 \text{ m}^3$$

$$G_{fund} := Volum_{found} \cdot 25 \cdot \frac{kN}{m^3} = 6906.173 \text{ kN}$$

$$Volum_{balast} := \pi \cdot \left(\frac{B_{eq}}{2} \right)^2 \cdot (H_2 - H_1) - \frac{1 \cdot \pi}{3} \cdot \left(R^2 + R \cdot \frac{B_0}{2} + \left(\frac{B_0}{2} \right)^2 \right) \cdot (H_2 - H_1) = 60.814 \text{ m}^3$$

$$G_{balast} := Volum_{balast} \cdot 18 \cdot \frac{kN}{m^3} = 1094.661 \text{ kN}$$

• Loading (foundation base - non factored):

$$Fz_{res_mp} := |Fzb_{total}| + G_{fund} + G_{balast} = 10347 \text{ kN}$$

$$F_{res_mp} := |Fb_{total}| = 871 \text{ kN}$$

$$M_{res_mp} := |MbI| + |Fb_{total}| \cdot (2 \cdot m + H_1) = 63634 \text{ kN} \cdot m$$

• Numerical results - micropile forces:

$$qs := 200 \text{ kPa} \quad l := 12 \text{ m} \quad d_{micro} := 200 \text{ mm} \quad \text{Micropile geometry}$$

Bearing 1 combination resistances

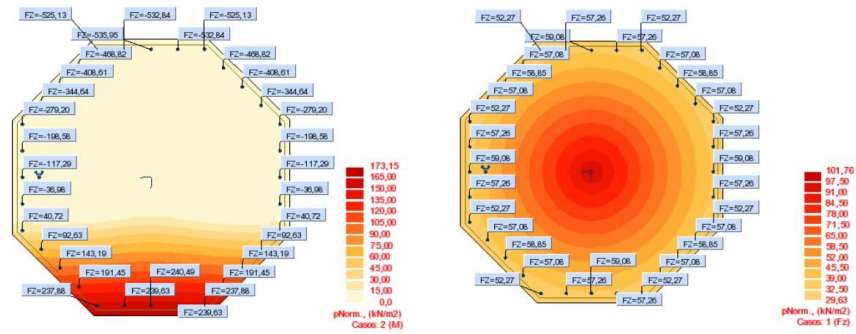
$$R_{c1d} := \frac{qs \cdot \pi \cdot d_{micro} \cdot l}{1 \cdot 1.5} = 1005 \text{ kN} \quad \text{Compression}$$

$$R_{c1d} := \frac{qs \cdot \pi \cdot d_{micro} \cdot l}{1.25 \cdot 1.5} = 804 \text{ kN} \quad \text{Tension}$$

Bearing 2 and overturning combination resistances

$$R_{c1d} := \frac{qs \cdot \pi \cdot d_{micro} \cdot l}{1.3 \cdot 1.5} = 773 \text{ kN} \quad \text{Compression}$$

$$R_{c1d} := \frac{qs \cdot \pi \cdot d_{micro} \cdot l}{1.6 \cdot 1.5} = 628 \text{ kN} \quad \text{Tension}$$

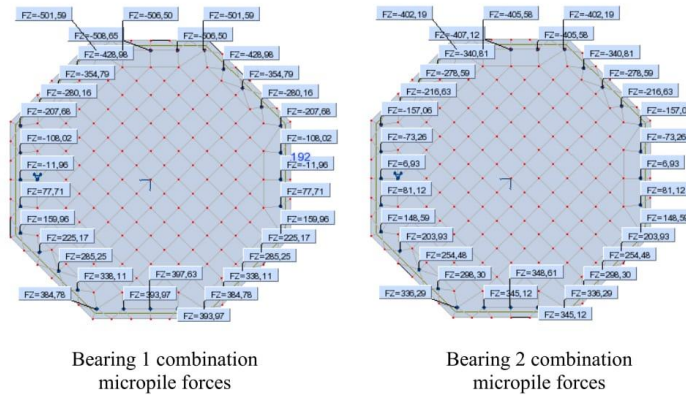


Bending moment reactions

Axial compression load reactions

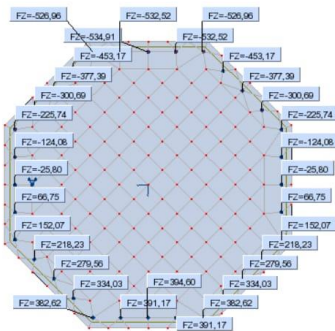
The soil was modelled to withstand and resist only to compression forces

For non-factored loading, the contribution of the micropiles for compression loading was 1805kN of the applied 10347kN and for the bending moment was 43290kN.m of the applied 63634kN.m



Bearing 1 combination micropile forces

Bearing 2 combination micropile forces



Overturning combination micropile forces

For all the combinations considered, the micropile forces never surpass their resistance in the correspondent combination

• **Shallow portion design:**

$\phi'_k := 42 \cdot \text{°}$ $c_k := 0 \cdot \frac{\text{kN}}{\text{m}^2}$ $\gamma := 18 \cdot \frac{\text{kN}}{\text{m}^3}$ $\delta_b := \phi'_k$ Soil parameters

- Loads on foundation base, non-factored (subtracting the micropile resistance contribution)

$Fz_{res} := Fz_{res_mp} - 1805 \cdot \text{kN} = 8542 \text{ kN}$

$F_{res} := F_{res_mp} = 871 \text{ kN}$

$M_{res} := M_{res_mp} - 43290 \cdot \text{kN} \cdot \text{m} = 20343.6 \text{ kN} \cdot \text{m}$

- Compression under the foundation

Found. total compressed if $ee := \frac{M_{res}}{Fz_{res}} = 2.382 \text{ m} < \frac{R}{4} = 1.798 \text{ m}$

50% found. compressed if $\frac{ee}{R} = 0.331 < 0.59$

- Pressure on foundation base for non-factored loads

$K := 2.4$

Coef.K (Reference graph)

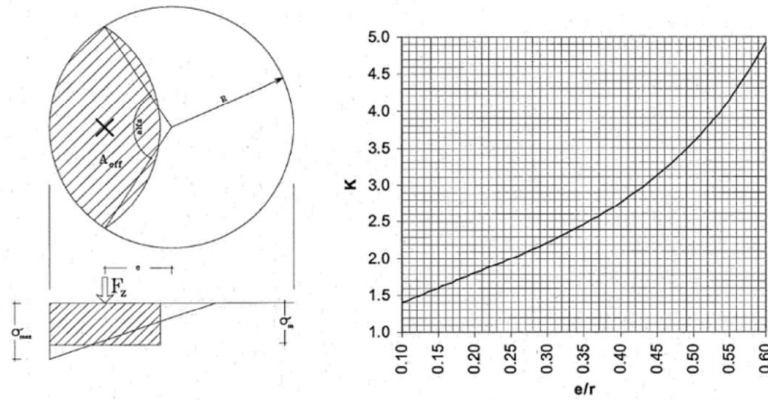


Figura 3 – Distribuição das pressões na base da fundação [2]

$\alpha := 2 \cdot \text{acos} \left(\frac{ee}{R} \right) = 141.311 \text{ °}$

$A_{eff} := R^2 \cdot (\alpha - \sin(\alpha)) = 95.186 \text{ m}^2$

Found. effective area

$$A_{eff} := R^2 \cdot (\alpha - \sin(\alpha)) = 95.186 \text{ m}^2 \quad \text{Found. effective area}$$

$$\sigma_{max} := K \cdot \frac{Fz_{res}}{\pi \cdot R^2} = 126.228 \text{ kPa} \quad \text{Max.}$$

$$\sigma_{med} := \frac{Fz_{res}}{A_{eff}} = 89.738 \text{ kPa} \quad \text{Av.}$$

- Limit state of equilibrium (EC7) $\gamma_{qi} := 1.50 \quad \gamma_{gi} := 0.9$

Design values

$$M_{Ed.res} := \gamma_{qi} \cdot M_{res} = 30515.4 \text{ kN} \cdot \text{m}$$

$$F_{Ed.res} := \gamma_{qi} \cdot F_{res} = 1306.35 \text{ kN}$$

$$Fz_{Ed.res} := \gamma_{gi} \cdot Fz_{res} = 7687.65 \text{ kN}$$

$$Fz_{Ed.res} \cdot \frac{B}{2} = 53813.55 \text{ kN} \cdot \text{m}$$

$$\frac{M_{Ed.res}}{Fz_{Ed.res} \cdot \frac{B}{2}} = 0.5671$$

- Bearing capacity

Verification for ULS-STR $\gamma_{qi} := 1.50 \quad \gamma_{gi} := 1$

$$M_{Ed.res} := \gamma_{qi} \cdot M_{res} = 30515.4 \text{ kN} \cdot \text{m}$$

$$F_{Ed.res} := \gamma_{qi} \cdot F_{res} = 1306.35 \text{ kN}$$

$$Fz_{Ed.res} := \gamma_{gi} \cdot Fz_{res} = 8541.833 \text{ kN}$$

$$ee := \frac{M_{Ed.res}}{Fz_{Ed.res}} = 3.572 \text{ m} \quad \text{Load eccentricity}$$

$$\alpha := 2 \cdot \arccos\left(\frac{ee}{R}\right) = 120.414^\circ \quad \text{Effective area}$$

$$A_{eff} := R^2 \cdot (\alpha - \sin(\alpha)) = 64.064 \text{ m}^2$$

$$L' := \frac{\sqrt{4 \cdot R^2 - (2 \cdot ee)^2}}{2} \cdot 2 \cdot 0.9 = 11.231 \text{ m} \quad B' := \frac{A_{eff}}{L'} = 5.704 \text{ m} \quad \text{Rectangular equivalent foundation}$$

$$\phi'_d := \phi'_k \quad c'_d := 0 \cdot \frac{\text{kN}}{\text{m}^2} \quad \gamma_d := 18 \cdot \frac{\text{kN}}{\text{m}^3} \quad \text{Soil parameters}$$

Capacity factors (EC7 D.4):

$$N_q := e^{\pi \cdot \tan(\phi'_d)} \cdot \tan\left(45^\circ + \frac{\phi'_d}{2}\right) = 85.374$$

$$N_c := (N_q - 1) \cdot \cot(\phi'_d) = 93.706$$

$$N_\gamma := \begin{cases} \text{if } 2 \cdot (N_q - 1) \cdot \tan(\phi'_d) \geq \frac{\phi'_d}{2} \\ \quad \left\| \left\| (2 \cdot (N_q - 1) \cdot \tan(\phi'_d)) \right\| \right. \\ \text{else} \\ \quad \left\| \left\| \frac{\phi'_d}{2} \right\| \right. \end{cases} \quad N_\gamma = 151.941$$

Shape factors (EC7 D.4):

$$s_q := 1 + \left(\frac{B'}{L'}\right) \cdot \sin(\phi'_d) = 1.34$$

$$s_\gamma := 1 - 0.3 \cdot \left(\frac{B'}{L'}\right) = 0.848$$

$$s_c := \frac{(s_q \cdot N_q - 1)}{(N_q - 1)} = 1.344$$

Inclination factors (H/B):

$$m_B := \frac{2 + \frac{B'}{L'}}{1 + \frac{B'}{L'}} = 1.663$$

$$i_q := \left(1 - \frac{F_{Ed,res}}{Fz_{Ed,res} + B' \cdot L' \cdot c'_d \cdot \cot(\phi'_d)}\right)^{m_B} = 0.759$$

$$i_\gamma := \left(1 - \frac{F_{Ed,res}}{Fz_{Ed,res} + B' \cdot L' \cdot c'_d \cdot \cot(\phi'_d)}\right)^{m_B + 1} = 0.643$$

$$i_c := i_q - \frac{1 - i_q}{N_c \cdot \tan(\phi'_d)} = 0.756$$

$$q' := H_f \cdot \gamma_d = 36 \text{ kPa}$$

Pressure on foundation level

Bearing resistance (EC7 eq.D.2):

$$R_d := (c'_d \cdot N_c \cdot (s_c \cdot i_c) + q' \cdot N_q \cdot (s_q \cdot i_q) + 0.5 \cdot B' \cdot \gamma_d \cdot N_\gamma \cdot (s_\gamma \cdot i_\gamma)) \cdot A_{eff} = 472406.59 \text{ kN}$$

$$Fz_{Ed,res} = 8541.833 \text{ kN}$$

$$Fz_{Ed.res} < R_d = 1 \quad \frac{Fz_{Ed.res}}{R_d} = 0.018$$

DNV verification (extremely eccentric loading)

$$i_q := 1 + \frac{F_{Ed.res}}{Fz_{Ed.res} + A_{eff} \cdot c'_d \cdot \cot(\phi'_d)} = 1.153 \quad i_c := i_q \quad i_\gamma := i_q^2 = 1.329$$

$$R_d := (c'_d \cdot N_c \cdot (s_c \cdot i_c) \cdot (1.05 \cdot \tan(\phi'_d))^3) + B' \cdot \gamma_d \cdot N_\gamma \cdot (s_\gamma \cdot i_\gamma) \cdot A_{eff} = 1126055.448 \text{ kN}$$

$$Fz_{Ed.res} = 8541.833 \text{ kN}$$

$$Fz_{Ed.res} < R_d = 1 \quad \frac{Fz_{Ed.res}}{R_d} = 0.008$$

$$\text{Verification ULS-GEO} \quad \gamma_{qi} := 1.30 \quad \gamma_{gi} := 1$$

$$M_{Ed.res} := \gamma_{qi} \cdot M_{res} = 26446.68 \text{ kN} \cdot \text{m}$$

$$F_{Ed.res} := \gamma_{qi} \cdot F_{res} = 1132.17 \text{ kN}$$

$$Fz_{Ed.res} := \gamma_{gi} \cdot Fz_{res} = 8541.833 \text{ kN}$$

$$ee := \frac{M_{Ed.res}}{Fz_{res}} = 3.096 \text{ m} \quad \text{Load eccentricity}$$

$$\alpha := 2 \cdot \arccos\left(\frac{ee}{R}\right) = 128.987^\circ$$

$$A_{eff} := R^2 \cdot (\alpha - \sin(\alpha)) = 76.197 \text{ m}^2 \quad \text{Rectangular effective area}$$

$$L' := \frac{\sqrt{4 \cdot R^2 - (2 \cdot ee)^2}}{2} \cdot 2 \cdot 0.9 = 11.681 \text{ m} \quad B' := \frac{A_{eff}}{L'} = 6.523 \text{ m} \quad \text{Rectangular equivalent foundation:}$$

$$\gamma_d := 18 \cdot \frac{\text{kN}}{\text{m}^3} \quad c'_d := 0 \cdot \frac{\text{kN}}{\text{m}^2} \quad \phi'_d := \text{atan}\left(\frac{\tan(\phi_k)}{1.25}\right) = 35.766^\circ \quad \text{Soil parameters}$$

Capacity load factors (EC7 D.4):

$$N_q := e^{\pi \cdot \tan(\phi'_d)} \cdot \tan\left(45^\circ + \frac{\phi'_d}{2}\right) = 36.651$$

$$N_c := (N_q - 1) \cdot \cot(\phi'_d) = 49.493$$

$$N_\gamma := \begin{cases} \text{if } 2 \cdot (N_q - 1) \cdot \tan(\phi'_d) \geq \frac{\phi'_d}{2} \\ \quad \left\| \left\| (2 \cdot (N_q - 1) \cdot \tan(\phi'_d)) \right\| \right. \\ \quad \text{else} \\ \quad \left\| \left\| \frac{\phi'_d}{2} \right\| \right. \end{cases} \quad N_\gamma = 51.36$$

Form factors (EC7 D.4):

$$s_q := 1 + \left(\frac{B'}{L'} \right) \cdot \sin(\phi'_d) = 1.326$$

$$s_\gamma := 1 - 0.3 \cdot \left(\frac{B'}{L'} \right) = 0.832$$

$$s_c := \frac{(s_q \cdot N_q - 1)}{(N_q - 1)} = 1.336$$

Inclination factors (H/B):

$$m_B := \frac{2 + \frac{B'}{L'}}{1 + \frac{B'}{L'}} = 1.642$$

$$i_q := \left(1 - \frac{F_{Ed,res}}{Fz_{Ed,res} + B' \cdot L' \cdot c'_d \cdot \cot(\phi'_d)} \right)^{m_B} = 0.792$$

$$i_\gamma := \left(1 - \frac{F_{Ed,res}}{Fz_{Ed,res} + B' \cdot L' \cdot c'_d \cdot \cot(\phi'_d)} \right)^{m_B + 1} = 0.687$$

$$i_c := i_q - \frac{1 - i_q}{N_c \cdot \tan(\phi'_d)} = 0.786$$

$$q' := H_f \cdot \gamma_d = 36 \text{ kPa} \quad \text{Tension on foundation level}$$

(EC7 eq.D.2)

$$R_d := (c'_d \cdot N_c \cdot (s_c \cdot i_c) + q' \cdot N_q \cdot (s_q \cdot i_q) + 0.5 \cdot B' \cdot \gamma_d \cdot N_\gamma \cdot (s_\gamma \cdot i_\gamma)) \cdot A_{eff} = 236967.513 \text{ kN}$$

$$Fz_{Ed,res} = 8541.833 \text{ kN}$$

$$Fz_{Ed,res} < R_d \quad \frac{Fz_{Ed,res}}{R_d} = 0.036$$

DNV verification (extremely eccentric loading)

$$i_q := 1 + \frac{F_{Ed.res}}{Fz_{Ed.res} + A_{eff} \cdot c'_d \cdot \cot(\phi'_d)} = 1.133 \quad i_c := i_q \quad i_\gamma := i_q^2 = 1.283$$

$$R_d := (c'_d \cdot N_c \cdot (s_c \cdot i_c) \cdot (1.05 \cdot \tan(\phi'_d))^3) + B' \cdot \gamma_d \cdot N_\gamma \cdot (s_\gamma \cdot i_\gamma) \cdot A_{eff} = 490663.937 \text{ kN}$$

$$Fz_{Ed.res} = 8541.833 \text{ kN}$$

$$Fz_{Ed.res} < R_d = 1 \quad \frac{Fz_{Ed.res}}{R_d} = 0.017$$

- Ultimate limit state of sliding

STR Combination $\gamma_{qi} := 1.50$ $\gamma_{gi} := 1$

$$\phi'_d := \text{atan}\left(\frac{\tan(\phi'_k)}{1.00}\right) = 42^\circ \quad \delta_b := \phi'_d$$

Design values

$$M_{Ed.res} := \gamma_{qi} \cdot M_{res} = 30515.4 \text{ kN} \cdot \text{m}$$

$$Mz_{Ed.res} := Mzb_{total} \cdot \gamma_{qi} = 1827 \text{ kN} \cdot \text{m}$$

$$F_{Ed.res} := \gamma_{qi} \cdot F_{res} = 1306.35 \text{ kN}$$

$$Fz_{Ed.res} := \gamma_{gi} \cdot Fz_{res} = 8541.833 \text{ kN}$$

$$F_{h,t} := \frac{3}{16} \cdot \frac{Mzb_{total}}{R} = 31.763 \text{ kN} \quad \text{Torsional contribution}$$

$$H_d := \frac{1}{8} \cdot F_{Ed.res} + \frac{3 \cdot Mz_{Ed.res}}{16 \cdot R} = 210.938 \text{ kN} \quad \text{Force on the most loaded triangle}$$

$$R_d := Fz_{Ed.res} \cdot \tan\left(\frac{2 \cdot \delta_b}{3}\right) = 4541.773 \text{ kN} \quad \text{Triangular resistance}$$

$$H_d := F_{Ed.res} + \frac{3 \cdot Mz_{Ed.res}}{2 \cdot R} = 1687.504 \text{ kN}$$

$$\frac{H_d}{R_d} = 0.372$$

GEO Combination $\gamma_{qi} := 1.3$ $\gamma_{gi} := 1$

$$\phi'_d := \text{atan}\left(\frac{\tan(\phi'_k)}{1.25}\right) = 35.766^\circ \quad \delta_b := \phi'_d$$

Design values:

$$M_{Ed, res} := \gamma_{qi} \cdot M_{res} = 26446.68 \text{ kN} \cdot \text{m}$$

$$Mz_{Ed, res} := Mzb_{total} \cdot \gamma_{qi} = 1583.4 \text{ kN} \cdot \text{m}$$

$$F_{Ed, res} := \gamma_{qi} \cdot F_{res} = 1132.17 \text{ kN}$$

$$Fz_{Ed, res} := \gamma_{gi} \cdot Fz_{res} = 8541.833 \text{ kN}$$

$$F_{h,t} := \frac{3}{16} \cdot \frac{Mzb_{total}}{R} = 31.763 \text{ kN} \quad \text{Torsional contribution}$$

$$H_d := \frac{1}{8} \cdot F_{Ed, res} + \frac{3 \cdot Mz_{Ed, res}}{16 \cdot R} = 182.813 \text{ kN} \quad \text{Force on the most loaded triangle}$$

$$R_d := Fz_{Ed, res} \cdot \tan\left(\frac{2 \cdot \delta_b}{3}\right) = 3775.246 \text{ kN} \quad \text{Triangular resistance}$$

$$H_d := F_{Ed, res} + \frac{3 \cdot Mz_{Ed, res}}{2 \cdot R} = 1462.504 \text{ kN}$$

$$\frac{H_d}{R_d} = 0.387$$

• Seismic analysis design (non-governing for this case (and generally non-governing for steel towers))

- Seismic loading evaluation (values considered in the tower design analysis)

Soil type B

$$Vq_{Ib} := 271 \text{ kN}$$

- Loads on foundation base, non-factored

$$Fz_{res} := Fz_{res_mp} = 10347 \text{ kN}$$

$$F_{res} := Vq_{Ib} + 0.30 \cdot F_{res_mp} = 532 \text{ kN} \quad (\text{seismic load cases lower than the wind action})$$

$$M_{res} := MbI + F_{res} \cdot (2 \cdot m + H_f) = 62279 \text{ kN} \cdot \text{m}$$

- For the design consider the same steps as for the design of the shallow portion under wind loading (limit state of equilibrium, bearing capacity, safety against sliding) adding the following verifications

E minimum to ensure minimum stiffness

$$E_{s_{dyn}} := 2.5 \cdot 10^{10} \cdot \frac{3}{4} \cdot \frac{1}{\left(\frac{R}{m}\right)^3} \cdot \frac{(1 + \nu_{so}) \cdot (1 - \nu_{so})^2}{(1 - \nu_{so} - 2 \cdot \nu_{so}^2)} \cdot 1 \cdot 10^{-6} = 61.795$$

$$E_{so} = 675 \text{ MPa}$$

$$G_{so} := \frac{E_{so}}{2 \cdot (1 + \nu_{so})} = 259.615 \text{ MPa}$$

$$vel := \sqrt[2]{\frac{200 \cdot \text{MPa} \cdot g}{18 \cdot \frac{\text{kN}}{\text{m}^3}}} = 330.095 \frac{\text{m}}{\text{s}} \quad \text{Propagation speed of seismic waves}$$

• EC8-5 Verification

$$B := B_{eq} = 14.38 \text{ m}$$

Found. width 150m

$$\rho := \frac{18}{g} \cdot \frac{\text{kN}}{\text{m}^3} = 1835 \frac{\text{kg}}{\text{m}^3}$$

Soil weight

$$S := 1$$

Coef do solo (EC8-1)

$$\gamma_I := 1$$

Importance factor

$$a_{gR} := 2 \cdot \frac{\text{m}}{\text{s}^2}$$

Reference design acceleration on Type A soil

$$a_g := a_{gR} \cdot \gamma_I$$

Design acceleration

$$a_v := 0.5 \cdot a_g \cdot S = 1 \frac{\text{m}}{\text{s}^2}$$

Vertical acceleration of ground, may be equal to 0.5a.g*S

$$\phi'_k = 42^\circ$$

$$\gamma_M := 1.25$$

$$\phi'_d := \text{atan}\left(\frac{\tan(\phi'_k)}{\gamma_M}\right) = 36^\circ$$

$$N_\gamma := 2 \cdot \left(\tan\left(45^\circ + \frac{\phi'_d}{2}\right) \cdot e^{\pi \cdot \tan(\phi'_d)} + 1 \right) \cdot \tan(\phi'_d) = 54.241$$

Capacity load coef.

$$F_i := \frac{a_g}{g \cdot \tan(\phi'_d)} = 0.283$$

Dimensionless inertial force of soil

$$N_{max1} := \frac{1}{2} \cdot \rho \cdot g \cdot \left(1 + \frac{a_v}{g}\right) \cdot \left(\pi \cdot \left(\frac{B}{2}\right)^2\right) \cdot B \cdot N_\gamma = 1256351 \text{ kN}$$

$$N_{max2} := \frac{1}{2} \cdot \rho \cdot g \cdot \left(1 - \frac{a_v}{g}\right) \cdot \left(\pi \cdot \left(\frac{B}{2}\right)^2\right) \cdot B \cdot N_\gamma = 1023837 \text{ kN}$$

$$N_{max} := \min(N_{max1}, N_{max2}) = 1023837 \text{ kN}$$

Table F.1 - Incoherent soils

$a := 0.92$	$b := 1.25$	$c := 0.92$	$dd := 1.25$
$ee := 0.41$	$f := 0.32$	$mm := 0.96$	$k := 1.00$
$k' := 0.39$	$c_T := 1.14$	$c_M := 1.01$	$\beta := 2.90$
$\gamma := 2.80$		$c'_M := 1.01$	

$$\gamma_{Rd} := 1$$

Partial Model coef.

$$M_{Ed, res} = 26447 \text{ kN} \cdot \text{m}$$

$$N_{res} := Fz_{res} = 10346.833 \text{ kN}$$

$$V_{res} := F_{res} = 532 \text{ kN}$$

$$N_t := \frac{\gamma_{Rd} \cdot N_{res}}{N_{max}} = 0.01$$

$$V_t := \frac{\gamma_{Rd} \cdot V_{res}}{N_{max}} = 0.001$$

$$M_t := \frac{\gamma_{Rd} \cdot M_{Ed, res}}{B \cdot N_{max}} = 0.002$$

$$0 \leq N_t \leq (1 - mm \cdot F_t)^{k'} = 1$$

Verification of F.8

$$\frac{(1 - ee \cdot F_t)^{c_T} \cdot (\beta \cdot V_t)^{c_T}}{(N_t)^a \cdot \left((1 - mm \cdot F_t)^{k'} - N_t \right)^b} + \frac{(1 - f \cdot F_t)^{c_M} \cdot (\gamma \cdot M_t) \cdot c_M}{(N_t)^c \cdot \left((1 - mm \cdot F_t)^{k'} - N_t \right)^{dd}} = 0.42 < 1$$